GOOGLE INVESTIGATION AND USE OF AN ELASTIN-LIKE PROTEIN, CONTAINING A STATHERIN DERIVED PEPTIDE SEQUENCE, TO CONTROL BIOMIMETIC FLUORAPATITE FORMATION

Kseniya Shuturminska (MEng)

Supervised by Dr Maisoon Al-Jawad, Dr Andy Bushby, Dr Helena Azevedo,
Prof. Paul Anderson and Dr Alvaro Mata

Thesis submitted to the University of London
for the Degree of Doctor of Philosophy

2017

Dental Physical Sciences Unit, Institute of Dentistry,

Barts and the London School of Medicine and Dentistry,

Queen Mary University of London

STATEMENT OF ORIGINALITY

I, Kseniya Shuturminska, confirm that the research included within this thesis is my own work or that where it has been carried out in collaboration with, or supported by others, that this is duly acknowledged below and my contribution indicated. Previously published material is also acknowledged below.

I attest that I have exercised reasonable care to ensure that the work is original, and does not to the best of my knowledge break any UK law, infringe any third party's copyright or other Intellectual Property Right, or contain any confidential material.

I accept that the College has the right to use plagiarism detection software to check the electronic version of the thesis.

I confirm that this thesis has not been previously submitted for the award of a degree by this or any other university.

The copyright of this thesis rests with the author and no quotation from it or information derived from it may be published without the prior written consent of the author.

Signature:

Date:

Details of collaboration and publications:

Collaboration: Some work was designed by KS, MAJ, AM, HA and AJ and carried out by third year Materials Engineering students (MES and MU) for the purpose of their thesis completion. The work, carried out by the third year students, will be accordingly highlighted.

Publication: Shuturminska K, Tarakina NV, Azevedo HS, Bushby AJ, Mata A, Anderson P and Al-Jawad M (2017) Elastin-Like Protein, with Statherin Derived Peptide, Controls Fluorapatite Formation and Morphology. Front. Physiol. 8:368. doi: 10.3389/fphys.2017.00368

ACKNOWLEDGMENTS

I would like to thank my project supervisors Dr Maisoon Al-Jawad, Dr Andy Bushby, Dr Helena Azevedo, Prof. Paul Anderson and Prof Alvaro Mata for all the help, patience and support throughout my PhD. My smooth and enjoyable experience as a PhD student is all thanks to their support and enthusiasm.

I would like to thank the Life Sciences Initiative, QMUL, and the panel of judges who interviewed me for choosing our project and providing the funding for my PhD.

I want to thank all of the members of the groups that I have been lucky to be part of. The list is endless and every single one has helped me in some way at some point or another. I would like to thank Prof. Robert Hill for always finding the time to discuss anything and everything, and always being happy to do so.

I want to thank some students in particular for all the extra support throughout the 3 years. Thank you to Mohammed and Sherif for sharing their knowledge and making conferences an extremely enjoyable experience, to Huda, Linda and Ali for all their support throughout the 3 years. I'd like to thank the Mata Group members, Estelle, Gastón and Esther, for all their help in the lab and out. In the MHAtriCell group I would like to thank Dominic, Elham and Daniella for being patient with me when teaching me peptide synthesis. I would like to thank all the lab managers and lab technicians, without whom the PhD work would be impossible, Jerome, Krystelle, Nadja, Russell, Alice, Chris and Geoff, for always finding the time to help and to train. I would also like to extend my gratitude to Prof. Henry Margolis, Forsyth Institute, and Dr. Seo-Young Kwak, and Dr. Hajime Yamazaki for their welcoming and helpful attitude towards me during my visit in Boston.

I would like to give a special thanks go to my family members, Mum, Dasha and Sofia, for constant support, and for always looking out for my best interests. Finally I

would like to thank my boyfriend, Greg, for his patience, support, motivation and encouragement through the ups and downs of the PhD.

ABSTRACT

Dental enamel is an excellent example of a highly mineralised tissue, composed of hierarchically organised apatite mineral. This unique organisation gives enamel superior mechanical properties. However, when mature, enamel becomes acellular and unable to repair itself during traumatic or carious damage. The lack of self-repair requires dental intervention, where the common treatment of decayed enamel is to remove the affected and healthy tissue, and replace with restorative materials.

The restorative materials, currently used, can cause further complications in the form of secondary caries or failure due to thermal and mechanical property mismatch with enamel. Problems associated with current restorative materials have driven researchers to explore biomimetic enamel treatment routes. To mimic the natural enamel formation, we can explore how proteins can guide mineral growth, in order to form enamel-like ordered mineral structures.

In this thesis, the use of a synthetic, recombinant protein called an elastin-like protein (ELP) containing the analogue of the *N*-terminal of statherin (STNA15) was under investigation. Statherin is a protein present in saliva that is said to aid in the remineralisation of enamel. ELP with STNA15 (STNA15-ELP) has already shown promise in biomimetic mineralisation. This thesis investigated how conformation and structure of STNA15-ELP can be affected and manipulated by different chemical environments, surface constraint and crosslinking. The STNA15-ELP characteristics were related to formation of fluorapatite. STNA15-ELP conformation changed due to presence if salts in solution and whether or not it was constrained. We linked the conformational changes within STNA15-ELP, in solution versus on the surface, to two different routes of mineral formation. FAp formed in an uncontrolled manner with free STNA15-ELP. Ordered FAp formed via a precursor when STNA15-ELP

was constrained on a surface. This work leads to an understanding of biomimetic mineralisation using STNA15-ELP. This information can aid in the design of novel biomimetic, enamel-like therapeutics.

CONTENTS

LIST OF FIGURES

LIST OF TABLES

LIST OF EQUATIONS

LIST OF ABBREVIATIONS

FAp	Fluorapatite
HAp	Hydroxyapatite
ELP	Elastin-like protein
STNA15	Analogue of the 15 amino acid *N*-terminal sequence of statherin
STNA15-ELP	Elastin-like protein containing the analogue of the 15 amino acid *N*-terminal sequence of statherin
SEM	Scanning electron microscope/ microscopy
DEJ	Dentino-enamel junction
CaP	Calcium phosphate
OCP	Octacalcium phosphate
DCPD	Dicalcium phosphate dihydrate
TCP	Tricalcium phosphate
ACP	Amorphous calcium phosphate
TEM	Transmission electron microscope/ microscopy
SAED	Selected area electron diffraction
EM	Electron microscopy
cryo-TEM	Cryo transmission electron microscope
XRD	X-ray diffraction
NMR	Nuclear magnetic resonance
FTIR	Fourier transform infrared spectroscopy
EDX	Energy dispersive X-ray analysis
DSP	Dentine sialoprotein
DPP	Dentine phosphoprotein
BSP	Bone sialoprotein
RGD	Arginine-glycine-aspartic acid

EMP	Enamel matrix protein
STN	*N*-terminal of statherin
STN15	15 amino acid N-terminal sequence of statherin
LRAP	Leucine rich amelogenin peptide
ITT	Inverse transition temperature
CD	Circular dichroism
UV	Ultra violet
SBF	Simulated body fluid
STN11	11 amino acid N-terminal sequence of statherin
DMP-1	Dentine matrix protein 1
LR-ELP	Lysine rich elastin like protein
GTA	Glutaraldehyde
UPW	Ultrapure water
ATR-FTIR	Attenuated Total Reflection Fourier Transform Infrared Spectroscopy
QCM	Quartz crystal microbalance
DLS	Dynamic light scattering
PDMS	polydimethylsiloxane
MRE	Mean residue ellipticity
PTA	phosphotungstic acid
DMAB	didodecyldimethylammonium bromide

Chapter 1. INTRODUCTION

Dental enamel is one of the most complex mineralised structures in the human body. The complexity of enamel arises from its hierarchical structure, which in turn gives it the superior mechanical properties (for detailed properties see for example Habelitz et al., (2001). The elastic modulus of enamel is higher than glass and its hardness is higher than steel (Marshall et al., 1982). Furthermore, enamel has exceptional wear properties in order to stay intact for the whole lifespan of a human being. Enamel is mostly composed of substituted hydroxyapatite, the mineral constituent of all mineralised human tissues (Donnelly and Boskey, 2011). Although hydroxyapatite is common within the human body, the structure it takes on in enamel is unique. A single hydroxyapatite crystal in enamel forms as a nanorod. About a thousand of these crystals align to form a single enamel prism. Each prism is oriented almost perpendicularly to the dentino-enamel junction (Al-Jawad et al., 2007).

The formation of such neatly ordered structures is not an accident. It is well established that enamel biomineralisation occurs via a complex, multistep and matrix mediated process (Simmer and Hu, 2001). The matrix is made up of many macromolecules including glycoproteins and proteins rich in negatively charged residues, such as amelogenin, enamelin and amelotin (Abbarin *et al*., 2015; Iijima *et al*., 2010; Moradian-Oldak and Paine, 2010). These negative residues can bind calcium ions, initiate nucleation and, *via* inhibition and promotion, carefully regulate the crystal growth, morphology and alignment (Mann, 2001). Specifically, biomineralizing proteins have stereochemical matching to crystal surfaces and can inhibit crystal growth in a particular direction. The crystal growth process is further controlled by local pH changes that are said to be crucial in normal enamel development (Lacruz *et al*., 2010).

The impressive hierarchy of enamel comes at a considerable cost – it is completely acellular when fully mature. The process of dental enamel formation is tightly controlled by ameloblasts and produces a highly organised mineral structure that protects us from infection and mastication forces. During enamel maturation, the process of enzymatic protein degradation and removal is essential in order to allow for the apatite crystals to fill up the space. As the tooth erupts, the ameloblasts die, and the mature crystals leave little space for the biomineralising matrix. The end result is a highly mineralised tissue with a high modulus and hardness arising from 96% by weight mineral content (Cuy *et al.*, 2002; Deakins and Volker, 1941; Ferguson *et al.*, 2004). The lack of cells, or proteinaceous mineralising matrix, in mature enamel deems it unable to regenerate. Therefore, unlike bone, when enamel is damaged beyond a certain point it can no longer repair itself and calls for intervention by a dentist.

The most common disease affecting enamel is caries (tooth decay) (Simmer and Hu, 2001). It is prevalent in all countries and amongst all ages. Since enamel is acellular when mature, its repair is purely a materials problem with no cell involvement. Today’s dentistry treats carious lesions by removing infected, and some intact, enamel and filling the excavated cavity with an amalgam or composite material. Although these materials work to some extent, they lack the intrinsic enamel structure and properties. Some filling materials have a hardness value that is half, or even less, of that of enamel tissue (Schmitt *et al.*, 2009). Further complications of treated caries occur due to the mismatch of the mechanical and thermal properties of the tooth and the filling materials. Today, there is no ideal, truly permanent treatment for carious lesions.

Research is now aimed at finding new and innovative ways of forming enamel-like structures for repair or remineralisation of early carious enamel lesions. Examples of these include the formation of enamel prism-like bundles of apatite needles synthesised in solution (Chen *et al*., 2005), the use of casein for remineralisation (Vashisht *et al*., 2010), use of a modified hydroxyapatite paste (Yamagishi *et al*., 2005) and synthetic or natural peptides which promote apatite formation (Brunton *et al*., 2013; Mukherjee *et al*., 2016). These examples provide evidence of ordered hydroxyapatite (HAp) formation, epitaxial growth or remineralisation, but not all at once.

Often, research investigates inclusion of fluoride ions (F^-) into therapeutics such as tooth pastes. The F^- ions can incorporate into the apatite structure by replacing the hydroxide ion (OH^-) located in the middle of the hexagonal apatite crystal. This exchange forms fluorapatite (FAp). The F^- causes a reduction in the a and b unit cell parameters of the apatite structure which directly decreases the crystal energy (Robinson *et al*., 1995). The reduced crystal energy attributes to the increased stability of FAp in acids, compared to HAp, increasing its usefulness in dental applications. FAp has been synthesised in a variety of ways, for example as a coating on implants (Czajka-Jakubowska *et al*., 2009; Dunne *et al*., 2015) or hydrothermally in solution (Chen *et al*., 2006). However, in order to mimic the natural biomineral formation, we must understand how synthetic proteins may be utilised in order to control the nucleation, growth and morphology of FAp, something that is seldom seen in natural biomineralisation.

Recently elastin-like proteins (ELPs) have been exploited for use in synthetic biomineralisation. These are recombinant proteins produced by genetically modified bacteria and can be engineered to contain various bioactive sites (Girotti and Reguera, 2004). One such bioactive site is the analogue of the 15 amino acid *N*-terminal of statherin (STNA15). Statherin, a 43 amino acid protein present in saliva, is thought to aid in the remineralisation of enamel on a daily basis *via* calcium ion chelation. It is believed that statherin's high affinity to apatite arises from its acidic *N*-terminal domain (Raj *et al*., 1992). However, more recent work showed that the basic residues, such as arginine and lysine, also play a crucial role in the interaction of statherin with an apatite surface (Ndao *et al*., 2010). In the STNA15 sequence, the phosphorylated serines (amino acid positions 2 and 3), present in natural statherin, are replaced with aspartic acid (Raj *et al*., 1992), removing the need for post-translational modification and still retaining the calcium affinity. ELP membranes, containing the statherin derived peptide sequence (STNA15-ELP), have already shown potential in bone repair (Tejeda-Montes *et al*., 2014a). We have previously demonstrated the ability of ELPs to form organised apatite structures (Elsharkawy *et al*., 2016a, 2016b).

In this thesis, the literature review (Chapters 2 through to 4) describes the relevant literature background. The literature begins with the structure and function of dental enamel, followed by the important calcium phosphates and their preparation. The review then moves to the present nucleation theories. Although the classic nucleation theories are important to understand, they don't quite fit in with biomineralisation. Biology has been able to induce mineralisation at will in theoretically unfavourable conditions. Therefore, Chapter 3 concludes with, perhaps, the most important section on biomineralisation: the most recent views and theories. Finally, the review settles on proteins involved in biomineralisation. Chapter 4 focuses on the mineralising proteins, natural and synthetic. The relationship of protein sequence and conformation to mineralisation is discussed followed by the recent synthetic proteins used in biomineralisation. The methods of the thesis follow the literature review and are contained within Chapters 6.

The focus of the experimental work presented here is to extend the use of the STNA15-ELP to biomimetic mineralisation for future enamel therapeutic applications. To do so, we study the ability of STNA15-ELP to promote organised fluoridated calcium phosphate structures. Since the structure of proteins is closely related to their function, the first results chapter (Chapter 7) studies the conformation of the elastin-like protein under a number of conditions. The conformational behaviour of ELPs can give some indication of whether it is a suitable protein for synthetic biomineralisation. The thesis then explores the aggregation behaviour of ELPs in Chapter 8. The control of aggregation of ELPs can enable us to control the amount of mineralising sites in one location and hence the mineralisation process. Chapter 9, the final results chapter, delves into the mineralisation of STNA15-ELP. To understand what role STNA15-ELP has in the formation of certain mineral phases and morphologies, the protein is mineralised in constrained and unconstrained conditions, and on different substrates. The minerals formed are characterised chemically and temporally. Finally, the general discussion of the thesis attempts to bring the three results chapters together to link the protein structure to the mineralisation behaviour.

LITERATURE REVIEW

Chapter 2. HYDROXYAPATITE AND OTHER BIOLOGICAL CALCIUM PHOSPHATES

In order to be able to repair and replace dental tissue lost due to caries or trauma, it is first important to understand the enamel structure and how it forms. The outermost layer of the tooth is enamel and is the hardest tissue in the human body. The following layer is the dentine, after which lies the pulp of the tooth. Figure 2.1 shows the structure of the tooth where afore mentioned tissues can be seen in addition to other dental tissues. This work, however, primarily focuses on the repair of enamel and not the other tissues.

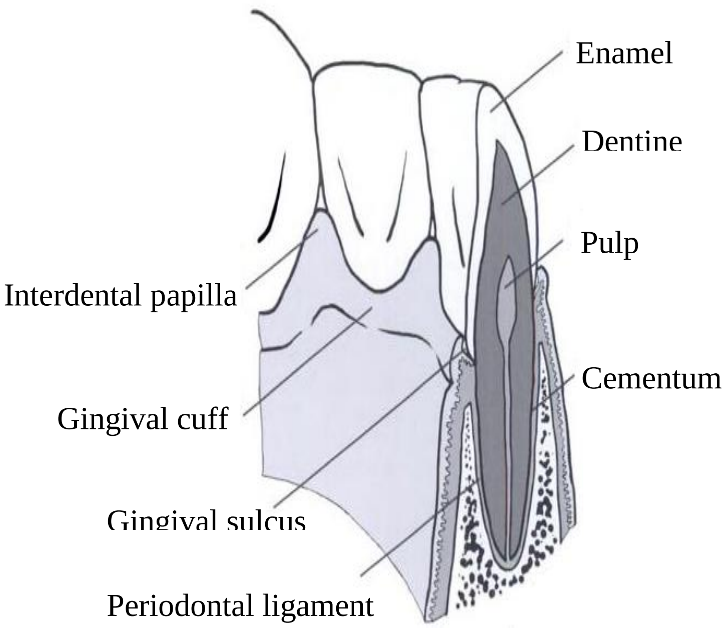

Figure 2.1: The structure of the tooth

This literature review will discuss the enamel tissue structure and its function followed by biologically relevant apatites. To further elucidate the biomineralisation process, the review will discuss nucleation theories, old and new, and the proteins involved in biomineralisation. This will lead to a discussion about synthetic proteins and peptides designed to mimic the natural process of mineral formation and how those have been recently used for mineralised tissue repair.

2.1 Enamel: Composition, Structure and Function

The process of dental enamel formation is tightly controlled by ameloblasts and produces a highly organized mineral structure that protects us from infection and mastication forces. During enamel formation, ameloblasts lay down the protein matrix, primarily made out of amelogenin. The secretion of these proteins initiates nucleation and growth of ribbon-like mineral (Figure 2.2). The mineral crystals continue to grow in length. The length of the crystals is dictated by how long the ameloblasts are able to lay down the matrix (Simmer and Hu, 2001).

The mineral phase of enamel is said to be a carbonated hydroxyapatite (HAp), although in some cases the hydroxyl group (OH^-) can be replaced with fluoride (F^-) to form fluorapatite (FAp). Other substitutions in the structure with ions such as sodium or magnesium can also be found in natural enamel (Al-Jawad *et al*., 2007; Robinson *et al*., 1981, 1995). For HAp in enamel, the lattice parameters are frequently calculated from a powder and therefore give an average value. Recently, synchrotron X-ray diffraction has been used to spatially map enamel crystal size (Al-Jawad *et al*., 2007). This research has shown that in enamel there is a distribution of lattice parameters, according to the position in the enamel and can vary by almost 1%. The difference in the parameters occurs due to differing crystal chemistry such as substitution of ions such as magnesium (Mg^{2+}) and carbonate (CO_3^{2-}).

In enamel, hundreds of HAp crystals, with a similar orientation, assemble together to form enamel prisms. These prisms have a diameter between 3 and 6 µm. The individual prism is created by an individual ameloblast and is separated from the next by an organic-rich layer termed the interprismatic enamel (Mann and Dickinson, 2006). Figure 2.3 shows a scanning electron microscope (SEM) image of natural enamel. In the image P denotes prismatic enamel and IP is the interprismatic enamel. From the image, the alignment of individual HAp crystals can be seen. SEM evidence suggests that the enamel HAp crystals take the form of nanorods. The HAp nanorods have the cross-sectional dimensions of 50 × 25 nm and can have lengths of up to 1 mm, the full enamel thickness. The prisms are arranged almost perpendicularly to the dentino-enamel junction (DEJ) (Al-Jawad *et al*., 2007).

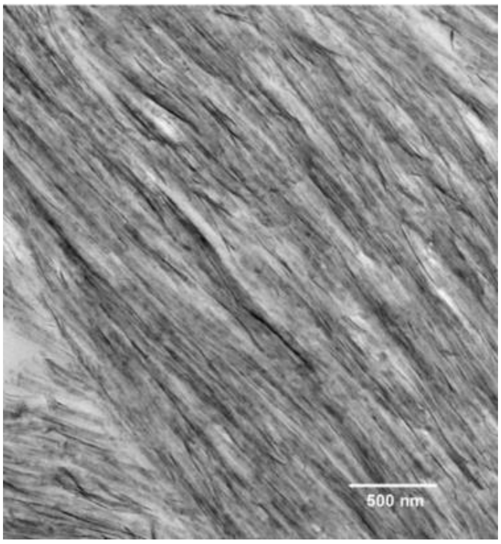

Figure 2.2: Bright field TEM image of secretory stage mouse enamel. Long ribbon-like mineral structures are seen as black lines in the image (Margolis et al., 2014). Reproduced with permission.

Enamel becomes completely acellular and almost completely depleted of the proteinaceous matrix when mature. During enamel maturation, the process of enzymatic protein degradation and removal is essential in order to allow for the apatite crystals to grow in thickness and fill up the majority of space. The end result is a highly mineralised tissue, arising from ~96% by weight mineral content (Cuy *et al*., 2002; Deakins and Volker, 1941). However, the 96% of weight accounts for only 88% of the enamel volume, with the rest taken up by water and proteins, making enamel a permeable tissue (Selvig and Halse, 1972).

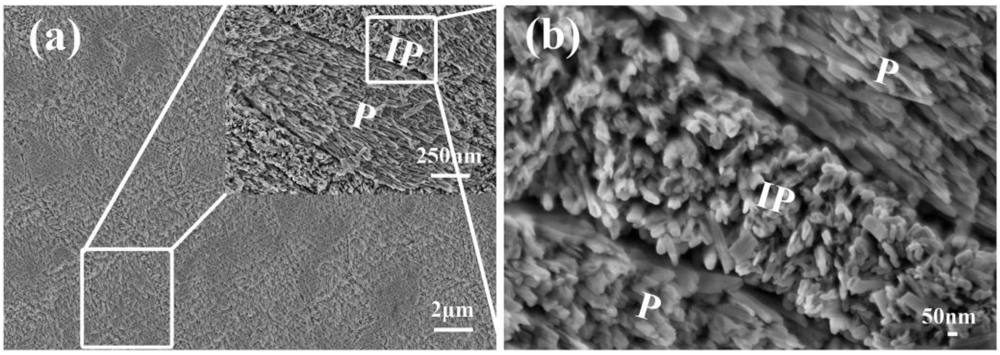

Figure 2.3: SEM images of natural bovine enamel. P) Prismatic enamel, IP) Interprismatic enamel. Adapted from Wang et al., 2015. Reproduced with permission. Copyright 2014 Royal Society of Chemistry.

The toughness of the enamel, related to the complex hierarchical composite structure, is about 3 times larger than that of apatite alone (White *et al*., 2001). Additionally, the high mineral content and the alignment of the crystals give enamel its high hardness (Ferguson *et al*., 2004). Figure 2.4 shows the modulus and hardness maps of enamel produced by nanoindentation mapping. These mapped values were an average of several test results.

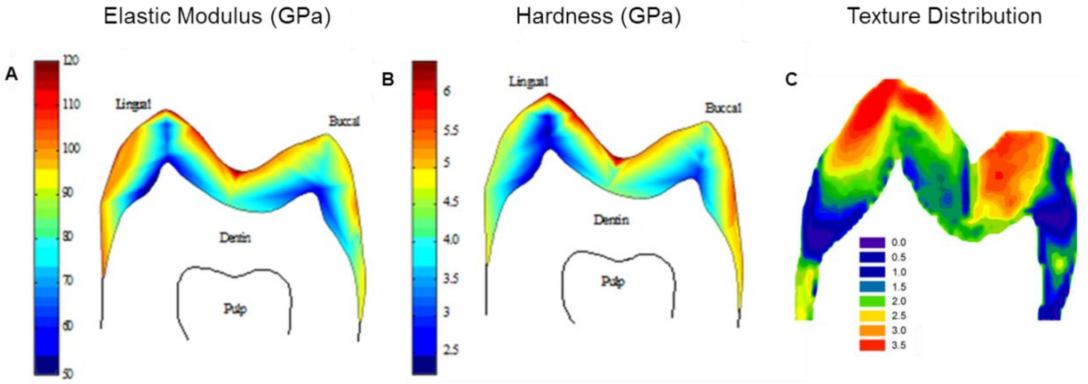

Figure 2.4: The distribution of mechanical properties throughout enamel of a first molar tooth. A) the elastic modulus map and B) the hardness map (Cuy et al. (2002), Copyright 2002 Elsevier) and C) a texture distribution map showing the distribution of crystal alignment within enamel (Al-Jawad et al. (2007), Copyright 2007 Elsevier). Reproduced with permission.

In another study, each indentation was taken as an individual data point (Ferguson *et al.*, 2004). The investigation led to the conclusion that the mechanical properties of enamel can vary from prism to prism, with about 3 fold difference between the lowest observed modulus and the highest. This may be due to the decussation of enamel prisms and not due to changes in mineral content across boundaries between prismatic and interprismatic enamel (see Figure 2.5). The local changes in mechanical properties add another level of complexity to the tissue and therefore creating difficulty in property matching of restorative materials.

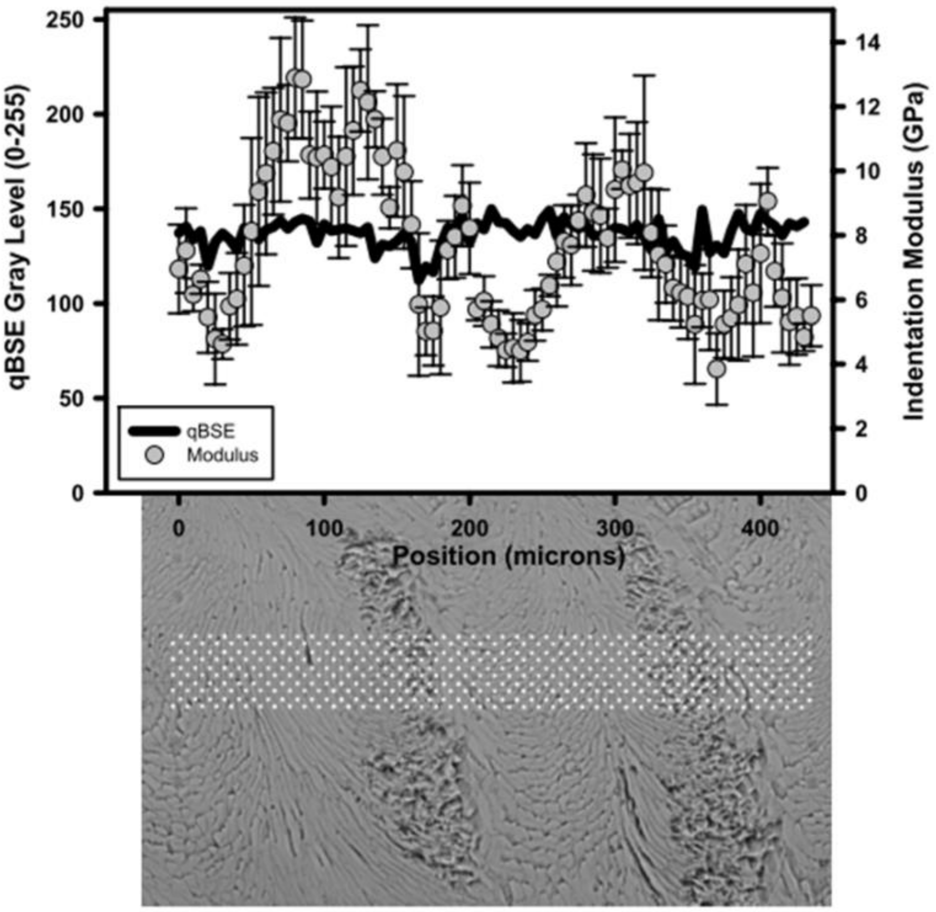

Figure 2.5: Graphed variations of the indentation modulus along the enamel surface shown in the image below the graph. Little variation in mineral content was observed compared to the variations in the modulus (Ferguson et al., 2004). Reproduced with permission. Copyright 2010 Cambridge University Press.

It is clear that, although enamel's properties are excellent, they vary highly across the tissue. The variability of the properties occurs due to the organisation of the crystals within the tissue, further adding to its complexity. Although enamel's hierarchical structure and composition give it its superior mechanical properties, the lack of cells in mature enamel makes it unable to regenerate following damage. Synthetic composite materials do not resemble the natural enamel structure; hence the interest lies in finding a successful biomimetic approach.

2.2 Hydroxyapatite

A number of calcium phosphates, aside from HAp, have been found in biological systems. Calcium phosphates (CaPs) are found from the first instance of mineral formation as well as in pathological calcifications. However, the formation and stability of calcium phosphates is highly dependent on many factors, including pH, supersaturation, temperature and the presence of biomacromolecules. Most calcium phosphates are a white solid and can be sparingly soluble or insoluble in water. However, all calcium phosphates are soluble in acids, the cause of acid erosion of enamel. The pH ranges in which some biologically relevant calcium phosphates are stable in are listed in Table 2.1, accompanied with their calcium to phosphate molar ratios. These CaPs have a range of crystal structures, from monoclinic to hexagonal, which will be described in some detail in section 2.4 Most are stable within physiological pH ranges, hence are readily found in biomineralisation. Those that are stable in a low pH are normally found in pathological calcifications.

Although a number of CaPs have been detected in human biomineralisation, it is HAp that is the mineral constituent of our mature bones and teeth. In biological systems, its formation normally involves a transition through other, less stable, CaP phases (for example Beniash et al. (2009) and Crane et al. (2006)). CaPs which tend to form in pathological calcification are not normally apatitic but consist of another calcium phosphate phase which is stable in acidic conditions, such as brushite or octacalcium phosphate (OCP) (Dorozhkin, 2013).

The stoichiometry of apatites is $Ca_{10}(PO_4)_6X_2$, where X dictates which apatite it is. For example HAp has the formula of $Ca_{10}(PO_4)_6(OH)_2$. Stoichiometric HAp is said to crystallise with a monoclinic crystal structure and space group of $P2_1/b$ (Dorozhkin, 2013). Even though monoclinic apatite is the most stable (Wang and Nancollas, 2008), monoclinic HAp is not commonly seen in mineralised tissues. Mostly, in bones and teeth, HAp appears to exists with a hexagonal crystal structure, the space group $P6_3/m$ and average unit cell parameters of a = 9.4176 and c = 6.8814 Å (Elliott, 1994; Young and Mackie, 1980). These parameters vary depending on the composition of the apatite (Al-Jawad *et al.*, 2007).

Ca/P molar ratio	Compound	pH stability range in an aqueous solution at 25°C
1.0	Brushite/ Dicalcium phosphate dihydrate (DCPD)	2.0-6.0
1.33	Octacalcium phosphate (OCP)	5.5-7.0
1.5	α-Tricalcium phosphate (α-TCP)	-
1.5	*β*- Tricalcium phosphate (*β*-TCP)	-
1.0-2.2	Amorphous calcium phosphate (ACP)	~5.0-12.0
1.5-1.67	Calcium-deficient hydroxyapatite	6.5-9.5
1.67	Hydroxyapatite (HAp)	9.5-12.0
1.67	Fluorapatite (FAp)	7.0-12.0

Table 2.1: A list of Ca/P ratios and pH stability ranges for some biologically relevant calcium phosphates. Adapted from (Dorozhkin, 2010). Reproduced with permission.

Despite the fact that we term biological mineral as HAp it is unusual to see pure HAp in mineralised tissues. Figure 2.6 shows the hexagonal apatite structure that is seen when looking at the crystal down the *c*- axis. The hydroxide ion fits within the crystal structure. However, normally, other substitutions are frequently seen, such as carbonated apatite or fluorapatite. Both carbonate (Yang et al., 2013) and fluoride (Elliott, 1994) ions are said to substitute the OH^- ion in the middle of the apatite crystal.

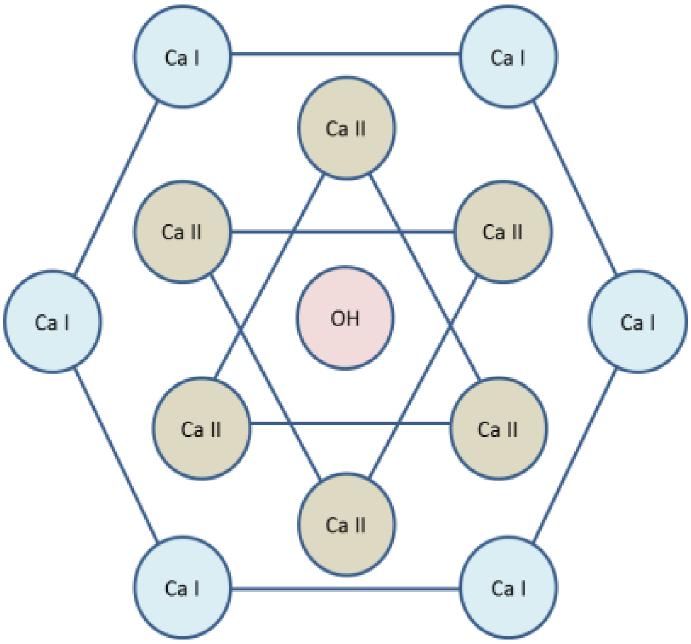

Figure 2.6: Hydroxyapatite structure viewed down the hydroxide ion axis, not showing the phosphate groups. Adapted from Robinson et al. (1995). Reproduced with permission.

Biological apatite has been found to exist in several forms. For example, in enamel it is in a rod form, as seen in Figure 2.3. However, in bone, apatite is found in a plate-like morphology (Wopenka and Pasteris, 2005). This is not common in geological examples, mainly due to the action of proteins on mineral growth in biological systems. Recent advances in microscopy have allowed scientists to probe the bio-apatite structure further. Some have reported that crystallites found in enamel have distinct domains (Robinson *et al.*, 2005). Earlier work, in conjunction with these findings, has given evidence that enamel crystallites are not perfect and are products of smaller particles fusing together causing the final crystals to have these domains (Figure 2.7).

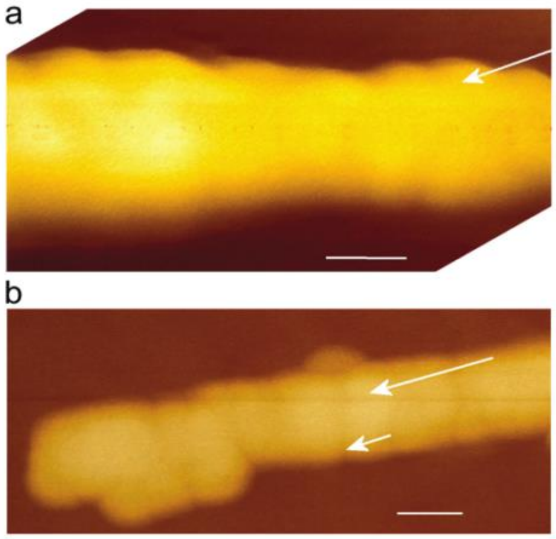

Figure 2.7: AFM images of a) AFM height image of a rat enamel crystal in air and b) AFM image of rat enamel crystal in a fluid (pH6). Long arrows point to subunits within the crystal. The short arrow points to a grove caused by dissolution (Robinson, 2007). Reproduced with permission. Copyright 2007 SAGE Publications.

2.3 Fluorapatite

Fluorapatite (FAp) has the formula of $Ca_{10}(PO_4)_6F_2$. It crystallises with the same crystal structure as HAp. FAp is particularly relevant in dentistry due to its increased stability in acid, compared to HAp. The fluoride ion (F^-) fits well within the hexagonal crystal, replacing the OH^- ion (Figure 2.6). The F^- is smaller and is highly electronegative, leading to a reduction in the *a* and *b* parameters. The resultant unit cell parameters of FAp have been reported as a = 9.391 and c = 6.878 Å (Elliott, 1994). The reduction in the unit cell parameters stabilises the crystal structure, giving a reduced crystal energy and hence the increased stability in acids (Robinson *et al*., 1995).

Fluoride has been added to public water supplies for many years. A long-term study, of 10 years, indicated that 1 p.p.m of fluoride in water greatly reduces the prevalence of caries. By drinking the fluoridated water from a young age, the forming mineral of maturing enamel is able to incorporate F^- and form FAp. Since FAp has increased stability in acids, the subjects in the study had teeth with a higher resistance to acid attacks and therefore a reduction in carious lesion formation (Arnold *et al.*, 1956).

More recent studies looked at the rate at which enamel demineralises in the presence of fluoride (Mohammed *et al.*, 2013, 2014). These studies have found that in the presence of fluoride the demineralisation rate of enamel reduces greatly. The evidence indicates that there is formation of CaF_2 and FAp and together these prevent demineralisation of enamel (Mohammed *et al.*, 2013, 2014).

2.4 Apatite Precursors

HAp in biological systems does not form directly but undergoes a transformation from some transient calcium phosphate (CaP) phase, which is only stable for a short amount of time. Several phases have been proposed to exist before HAp or to transform to HAp. These include tri-calcium phosphate (TCP) (Espanol *et al.*, 2010), octacalcium phosphate (OCP) (Cuisinier *et al.*, 1992), amorphous calcium phosphate (ACP) (Iijima *et al.*, 2010) and brushite (Johnsson and Nancollas, 1992a). The crystal structures and chemical composition of these mostly differ from HAp, having differing amounts of calcium, phosphate and water. The chemical compositions and crystal structures will be described in more detail later.

Different routes of precursor to apatite transformation have been hypothesised. These are surface dissolution and re-precipitation or direct solid state transformation (Mann, 1983). The second route is possible for crystals of similar unit cell parameters. There must also be a low interfacial energy between the old phase and the new for direct solid-state transformation to occur. An example of solid-state transformation is OCP to HAp.

Which CaP phase is present depends on several factors. These include the concentrations of Ca^{2+} and PO_4^{3-} in solution, and on the pH. At physiological pH (7.4), the solubility isotherm (Figure 2.8) expressed as the log of $Ca^{2+} \times PO_4^{3-}$ concentration against pH shows that HAp is the most stable of the calcium phosphates and brushite is the most unstable (the DCPD line in Figure 2.8). However, this is only true for certain pH and concentrations. The following sections will describe the four most important calcium phosphate phases.

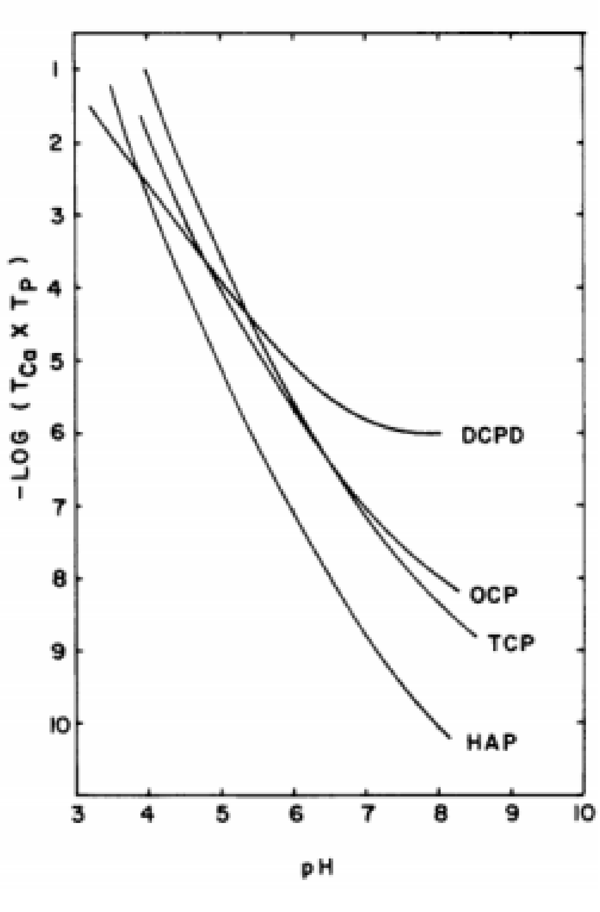

Figure 2.8: Solubility isotherm of several calcium phosphate phases at 37°C. DCPD denotes di-calcium phosphate dihydrate or, otherwise known as, brushite (Elliott, 1994).

2.4.1 Amorphous Calcium Phosphate

Amorphous calcium phosphate (ACP), as a precursor to HAp, was first described in 1965 by Posner (Eanes *et al.*, 1965). However, the existence of ACP remained a debate for several decades after (Boskey, 1997). Out of the several phases that are said to transform to HAp, ACP is the only amorphous one. Typically, in X-ray diffraction of ACP, only a broad amorphous peak is observed.

In 1973 the conversion of ACP to HAp was described by Posner (Dorozhkin, 2011). It was evident that the conversion process is highly pH dependent and needs water for this reaction to occur. The fastest conversion rate was observed at pH below 7. At that point it was speculated that small clusters of HAp made up the ACP particle, albeit the chemical evidence did not fit. In 1980 Posner proposed the ACP cluster model (Figure 2.9) where calcium phosphate clusters make up the particle (Posner *et al.*, 1980). The ACP particle sizes can vary from around 30 to 100 nm in diameter (Dorozhkin, 2010).

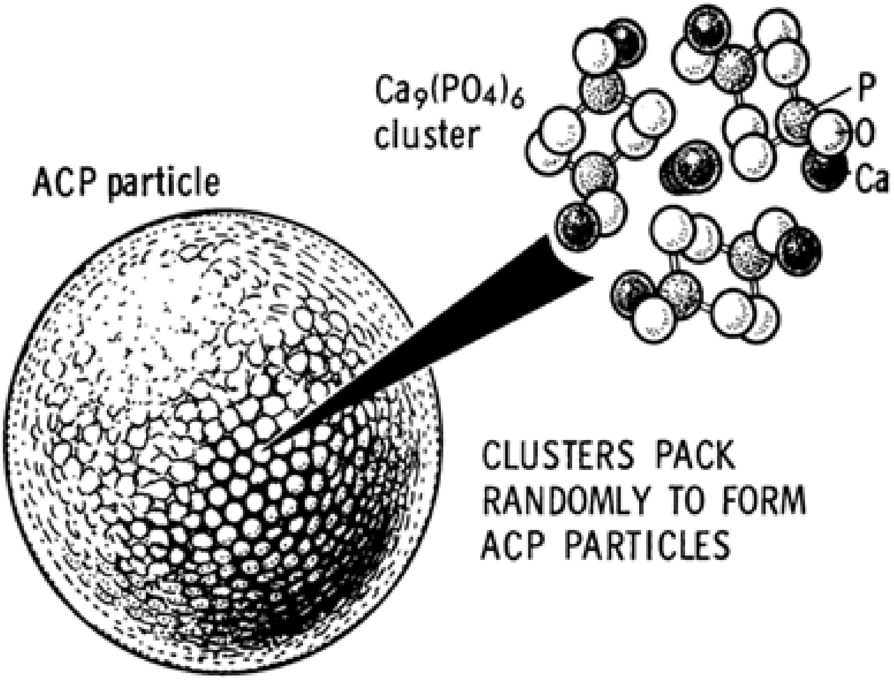

Figure 2.9: ACP cluster model developed by A. Posner (Posner et al., 1980). Reproduced with permission. Copyright 1980 Elsevier.

Today, ACP is widely accepted as a precursor of HAp in biological systems. The relation of the ACP structure to the apatite structure can be seen in Figure 2.10. ACP has been reported as a transient phase during HAp formation in the presence of proteins during biomineralisation (Beniash *et al.*, 2009; Le Norcy *et al.*, 2011a, 2011b) and in mineralising solutions without proteins (Habraken *et al.*, 2013). Furthermore, the domain structure of HAp, for example as the one seen in enamel, has been described to occur due to the initial alignment of protein stabilised ACP particles that phase transform into apatite (Robinson, 2007). Due to its presence in early enamel formation, ACP has also found use in dental applications (Zhao *et al.*, 2011).

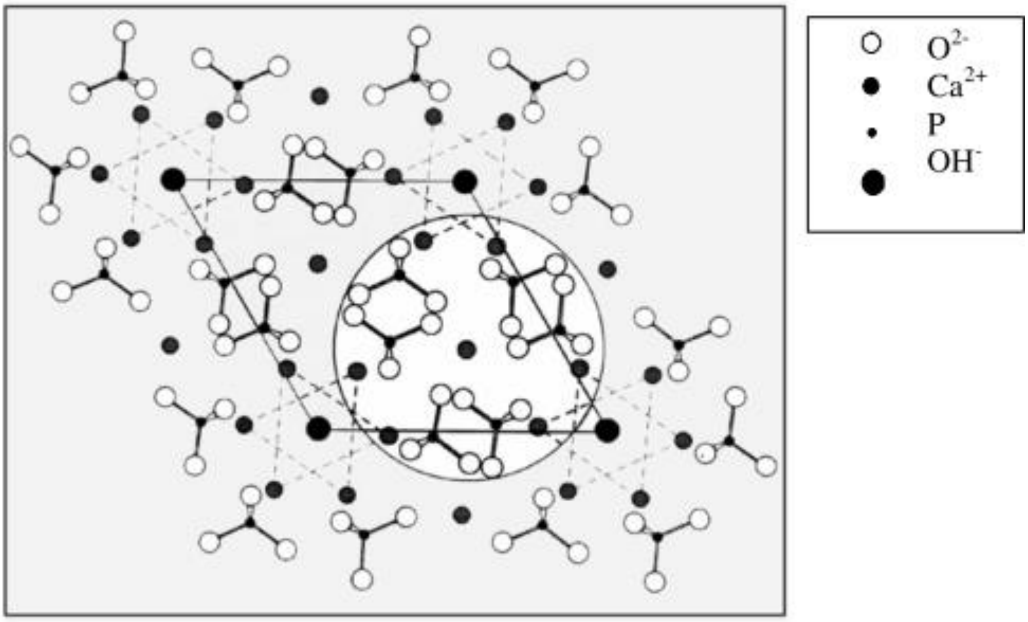

Figure 2.10: The relation of the ACP chemical structure (encircled) to the HAp chemical structure. Adapted from Combes and Rey, 2010. Reproduced with permission. Copyright 2010 Elsevier.

2.4.2 Brushite

Brushite, with the formula of $CaHPO_4.2H_2O$, has a monoclinic crystal structure with a space group *I*112/*m*. Its unit cell parameters are: *a*=6.41 Å, *b*=15.18 Å and *c*= 5.86

Å (Sainz-Díaz *et al*., 2004). In brushite, chains of $CaPO_4$ are separated by layers of water (Johnsson and Nancollas, 1992a). Upon transformation to HAp brushite is said to undergo dehydration and therefore the crystal shrinks in size (Chow and Brown, 1973). Although brushite is mostly found in pathological calcifications, such as kidney stones, it has found uses in coatings where it acts as a bioactive material that is able to transform to HAp (Kumar *et al*., 1999).

Some studies suggest that brushite forms during demineralisation of enamel (Chow and Brown, 1975; Shellis *et al*., 1997). The formation of brushite on enamel occurs during acid attack, causing the dissolution of apatite. Perhaps it is actually the re-precipitation of calcium phosphate that is observed, since brushite is said to form in conditions that are more acidic in comparison to those that favour apatite formation (Table 2.1).

2.4.3 Octacalcium Phosphate

For a long time octacalcium phosphate (OCP) has been considered as the precursor to bioapatite formation (Brown *et al*., 1987). OCP has also been reported to occur in pathological calcifications such as dental calculus (Kakei *et al*., 2009). Similar to brushite, OCP formation is favoured at lower pH compared to HAp (Table 2.1).

OCP crystals have a triclinic lattice with a P-1 space group. Reported OCP unit cell parameters are: a=19.6920, b=9.5230, c=6.8350 (Mathew *et al*., 1988). The OCP structure is said to consist of apatitic layers which are separated by water molecules (Brown *et al*., 1979). However, OCP has only one fifth of brushite’s water content. The water content in OCP has been linked to its solubility, which is lower than that of apatite (Wang and Nancollas, 2008). The apatite that forms from OCP has been termed as the most acidic apatite and therefore a defect apatite (Brown *et al*., 1957).

The acidity arises from H^+ ion inclusion within the structure in order to maintain electrical neutrality (Posner and Perloff, 1957).

2.4.4 Tri-calcium phosphate

Tri-calcium phosphate (TCP) is found in pathological calcifications such as dental calculus. One TCP unit has the formula of $Ca_3(PO_4)_2$. TCP has a rhombohedral crystal lattice with the space group *R3c* (Elliott, 1994). The form of TCP found in dental calculus is β –TCP or whitlockite. β –TCP contains calcium ion vacancies that cause it to be unstable. However, this also allows for ion inclusions in the lattice which can stabilise the crystal. In Whitlockite this space is filled with magnesium ions (Wang and Nancollas, 2008).

2.5 Synthetic Apatite Preparation

In general, for apatite preparation a calcium and phosphate containing solution of pH higher than 7 has to be heated to some extent (usually a biological temperature of 37°C, sometimes more) and sometimes subjected to increased pressures (for example Chen *et al*., 2005, 2006). Increased temperatures, such as 70 °C, can promote the formation of stoichiometric FAp crystallites within 5 days (Chen *et al*., 2006). However, these crystals are short and thin, in comparison to enamel HAp. Subjecting the same mineralising solution to much higher temperatures and pressures of 2 atm can increase the crystal width to widths which are comparable to enamel HAp.

Many studies have been conducted on the use of apatite coating for implants in order to increase bioactivity. In these cases the apatite is grown on bioactive surfaces such as titanium (Aparicio *et al*., 2007; Ciobanu *et al*., 2008, 2009). Apatite formation on titanium surfaces is achieved through a multistep process whereby the surface is first pre-treated with sodium hydroxide and then soaked in simulated body fluid (SBF)

(Kokubo *et al*., 2004). Other calcium phosphate coatings have also been used as they are known to transform to apatite *in vivo* (e.g. brushite) (Brundavanam *et al*., 2014).

During any preparation of apatite it is important to consider the solubility isotherm described by Elliott (1994) (Figure 2.8). Some calcium phosphates form in acidic conditions whilst others, such as HAp, form under basic conditions. However, the formation also depends on the calcium concentration in solution. In general, the solution has to be supersaturated with respect to the desired phase. For example, in the oral environment the saliva concentration is around 1 mmol, however the pH is highly variable. From Figure 2.11, at a salivary calcium concentration, it would seem that hydroxyapatite would precipitate out of solution when the pH of saliva rises above 6, but our enamel would dissolve. In reality, dental enamel can be quite stable in slightly acidic conditions due to the complexity of the oral environment. The reason for this will be further described in Chapter 3.

In the oral environment, F^- containing therapeutics, such as toothpastes and mouthwashes, are used in order to form FAp on the enamel surface. However, the treatment of HAp with F^- gives poor yields of FAp due to low penetration of F^- ions into the existing apatite. The HAp to FAp transformation occurs with little crystal volume change since the two compounds are isostructural. A layer of FAp would first form on the HAp crystal surface and the following reaction is expected to be a solid state transformation, requiring long periods of time for full transformation. On the other hand, brushite to FAp transformation occurs much faster due to the shrinkage of brushite crystals via the loss of water during the reaction with F^- (Chow and Brown, 1973). The shrinking crystals allow fluoride ions to penetrate deep into the structure, eventually forming FAp. However, in order to form brushite mineral on the surface of the tooth, the enamel must be treated with acid and essentially partially demineralise the surface of the tooth and can be detrimental to the surrounding sound enamel. In normal oral conditions teeth are subjected to acidic environments, due to ingested food or acid produced by bacteria as a by-product of metabolic activity. Therefore, teeth may not need to be treated with acidic solution to demineralise the outer enamel layer in order to increase the efficiency of FAp formation. Instead, the natural acidic environment created during the day in the oral cavity can be taken advantage of.

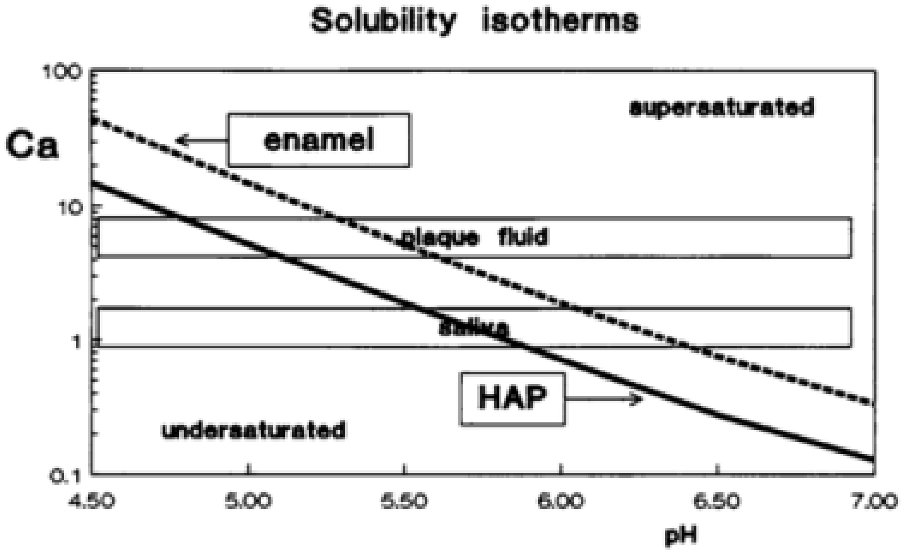

Figure 2.11: Solubility isotherms of enamel and hydroxyapatite compared to concentrations and pH of saliva and plaque fluid (Ten Cate and Featherstone, 1991). Reproduced with permission.

When enamel is treated with high concentrations of fluoride, calcium fluoride (CaF_2) is likely to form on the tooth surfaces along with FAp (Mohammed *et al.,* 2014). Unlike HAp or FAp, CaF_2 is extremely stable in acidic environments (Gerould, 1945). The formation of the stable CaF_2 layer has been said to act as a protective layer and prevent demineralisation of enamel (Ganss *et al.*, 1998). However, considering the fact that CaF_2 is stable in acids, the presence of CaF_2 has been said to be unfavourable in oral environments since it locks away Ca^{2+} ions and therefore can aid in further enamel dissolution (Mohammed *et al*., 2013).

The above routes of apatite formation do not resemble the natural biomineralisation process. Methods that do resemble natural biomineralisation involve the use of proteins or peptides and some have been successful in bone regeneration (Tejeda-Montes *et al.*, 2014a), and enamel remineralisation (Kirkham *et al.*, 2007). In these cases a protein or peptide is used with an amino acid sequence that has known mineralising capabilities. The solution in which they are incubated is again supersaturated with respect to apatite and the pH is often buffered at a physiological value of 7.4. However, when considering enamel biomimetics, these routes are still lacking in providing a guiding scaffold that is able to promote oriented growth of enamel-like structures.

In Summary: The evidence for amorphous phases present before the formation of crystalline phases has been seen in enamel. Likewise, there is sufficient evidence for the existence of the crystalline calcium phosphate phases, described here, in biomineralisation. However, the process of biological calcium phosphate formation is still poorly understood. This, in part, is due to the complexity of the environment in which it occurs. Therefore, great care must be taken in the analysis of mineral phases formed via biomimetic mineralisation to build an accurate picture. The synthetic routes have been able to produce various CaP phases but not always with the crystal morphology seen in nature. To understand the basic nucleation and crystal growth processes it is imperative to understand the classical nucleation theory, described next.

Chapter 3. CRYSTAL NUCLEATION AND GROWTH

3.1 Gibb's Free Energy

The formation of crystals consists of two stages: nucleation and growth. Nucleation is, arguably, the most important step in the formation of the mineral. By controlling nucleation the crystal size, size distribution and other properties can be controlled. In 1870's Gibbs published the thermodynamic part of the classical nucleation theory (Gibbs, 1876). From those publications we now have the Gibb's free energy, describing the energy of nucleation. The Gibb's free energy of nucleation ($\Delta G(n)$) (Figure 3.1), for a nucleus of a critical size n, is the total of two terms, the surface energy and the volume energy. Assuming the initial cluster is cubic, rather than a liquid droplet as initially described by Gibbs, $\Delta G\ (n)$ can be defined by equation 3.1 (Vekilov, 2010):

$$\boldsymbol{\Delta G(n) = -n\Delta\mu + 6a^2}$$

Equation 3.1

Here, $-n\Delta\mu$ is the free energy loss due to the formation of a cluster (volume energy) where $\Delta\mu$ is the difference in supersaturation between the solute and the crystal. Vekilov (2010) describes $\Delta\mu$ to be greater than 0 i.e. the chemical potential of the solute must be more than the molecules within a crystal. $6a^2n^{2/3}\alpha = S\alpha$ is the free energy gain due to the creation of a boundary of an S area and the surface free energy, α, between the solution and the cluster. Furthermore, n denotes the nucleus size a^2 the surface area of the nucleus.

A differentiation of equation 3.1 gives the critical nucleus size needed for a stable nucleus (n^*) and the energy barrier to be overcome to form a stable nucleus (ΔG^*) in the following terms:

$$n^* = \frac{64\Omega^2\alpha^3}{\Delta\mu^3}$$

Equation 3.2

$$\Delta G^* = \frac{32\Omega^2\alpha^3}{\Delta\mu^2} = \frac{1}{2}n^* \times \Delta\mu$$

Equation 3.3

where $\Omega = a^3$ defines the volume occupied by a molecule. Equation 3.3 describes the critical nucleus size, for which ΔG is at its maximum (ΔG^*) (see Figure 3.1).

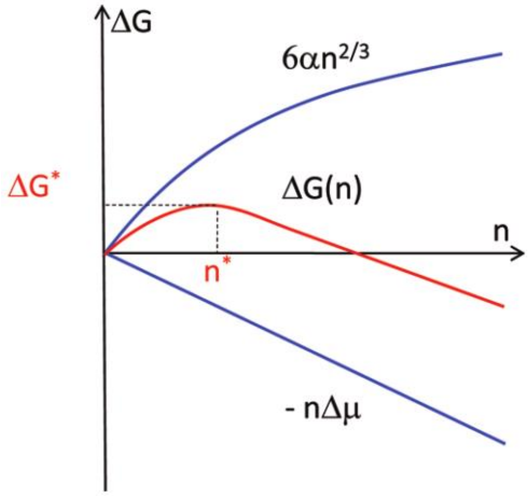

Figure 3.1: Thermodynamic effect of nucleus formation. ΔG* denotes Gibb's free energy, n* the critical nucleus size required for a stable nucleus to form (Vekilov, 2010). Reproduced with permission. Copyright 2010 American Chemical Society.

Examination of Figure 3.1 tells us that the formation of a nucleus of a size below n^* must cause an increase in the free energy and therefore is unfavourable. However, as soon as the nucleus size exceeds n^*, and ΔG starts decreasing, spontaneous growth can occur since an increasing n diameter becomes energetically favourable.

3.2 Thermodynamics of Nucleation

Several orders of phase transitions exist, most common of which are first and second-order (Cambridge, 2015). First-order transitions are discontinuous and second order transitions are continuous. Here the interest lies in first-order phase transition. This transition occurs when a metastable phase transforms into a new truly stable phase. Supersaturation (Δμ) is the thermodynamic driving force for the first-order phase transition process and is described by the minimum Gibb's free energy of the old and the new phases with the following equation (Kashchiev, 2000):

$$\boldsymbol{\Delta}\mu \equiv \frac{\boldsymbol{G_{old} - G_{new}}}{\boldsymbol{M}} \equiv \mu_{\boldsymbol{old}} - \mu_{\boldsymbol{new}}$$

Equation 3.4

G_{old} and G_{new} are the lowest Gibb's free energy of the metastable phase and the lowest Gibb's free energy of the new stable phase, respectively, μ is the chemical potential of each phase and M is the number of molecules.

3.2.1 Homogeneous Nucleation

Two types of nucleation processes exist, homogeneous and heterogeneous. Homogeneous nucleation occurs when the new phase is formed only from the old phase (i.e. from a solution to a solid crystal), without the influence of any other phases or particles. If we assume the new phase is when a cluster of particles is of n size (n=1, 2…) the energy of the old phase (G_1) and the new phase (G_2 (n)) can be defined by:

$$\boldsymbol{G_1 = M\mu_{old}}$$

Equation 3.5

$$\boldsymbol{G_2(n) = (M - n)\mu_{old} + G(n)}$$

Equation 3.6

G (n) considers the energy change that accompanies the formation of the n sized particle. If we consider the new cluster to be a part of the new bulk phase then we can describe the Gibb's free energy for this particle in $n\mu_{new}$ terms as:

$$\boldsymbol{G(n) = n\mu_{new} + G_{ex}(n)}$$

Equation 3.7

where $G_{ex}(n)$ is the cluster excess energy (Kashchiev, 2000).

The work done to form the cluster can then be expressed as the difference between G_1 and $G_2(n)$, giving:

$$\boldsymbol{W(n) = -n\Delta\mu + G_{ex}(n)}$$

Equation 3.8

3.2.2 Heterogeneous Nucleation

In contrast heterogeneous nucleation occurs in the presence of other external phases and/ or molecules. This process is commonly seen in nature, including the biomineralisation processes discussed in this work (for example see Rey et al., 2009). The free energy equations for heterogeneous nucleation must include a surface energy of the substrate/ old phase interface and substrate/new phase interface, $\varphi_{s,0}$ and $\varphi_s(n)$, respectively. The homogeneous equations for G_1 and $G_2(n)$ can now be modified and given as:

$$\boldsymbol{G_1 = M\mu_{old} + G_s + \varphi_{s,0}(n)}$$

Equation 3.9

$$\boldsymbol{G_2(n) = (M - n)\mu_{old} + G(n) + G_s + \varphi_s(n)}$$

Equation 3.10

The cluster Gibb’s free energy, G_n, can be expressed as previously, therefore giving the work of heterogeneous nucleus formation as:

$$\boldsymbol{W(n) = -n\Delta\mu + G_{ex}(n) + \varphi_s(n) - \varphi_{s,0}}$$

Equation 3.11

Equations 3.8 and 3.11 suggest that for heterogeneous nucleation $G_{ex}(n) + \varphi_s(n) - \varphi_{s,0}$ has to be sufficiently small, compared to homogenous nucleation, in order for it to be more favourable than homogeneous nucleation. Heterogeneous nucleation is more likely to occur in most circumstances since external substrates reduce the energy required to overcome the barrier for nucleation.

3.3 Kinetics of Nucleation

The thermodynamics of nucleation give a description of the cluster as a static formation that exists in a thermodynamic equilibrium. In real nucleation processes these small clusters only exist for nano-seconds, or less. It is therefore important to consider the kinetic aspect of the nucleation process. To do so two critical assumptions must be made (Kashchiev, 2000):

1. Clusters of the old phase exist with n number of molecules/ atoms ($n=1, 2\ldots$)
2. A time dependent frequency is assigned to the transformation of n-sized particle to m-sized: $f_{nm}\,(t)\,(s^{-1})$ ($n, m=1, 2\ldots$).

Volmer (1939) hypothesized that the model of the nucleation rate, J, can be expressed by

$$\boldsymbol{J = J_0 exp(-\Delta G^*/k_B T)}$$

Equation 3.12

where k_B is the Boltzmann constant and T is the Kelvin temperature. According to equation 3.12 environmental factors such as the pressure, temperature and concentration do not have a great effect on the nucleation rate. However, they do influence ΔG to a larger extent, whereby ΔG may decrease with increasing T or k_B (Vekilov, 2010).

Further derivations of the rate of nucleation has given the following expression

$$\boldsymbol{J = v^* Z n exp(-\Delta G^*/k_B T)}$$

Equation 3.13

where v* denotes the rate of attachment of monomers to the nucleus, Z, Zeldovich factor, gives the width of the ΔG profile where ΔG is at its highest and n accounts for the number of molecules present in the solution. In reality, the nucleation rate is actually 10 times slower than equation 3.13 predicts (Vekilov, 2010). The nucleation rate is slower than expected because the effect of dissolving nuclei on the concentration is not considered.

The rate of nucleation can be compared for heterogeneous and homogenous nucleation (Figure 3.2). The rate of heterogeneous nucleation, in the presence of particles with the same nucleation efficiency, is constant for all supersaturation levels, up to the threshold for homogenous nucleation (S_R^*). However, homogenous nucleation cannot be controlled and the rate increases as the supersaturation increases.

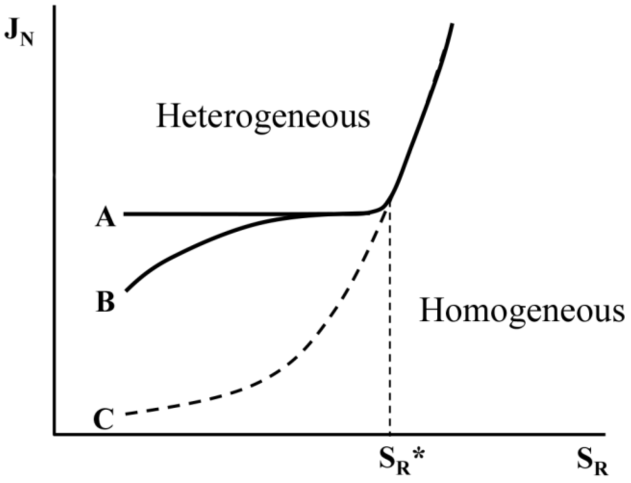

Figure 3.2: Rate of nucleation (J_N) vs supersaturation (S_R). Heterogeneous nucleation rate A) in the presence of particles with equal nucleation efficiency, B) in the presence of particles with variable nucleation efficiency and C) homogenous nucleation (no extraneous particles). S_R^* denotes the threshold for homogenous nucleation. (Mann, 2001)

3.4 The Two-Step Nucleation Mechanism

Equation 3.13 makes an assumption that the monomer directly interacts with the crystalline nucleus. However, generally in biomineralisation this is not the case and an amorphous phase is present before the crystalline phase exists. A mechanism which best describes this type of crystal formation is a two-step mechanism of nucleation (Vekilov, 2010). Literature describes an initial amorphous phase, in biomineralization, as an amorphous liquid-phase precursor (Gower and Odom, 2000). This amorphous phase is said to be a highly hydrated cluster of proteins and ions with an average diameter of 1-2 μm (Gower and Odom, 2000; Olszta et al., 2003). The two-step mechanism suggests the formation of a dense liquid phase by overcoming an initial ΔG_1. This liquid phase in calcium phosphates may contain ACP, highly hydrated particles made up of many calcium phosphate molecules. The second step has to overcome ΔG_2 in order to transition to a crystalline phase (Vekilov, 2010). The two-step mechanism, illustrated in Figure 3.3, is still not complex enough to describe the biomineralisation process. A pathway with many steps from a solution species to a truly stable crystalline phase has been proposed not long after the presence of ACP was accepted (Mann, 1983).

In an extensive review of biomineralisation, Gower (2008) describes the polymer-induced liquid precursor (PILP). She describes the early precursor stage to have a "liquid-like character" as it is highly hydrated. In Gower's publication calcium carbonate was the focus but the principle can be extended to calcium phosphates. Furthermore, the text refers to the Ostwald-Lussac rule of stages. The rule states if a solution is supersaturated with respect to several phases, the least stable phase with highest solubility will be the first phase formed (Gower, 2008). Indeed this is what is known to occur in the formation of biological apatites (for example Dey et al., 2010; Johnsson and Nancollas, 1992b).

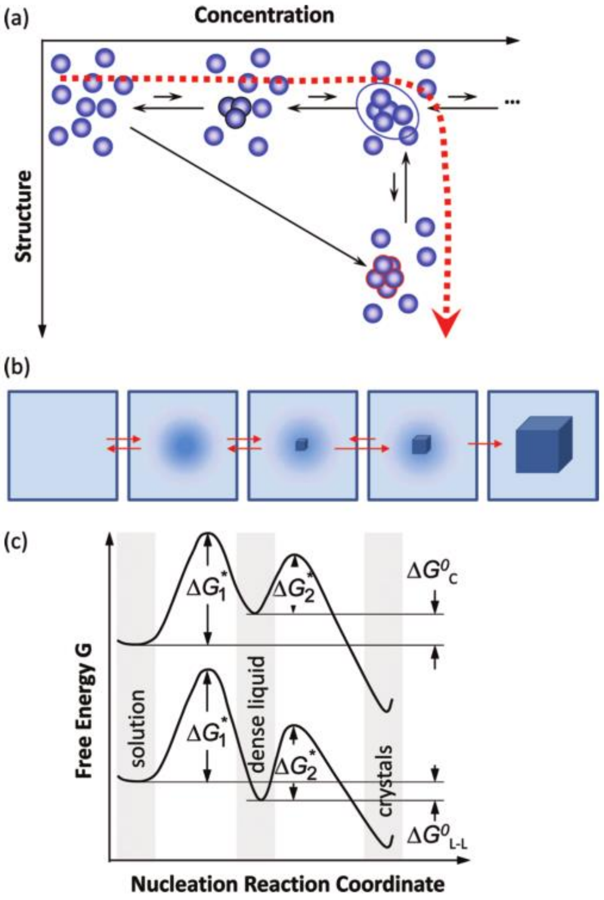

Figure 3.3: A schematic representation of the two-step nucleation mechanism. a) A microscopic representation of the concentration/ structure graph, b) a macroscopic representation following the dashed red line, c) the free energy graph of two possible nucleation routes (Vekilov, 2010). Copyright 2010 American Chemical Society.

3.5 Current Views and Theories on the Biomineralisation Process

Before Posner's description of the ACP particle, its presence was purely speculation. The discovery of ACP changed the view on biomineralisation significantly. However, for decades amorphous phases have been notoriously elusive. Recent technologic advances have allowed scientists to model (Demichelis et al., 2011) and, more importantly, view (Habraken et al., 2013) the process of nucleation as it is happening. The ability to see nucleation live has led scientist to probe the process of biomineralisation at time points that are earlier than the appearance of ACP, providing more interesting and novel theories and views. Faster computers, better microscopes and higher resolution have led to further development of the traditional biomineralisation views. The previous sections of this review have, in some detail, described relevant CaPs and how they nucleate and grow. However, the complexity of the multistep biomineralisation process calls for an understanding of how these phases can be identified from the very first metastable phase to the final stable phase. In this section, the characterisation of apatites will be discussed alongside recent developments of well-known techniques to build a picture of what we know regarding the multistep biomineralisation and how we came to know it.

3.5.1 Modelling Biomineralisation

Since Gibb's initial publication, the nucleation theory has been revisited numerous times. The model acts as a basis to further understand the nucleation process. Recently, basic understanding of heterogeneous nucleation was used to understand the role of different protein side-groups in the nucleation process (Hamm *et al*., 2014). Since heterogeneous nucleation depends on external effects of a substrate (e.g. proteins), interfacial energy (γ) between the forming crystal and the substrate are first considered with the following equation:

$$\boldsymbol{\gamma = \gamma_{CL} - h(\gamma_{SL} - \gamma_{CS})}$$

Equation 3.14

In, γ_{CL} is derived from the interaction of the crystal with the liquid, γ_{SL} from the substrate and liquid interaction and γ_{CS} from the crystal-substrate interaction, and the constant h describes the relative surface areas of the interfaces present between the crystal and the substrate, and between the crystal and the liquid. We can now consider the free energy of binding between a crystal and the template it formed on with the following equation (ΔG_b):

$$\boldsymbol{\Delta G_b = a(\gamma_{CL} + \gamma_{SL}) - a\gamma_{CS}}$$

Equation 3.15

Where a can be described as the total contact area of the crystal and a given substrate. ΔG_b is the difference in free energy of a crystal bound to a substrate and the free energy of an unbound crystal. When equation 2.14 and 2.15 are combined, the following expression is achieved:

$$\boldsymbol{\gamma = -\frac{h}{a}\Delta G_b + (1 + h)\gamma_{CL}}$$

Equation 3.16

Furthermore, the thermodynamic barrier to formation of a nucleus of a critical size (with a volume of a^3) can be given by the following equation:

$$\boldsymbol{\Delta G^* = \frac{Fa^6\gamma^2}{\sigma^2 k_B^2 T^2}}$$

Equation 3.17

Where T is the temperature, F is a nucleus shape dependent constant and σ is the supersaturation of ions. Looking at equations 3.16 and 3.17 it is clear to see that the interfacial energy (γ) has an effect on both the binding energy of the crystal to the substrate (ΔG_b) and on the energy barrier to forming a critical nucleus size (ΔG^*).

When considering the organic matrix as a substrate, it is commonly believed that carboxylic side groups and phosphorylated serines are the nucleating groups (more detail given later). However, Hamm *et al.* (2014) found, through the application of equations 2.14-2.17, that monolayers of thiols and phosphates are also effective nucleators. These findings shed a new light on the view of biomineralisation and may be used in future designs of biomimetic mineralising systems.

Hamm *et al*. (2014) publication brings us one step closer to understanding the initial interaction of protein side groups with ionic species both numerically and experimentally. However, even before the ionic species come into contact with organic matrices, there is still more to be known about the ionic clusters that form in saturated solutions. A simplified view of nucleation in biomineralisation is the initial binding of an ion, in most cases calcium, to a carboxylic group, followed by binding of anions. Demichelis *et al*., (2011) modelled the formation of pre-nucleation calcium carbonate clusters. They found that, initially, ions form chain-like structures which are held together by ionic forces. Due to the dynamic nature of the bonds within the clusters, the chains constantly break and reform. The formation of chains was reported to occur in a range of pH and concentrations (Figure 3.4).

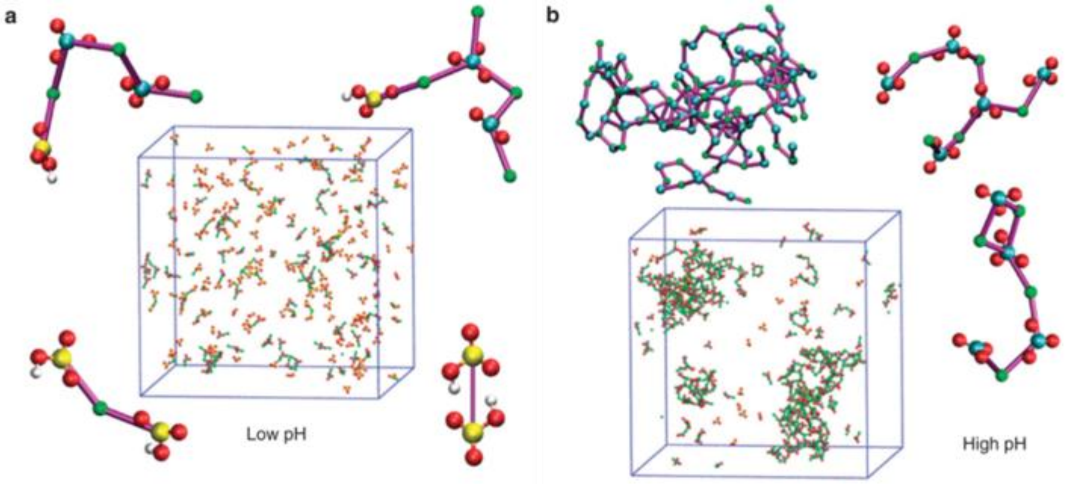

Figure 3.4: Simulation of polymer-like calcium carbonate chains forming in low pH (a) and high pH (b) (Demichelis et al., 2011). Reproduced with permission. Copyright 2011 Nature Publishing Group.

3.5.2 Characterising Biomineralisation

Transmission electron microscopy (TEM) is a widely used technique for characterisation of minerals. However, previous TEM studies of biominerals proved to be difficult for a number of reasons. TEM is normally operated at high voltages, from 100 kV to 200 kV, and therefore the biggest obstacle for this technique is the thermal stability of the material in the electron beam. Under high voltage beams, unstable crystals sustain beam damage, undergo dehydration and can transform phases. This problem is not often seen with apatite crystals, but is common with apatite precursors such as brushite (Dosen and Giese, 2011) and OCP (Kakei *et al*., 2009). In one particular example, the beam damage was taken advantage of in order to observe the phase transformation of OCP to HAp (Xin *et al*., 2006). However, in most cases this transformation is more of a hindrance than an advantage. One advantage of using a TEM is having a high-energy beam that is used for *in situ* selected area electron diffraction (SAED). SAED can be used to distinguish most CaP phases.

With increasing popularity of cryo-electron microscopy (EM) techniques in the past decade, it is no surprise that the biomineralisation process became scrutinised by it. Its popularity may be attributed to the fact that using cryo-transmission electron microscopy (cryo-TEM) for analysing early minerals can overcome the problem of beam damage and phase instability. In 2010 Dey *et al*., using the cryo-TEM technique, found the presence of small ionic clusters within a simulated body fluid solution. The clusters densify, at a nucleating interface, and form amorphous particles. The presence of clusters has been described decades before the Dey *et al.* findings (Onuma and Ito, 1998). However, in 1998 microscopy techniques were limited and so such pre-nucleation clusters were difficult to see and were only confirmed with light-scattering techniques.

Later, Habraken *et al*., (2013) published an in depth study of calcium phosphate nucleation in a Cryo-TEM, in order to further understand the role of the pre-nucleation clusters. Upon mixing calcium and phosphate solutions, calcium phosphates were said to form in strands composed of nano-sized ionic units, similar to the computational findings described for calcium carbonate. These strands develop into branched networks and grow nodules. Each structural conformation of the developing strand is accompanied with changes in pH and calcium concentration, suggesting that each structure is a phase in itself (Figure 3.5a). However, within the first few minutes there are negligible changes in pH and calcium concentration, indicating that the initial polymeric structures seen are not a CaP phase (CaP formation is normally accompanied with a drop in pH, for example see Kwak et al., 2011). Therefore, the polymeric structures are likely to be the pre-nucleation clusters that aggregate and transform to ACP particles.

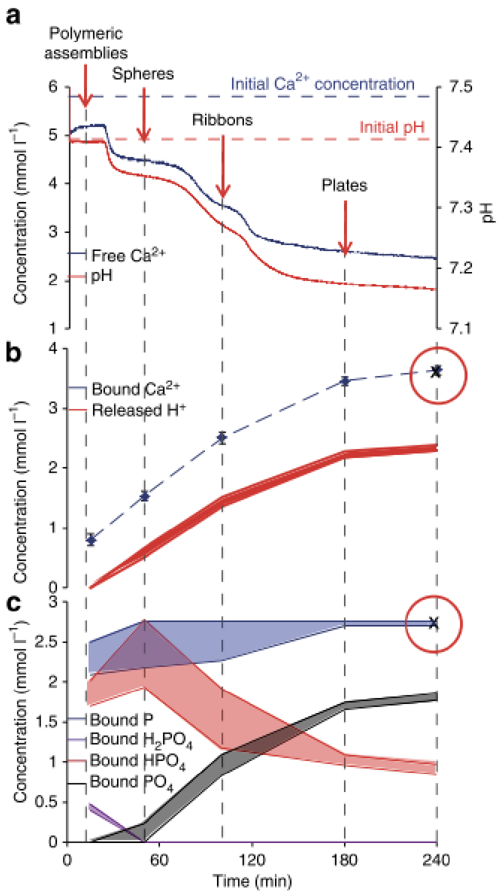

Figure 3.5: a) Calcium concentration and pH during the in situ reaction, b) calculated bound calcium and released H$^+$, c) calculated bound phosphate and phosphate ions. Adapted from Habraken et al., 2013. Reproduced with permission. Copyright 2013 Nature Publishing Group.

Spectroscopic techniques have also allowed us to develop a better understanding of mineralisation, mainly through the characterisation of the apatite precursors at early stages of mineralised tissue formation. OCP has been reported to form as a precursor phase in bone (Brown and Chow, 1973). However, as discussed in section 1.4, OCP crystal structure has a resemblance to that of HAp. This resemblance makes it difficult to identify OCP in some ways. The similarity of the apatite-like planes in OCP and apatite itself give OCP an X-ray diffraction (XRD) trace comparable to biomimetic HAp (Drouet, 2013). The main way the two can be distinguished in XRD is by measuring at very low 2θ angles, where the 100 plane of OCP gives a strong diffraction peak (see Figure 3.6). However, these low angle measurements sometimes require special equipment adjustment and so are not always included.

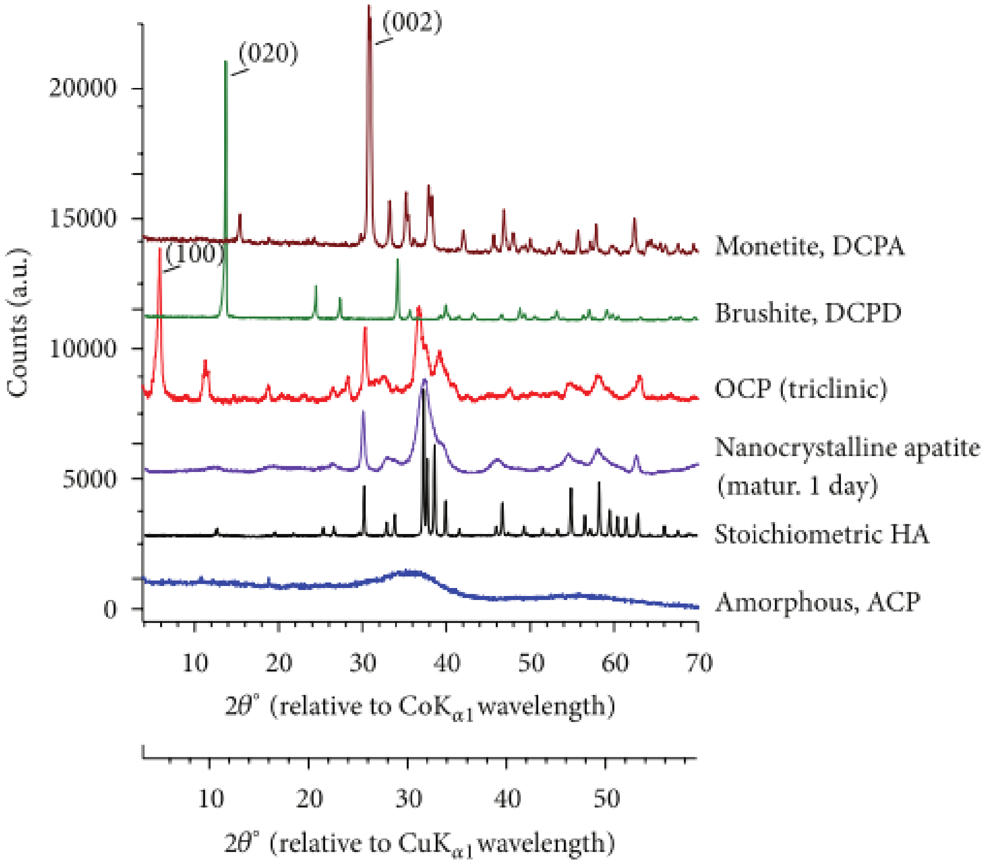

Figure 3.6: Typical XRD patterns for a number of calcium phosphates (Drouet, 2013). Reproduced with permission. Copyright 2013 Christophe Drouet.

The characterisation of OCP is further complexed since some have found that nanocrystalline HAp may be almost indistinguishable from OCP in several spectroscopic techniques. Rey *et al*. have extensively analysed nano-crystalline HAp with techniques such as Fourier transform infrared spectroscopy (FTIR), nuclear magnetic resonance (NMR) and XRD (Drouet *et al*., 2009; Eichert *et al*., 2004; Rey *et al*., 2007a, 2007b). Rey *et al*. have hypothesized that nano-crystalline apatite is imperfect and is surrounded by a hydration layer similar to the hydrated layers within the OCP crystals. Due to this hydration layer, nano-apatite has a striking likeness to OCP when analysed with techniques such as FTIR (see Figure 3.7). This is especially true for freshly prepared HAp with an intact hydration layer (Drouet, 2013). The molecular ions, present in biological CaPs, that give rise to FTIR spectra are phosphate (PO_4^{3-}), hydroxide (OH^-), acidic phosphate (HPO_4^{2-}) and carbonate (CO_3^{2-}) (for specific positions see Kim *et al*., 2002). The acidic phosphate group, at 500-550 cm^{-1}, is normally detected in OCP. However, nanocrystaline apatite can also exhibit the same acidic phsophate peaks.

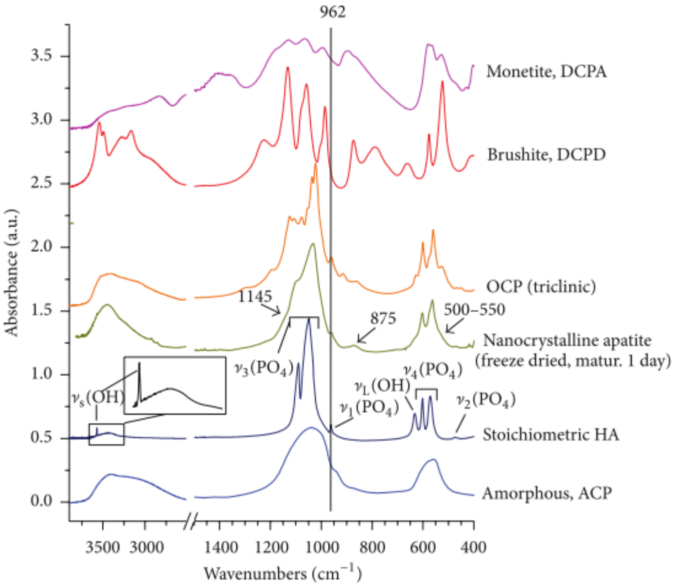

Figure 3.7: FTIR traces of several, biologically relevant, calcium phosphates (Drouet, 2013). Reproduced with permission. Copyright 2013 Christophe Drouet.

Some of the characterisation obstacles present in FTIR may be overcome with the use of other infrared techniques such as Raman. Raman spectroscopy is based on inelastic scattering of incident radiation from the sample due to the vibration of bonds (Bumbrah and Sharma, 2016). In Raman spectra, the PO_4^{3-} band is quite sensitive to apatite inclusions. For example, reports have shown that the PO_4^{3-} band shifts away from the wavenumber measured in normal apatites (Bax *et al*., 1983). Furthermore, the sensitive PO_4^{3-} has a significant shift between different CaP phases and so can be used to easily distinguish phases such as brushite, HAp and OCP.

NMR is, perhaps, the most sensitive technique that can be used to analyse calcium phosphates. Magic-angle spinning (MAS) NMR is commonly used in order to increase the resolution of the signal. The elements, such as ^{19}F or ^{31}P, are typically probed individually. NMR gives information of the local chemical environment of an atom and so can indicate which atoms the probed element is bonded to. Unlike, other techniques such as FTIR and XRD, calcium phosphates have quite different traces in NMR (Figure 3.8). NMR is especially useful when distinguishing nano-apatite and OCP, as they do not have any particular resemblances. NMR is a non-destructive technique and does not have many sampling disadvantages (Bax *et al*., 1983). However, in order to detect elements such as fluorine, relatively long run times are required. For NMR, long run times are normally accompanied with hefty costs.

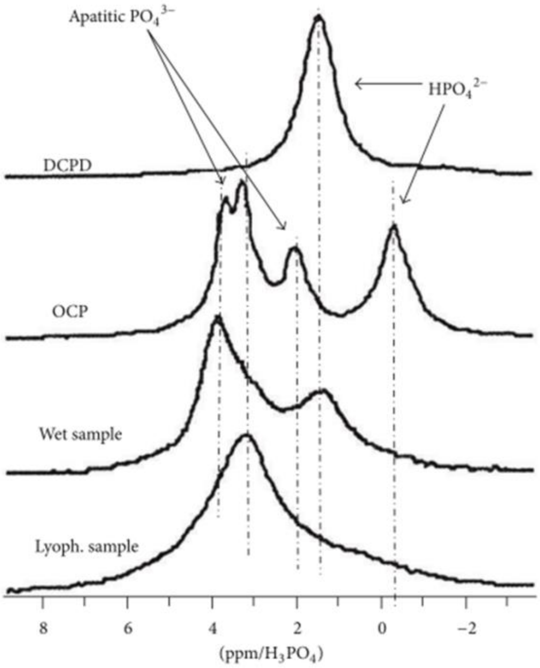

Figure 3.8: ^{31}P MAS-NMR traces of several calcium phosphates. Wet samples and lyophilised samples are NMR traces of nano-crystalline apatite in wet and dry states, respectively (Drouet, 2013). Reproduced with permission. Copyright 2013 Christophe Drouet.

Elemental analysis techniques have also proven useful in identifying CaP phases. For example, energy dispersive X-ray analysis (EDX) is useful in initial characterisation of calcium phosphates. EDX can give an indication of the Ca/P ratio of the phase present. It is most accurate on flat surfaces, therefore can give slightly varied results when used on rough surfaces. However, EDX cannot be used to definitively identify calcium phosphate phases. This is mainly due to similarities in Ca/P ratios of different calcium phosphates. For example, looking at Table 2.1, ACP has been reported to have a wide range of Ca/P ratios which overlap with apatites, OCP and TCP. Furthermore, apatites can have a large variation in the Ca/P ratio where, for example, a calcium deficient apatite can have a ratio that is close to TCP. Like other techniques, such as XRD and TEM, EDX cannot distinguish different apatites. Although EDX is sensitive enough to detect fluoride in a sample, it cannot accurately measure atomic % of low atomic number elements. Similarly to FTIR, EDX cannot discriminate nano-apatite and OCP. Reports have shown that the nano-apatite Ca/P ratio is somewhere in between OCP and apatite. As the crystal mature and fuse the Ca/P ratio increase to a ratio closer to apatite (Drouet *et al*., 2009). Lastly, EDX gives an average of an area, even if it is the size of the beam spot, and so if there are several phases present in one space then the spectrum will reflect the average of those phases.

In summary: The kinetics and thermodynamics of nucleation and crystal growth have been widely studied and are now thought to be well understood. However, during biomineralisation, this process is much more complex due to the multiple precursors that may be present before the truly stable mineral has formed. The multistep nucleation process has been demonstrated in both calcium carbonate and calcium phosphate with quite different techniques. Presently, current technologies allow us to see real-time nucleation, during crystal growth processes, for example using TEM.

Similarity in the chemistry of CaPs adds another level of complexity to understanding biomineralisation. The use of a number of analytical methods is frequently employed in characterisation of CaPs, from the earliest clusters to the final stable phases. However, due to certain limitations, the techniques often do not perform well alone. It is clear that care must be taken in the analysis of results obtained from various spectroscopic, microscopic and diffraction techniques. Nonetheless, a mixture of a number of these techniques can give a good picture of biomineral formation. These techniques, in conjunction with the original nucleation theories, are enabling scientists to understand in more detail the process of biomineralisation. However, the real biomineralisation environments are much more complex and involve the action of the organic matrix. The effect of the organic matrix on the biomineral formation is going to be described in some detail in the next chapter.

Chapter 4.Proteins and Biomineralisation

4.1 Naturally Occurring Proteins and Peptides Involved in Biomineralisation

Proteins are chains of amino acids bonded by an amide bond (also called a peptide bond) via a condensation reaction. Proteins are normally a chain of 50 amino acids or more. A chain of fewer than 50 amino acids is termed a peptide. The amino acids that make up proteins or peptides have the general structure depicted in Figure 4.1. The R-group differs between each amino acid. There are 21 essential amino acids, all illustrated in Figure 4.2. The amine end of a protein or peptide is called the *N*-terminal and the carboxylic end the *C*-terminal.

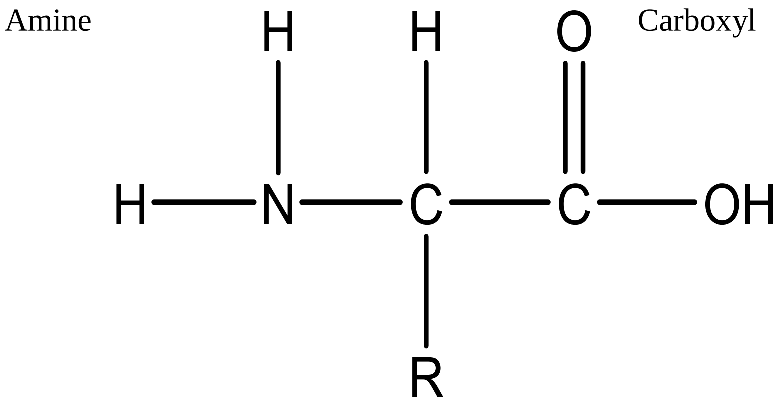

Figure 4.1: General structure of an amino acid. R is a side group which differs between each amino acid. The amine group is the N-terminal and the carboxyl group is the C-terminal of the amino acid.

Most proteins have a characteristic structure. Several levels of protein structure exist: primary, secondary, tertiary and quaternary. The primary structure is the sequence of the amino acids within the protein chain. The primary protein structure is, effectively, the most important. The sequence of amino acids will dictate the secondary structure. The secondary structures of proteins include random coil, *β*-sheet and α- helix. Some examples of known structure promoting amino acid sequences include the *β*-sheet forming sequence of an amyloid-forming protein (Leu-Met-Val-Gly-Gly-Val-Val-Ile-

Ala) (Halverson *et al.*, 1991) and the α-helix forming sequence of salivary statherin (Asp-Ser_{P}-Ser_{P}-Glu-Glu-Lys-Phe-Leu-Arg-Arg-Ile-Gly-Arg-Phe-Gly) (see corresponding amino acid names in Figure 4.2). The tertiary structure describes the folding of the protein, as a result of a mixture of secondary structures. Finally, the quaternary structure is the structure of multiple protein monomers bonded to form complex structures such as enzymes. These structures are held together by van der Waals forces, hydrogen bonds, electrostatic interactions and/or sulphur bonds.

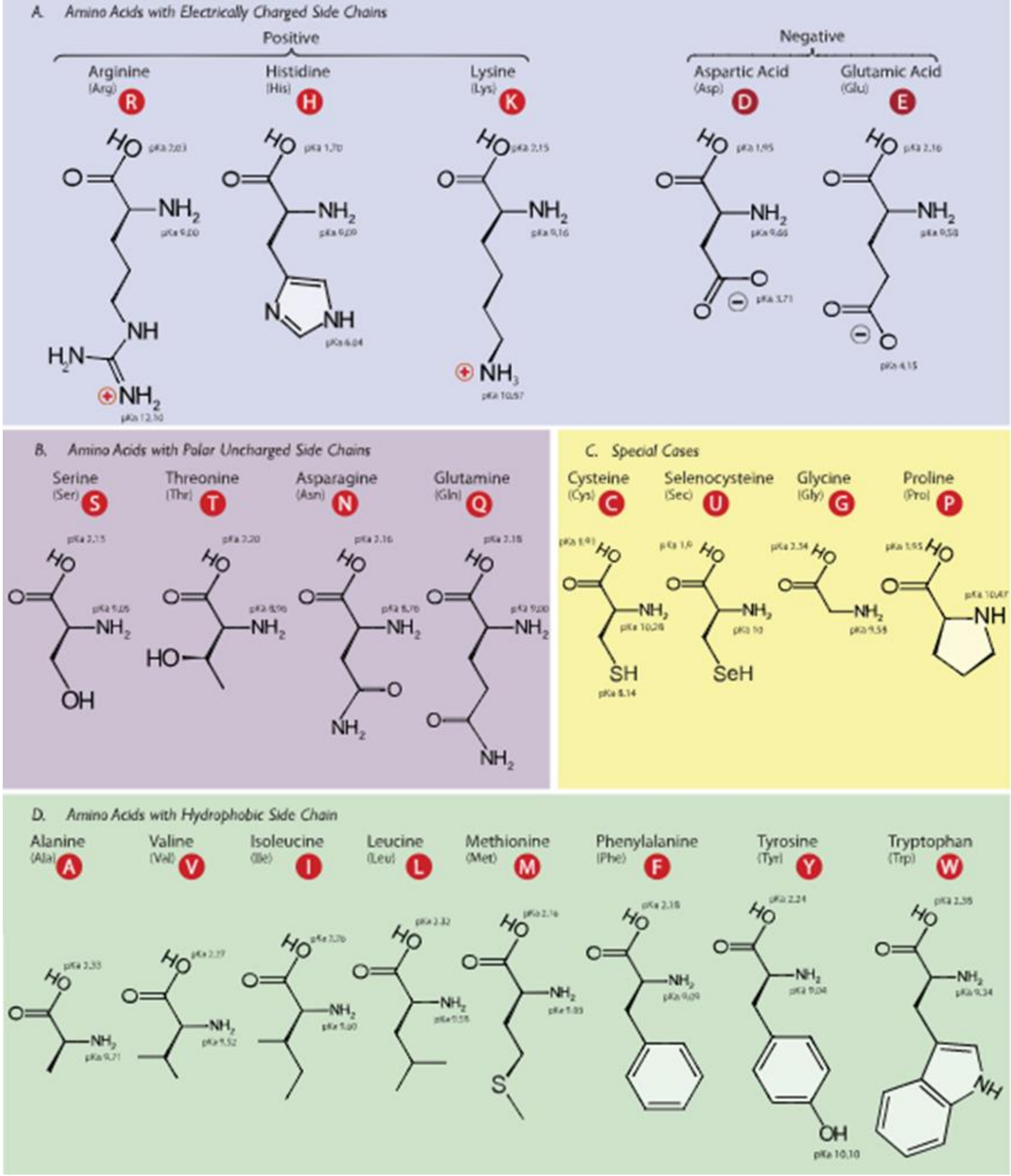

Figure 4.2: 21 essential amino acids. (Cojocari, 2016, Accessed 31st August 2017)

Many proteins have been linked to the formation of enamel and bone mineral structures. Some examples of proteins that have been reported to interact with mineral ions, or bind to HAp, are dentine sialoprotein (DSP), dentine phosphoprotein (DPP), osteopontin and bone sialoprotein (BSP) (Firth *et al*., 2006). The main similarity between all these proteins is that they contain acidic amino acid domains (i.e. containing aspartic and/or glutamic acid residues). Proteins such as DSP, DPP, BSP and osteopontin have a further similarity in that they contain the RGD amino acid sequence (arginine-glutamine-aspartic acid). One proposed reason for these similarities was discussed by Kawasaki and Weiss (2003). Their research looked at the evolution of the genes coding for proteins involved in biomineralisation. They concluded that all proteins present in the oral environment have diverged from a single primordial enamel matrix protein (Figure 4.3).

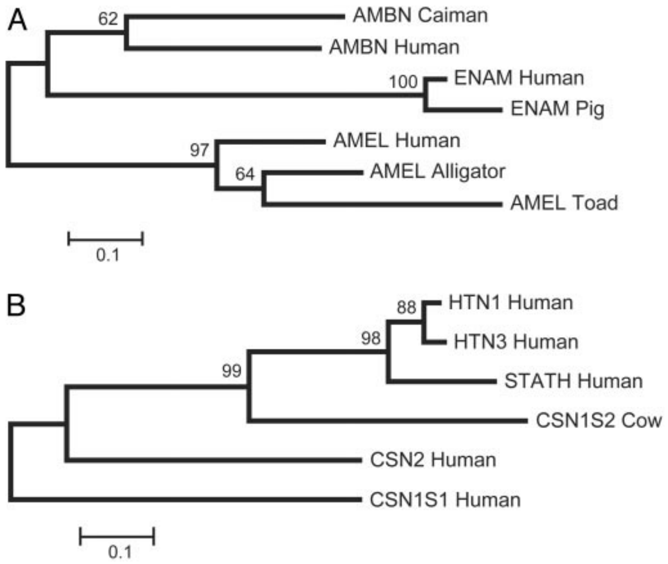

Figure 4.3: Phylogenetic trees of enamel matrix proteins and casein-salivary proteins (Kawasaki and Weiss, 2003). Reproduced with permission. Copyright 2003 National Academy of Sciences.

During enamel formation there is about 25% of protein concentration in early enamel (Sasaki and Shimokawa, 1995). Almost all of this protein is eventually replaced by HAp. The three main enamel matrix proteins (EMPs) are amelogenin, ameloblastin and enamelin (Kawasaki and Weiss, 2003). In the protein matrix of forming enamel only 1-5% of the protein is enamelin. It is said to have an important role in enamel formation and has the ability to stabilise ACP for prolonged periods of time (Iijima *et al.*, 2010). Amelogenin, in particular, is the major protein constituent found in developing enamel and is also linked to mineral formation (Sasaki and Shimokawa, 1995). Amelogenin has been reported to act as an inhibitor of crystal growth, prolonging the ACP phase, similarly to enamelin, and buffer the pH of a mineralising solution. These actions of amelogenin prevent spontaneous mineralisation and therefore allow slow controlled crystal growth (Le Norcy *et al.*, 2011b; Margolis *et al.*, 2014).

Saliva also contains proteins that are able to control biomineralisation and aid in remineralisation of enamel. These proteins can prevent calcium phosphate from precipitating out of the supersaturated solution (Kawasaki and Weiss, 2003) and the same salivary proteins are able to prevent demineralisation of enamel. Some of the known proteins and peptides in saliva include statherin, histatin and several proline-rich proteins (Kawasaki and Weiss, 2006). These molecules are also effective at preventing apatite crystal growth particularly when they are adsorbed to apatite surfaces by assisting in the formation of the acquire enamel pellicle (Johnsson *et al.*, 1991). The enamel pellicle has resistance to acid dissolution and therefore acts as a protective layer in vivo (Balz, 1999). The action of statherin requires the presence of phosphorylated serine (Ser) residues in the *N*-terminal. The phosphorylated Ser is negatively charged and attracts the positive Ca^{2+}. In addition, statherin has glutamic acid (Glu) residues, which also contribute to the acidity of the protein and attraction of Ca^{2+}.

Hunter *et al.* (1994) showed that Glu residues are the key players in the nucleation of HAp and that the phosphate groups are not specifically required for nucleation. A chain of glutamic acid residues (present in BSP) can cause a larger accumulation of calcium and phosphate ions than the BSP itself. Additionally, Hunter *et al.* showed that a chain of aspartic acid (Asp) residues does not have the same effect as Glu on HAp formation.

Other examples of proteins that interact with calcium ions are casein proteins present in milk (for example see Guo et al., 2003; Tercinier et al., 2014). 80% of milk proteins is casein and therefore is the main protein content in milk (Silva and Malcata, 2005). It is believed that the main role of casein in milk is the prevention of calcification in the mammary gland. Similarly to the function of statherin, it is believed that casein's ability to bind to calcium ions is due to the presence of phosphorylated Ser and Glu residues.

4.2 Stereochemical Interaction between Proteins and Biominerals

Biomineralisation is controlled by many mechanisms, which have been divided by Mann (1993) into 3 main groups: supramolecular preorganisation, interfacial recognition and cellular processing (Figure 4.4). Although, all of the processes are equally important, for the purpose of this thesis, we are mainly concerned with the interfacial recognition between proteins and ions.

Biominerals are often found to have shapes and sizes unlike those found in non-biological minerals. For example, apatite can be found in a plate-like form in bone (Dorozhkin and Epple, 2002) compared to the needles grown without protein (Li et al., 2007). It is thought that this occurs due to the surrounding acidic proteins. These acidic proteins, commonly with a β-sheet conformation (Addadi *et al.*, 1989), are said to be able to control the crystal morphology and the rate of crystal growth (Addadi and Weiner, 1985). This control occurs due to the adsorption of the proteins to specific crystal faces. One example described in literature is the formation of aragonite, a calcium carbonate found in mollusc shells. Some of the organic molecules found in the mineralised matrix of the shells are said to align with the aragonite *a* and *b* axes (Weiner *et al*., 1983).

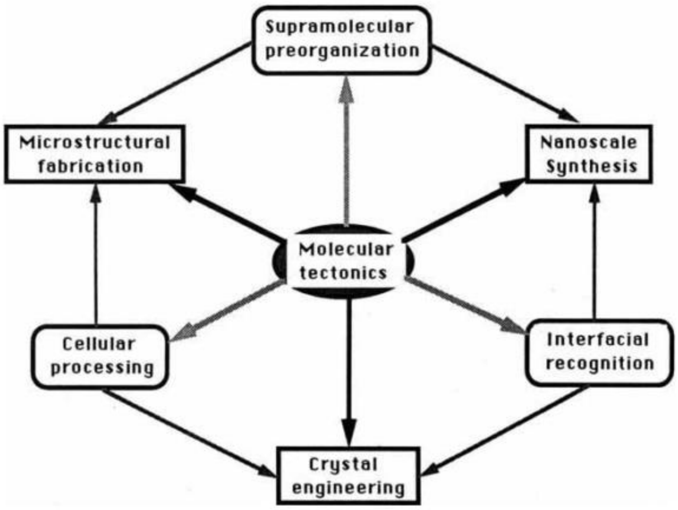

Figure 4.4: The connection of molecular tectonics (the building of molecules) to processes involved in biomineralisation (in round boxes) and processes used to mimic biomineralisation (in square boxes). Reproduced with permission from Mann, (1993). Copyright 1993 Nature Publishing Group.

Salivary statherin is also said to have stereochemical interaction with apatite surfaces. Stereochemical interaction, between proteins and apatite, occurs when the spatial arrangement of carboxylic amino acids within the protein corresponds to the spatial distribution of calcium ions in apatite. Studies have shown that it is the *N*-terminal of statherin (STN) that is mostly responsible for apatite binding. Raj *et al*., (1992) developed a model of STN, describing the alpha helical conformation (see Figure 4.9 later), and speculated that the spacing between the glutamic acid residues and phosphorylated serine is closely related to the spacing between calcium ions in the (001) HAp plane. With recent advances in solid state NMR, the structure of statherin on HAp surfaces has been studied in detail (for example Goobes *et al*., 2006, 2007; Ndao *et al*., 2009). These studies supported the initial assumption that the alpha helical STN interacts with the HAp surface (Goobes *et al.*, 2007a). Furthermore, the results highlighted the importance of bridging water molecules. However, some are still unsure whether it is a stereochemical interaction or if it is a simple electrostatic attraction (Chen *et al.*, 2008). In other studies, the interaction of STN with HAp was tested with respect to the basic amino acids within the sequence (Goobes *et al.*, 2007b). Although it is considered that protein-calcium or protein-mineral interactions occurs due to the presence of acidic residues, the study found that removal of the basic residues negatively affects statherin-HAp interaction. On the other hand, the removal of only one of any of the basic residues does not have an effect (Goobes *et al.*, 2007b).

4.3 Designed Proteins and Peptides for Mineralisation

It is often difficult to acquire the naturally occurring proteins and peptides involved in biomineralisation as they must be extracted from a mixture of matrix proteins. Even if these proteins can be obtained they are extremely costly. Today there are many processes that scientists can take advantage of in order to synthesise man-made proteins and peptides.

In 1992 analogues of *N*-terminal of statherin were synthesised using the solid phase peptide synthesis route (Raj *et al.*, 1992). Normally, the statherin sequence is a 43 amino acid residue protein. In the 1992 study only 15 amino acids of the *N*-terminal were synthesised (STN15). In the analogue sequence the phosphorylated serines (2nd and 3rd residues) were replaced by aspartic acid. The adsorption of this analogue (STNA15) to hydroxyapatite was the same as the phosphorylated *N*-terminal.

Amelogenin, the protein mainly responsible for enamel formation has also been produced via synthetic routes. For example the leucine rich amelogenin peptide (LRAP), a 56 amino acid splice of native amelogenin has been synthesised with and without phosphorylated sites (Le Norcy *et al.*, 2011a). The phosphorylated LRAP inhibits apatite formation and prolongs the existence of ACP, just as the full amelogenin sequence has been reported to do. Although this splice has been detected in forming enamel, the solid phase peptide synthesis route, used here, provides a cheaper more accessible option.

Another example of a synthetic peptide designed for biomineralisation was described by Kirkham *et al.*, (2007). The peptide was rationally designed with the aim to re-mineralise carious enamel. This peptide, like the native proteins involved in biomineralisation, contains negative amino acid residues. The peptide, named P_{11}-4, is the main component of a peptide-based product Curodont^{TM}. More recently a clinical study was published regarding its safety (Brunton *et al.*, 2013). The peptide became a success, opening up a new route for treatment of caries.

4.4 Elastin-like Proteins

Elastin-like proteins/ polypeptides (ELPs) have gained some attention in recent years as a biomaterial for various applications. These proteins are a type of a synthetic protein produced by recombinant bacteria. However, ELPs have interesting intrinsic properties and so it is important to specifically review the properties and current uses of ELPs. ELPs are recombinant proteins based on the repeating pentapeptide of elastin with the sequence VPGXG, where X is a guest residue and can be any amino acid apart from proline. The VPGXG pentapeptide and its repeat sequence has been characterised in some detail (for example Urry *et al.*, 1974, 1976). The structure of the VPGXG sequence is said to have a β-turn and so the polypeptide forms a β-spiral of repeating β-turns upon heating. A proposed structure of the β-turn and β-spiral of a polypeptide in a fully folded state is shown in Figure 4.5A and B/C, respectively.

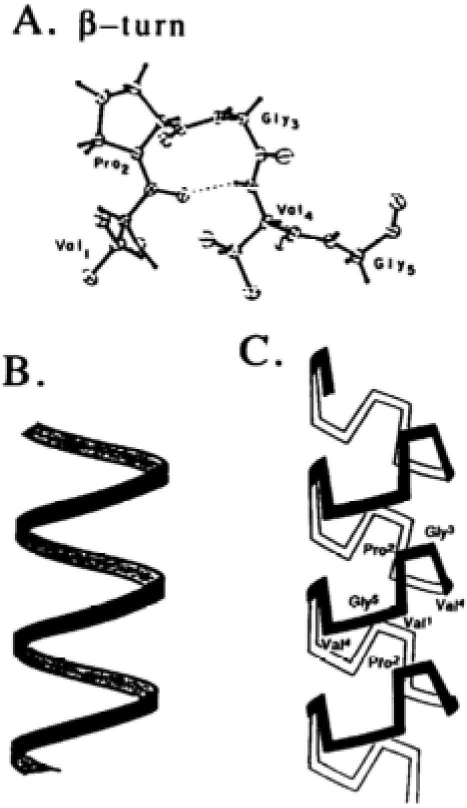

Figure 4.5: A) One single β-turn which recurs within an ELP. B)/ C) The β-spiral formed by the ELPs above the inverse transition temperature, where the hydrophobic interactions are maximised within the molecule. Adapted from Urry, 1992. Reproduced with permission. Copyright 1992 Elsevier.

Circular dichroism (CD) is a technique often used to study the structure of proteins or peptides. CD is a technique that measures the difference between right and left circularly polarised light. Chemical groups that give rise to CD spectra include peptidic bonds, disulphide bridges and aromatic side groups of amino acids. The absorption of these depends on their local environment and therefore the secondary structure of peptides and proteins (Calero and Gasset, 2005). CD data of a cyclic tetrapeptide was deconvoluted in order to understand the contributions of the different structural components of the secondary structure (Perczel and Fasman, 2008). In the reported CD data, it was found that both type I and type II β-turns are simultaneously present in the ELP structure when it is unfolded (Figure 4.6). The two types of β-turns mainly differ in preference of amino acid sequence. For a detailed description of type I and II *β*-turns see for example What-when-how.com (2018). Although the CD curve deconvolution was carried out for cyclic peptides, Perczel and Fasman (2008) postulated that in non-cyclic polypeptides, like the ELPs, the random coil conformation may always be present in the largest amount.

ELP structure is clearly difficult to decipher, due to the presence of the random coil and different *β*-turns. For those with only the basic understanding of CD, the interpretation of the spectra can be further complicated due to the similarity of some spectra, such as *β*-sheet and *β*-turn. Furthermore, due to the chain flexibility, the spectral interpretation is difficult not only in CD but also NMR (Li *et al.*, 2001).

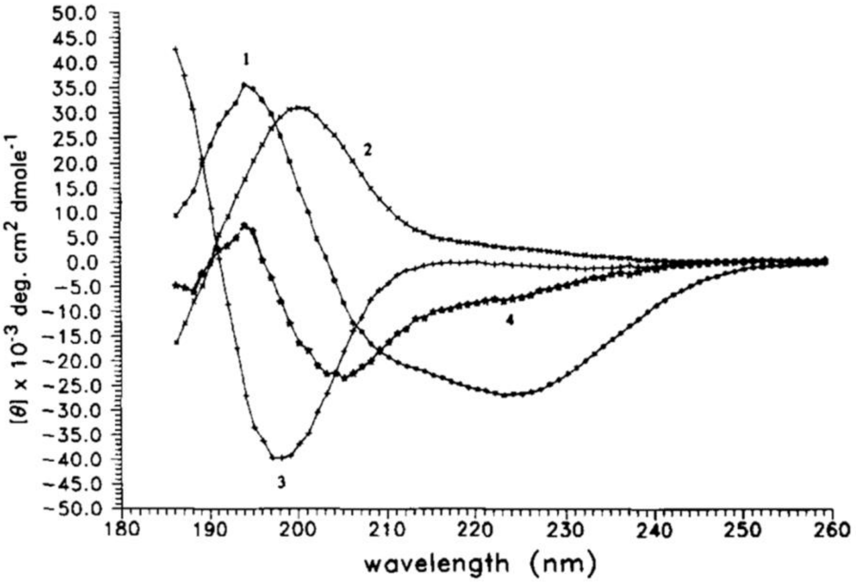

Figure 4.6: Deconvoluted CD spectrum of a cyclic peptide showing the different contributing structures. Curve 1 and 4 are two forms of type I β-turn, curve 2 shows the type II β-turn contribution and 3 is the random coil conformation signal (Perczel and Fasman, 2008). Reproduced with permission. Copyright 1992 The Protein Society.

Structural modelling of the ELP molecules has shown that the ELPs are not likely to assume the perfect *β*-spiral structure (Li *et al.*, 2001). However, the *β*-turns are present below and above the inverse transition temperature (ITT), mainly due to the presence of the rigid prolines in the sequence. Figure 4.7 shows the comparison of the ideal β-spiral, originally proposed by Urry (such as the one depicted in Figure 4.5), and accompanied with the modelled preferred structures either side of the transition. In neither of the cases, below or above ITT, is there a perfect β-spiral structure, such as the one seen in Figure 4.5B, most probably due to the inherent chain flexibility that arises from a large number of glycines.

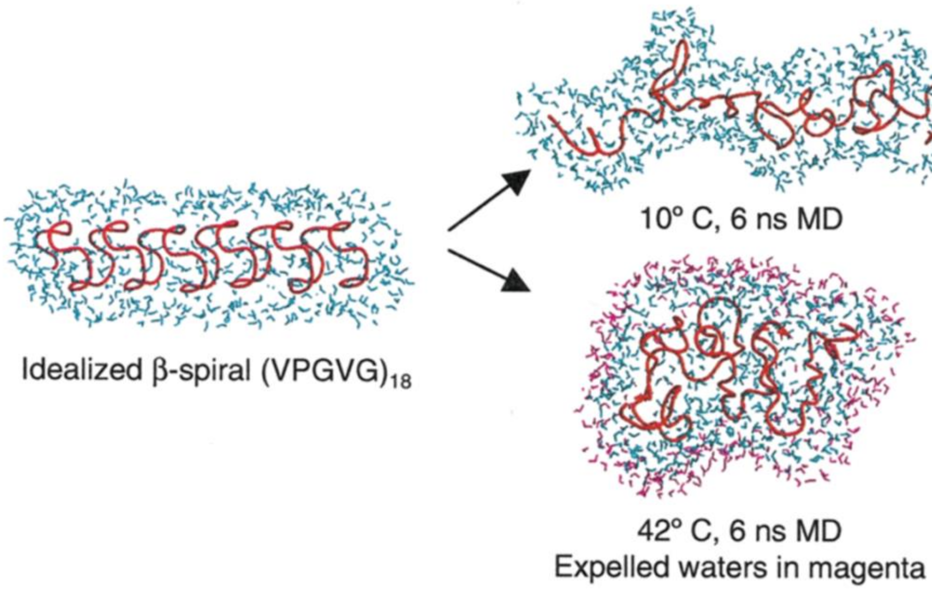

Figure 4.7: Modelled idealised β-spiral ELP molecule (red) surrounded by a hydration shell of water molecules (blue). The two forms of the ELP on the right show the proposed structures above and below the ITT. The water expelled from the ELP interface is highlighted in magenta (Li et al., 2001). Reproduced with permission. Copyright 2001 Elsevier.

Although there are complications in understanding the ELP behaviour, they do possess a number of advantages. Firstly, the ELP sequence is based on natural elastin and therefore it does not elicit an immune response, and is biodegradable. Since ELPs are recombinant, they can be easily modified and guest sequences inserted. Examples of ELP modifications include a number of different guest sequences and/or residues in the protein sequence such as the cell adhesion motif REDV (Girotti *et al*., 2004b), silk derived sequences (Zeng *et al*., 2014), calmodulin (Hassouneh *et al*., 2013) and the *N*-terminal peptide sequence of statherin (Li *et al*., 2015), increasing the versatility of this protein. ELP's wide availability and desirable properties have made it one of the most well characterised proteins (Banta *et al*., 2010).

4.4.1 Thermoresponsive Properties of Elastin-like Proteins

ELPs are known to have thermoresponsive properties, attributed to their ITT (Urry *et al*., 1998). It has been reported that below the ITT the protein is unfolded, mostly with a random coil structure, and the hydrophobic residues are hydrated with ordered clathrate-like water structures. Above the ITT the ordered water molecules surrounding the protein are disrupted and the protein becomes dehydrated. The dehydration process causes the protein to fold, via an increase in the *β*-sheet structure and simultaneous decrease in random coil structure (Figure 4.8), and phase separate. This dehydration process can be affected by changes in pH (Girotti *et al*., 2004a), protein concentration (Meyer and Chilkoti, 2004) and the addition of ions to the solution (Hassouneh *et al*., 2013). Furthermore, the ELPs can be designed to be of many lengths, with different guest sequences and guest residues, all affecting the ITT (Girotti *et al*., 2004a; Meyer and Chilkoti, 2004).

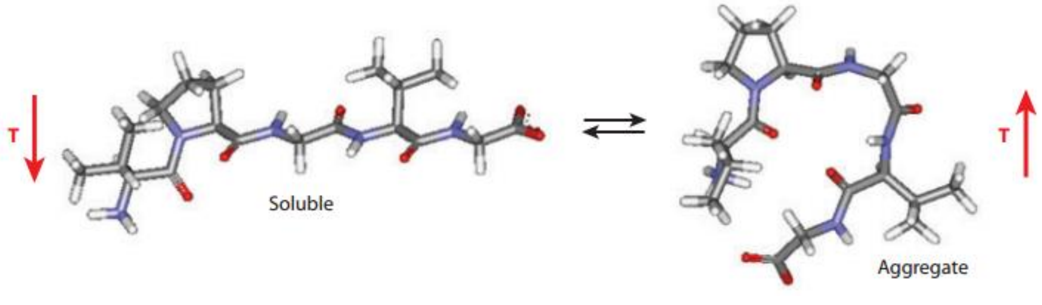

Figure 4.8: Two forms the ELP can take on, with the unordered structure on the left and the β - turn on the right (Banta et al., 2010). Reproduced with permission. Copyright 2010 Annual Reviews.

The precipitation of ELPs above an ITT has been termed as coacervation and is said to be reversible upon cooling back below the ITT. Some experimental and computational data suggests that the collapsed and open states of an ELP exist in equilibrium (Cirulis and Keeley, 2010). This equilibrium is shifted when there is a critical concentration of collapsed ELPs in solution, causing coacervation and appearance of larger particles. In early ELP work, the coacervate was found to form fibrillar structures (Urry *et al*., 1974). However, in most of the recent examples the coacervate forms spherical particles (for example: Bessa *et al*., 2010; Fujita *et al*., 2009; Herrero-Vanrell *et al*., 2005; McDaniel *et al*., 2010). The structure of the coacervate is clearly dependent on the ELP sequence and may be tuneable.

Characterisation of the ELP structure, below and above the ITT, has been carried out in several ways, including circular dichroism (Urry *et al*., 1974), DSC (Girotti *et al*., 2004b) and FTIR (Moscarelli *et al*., 2014). FTIR is commonly used to distinguish chemical groups by their stretching and vibrational spectra. FTIR of proteins gives the amide I peak, amongst others. This amide I peak is composed of several components, the number of which is dictated by the protein structure. Since these components are so close together on the FTIR spectrum they become indistinguishable and blend into one peak. However, there are mathematical techniques that enable us to find these peaks via deconvolution, normally using a Gaussian fit. Previous work by Serrano *et al*. (2007) investigated ELP structure with FTIR. Serrano *et al*. concluded that below the ITT the protein contains the β-sheet aggregation component (1616 cm^{-1}) (different from the β-sheet seen above the ITT), but this completely disappears upon heating above the ITT. As with the ITT of ELPs, the results of all of these techniques are highly dependent on the ELP concentration, the envionment (i.e. ion present in solution, solvents) and the ELP sequence.

Therefore, careful consideration of a number of techniques is required to accurately desipher the ELP structure in a set of given conditions.

4.4.2 Recent Examples in ELP Coatings

The versatility of ELPs has given scientists new paths for designing smart biomaterials. For example, these synthetic proteins have been researched for applications such as biomineralisation (discussed below) and drug delivery (Kim and Chaikof, 2010). Furthermore, due to the ease of changing the sequence, the ELPs can be designed with residues that can be easily cross-linked or functionalised to make robust, biocompatible materials.

Another prominent example of ELP use is in coatings. ELPs can form stable coatings on dental implants through a UV activated reaction (Raphel *et al*., 2016). These coatings are able to promote osseointegration of implants and mineral deposition. In other studies the ELP coatings are used in order to prevent platelet deposition on coatings reducing the thrombogenic response, a valuable trait for biomaterials such as heart valves (Jordan and Chaikof, 2007).

4.4.3 Examples in Biomineralisation

More recently, elastin-like proteins (ELP) with smart properties have become an object of biomineralisation research. Since statherin is known for binding to HAp and its calcium chelation properties, ELPs have been synthesised with the STNA15 sequence (STNA15-ELP). The ability of this protein to mineralise has been investigated in simulated body fluid (SBF) over a 7 day period at 37°C (Prieto *et al*., 2011). In particular, three ELPs which contained 1, 2 or 3 repeats of the STNA15 sequence were compared. The study found that the ELP containing 3 repeats of STNA15 within its sequence had the best nucleating ability. However, the mineral characterisation results were not clear and showed either a calcium deficient apatite or a mixture of apatite and brushite present after 1 week of incubation.

Later, membranes were fabricated using the STNA15-ELP (Tejeda-Montes *et al*., 2014a, 2014b). The membranes were implanted into mouse bone defects and showed increased apatite formation and healing. STNA15-ELP membranes, with a patterned relief, have also shown the ability to direct fluorapatite growth along their surface (Elsharkawy *et al*., 2016b). Perhaps the most interesting use of these membranes has been in the formation of hierarchical enamel-like FAp mineral grown on the surface (Elsharkawy *et al*., 2016a). In this example, FAp nucleates within the ELP membrane. Once the FAp erupts onto the surface, the STNA15-ELP membrane guides the mineral growth, causing alignment of the crystals into enamel prism-like bundles. This recent work suggests that STNA15-ELP scaffolds are not only efficient apatite nucleators but also have the ability to guide mineral growth, as a natural biomineralisation matrix would. Assessment of the literature leads us to believe that STNA15-ELP has promise in future treatment of dental tissues. However, the mechanism of STNA15-ELP mineralisation is still poorly understood, mainly due to the complexity of the ELP properties.

4.5 Effect of Ionic Solutions on Protein Solubility and Structure

In 1888, Franz Hofmeister famously reported the concentrations of different ionic species needed to precipitate proteins from egg whites (Hofmeister, 1888). These ionic series are now known as the Hofmeister series. The ions in the series are arranged in order of their tendency to salt out a protein. Salting out is the process which causes precipitation of proteins from an aqueous solution due to the disruption of the protein hydration shell. The Hofmeister ions are divided into chaotropic and kosmotropic groups. Kosmotropic ions are said to salt out or precipitate proteins, whereas chaotropic ions tend to salt-in proteins, i.e. assists with solubility. The anion series is as follows (Cho *et al*., 2008):

$CO_3^{2-} > SO_4^{2-} > S_2O_3^{2-} > H_2PO_4^{-} > F^{-} > Cl^{-} > Br^{-} \sim NO_3^{-} > I^{-} > ClO_4^{-} > SCN^{-}$

In this series of ions, species that are on the right of chloride are said to be chaotropic. The effect of these ions on proteins is due to their hydration shell. Those ions which are weakly hydrated, such as the ones on the right of chloride, help protein solubility (Kherb *et al.*, 2012). On the other hand, ions that strongly interact with water are those that precipitate proteins, such as the ions on the left of chloride. The following series shows the cationic Hofmeister ion order:

$N(CH_3)_4^{+} > NH_4^{+} > Cs^{+} > Rb^{+} > K^{+} > Na^{+} > Li^{+} > Ca^{2+} > Mg^{2+}$

The effect of cations on salting out proteins is the opposite of anions, where the cations with the higher charge, such as calcium, are more efficient at assisting protein solubility.

The effect of these Hofmeister ions has been reported for various proteins, including ELPs (for example Cho *et al*., 2008; Kherb *et al*., 2012). Low concentrations of calcium or sodium ions can cause an exponential decrease in the ITT of an ELP containing negative amino acids in the sequence (Kherb *et al*., 2012). Other work employed two, different, hydrophobic ELPs and investigated the effect of anions on their ITTs (Cho *et al*., 2008). In this report, chlorine behaviour was described as an intermediate between that of a chaotropic and a kosmotropic ion. In other words, the observed precipitation was consistent with a kosmotropic anion but the ion did not interact with the protein in the same way as a chaotropic anion would.

Consideration of the Hofmeister effect is important when studying mineralisation of proteins, especially ones that can easily undergo a transition upon a small change in the aqueous environment. Ions present in biomineralisation clearly have an effect on ELPs and so will be part of the focus of this work.

4.6 Effect of Protein/ Peptide Structure on Mineralisation

The mineralisation process is not only dependent on the sequence of the protein or peptide but also on the structure and conformation. Some have concluded that it is mostly the beta sheet structured proteins that are involved in biomineralising processes (Addadi *et al*., 1989). For example sericin (a type of silk protein), when coated on a surface as a film, only mineralises when in a β-sheet conformation. It is hypothesised that this occurs due to the optimal distribution of carboxyl groups on the surface of the film that is only achieved by the β-sheet conformation (Takeuchi *et al*., 2005).

In other studies, of the dependence of statherin sequence on HAp binding, it was found that the secondary helical structure has a role in the binding ability. An 11 amino acid *N*-terminal sequence of statherin (STN11) loses the rigid conformation that the STN15 has (Figure 4.9). STN11 does not have the same binding ability to HAp, as STN15, due to this loss of conformation. It is believed that the reason for STN15 binding affinity of HAp is due to its stable α-helix formation which in turn provides electrostatic attraction to HAp (Raj *et al*., 1992).

Dentine matrix protein 1 (DMP-1), a protein considered to have a random coil structure, also has conformation dependent mineralisation properties (Gericke *et al*., 2010). DMP gains conformation in calcium rich solutions, increasing in β-sheet structure. This change in DMP conformation is what is said to drive the HAp formation (Sarem and Lüdeke, 2015). The effect of conformation on mineral interaction has also been demonstrated with leucine-rich amelogenin peptide (LRAP). Phosphorylated serine in LRAP plays a crucial role on the conformation of the peptide. The phosphorylation of LRAP causes structural changes that allow for the formation of large peptide assemblies. The conformation of phosphorylated LRAP allows for the binding of calcium ions in solution (Le Norcy *et al*., 2011a).

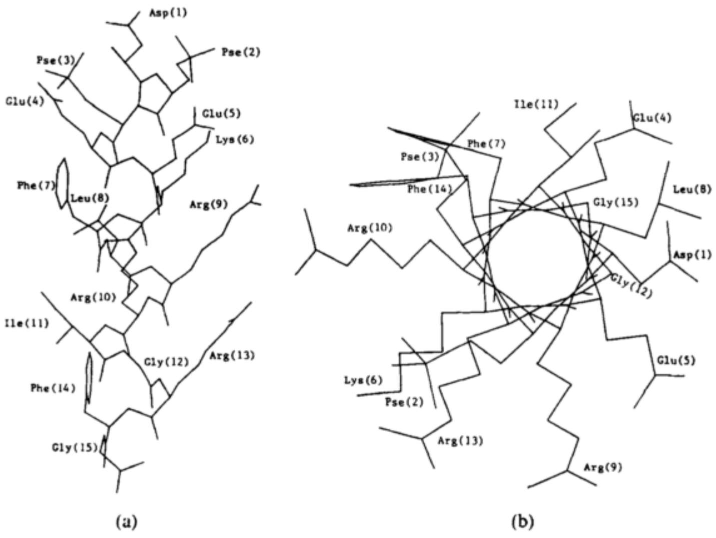

Figure 4.9: A: Side view of the STN15 alpha helix, B: top view of the STN15 alpha helix (Raj et al., 1992). Reproduced with permission. Copyright 1992 American Society for Biochemistry and Molecular Biology.

In summary: In this section, only a small fraction of proteins and peptides that are able to contribute to biomineralisation have been described and discussed. However, it is quite clear that researchers are looking to synthetic routes in order to find financially viable alternatives to the optimally designed (by Nature) proteins and peptides.

ELPs are being researched for many applications and are now being developed for mineralising purposes. However, the mechanism of their mineralisation is not well understood and therefore, as of yet, difficult to control. The complexity of the ELPs comes from their ITT, which can alter upon changes in the chemical environment, their sequence and their length. If the process of mineralisation can be somewhat understood, these smart proteins can be part of the future of synthetic biomineralisation.

Apart from the protein or peptide sequence, the protein structure is crucial in mineralisation. The importance of conformation is clear even from the present evidence. However, it is important to note that protein conformation is the consequence of its sequence and so both are extremely important to consider in design and use of mineralising proteins/peptides.

Chapter 5. RATIONALE FOR THE THESIS

Apatite formation has now been studied for decades. However, many questions still remain to be answered, especially around the topic of ordered apatite formation for therapeutic uses. We now know that proteins with negative amino acids, predominantly those with beta sheet conformations, can influence the formation of apatite. These biomineralisation processes are complex and have to undergo several phase transformations before the minerals reach the final, stable phase. Hence, the classical nucleation theory, although useful for basic understanding, does not explain biomineral formation well. Biological apatite has been said to form via transformation of several phases. ACP is now most commonly believed to be the initial phase formed, however its presence is still debated. Other phases that can transform to apatite include brushite, TCP and OCP, making biological HAp formation a tightly controlled, complex process.

Matrix mediation in biomineralisation is evident in all mineralised tissues. However, enamel is the most interesting since it has an ordered, hierarchical structure, unlike any other tissue. During amelogenesis a proteinaceous matrix is laid down, consisting mainly of amelogenin. There is now sufficient evidence to show that initially amelogenin acts as an inhibitor to HAp formation, until it is enzymatically degraded. The protein matrix is almost completely removed during the maturation of enamel, suggesting that its presence acts as a temporary guiding scaffold. However, it’s still not quite clear how such a highly ordered hierarchical structure is able to form in the end. A particularly fascinating feature of enamel is that it becomes acellular by the time it is completely mature. The structure of enamel gives it superior mechanical properties; however, the lack of cells means that it is unable to self-repair. This lack of self-repair has driven research towards biomimetic treatments, with the use of peptides and proteins, to re-create the natural hierarchical structure. The emerging use of synthetic minerealising proteins, such as ELPs, in biomimetics is of particular interest here.

FAp is of particular interest in dental applications due to its increased stability in acidic environments. However, although FAp has been known to form in biology (Enax *et al*., 2012) and geology (Levitt and Condrate, 1970), it does not form naturally in the human. Hence, due to the desirable properties of FAp, this study attempts to form ordered FAp structures via a biomimetic route.

This thesis will investigate the behaviour of existing synthetic proteins that have proven to be successful in bone regeneration, in particular the STNA15-ELP. It is assumed that STNA15-ELP is suitable for biomineralisation applications from previously reported literature. However, studies have not investigated this suitability in terms of protein conformation. Therefore, the first and foremost question is whether or not STNA15-ELP, as a protein, is a good candidate in use for biomimetic mineralisation. STNA15-ELP has been shown to mineralise *in vivo* and form hydroxyapatite. However, for dental applications, it is important to study the efficacy of STNA15-ELP in inducing biomimetic formation of FAp *via* precursor phases. Since proteins are normally constrained in natural biomineralising processes, where the mineralising proteins exist within a gel-like matrix, the second question is regarding the effect of ELP immobilisation on FAp mineral formation.

MATERIALS AND METHODS

Chapter 6. MATERIALS AND METHODS FOR PROTEIN AND MINERAL PREPARATION AND CHARACTERISATION

6.1 Protein Preparation

The elastin-like protein containing the analogue of the 15 amino acid *N*-terminal of statherin (STNA15-ELP) and a lysine-rich elastin-like protein (LR-ELP) were acquired from Technical Proteins Nanobiotechnology (Valladolid, Spain). These recombinant proteins are produced by genetically modified bacteria and extracted at the company (Girotti *et al.*, 2004b). The full sequences of the proteins used in this study are:

STNA15-ELP:

$\mathit{MESLLP\text{-}[((VPGIG)_2VPGKG(VPGIG)_2)_2\text{-}}\boldsymbol{DDDEEKFLRRIGRFG}\mathit{\text{-}((VPGIG)_2VPGKG(VPGIG)_2)_2]_3\text{-}V}$

where the STNA15 sequence is highlighted in bold, it has an inverse transition temperature (ITT) of 23 °C and isoelectric point (pI) at pH 9.9 (details provided by the supplier, Appendix A).

LR-ELP:

$\mathit{MESLLP\text{-}[VPGIG\ VPGIG\ VPGKG\ VPGIG\ VPGIG\ VPGIG\ VPGIG\ VPGKG\ VPGIG\ VPGIG]_{12}\text{-}V}$

LR-ELP has a transition temperature between 32 and 34 °C at pH 7.2, in UPW. Its pI is at pH of 11.0 (details provided by the supplier, Appendix B).

Acid Tetrablock ELP:

MESLLP-[(VPGVG VPGVG VPGEG VPGVG VPGVG)10-(VGIPG)60]2-V

The acidic tetrablock ELP has a transition temperature of 16 °C in UPW and pH 7.2. Further details can be found in Appendix C, the suppliers' information.

6.1.1 ELP in UPW and Ionic Solutions Preparation

To prepare the ELP stock solutions 2 mg of protein was dissolved in 1 ml of ultrapure water (18 MΩ.cm). The 2mg/ml of stock protein solution was mixed with either UPW or one of the two ionic solutions at a 1:1 ratio. Table 6.1 gives the details of the two ionic solutions used.

	Ionic strength/ mM	Final Concentration (after mixing with protein)/ mM
NaCl	30	20
$CaCl_2$	20	10

Table 6.1: Details of the solutions in which STAN15-ELP and LR-ELP were dissolved in.

6.1.2 Crosslinked Protein Aggregate Preparation

ELP particles were prepared by heating 1mg/ml of ELP, in UPW/NaCl/$CaCl_2$, to 50 °C. The ELPs were kept at the high temperature, in the corresponding solutions, for 15 minutes to equilibrate. 25% glutaraldehyde solution (GTA) (Sigma Aldrich, Dorset, UK) was added to the ELP solutions at 2.5, 1.25, 0.50 and 0.25 % v/v.

The crosslinking reaction was left for an hour at 50 °C. After, the particles were washed with ethanol 3 times and dried at room temperature. Once the samples were clean and dry, they were suspended in ethanol and kept at 5 °C until SEM analysis.

6.1.3 Constrained/ Unconstrained Sample Preparation

To prepare the stock protein solutions, 1 mg of ELP was dissolved in 1 ml of UPW (18 MΩ·cm). The stock solution was then diluted to yield a 100 µg/ml concentration. To prepare constrained protein samples, 100 µl of the dilute solution was pipetted onto borosilicate glass slides (VWR International Ltd, Lutterworth, UK) and left to completely dry at 21 °C overnight.

To prepare the unconstrained STNA15-ELP samples, 100 µl of the 1 mg/ml protein stock solution was pipetted directly into 1 ml of the mineralising solution. After the mineralisation period of either 3 hours or 8 days, the samples were frozen in liquid nitrogen and lyophilised. The lyophilised samples were washed with ethanol and dried prior to chemical and morphological analysis.

6.2 Techniques to Characterise Protein Structure and Adsorption

6.2.1 Circular Dichroism (CD)

Measurement

CD was carried out on the protein solutions using the Chirascan Spectrometer (Photophysics, Leatherhead, UK). The stock protein solutions of 1mg/ml were diluted to 0.05 mg/ml. The measurements were taken between 185 and 260 nm with a path length of 1 mm. Four repeats were taken at each temperature with the acquisition time set at 1.5 s. The measurements were taken at 19, 23, 37 and 40 °C. Baselines were measured for each of the solutions without the protein in the same manner at 19 °C only.

Deconvolution

The CD data was deconvoluted using the CD Apps software provided by Diamond Light Source (for details of the documentation see Benning, (2014)). To deconvolute the data, the curves were analysed with a corresponding data. The baselined data was offset between 255 and 258 nm and restricted from 190 to 240 nm wavelength. Finally the baselined data was fitted with a CONTINLL algorithm using the SP43 reference set (for details of the reference set see Sreerama and Woody, 2004). The SP43 reference set contains both types of helices, both types of β-strands, β-turn and random coil secondary structures. The deconvolution was carried out to see the changes in the secondary structure of ELPs at a range of temperatures and in different ionic solutions. Since the main structural features of ELPs are *β*-strands and turns, and random coil, the output ratios were re-calculated to only give those fractions. The residual mean standard deviation (RMSD) of each fit, given by the fitting software, is quoted below each figure.

6.2.2 Attenuated Total Reflection Fourier Transform Infrared Spectroscopy (ATR-FTIR)

Measurement

ATR-FTIR was carried out using a Bruker Tensor 27 IR spectrometer. The protein was dissolved at 1 mg/ml in deuterium oxide (D_2O) prior to measurement. The solution was pipetted directly onto the ATR window. The measurements were all taken at 19 °C. 80 scans per measurement were taken between 400 and 2000 cm^{-1} and repeated 3 times. The FTIR chamber was purged with nitrogen during readings.

Deconvolution

The FTIR spectra were analysed using Origin Pro software. First, the three spectra of each sample were averaged. The amide I region (1600-1700 cm^{-1}) of each averaged spectrum was deconvoluted in Origin Pro using the Gaussian fit and previously reported literature values (Serrano *et al*., 2007).

6.2.3 Quartz Crystal Microbalance (QCM)

Quartz crystal microbalance measurements were carried out in order to check the affinity of the protein to the borosilicate glass. Borosilicate coated quartz sensor crystals (Biolin Scientific Ltd, Stockholm, Sweden) were first washed in a 2 % w/v SDS (Sigma Aldrich, UK) solution for 30 minutes followed by a 10 minute UV/ ozone treatment as a cleaning procedure. In the QCM (Q-sense, Biolin Scientific Ltd, Stockholm, Sweden) the crystal was stabilised in UPW then, a solution of STNA15-ELP (100 µg/ml) was added and the QCM measurement was taken until equilibrium was reached. Finally, the crystal was washed again with ultrapure water to remove any unbound or loosely bound protein. The change in resonant frequency of the quartz crystal was converted to mass of protein adsorbed using the Sauerbery equation (Equation 1) where Δm is the change in mass, Δf the measured change in frequency upon protein adsorption, n is the overtone number (3) and C is a constant specific to the crystal.

$$\boldsymbol{\Delta m = -\frac{C.\Delta f}{n}}$$

Equation 6.1

QCM was carried out at a range of temperatures and concentrations. The temperatures at which adsorptions were examined are: 20, 24, 27, 31 and 37 °C. The concentrations of STNA15-ELP examined were: 100 µg/ml, 1mg/ml and 10 mg/ml.

LR-ELP QCM was carried out in the same manner at 37 °C and 1 mg/ml concentration as a control for STNA15-ELP.

6.2.4 Contact Angle

A DSA100 Drop Shape Analyser from Krüss (Hamburg, Germany) was used to measure the contact angle of water on uncoated and ELP coated borosilicate glass slides. 5 µl of water was pipetted onto the slide and the angle measured immediately. The measurements were carried at ambient conditions and 19 °C. Three repeats were taken and averaged.

6.2.5 Dynamic Light Scattering (DLS)

The dynamic light scattering measurements were taken using the DynaPro MSXTC/12 (Wyatt Technology Inc., Santa Barbara, CA, USA). DLS measurements were carried out on STNA15-ELP and LR-ELP in UPW, 20 mM NaCl and 10 mM $CaCl_2$, and a range of temperatures to see the effect of ionic solutions on protein size and aggregation. The ELP samples were first centrifuged at 4°C, 8000 rpm for 20 minutes. 45 µl of the supernatant was placed in the DLS cuvette. The readings were taken at temperatures ranging from 19 to 58 °C, taken at 3 °C intervals, in UPW, NaCl and $CaCl_2$ solutions. 10 acquisitions were taken per each reading. The values obtained were listed without errors and are recorded in the results section as the software gave them.

6.2.6 ATR-FTIR on Coated Borosilicate Glass Slides

ATR-FTIR was carried out using a Bruker Tensor 27 IR spectrometer (Billerica, Massachusetts, USA) to analyse the protein conformation. STNA15-ELP coated glass slides were prepared, as previously described in "6.1.3 Constrained/ Unconstrained Sample Preparation", with the ultrapure water exchanged for deuterium oxide (D_2O) (VWR International Ltd, Lutterworth, UK).

Before FTIR measurement, STNA15-ELP coated glass slips were rinsed with D_2O to remove excess protein. The measurements on the coating were taken in a wet condition. 80 scans per measurement, 400 to 2000 cm^{-1} range, three repeats were acquired and averaged. The FTIR chamber was purged with nitrogen during readings to remove atmospheric water and carbon dioxide. The amide I region was deconvoluted in Origin Pro using the Gaussian fit and reported literature values, as described in section 6.2.2.

6.2.7 Variable Surface Hydrophobicity: PDMS

In order to create surfaces with differing hydrophobicity polydimethylsiloxane (PDMS) was treated with UV/ Ozone. SYLGARD® 184 PDMS was purchased from Scientific Laboratory Supplies, UK. The PDMS was mixed at the specified ratio (10 (base): 1 (curing agent)) and poured into petri dishes. Any bubbles were removed from the viscous mixture using a pipette. The PDMS was cured at 70 °C for 2 hours.

The cured PDMS was then treated with UV/ Ozone using the UVOCS® system for 10, 30, 60 and 90 minutes.

The hydrophobicity of the PDMS surface pre and post-UV/ Ozone treatment was checked using the contact angle method detailed in section 6.2.4 Contact Angle. The contact angle of an enamel section was also measured for comparison.

6.3 Preparation and Characterisation of Mineralising Solution

6.3.1 Mineralising Solution Preparation and Use

The mineralising solution was used as previously described by Chen *et al*. (2006). In short, 104.7 mg sinter grade HAp (Plasma Biotal Ltd., Derbyshire, UK) and 8.49 mg sodium fluoride (Sigma Aldrich, UK) was added to 100 ml of ultrapure water (18 MΩ·cm). 69% analytical grade nitric acid (VWR International Ltd, Lutterworth, UK) was added drop-wise until the solution became clear and colourless and a pH of 2.4 was reached. 28-30% ammonium hydroxide (Sigma Aldrich, UK) was added drop-wise to the solution until pH of 6 was reached.

The solution was prepared at room temperature and stirred continuously during preparation.

3 ml of solution was incubated with each coated sample and 1 ml with STNA15-ELP solution samples. For the coated glass samples, uncoated borosilicate glass was incubated in the mineralising solution as a control. Precipitate from pure mineralising solution, without any protein, was used as a control for unconstrained protein samples. All samples were incubated in 3 ml of mineralising solution for either 3 hours or 8 days at 37 °C in sealed containers.

6.3.2 Ion Selective Electrode Method

An ion selective electrode (ISE) ELIT system was used to measure the Ca^{2+} and pH simultaneously in the bulk solution for 8 days. A silver chloride electrode was used as the reference electrode for measurement of Ca^{2+} ions. The solution was left on a hot plate, at 37ºC, without stirring to replicate the conditions of the protein incubation.

6.4 Characterisation of Minerals Formed in the Presence of Proteins

6.4.1 Mineral Preparation for Characterisation

Mineral Formed in the Presence of Constrained Protein on Glass

At the end of each incubation period in the mineralising medium, the cover slips were removed from the solution, rinsed with UPW water and air-dried at room temperature overnight.

Mineral Formed in the Presence of Unconstrained Protein

Following either the 3-hour or 8 day incubation periods, the precipitate formed was frozen in liquid nitrogen and lyophilised. The samples were stored at -18 °C until characterisation.

6.4.2 Scanning Electron Microscopy (SEM) /Energy Dispersive X-ray Analysis (EDX)

Prior to SEM inspection the borosilicate cover slips, both control and protein coated, were attached to aluminium stubs. The precipitate collected from the unconstrained protein samples were suspended in ethanol, pipetted onto aluminium stubs and air-dried.

SEM images were recorded, using a secondary electron (SE) and back-scattered electron (BSE) detectors, on an FEI Inspect F SEM (Hillsboro, Oregon, USA) in the NanoVision Centre, Queen Mary University of London. An X-Act Oxford Instruments EDX detector was used for EDX measurements (20kV accelerating voltage) (Abington, Oxfordshire, UK). The samples were coated with carbon for EDX studies and 20 nm of gold for morphological examination.

6.4.3 Transmission Electron Microscopy (TEM)/ Selected Area Electron Diffraction (SAED)

TEM images and SAED patterns were recorded on a JEOL 2010 transmission electron microscope operated at 200 kV (Tokyo, Japan). For the 3-hour incubation point of constrained ELP mineralisation, the crystals were grown directly on a TEM grid. The 8 day mineralised samples were scraped off the borosilicate glass into ethanol and then pipetted onto grids.

The 3-hour and 8 day unconstrained samples were first suspended in ethanol then pipetted onto copper grids and dried prior to TEM inspection.

6.4.4 ATR-FTIR

The precipitate formed in the presence of unconstrained STNA15-ELP was suspended in pure ethanol, pipetted directly onto the ATR window and air-dried. 60 scans, in the range of 400-4000 cm^{-1}, were taken for each mineralised sample. All measurements were carried out at 21 °C.

6.4.5 Raman Spectroscopy

Since the FTIR spectrum of borosilicate glass has large absorptions in the range where calcium phosphate peaks are present, Raman spectroscopy was chosen to analyse the mineral grown on constrained ELP surfaces. A Renishaw inVia Raman Microscope (Wotton-under-Edge, Gloucestershire, UK), equipped with a 633 nm wavelength (20 mW power) laser, was used to record the spectra of the mineral formed in the presence constrained STNA15-ELP at 3 hours and 8 days. A 20x objective was used, giving a spot size of 1.93 μm. The spectra were obtained in the

170-1370 cm^{-1} range with an exposure time of 5 seconds. 60 accumulations were recorded for each reading.

RESULTS AND DISCUSSION

Chapter 7. INVESTIGATING THE STRUCTURE AND ADSORPTION BEHAVIOUR OF ELASTIN-LIKE PROTEINS

7.1 Introduction

Since the structure of proteins is closely related to their function, the purpose of the studies reported in this chapter is to investigate the conformational behaviour of the STNA15-ELP and LR-ELP (as a control) under a number of conditions. ELPs can easily change conformation due to a variation in the chemical environment, temperature and adsorption. All of these aspects are investigated to some extent. Consideration of the conformational behaviour of ELPs, under a number of conditions, can give indication on the extent of suitability of the ELP for synthetic biomineralisation.

7.2 Experimental Details

7.2.1 Circular Dichroism

To analyse the conformational changes within both STNA15- and LR-ELPs, the two proteins were investigated using circular dichroism (CD) and Fourier transform infrared spectroscopy (FTIR). The ELPs were acquired from Technical Proteins Nanobiotechnology.

For the CD studies in UPW (pH 7), the ELPs were dissolved at a concentration of 1mg/ml and diluted to 0.05 mg/ml in. The samples were placed in a cuvette with a 1 mm pathlength. The CD measurements were taken at 4 temperatures (19, 23, 37 and 40 °C), to measure below, at and above the ITT. Each measurement was taken in the range of 185-260 nm and plotted is an average of three readings that have been baselined against UPW.

For the CD studies in ionic solutions, the same experimental set up was used. The solutions used were 10 mM $CaCl_2$ and 20 mM NaCl. The salts were first dissolved in UPW (pH 7). Prior to CD measurements, 950 μl of the ionic solutions were mixed with 50 μl of ELPs (concentration of 1 mg/ml), yielding final solutions with ELP concentration of 0.05 mg/ml.

The acquired data was imported, as is, into CD apps software. Within the CD software, the data was averaged and baselined again. The software was then used to deconvolute the signals to acquire the proportions of structural components present with the proteins. The software uses the CONTINLL algorithm to deconvolute the imported data. SP43 was used as a reference set for the deconvolution. The SP43 reference set contains both types of helices, both types of β-strands, β-turn and random coil secondary structures. The deconvolution was carried out to see the changes in the secondary structure of ELPs at a range of temperatures and in different ionic solutions. Since the main structural features of ELPs are β-strands and turns, and random coil, the output ratios were re-calculated to only give the percentage of those structures.

7.2.2 FTIR

For the FTIR studies, the ELPs were dissolved at a 1 mg/ml concentration in D_2O. D_2O is often used for FTIR characterisation of proteins since water has an adsorption peak at similar wavelength to the amide I band. 20 μl of an ELP solution was pipetted directly onto the FTIR window. 80 scans per measurement were taken between 400 and 2000 cm^{-1} and repeated 3 times. The FTIR measurements were carried out at room temperature (19 °C), whilst the air was purged with nitrogen to avoid any water or carbon dioxide interference. The 3 obtained spectra were averaged and deconvoluted in Origin software. The deconvolution method used a Gaussian fit. The number of peaks and their positions were chosen according to previously published literature and more detail on that is given in this chapter.

For the FTIR studies in ionic solutions, the same experimental set up was used as with UPW. The solutions used were 10 mM $CaCl_2$ and 20 mM NaCl. The salts were first dissolved in D_2O (pH 7). The ELPs were added to the ionic solutions at 1 mg/ml.

The experimental set up to measure STNA15-ELP conformation following adsorption to borosilicate glass was carried out in a similar manner. The ELPs, dissolved at 100 μg/ml concentration in D_2O (pH7), were coated onto glass cover slips and left to dry completely overnight at room temperature (19 °C). The cover slip was rinsed with D_2O to remove excess ELP and, whilst still wet, was placed protein side down on the ATR window. The same measurement routine and data processing, as describe above for UPW, was applied after data acquisition.

7.2.3 QCM

Since STNA15-ELP is the protein with a biomineralising sequence and therefore the protein of interest here, its adsorption behaviour was examined using the QCM> Borosilicate coated quartz sensor crystals (Biolin Scientific Ltd, Stockholm, Sweden) were first washed in a 2 % w/v SDS solution for 30 minutes followed by a 10 minute UV/ ozone treatment as a cleaning procedure. In the QCM, the crystal was stabilised in UPW (pH 7). Once the crystal was stable, a solution of STNA15-ELP (100 μg/ml in UPW, pH 7) was added and the QCM crystal was equilibrated for the second time. Finally, the crystal was washed again with UPW (pH 7) to remove any unbound or loosely bound ELP. The change in resonant frequency of the quartz crystal was converted to mass of ELP adsorbed using the Sauerbery equation (Equation 6.1) where Δm is the change in mass, Δf the measured change in frequency upon protein adsorption, n is the overtone number (3) and C is a constant specific to the crystal.

$$\boldsymbol{\Delta m = -\frac{C.\Delta f}{n}}$$

Equation 7.1

The ELP adsorption to the borosilicate surface was tested as a function of temperature and concentration. The temperatures at which adsorptions were examined are: 20, 24, 27, 31 and 37 °C, all in UPW and pH 7. The temperatures were chosen to capture a range which encompasses temperatures around the ITT and well above the ITT. The QCM used did not have the capability to cool the chamber and therefore temperatures below 20 °C could not be achieved. The concentrations of STNA15-ELP examined were: 100 µg/ml, 1mg/ml and 10 mg/ml, all in UPW and pH 7.

7.3 Results and Discussion

7.3.1 Effect of Temperature on ELP Conformation

CD is often used to identify the secondary structure present within proteins and peptides. The measured data is normally given in ellipticity values and then converted to the normalised mean residue ellipticity (MRE) value using the following equation:

$$\boldsymbol{MRE = \theta/(10 \times c_r \times l)}$$

Equation 7.2

where θ is the measured ellipticity, *l* is the pathlength in cm and c_r is the mean residue molar concentration given by:

$$\boldsymbol{c_r = n \times \frac{1000 \times n \times c_g}{M_r}}$$

Equation 7.3

where *n* is the number of peptide bonds, c_g is the protein concentration in g/ml and M_r is the molecular weight of the species. Converting the measured ellipticity to the mean residue ellipticity normalises the data per residue and makes it more comparable between proteins of different lengths. Ellipticity defines the angle whose tangent is the ratio of the minor to major axis of an ellipse created by clockwise and anti-clockwise vectors of the electric field of light. For a detailed description see Greenfield, (2006).

The plotted MRE data can be further analysed by using CD apps deconvolution software (for software details see Benning, (2014)). In this study the software used employs the CONTILL deconvolution method to estimate the fraction of the signal which contributes to a particular protein folding.

In previously reported CD spectra of ELPs two dips are observed, one at 198 nm (associated with the random coil) and one at 220 nm (associated with the β turn/ strand) (Reiersen *et al*., 1998). As expected, both STNA15-ELP and LR-ELP have typical ELP CD traces in H_2O, pH 7 (Figure 7.1). The changes in conformation, as a function of temperature, cause the dip at 198 nm to become less negative and the dip at 220 nm to become more negative. These changes in the CD spectra suggest that, during heating from 19 °C up to 40 °, the proportion of random coil (198 nm) decreases as the proportion of β turn/ strand increases.

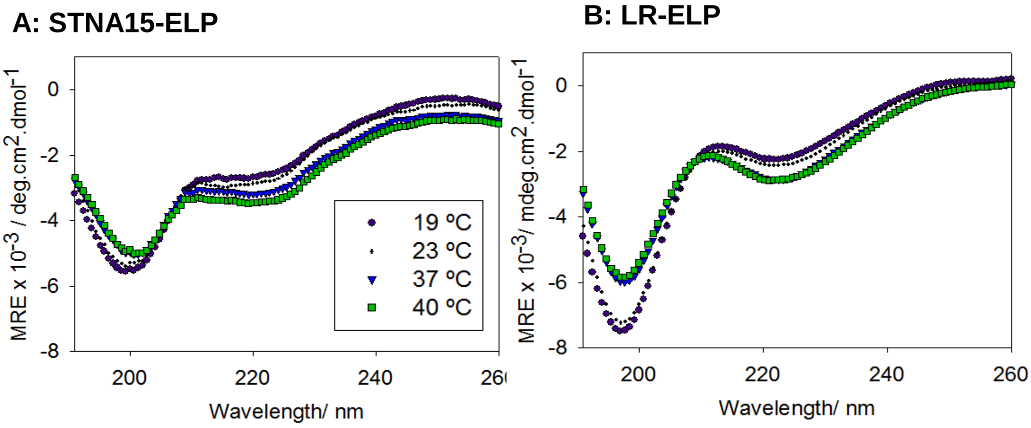

Figure 7.1: CD spectra of A: STNA15-ELP and B: LR-ELP at different temperatures.

To further analyse the CD spectra, the curves were deconvoluted using CD Apps software. All the deconvolutions of the traces gave a good fit, with the residual mean standard deviations all below 0.40. The deconvolution of the traces in Figure 7.1 is shown in Figure 7.2. The deconvolution gives an output of several components: β-turn, β-strand and random coil. STNA15-ELP exhibits a very small change in structure when it is heated from 19 to 40 °C in UPW. Likewise, little change occurs in the β-strand signal of STNA15-ELP traces upon heating.

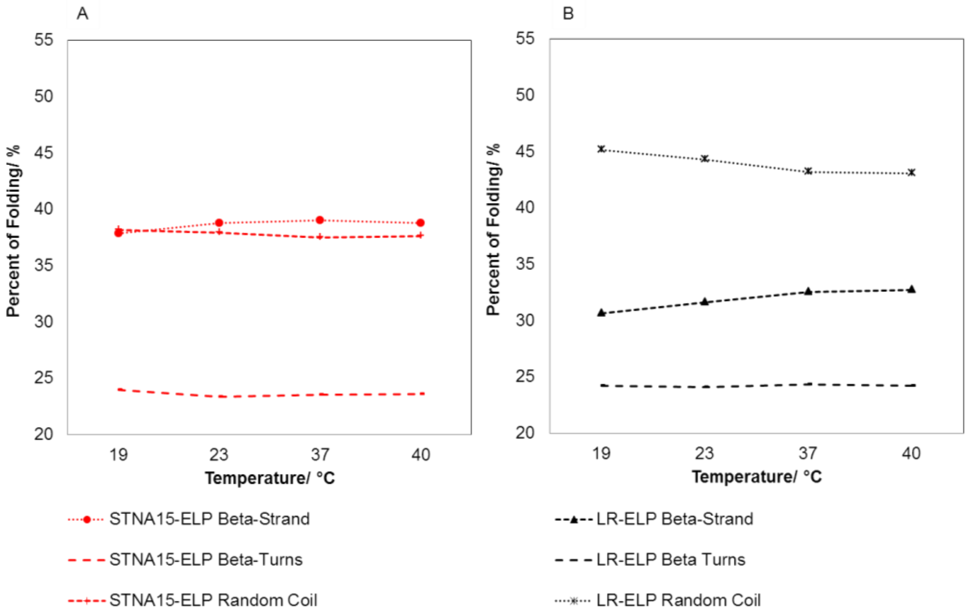

Figure 7.2: Temperature dependent variation in fractions of structural components present in STNA15-ELP (A) and LR-ELP (B) in UPW obtained from the deconvolution of the CD data in Figure 7.1. The RMSD calculated by the CD apps software is: STNA15-ELP 19 °C – 0.18, STNA15-ELP 23 °C – 0.10, STNA15-ELP 37 °C – 0.13, STNA15-ELP 40 °C – 0.09, LR-ELP 19 °C – 0.35, LR-ELP 23 °C – 0.34, LR-ELP 37 °C – 0.37, LR-ELP 40 °C – 0.37.

Unlike STNA15-ELP, LR-ELP appears to undergo the typical transition when heated. The change in the random coil fraction is 1.8% in LR-ELP, compared to only 0.5% in STNA15-ELP, upon heating from 19°C to 40°C. Moreover, at any given temperature LR-ELP contains a larger fraction of the random coil structure in comparison to

STNA15-ELP. The lack of structural change upon heating the STNA15-ELP may suggest that it is already in the folded, dehydrated state at 19 °C when it is in UPW.

The deconvolution of the STNA15-ELP and LR-ELP CD traces shows that there is little change in the *β*-turn structure in either of the proteins upon heating. This can be expected since the *β*-turn arises from the repetitive sequence of VPG**X**G and has been said to be present regardless of the temperature (Li *et al*., 2001).

FTIR studies of the two ELPs in D_2O can further contribute to the CD data findings. The amide I bands of both ELPs, along with the band deconvolution, are shown in Figure 7.3. The FTIR amide peaks are normally made up of several components arising due to the stretching vibration of C=O (amide I) and C-N and N-H bending (amide II) (Lenk *et al*., 1991). The position of the peak components changes depending on the secondary structure of the protein as the hydrogen bonding within the protein alters upon adsorption and/or conformational changes. The deconvolution of the amide I peak of the ELPs in this study is based on previous literature by Serrano *et al*., (2007). Serrano *et al.* (2007) compared the amide I deconvolution to simulated data. The 2007 publication showed that there are 5 peaks that collectively make up the ELP amide I FTIR peak. The amide I peak components were named as *β*-sheet aggregation, *β*-sheet, *β*-sheet/ *β*-turn, α-helix and *β*-turn. Although Serrano *et al.* named one of the components the α-helix, it is quite well known the in water the α-helix and random coil overlap in FTIR (Calero and Gasset, 2005). In contrast to the previous study, this work has analysed the ELPs in D_2O rather than water. Therefore, this work does not include an α-helix and instead a random coil in the results.

It is generally accepted that the components of the amide I peak shift in wavenumber according to the solvent, i.e. they will be slightly different in water and in D_2O (Calero and Gasset, 2005). So, even though the peak values were chosen according to the previous literature, during the Gaussian fitting no bounds are set on the wavenumber position. Hence, the wavenumber positions are in a place that gives the optimal fit. The fitting of the curves is done until the fit converges and the software tolerance criteria are satisfied. In the software, the criterion is satisfied when the scanned fit line data finds two points (X1, Y1) and (X2, Y2) where the specified Y value lies between Y1 and Y2 (description of criterion satisfaction is taken from OriginLAB, 2017).

Out of the 5 peaks that can be present in an amide I peak of an ELP, the β-sheet aggregation peak is said to disappear upon ELP collapse whereas the β-sheet peak is said to appear instead. The other 4 components are said to remain as part of amide I regardless of the temperature. However, the position and percent contribution of these does change when the ELP collapses. The reported changes are a decrease in random coil and β-turn.

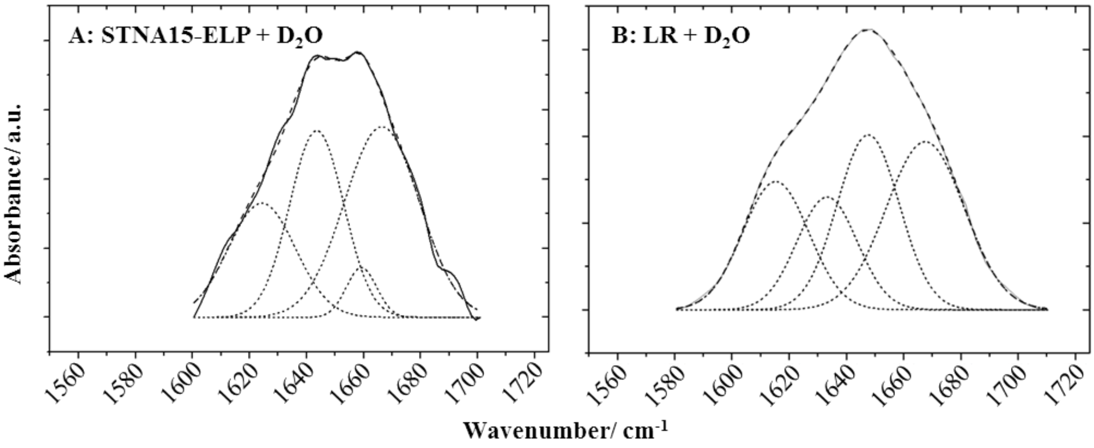

Figure 7.3: FTIR traces of the amide I band (solid line) of A) STNA15-ELP and B) LR-ELP in D_2O. The short dashes lines show the deconvoluted bands of the secondary structure components and long dashes show the fitted curve.

The deconvolution of the amide I band of STNA15-ELP and LR-ELP gives the peaks shown in Figure 7.3A and B respectively. The peak centres of each of the secondary structure components are listed in Table 7.1. The percentage area of each peak denotes the calculated proportion of each of the secondary structures present (Calero and Gasset, 2005). In an aqueous, ion free environment, STNA15-ELP (19°C, pH 7.0) exhibits a folded state. In contrast, FTIR of LR-ELP suggests that it is not in the completely folded state at 19°C, pH 7.0. Comparing the results suggests that LR-ELP has a greater proportion of random coil than STNA15-ELP in the same environment (27.7% compared to 4.54%). The LR-ELP FTIR deconvolution is consistent with the CD data and with the expected result (Figure 7.3 and Figure 7.2 respectively). The manufacturers suggest that at pH of 7.2 LR-ELP's ITT is at 32-34 °C (see 0), well above the FTIR test conditions.

Structure	**STNA15-ELP**		**LR-ELP**	
	Peak center/ cm^{-1}	Area/ %	Peak center/ cm^{-1}	Area/ %
β-sheet aggregation	-	-	1617±3	21.5
β-sheet	1624±6	22.5	-	-
β-sheet/ β-turn	1643±2	30.3	1633±8	17.3
Random coil	1659±1	4.5	1646±9	27.7
β-turn	1666±4	42.7	1666±4	33.5

Table 7.1: FTIR peak centres and relative area percentages of the peaks obtained from the deconvolution of amide I peaks of STNA15-ELP and LR-ELP in D_2O at 19°C, pH 7, and 1mg/ml concentration. The values correspond to the peaks displayed in Figure 7.3. The peak centres are accompanied by the Standard error, given by Origin post deconvolution.

The FTIR data of STNA15-ELP, coupled with the CD data, does not follow the expected results. According to the manufacturers, the ITT of STNA15-ELP, at pH of 7.2, is at 23°C (see Appendix A). The specified ITT should be 4°C higher than the lowest temperature used experimentally (19°C). The sequences of the two ELPs are almost identical, apart from the STNA15 sequence inserted 3 times in STNA15-ELP. The findings suggest that the insertion of the STNA15 sequence greatly affects its thermoresponsive properties. However, considering that proteins which contain the β-

sheet structure are said to take part in biomineralisation processes (for example Addadi *et al*., 1989), it can be assumed that STNA15-ELP is a good candidate for biomimetic mineralisation.

Although both the CD (Figure 7.2) and FTIR (Figure 7.3) data suggest the same trend in the ELP behaviour, there are discrepancies in the amounts of random coil and *β*-turn detected by the two analytical methods. For example, STNA15-ELP CD suggests that 38% of the signal is due to the random coil, this is almost 9 times more than indicated by the FTIR (4.5%). This may be due to the model used in the CD deconvolution, where several model proteins are available as references for the deconvolution. ELPs are quite different from most proteins and therefore some error may be introduced when basing the deconvolution on natural protein structure. All CD analysis software contains a number of reference protein or polypeptide structures and base their deconvolution outcome on those (Greenfield, 2006; Sreerama and Woody, 2000). However, the main purpose of the presented deconvolution in this study is to detect the rises and falls within the structural components of the ELPs. Furthermore, the concentration of the ELPs in the solutions is different in the CD and FTIR due to the experimental requirements for good signal to noise ratio. Since the ITT of ELPs is partly influenced its concentration in solution, the ITT may be different in the two experiments. On this basis, we can observe relative trends in the changes in the structural components and compare between different solutions, but no conclusion will be drawn with regard to the absolute amounts of each component present at a given temperature.

7.3.2 Effect of Solution Chemistry and Temperature on Conformation of ELPs

Hofmeister has shown that ions can affect precipitation and solubility of proteins (see section 3.5). In this light, CD and FTIR were used to study the behaviour of ELPs in two different ionic solutions. The ELPs were dissolved in a calcium solution (10 mM) to mimic the calcium rich environment in the mineralisation studies (explained later). The sodium chloride solution was used as a control to the chloride ions in the $CaCl_2$ solution.

The CD data, taken at 4 different temperatures, for both ELPs in the two solutions is shown in Figure 7.4. Figure 7.5 and Figure 7.6 show the variability, with temperature, in the structural components of STNA15-ELP and LR-ELP in NaCl and $CaCl_2$, respectively, obtained *via* the deconvolution of the Figure 7.4 curves.

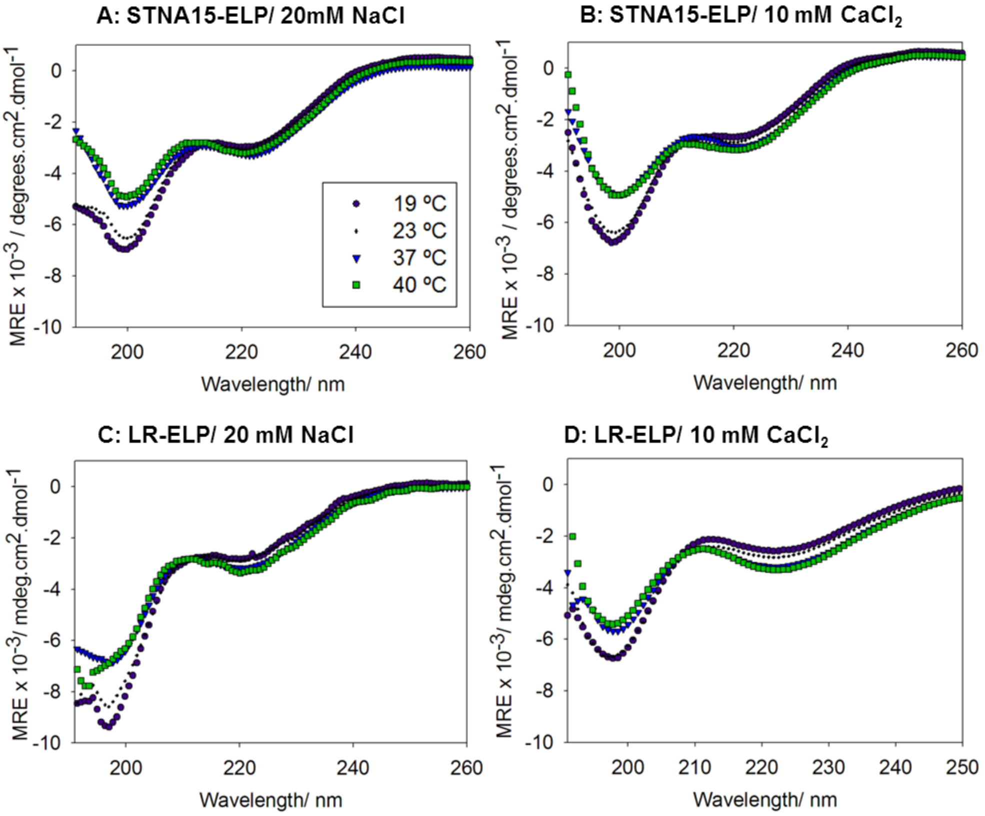

Figure 7.4: CD data of ELPs at 19, 23, 37 and 40 ºC, where A: STNA15-ELP in 20 mM NaCl, B: STNA15-ELP in 10 mM of $CaCl_2$, C: LR-ELP in 20 mM NaCl and D: LR-ELP in 10 mM of $CaCl_2$. The minimum at around 200 nm is indicative of a random coil structure and the minimum at around 220 nm originates from the β-turn structures.

The proportion of random coil structure, in STNA15-ELP, increases in both the $CaCl_2$ (Figure 7.5A) and NaCl (Figure 7.6A) solutions, in comparison to UPW (Figure 7.2A). For example, the amount of random coil structure in STNA15-ELP in NaCl at 19 °C is 45%, compared to 38% in UPW (Figure 7.2). The deconvolution of the CD curves suggests that, at 0.05 mg/ml, there is almost no difference in the STNA15-ELP random coil structure when in either of the ionic solutions. In NaCl the random coil structure accounts for 45% of the folding, compared to 44% in $CaCl_2$. A negligible difference is also observed in the amount of β-strand structure present in STNA15-ELP in the two ionic solutions.

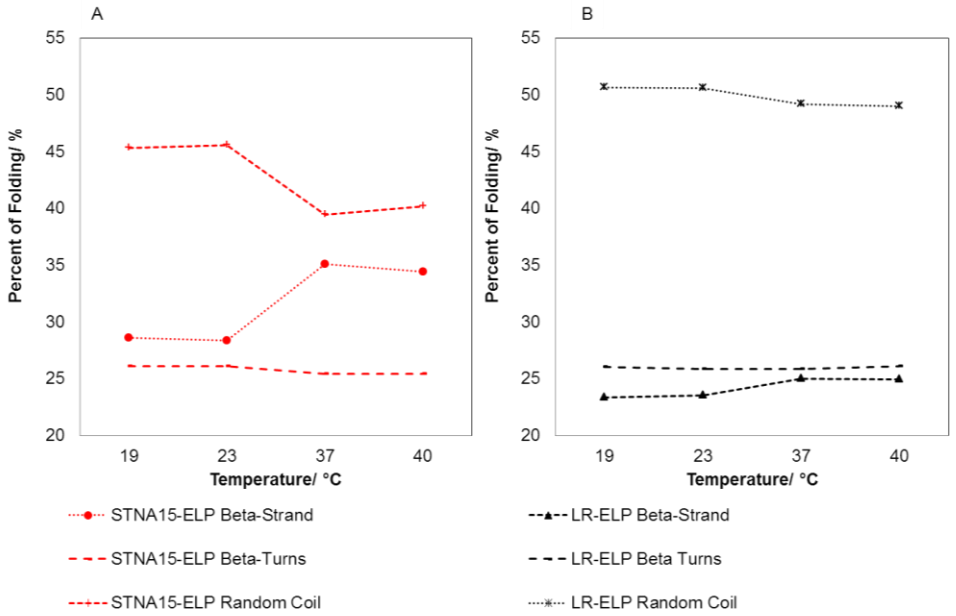

Figure 7.5: Temperature dependent variation in fractions of spectral components obtained from the deconvolution of the CD data of STNA15-ELP (A) and LR-ELP (B) in 20 mM NaCl, pH 7. The RMSD calculated by the CD apps software is: STNA15-ELP 19 °C – 0.10, STNA15-ELP 23 °C – 0.08, STNA15-ELP 37 °C – 0.18, STNA15-ELP 40 °C – 0.17, LR-ELP 19 °C – 0.06, LR-ELP 23 °C – 0.09, LR-ELP 37 °C – 0.075, LR-ELP 40 °C – 0.11.

In NaCl there is 29% β-strand, compared to 31% when in $CaCl_2$. The β-turn component of STNA15-ELP CD spectra also remains mainly the same in the two solutions, similar to what is observed in UPW (Figure 7.2A). However, there is a larger proportion of random coil when STNA15-ELP is in either of the ionic solutions compared to in UPW.

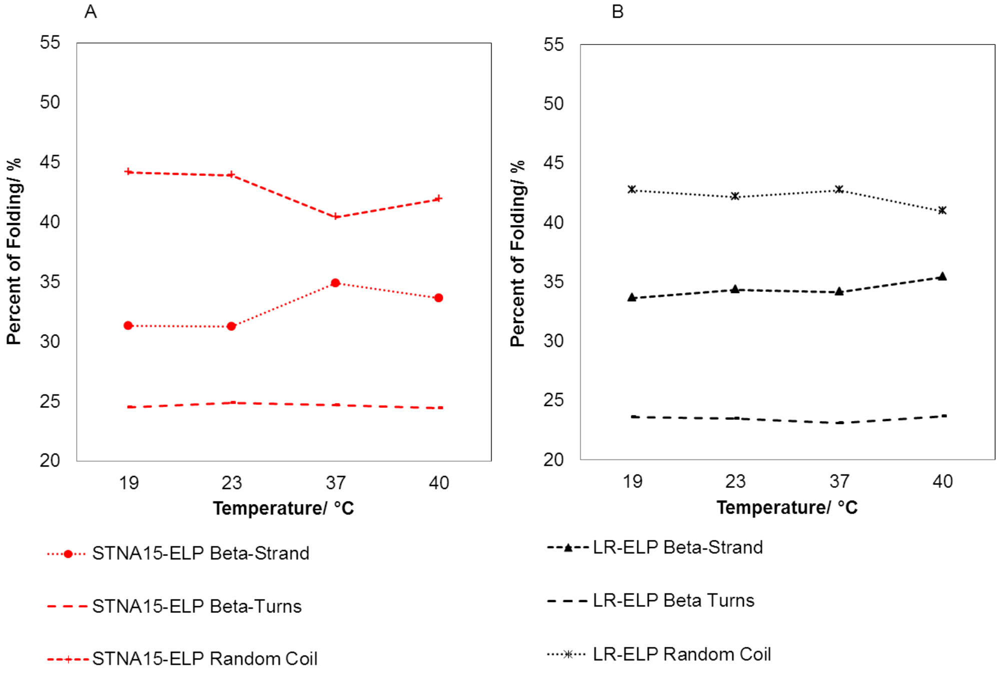

Figure 7.6: Temperature dependent variation in fractions of spectral components obtained from the deconvolution of the CD data of STNA15-ELP (A) and LR-ELP (B) in 10 mM $CaCl_2$, pH 7. The RMSD calculated by the CD apps software is: STNA15-ELP 19 °C – 0.13, STNA15-ELP 23 °C – 0.07, STNA15-ELP 37 °C – 0.22, STNA15-ELP 40 °C – 0.16, LR-ELP 19 °C – 0.11, LR-ELP 23 °C – 0.09, LR-ELP 37 °C – 0.13, LR-ELP 40 °C – 0.39.

Unlike STNA15-ELP, LR-ELP exhibits a structural change between UPW NaCl and $CaCl_2$ solutions (Figure 7.2B, Figure 7.5B, and Figure 7.6B respectively). The random coil structure, at 19°C, increases in NaCl to a fraction of 51%, compared to 45% in UPW and 43% in $CaCl_2$. Concurrent with the large amount of random coil, the proportion of β-strand LR-ELP contains is lowest in NaCl. In $CaCl_2$, LR-ELP exhibits little structural change upon heating to 40 °C. The lack of structural changes in LR-ELP during heating may indicate that LR-ELP is already folded at 19 °C when dissolved in $CaCl_2$. If the LR-ELP is already folded, the results may show that the LR-ELP ITT is depressed by over 12 °C in $CaCl_2$.

The FTIR of STNA15-ELP in the ionic solutions is shown in Figure 7.7. The deconvoluted peak centres and corresponding areas are shown in Table 7.2. FTIR suggests that STNA15-ELP has a larger proportion of the random coil component in NaCl compared to $CaCl_2$. In both the ionic solutions, FTIR traces of STNA15-ELP are consistent with an unfolded ELP state (Figure 7.7). Little change occurs in the β-sheet/ β-turn spectral component, in comparison to β-sheet aggregation ($CaCl_2$ – 4.1%, NaCl – 14.9%) and β-turn relative amounts ($CaCl_2$ – 69.4%, NaCl – 26.8%). In fact, STNA15-ELP contains the least amount of β-sheet aggregation signal when dissolved in the calcium solution.

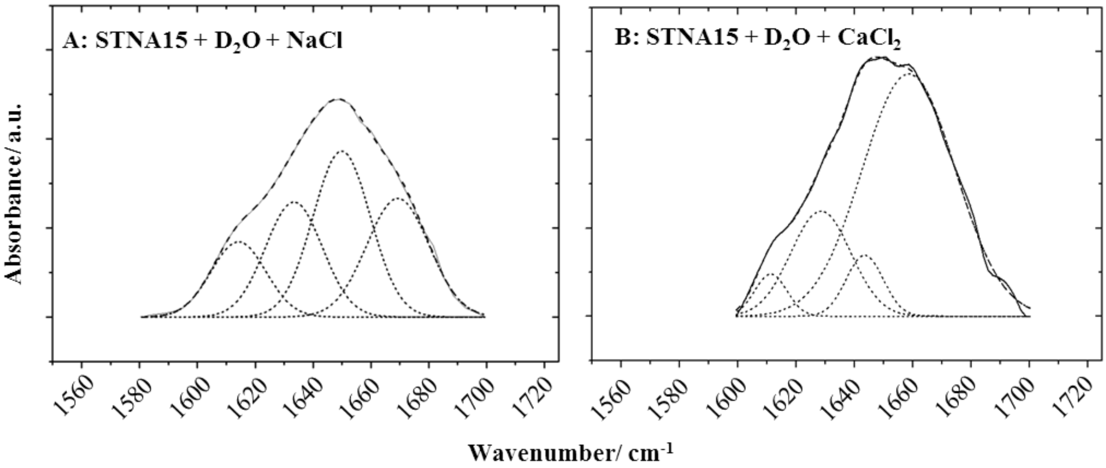

Figure 7.7: ATR-FTIR of the amide I band of STNA15-ELP in (A) 20 mM NaCl and (B) 10 mM $CaCl_2$ dissolved in UPW, pH 7.

The STNA15-ELP sequence has repetitive blocks of positive and negative charged domains. It may be possible that the STNA15-ELP forms intramolecular electrostatic interaction, between the negative and positive blocks, and folds to form a β-sheet conformation when in UPW. This is perhaps the cause of the lack of change in structural components of STNA15-ELP in UPW, seen in the CD data in Figure 7.2. The Ca^{2+} ions may bind to the STNA15 sequence, screen the negative charges and prevent the intramolecular interactions. Therefore, in a Ca^{2+} solution, the real thermoresponsive behavior of STNA15-ELP is observed.

Structure	**STNA15-ELP + 20 mM NaCl**		**STNA15-ELP + 10 mM $CaCl_2$**	
	Peak center± Standard Error/ cm^{-1}	Area/ %	Peak center± Standard Error/ cm^{-1}	Area/ %
β-sheet aggregation	1614±7	14.9	1611±2	4.1
β-sheet	-	-	-	-
β-sheet/ β-turn	1633±12	23.8	1628±5	19.4
Random coil	1650±6	34.5	1644±3	7.01
β-turn	1669±17	26.8	1668±1	69.4

Table 7.2: FTIR peak centres and relative area percentages of the peaks obtained from the deconvolution of amide I peaks of STNA15-ELP 10 mM NaCl and 20 mM $CaCl_2$ at 19°C, pH 7, and 1mg/ml concentration. The values correspond to the peaks displayed in Figure 7.7. The peak centres are accompanied by the Standard error, given by Origin post deconvolution.

LR-ELP FTIR traces in NaCl and $CaCl_2$ are shown in Figure 7.8A and Figure 7.8B, respectively. The deconvoluted peak positions and their areas are shown in Table 7.3. The two traces are almost identical to each other. In both cases, the FTIR trace resembles an unfolded ELP trace when compared to the findings of Serrano *et al.* (2007). However, these results are not consistent with the CD data presented above.

The discrepancy between the CD (Figure 7.5B and Figure 7.6B) and FTIR data Figure 7.8) of LR-ELP may occur due to the dependence of ELP folding on the concentration of ELP and ions in solution. In comparison to FTIR of LR-ELP in UPW (Figure 7.3B, Table 7.1), there is less random coil when the LR-ELP is in an ionic solution, falling from 27.7% in UPW to 23.2% in NaCl and 24.4% in $CaCl_2$ (see

Table 7.3). This result is not quite in agreement with the CD data, where the largest amount of random coil is observed in a NaCl containing solution (Figure 7.5).

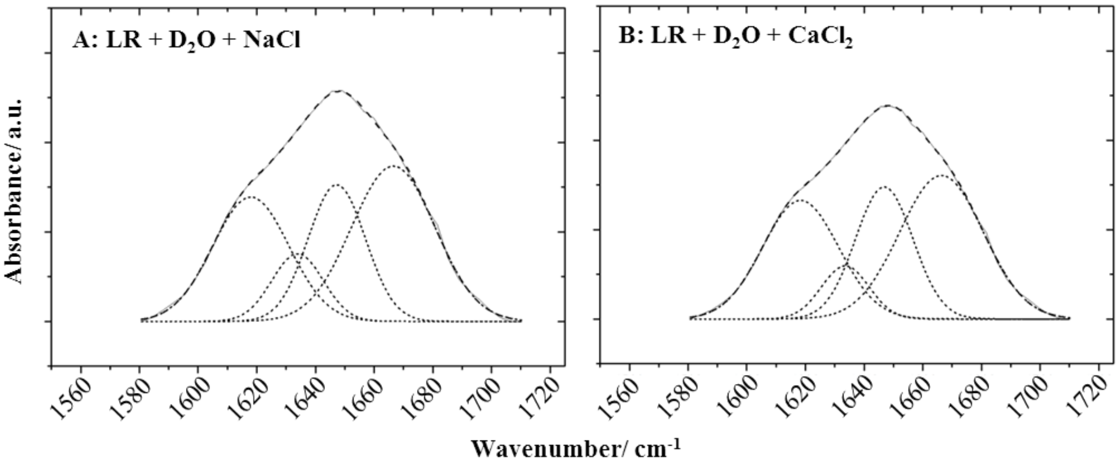

Figure 7.8: ATR-FTIR of the amide I band of LR-ELP in (A) 20 mM NaCl (B) 10 mM CaCl₂ dissolved in deuterated water, pH 7.

Structure	**LR-ELP + 20 mM NaCl**		**LR-ELP + 10 mM CaCl₂**	
	Peak center± Standard Error/ cm^{-1}	Area/ %	Peak center± Standard Error/ cm^{-1}	Area/ %
β-sheet aggregation	1618±5	28.0	1618±3	28.9
β-sheet	-	-	-	-
β-sheet/ β-turn	1634±15	10.3	1634±8	8.13
Random coil	1647±12	23.2	1647±6	24.4
β-turn	1667±4	38.4	1666±3	38.5

Table 7.3: FTIR peak centres and relative area percentages of the peaks obtained from the deconvolution of amide I peaks of LR-ELP 10 mM NaCl and 20 mM CaCl₂ at 19°C, pH 7, and 1mg/ml concentration. The values correspond to the peaks displayed in Figure 7.8. The peak centres are accompanied by the Standard Error, given by Origin post deconvolution.

The structure of LR-ELP, as measured by FTIR, in any of the solutions is as expected. The LR-ELP contains the largest amount of random coil when in UPW. The addition of salts into the water causes a simultaneous decrease in random coil and increase in β-strands. When measured by FTIR, LR-ELP displays the typical

Hofmeister salting-out effect. In this case the ITT of LR-ELP is, effectively, lowered. The different effect NaCl has on LR-ELP is an oddity in these experiments. Perhaps the difference occurs due to the different ELP concentrations in CD (0.05 mg/ml) and FTIR (1 mg/ml). Past literature has described the effect of NaCl on ELPs (Reguera *et al*., 2007). NaCl is said to promote order within the clathrate-like structure that surrounds the hydrophobic moieties within the ELP. The better order of the water molecules may be the cause of the larger proportion of random coil structure observed with the CD (Figure 7.5). Since the concentration of LR-ELP is higher in the FTIR study, there may not be enough NaCl to aid in such a drastic rise in the proportion of random coil.

In contrast to LR-ELP, addition of $CaCl_2$ and NaCl causes an increase in the random coil structure of STNA15-ELP. This result was not expected, even when comparing to other previous studies where ELPs with carboxylic acid residues were used (for example Kherb *et al*., 2012). It is evident that the addition of STNA15 into the LR sequence causes either additional interaction to be present within the protein molecule or between different molecules. The negatively charged STNA15-ELP sequence may be interacting with the positively charged lysine sequence, causing folding in UPW. However, upon addition of ions this interaction may be disrupted, showing the real structure of the ELP. This can be supported by looking at STNA15-ELP CD trace in $CaCl_2$ (Figure 7.4D) and comparing to LR-ELP in UPW (Figure 7.1B). The two traces resemble each other and so it is plausible that the STNA15 sequence interacts with Ca^{2+} and therefore charge screening occurs, causing the opening of the ELP to reveal the expected ELP structure.

7.3.3 Effect of Temperature on STNA15-ELP Adsorption[1]

Prior to mineralisation studies, the ELP was immobilised on a borosilicate glass surface at 37 °C. In order to check whether or not STNA15-ELP has an affinity to the borosilicate glass, a quartz crystal microbalance (QCM) study was carried out in an aqueous environment. The QCM is a technique often used to accurately measure the amount, in mass, of molecules adsorbed to a surface. The resonant frequency of quartz is sensitive to change of mass adsorbed or settled on the crystal. The frequency and mass relation is described by the Sauerbery equation (see Equation 6.1, section 6.2.3).

Figure 7.9 shows the change in mass, measured by QCM, during equilibration of the crystal in the ELP solution (A) and after washing away unbound ELP with UPW (B). The mass in Figure 7.9A is higher than in Figure 7.9B due to the unbound ELP lying on top of QCM crystal.

The QCM study confirmed that the STNA15-ELP, in ultrapure water, does bind to the borosilicate glass (Figure 7.9). The data shows a good binding of STNA15-ELP where 15.2 mg/m^2 remained adsorbed to the substrate after washing with ultrapure water (Figure 7.9B).

Table 7.4 shows the contact angles of water droplets on the clean and ELP coated borosilicate glass, along with the isoelectric point (pI) of the glass. The contact angle of the ELP coated glass suggests that the STNA15-ELP coating forms a hydrophilic surface when adsorbed to the glass (contact angle (θ) = 18.7 °C, Table 7.4), indicating that the hydrophilic mineralising sequence is exposed on the surface rather than in contact with the glass.

---

[1] The experimental work was designed by KS and the laboratory measurements were carried out by Mohammad Edris Saleem, a 3rd year SEMS project student, under the supervision of KS. As such, the description, analysis and interpretation of the measurements presented here are entirely the work of KS.

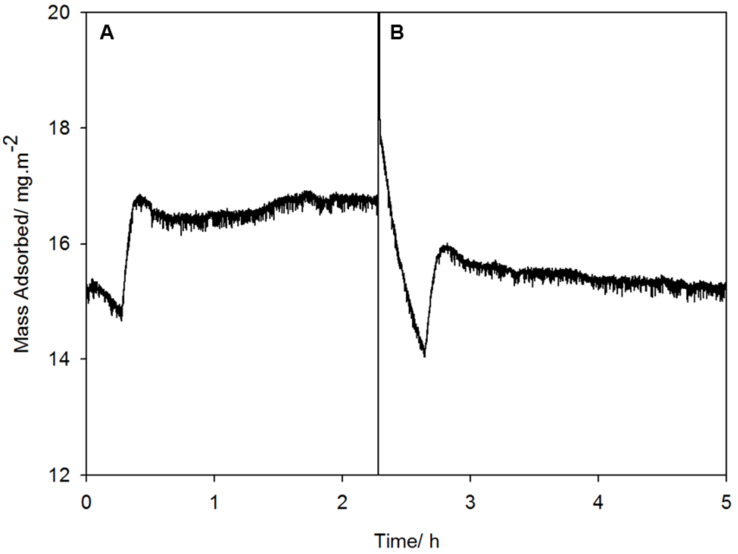

Figure 7.9: QCM data showing the (A) protein injection and (B) washing cycles at 37 °C and a 100 µg/ml concentration. After the washing cycle the final measured mass adsorbed to the surface was 15.2 mg/m^2.

The contact angle of the borosilicate glass, displayed in Table 7.4, is indicative of a surface with low hydrophilicity (contact angle (θ) = 70.9°). Reports have shown that protein adsorption is favoured when contact angle (θ) > 65° (Vogler, 2012). Vogler (2012) described the contact angle (θ) > 65° as the dividing line between hydrophobic and hydrophilic surfaces (where hydrophobic surfaces exhibit angles of above 65°) and the pivot point about which protein adsorption goes from low to high. Under the given experimental conditions, according to literature value for the pI, the glass carries a net negative charge (Blass *et al*., 2013). Therefore, the protein may arrange itself on the glass surface in such a way that the negative STNA15 (mineralising) sequence is exposed to the mineralising solution due to repulsion from the negatively charged glass surface. The positively charged lysine residues in STNA15-ELP are expected to interact with the negative glass surface. This hypothesis is based on these indirect evidences since the conformation of the protein cannot be directly determined from QCM measurements alone.

Borosilicate Glass Property	Value ± SE
Water contact angle (θ) (experimental)	70.9 ° ± 2.0
Water contact angle (θ) of protein coated glass (experimental)	18.7 ° ± 1.25
Isoelectric point/ pH	3.62 ± 0.12

Table 7.4: Contact angle measured for ultrapure water on uncoated borosilicate glass substrate and on a protein-coated borosilicate glass (n=3) are given accompanied with the standard error (SE). The value for the isoelectric point of the glass was obtained from literature (Blass et al., 2013).

The mineralising protein, STNA15-ELP, was adsorbed onto a borosilicate at 20, 24, 27, 31 and 37 °C. The adsorption results are shown in Figure 7.10. The mass of ELP adsorbed to the surface of the glass is similar between the temperatures of 20 °C (23.1 ± 0.57 mg/m^2), 24 °C (23.3 ± 0.26 mg/m^2) and 27 °C (25.0 ± 1.99 mg/m^2). At 31 and 37 °C the mass adsorbed decreases to 15.04 ± 0.69 mg/m^2 and 15.02 mg/m^2, respectively. The ITT of STNA15-ELP in UPW, according to the manufacturers is 23 °C (Appendix A). The change in adsorption occurs well above the ITT and therefore cannot be directly related to the folding of the protein when considering Figure 7.10 alone.

QCM measures the mass adsorbed onto the crystal surface, including the hydration layer of the protein. It could be possible that the ELP appears to adsorb in a higher quantity when it is below the ITT since it is hydrated. However, even that is questionable since the amount absorbed at 27 °C, 4°C above the ITT, is still similar to the mass adsorbed below the expected ITT. The ITT of ELPs is said to be concentration dependant and decreases logarithmically with increasing concentration (Meyer and Chilkoti, 2004). The slightly higher transition in the ELP behaviour may be the cause of the difference in concentration, between the 0.1 mg/ml used here and 50 mg/ml reported in the manufacturer specifications (Appendix A).

Protein adsorption, as a function of temperature, has been investigated previously. One relevant example is of bovine serum albumin (BSA) adsorption onto surfaces (for example see Kiss, 1993; Norde and Favier, 1992). BSA is said to be a relatively soft protein since it can unfold at higher temperatures. BSA undergoes denaturation when heated above high temperatures, around 55 °C. The BSA unfolding is irreversible upon cooling down to the original temperature. Furthermore, the highest amount of BSA adsorption occurs at temperatures where it is denatured. Kiss (1993) studies suggested that BSA adheres to hydrophobic surfaces due to the unfolding during denaturation, where the hydrophobic parts of the protein become exposed to the sorbate.

ELPs, like BSA, can be termed as soft proteins since they can fold and unfold easily. However, the main difference between ELPs and most natural proteins is that the former normally fold at high temperatures and unfold at low. Considering the fact that BSA adsorbs at higher amount when it is unfolded, it may be a similar case for STNA15-ELP. The adsorption of STNA15-ELP to surfaces may be somewhat similar to other soft proteins, such as BSA. However, due to the unique thermal properties of ELPs, the adsorption process is reversed with regards to the temperature. At lower temperatures, the ELP is unfolded and can have more favourable interaction with a hydrophobic surface. During heating, the ELP collapses and aggregates causing the hydrophobic parts to be hidden from the sorbate, within the aggregate, hence lowering the adsorption affinity.

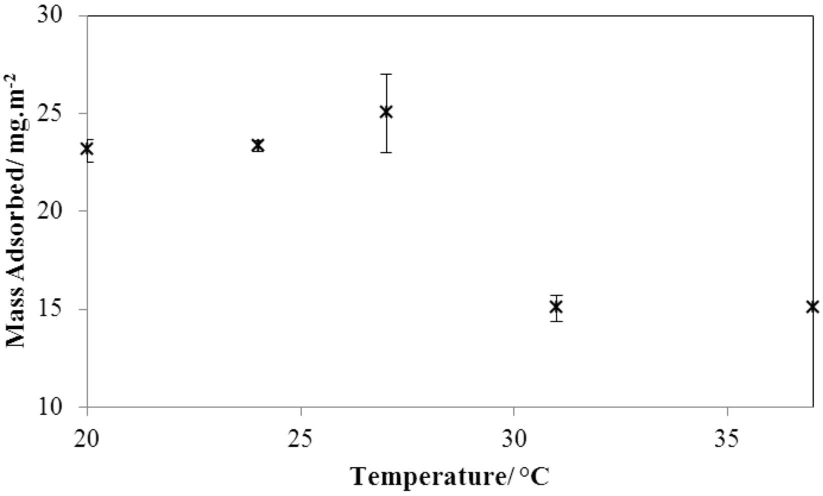

Figure 7.10: Graph displaying the average adsorbed mass of STNA15-ELP on a borosilicate coated quartz crystal at a range of temperatures. For values at 20, 24 and 27, 31 °C n=3 (3 different samples) and scale bars show the standard error.

From this work, it can be concluded that the optimal temperature for STNA15-ELP adsorption onto a borosilicate surface is below 27 °C. For this reason, the following adsorption work will be carried out at room temperature, rather than elevated temperatures.

7.3.4 STNA15-ELP Adsorption as a Function of Concentration

It is well known that protein adsorption onto a surface is affected by the concentration of the protein in solution. Studies of concentration dependent adsorption can be found on a range of proteins. For example, BSA adsorption onto a polystyrene surface increases until around 50 mg/ml (Shirahama and Suzawa, 1985). Fibronectin is another protein that has an increased adsorption as a function of concentration (Al-Jawad *et al.*, 2009). Often, the adsorption of a protein will initially increase steeply followed by a plateau at a certain concentration, after which not much more can be adsorbed.

The STNA15-ELP was adsorbed to the borosilicate glass from a large range of concentrations. Figure 7.11 shows the mass adsorbed at 10, 100 and 1000 μg/ ml. The initial increase of adsorbed protein, from 10 μg/ ml to 100 μg/ ml concentrations, is 2-fold (from 7.6 to 15.2 mg/m^2). However, upon a further 10-fold increase in ELP concentration there is only an increase of 4.1 mg/m^2 adsorbed to the surface, giving a final adsorbed mass of 19.4 mg/m^2. Although the full range of protein concentration was not examined, since there is only little change in adsorption between 100 μg/ ml and 1000 μg/ ml, 100 μg/ ml was chosen for the rest of the studies. It was determined that 100 μg/ ml of STNA15-ELP provided sufficient adsorption to the substrate whilst minimising the experimental costs.

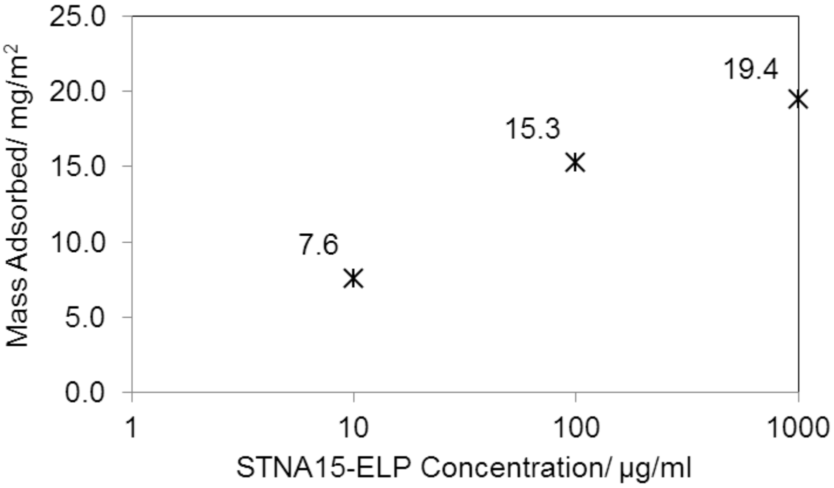

Figure 7.11: QCM data showing the mass of STNA15-ELP adsorbed to borosilicate glass at concentrations of 10, 100 and 1000 μg/ml, plotted on a log scale. The adsorptions were carried out at 37°C in ultrapure water and pH 7.0.

7.3.5 Effect of Adsorption on STNA15-ELP Conformation

The FTIR spectra of unconstrained STNA15-ELP versus constrained STNA15-ELP are shown in Figure 7.12. There is a noticeable difference in the amide I (1600-1700 cm^{-1}) and amide II (1400-1500 cm^{-1}) relative intensities (Figure 7.12A). The dipole moments of the amide I and amide II peaks are almost perpendicular to one another (Miyazawa and Blout, 1961), hence the change in amide I and amide II intensity is consistent with differences in conformation between the bound and unbound proteins.

The overall amide I peak increases in intensity when STNA15-ELP is adsorbed on glass, conversely there is a reduction in the amide II intensity, compared to STNA15-ELP prior to adsorption (Figure 7.12A). Conformational changes of the ELP, upon binding, agree with previous reports of natural elastin structural changes during surface adsorption. Natural elastin is globular in solution and undergoes conformational changes in order to assemble into an ordered structure upon surface adsorption (Subburaman *et al*., 2006).

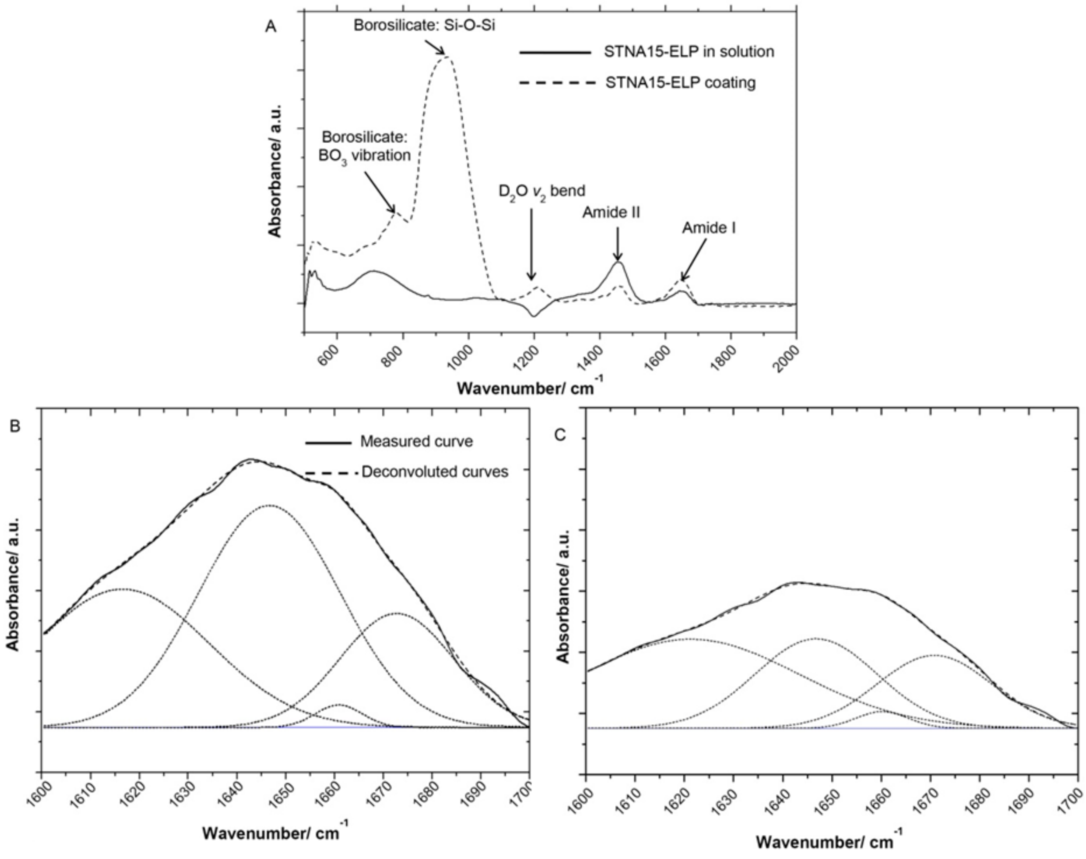

Figure 7.12: FTIR results of A: coated ELP (dotted line) vs. STNA15-ELP in solution (solid line) showing the difference in the absorbance, especially noticeable difference in the intensity of amide I and II peaks. The Gaussian fit deconvoluted amide I band of (B) STNA15-ELP coated on glass and (C) protein in solution. The dashed line represents the data and the smooth line is the Gaussian fit.

To investigate further, the solution (Figure 7.12B) and coating (Figure 7.12C) samples' amide I peaks were deconvoluted using a Gaussian fit. The peak values were chosen according to previous indexed values in literature (Serrano *et al*., 2007). The results given in Table 7.5 indicate an increase in the amount of β-sheet/ β-turn structure (1647 cm^{-1}), when the protein is constrained on glass, accompanied with a small decrease in the random coil component (1660/1661 cm^{-1}). The increase in the amount of β-sheet/ β-turn structure and a decrease of the random coil in the amide I band is indicative of an increase in STNA15-ELP conformation, when adsorbed on a glass substrate.

Structure	**Constrained STNA15-ELP**		**STNA15-ELP in solution**	
	Peak center± Standard Error/ cm^{-1}	Area/ %	Peak center± Standard Error/ cm^{-1}	Area/ %
β-sheet aggregation	1617±7	30.2	-	-
β-sheet	-	-	1624±6	22.5
β-sheet/ β-turn	1647±1	48.4	1643±2	30.3
Random coil	1661±2	1.6	1659±1	4.5
β-turn	1673±2	19.7	1666±4	42.7

Table 7.5: Wavenumber values of the peak centres and the % area of each assigned peak taken from the deconvolution of the amide I peaks of STNA15-ELP coating and in solution (plotted in Figure 7.12).

ELPs' thermoresponsive properties are attributed to their inverse transition temperature (ITT) (Urry *et al*., 1998). Reports have shown that below the ITT the protein is unfolded, mostly with a random coil conformation, and the hydrophobic parts are hydrated with ordered water (Rodriguez-Cabello, 2004). Above this temperature, the water structure is disrupted and the protein becomes dehydrated causing the protein to fold, via an increase in the β-sheet/ β-turn component and simultaneous decrease in random coil. This process is not instantaneous and structural changes occur over a range of temperatures above and below the ITT (for example Reiersen *et al*., 1998).

Previous work by Serrano *et al*. (2007) investigated ELP conformation with FTIR and concluded that below the ITT the protein contains the β-sheet aggregation component

(1616 cm^{-1}), but this completely disappears upon heating above the ITT. Furthermore, the β-sheet/ β-turn proprotion increases whilst the random coil and the proportion of β-turn decreases. The FTIR data presented in Table 7.5 shows a similar change between the unconstrained and the constrained STNA15-ELP. Although, the β-sheet aggregation peak is present after adsorption, there is an increased amount of the β-sheet/ β-turn stucture and a smaller amount of the β-turn structure. There may also be a decrease in the random coil structure, although it is very small and may be part of the fitting error. From the results presented in Figure 7.12 and Table 7.5, it can be expected that upon adsorption on the glass surface the ELP folds into a similar conformation as it would when heated well above the ITT, i.e. the protein gains order in its conformation. However, the presence of the β-sheet aggregation peak after adosprtion may suggest the presence of a different conformation on the galss compared to the ones assumed in solution above and below the ITT.

Protein adsorption is a complex process and can change dramatically with alteration in the surface and solution chemistry. A number of factors that affect adsorption of proteins onto surfaces have been identified. These include pH (pH close to pI promotes adsorption) (Norde, 1986; Norde *et al.*, 1986); substrate hydrophobicity (Shirahama and Suzawa, 1985); dehydration (Lee and Ruckenstein, 1988); surface-solution equilibrium (Wojciechowski *et al.*, 1986). Although protein adsorption mechanisms can be the result of multiple factors, the adsorption behaviour is specific to each protein and the surface it is adsorbing to. In this study, the STNA15-ELP is dissolved in ultrapure water (pH ~7.0) and is far from its pI (see pI details in Appendix A). Thus, according to Norde *et al.* (1986), STNA15-ELP would not favourably adsorb to the glass. However, the QCM results (Figure 7.9) confirm that the protein is well bound to the glass surface. Lee and Ruckenstein (1988) proposed that proteins gain entropy upon adsorption to surfaces due to dehydration and conformational changes. This explanation is more suitable for the system described here, since STNA15-ELP appears to gain conformation upon adsorption and this is known to occur during the dehydration of the ELP chains and subsequent hydrophobic collapse.

7.4 Summary

A large number of ELPs have been investigated in previously published literature. However, each ELP is unique in its thermoresponsive behaviour. In this chapter we investigated the thermoresponsive properties of two ELPs in particular, LR-ELP and STNA15-ELP. The thermoresponsive behaviour was tested as a function of temperature, solution chemistry and adsorption. It is clear the STNA15-ELP has a distinct relationship with calcium ions, which the LR-ELP did not show. However, the behaviour of STNA15-ELP in ionic solutions was somewhat unexpected, in particular the $CaCl_2$ solution. In the Hofmeister ion series, Ca^{2+} is considered to be on the side of the salting-in ions, i.e. they assist with solubility (Kherb *et al.*, 2012). On the same ion scale, Na^+ is somewhere in the middle and has a lesser effect on the protein solubility. However, FTIR results suggest that in NaCl STNA15-ELP had the largest proportion of random coil, in comparison to $CaCl_2$ or UPW (Table 7.2).

Some have reported that mineralising proteins conform to a β-sheet structure (Addadi and Weiner, 1985). STNA15-ELP has a larger β-sheet proportion, compared to LR-ELP, in any of the solutions, indicating that it may be effective as a protein for biomimetic mineralisation.

The adsorption of STNA15-ELP to borosilicate was best at and below 27 °C and the amount adsorbed was sufficient at a concentration of 100 μg/ml. The adsorption of STNA15-ELP caused a restructuring of the molecule, in a different configuration to when it is in any of the solutions, with an increased β-sheet proportion. The results, presented here, indicate that STNA15-ELP may be more effective in biomimetic mineralisation when it is restricted on glass, compared to when it is in solution. The biomimetic mineralisation experiments will, therefore, be based on these findings.

Chapter 8. UNDERSTANDING AND CONTROLLING ELP AGGREGATION [2]

8.1 Introduction

The ability to control the size[2] of an elastin-like protein (ELP) aggregate prior to mineralisation can lead to the possibility of controlling the amount of mineralisation sites present in a volume of ELP and controlling the way the ELP guides the mineralisation process. The aggregation of ELPs can be triggered thermally, due to their thermoresponsive nature. The thermoresponsive behaviour of ELPs is known to be affected by the local chemical environment. However, thermally triggered aggregation is not a particularly well-controlled process. The ELP aggregation was investigated in ultrapure water (UPW), 10 mM $CaCl_2$ and 20 mM NaCl. In this chapter we explore the thermally triggered formation of ELP particles, how we can control their size and stabilise them.

8.2 Experimental Details

8.2.1 ELP Aggregate Characterisation

The ELP aggregation above ITT was analysed with dynamic light scattering (DLS) and transmission electron microscopy (TEM). In all cases the ELPs were dissolved in UPW, 10 mM $CaCl_2$ and 20 mM NaCl (pH 7) at 1 mg/ml concentration. For DLS studies, the ELPs were centrifuged, in order to remove large particulate matter such as dust particles or ELP particles that aggregated prior to measurement. The ELP solutions were placed within quartz cuvettes and into a temperature controlled chamber. The ELPs were heated from 19 °C to 58 °C, at 3 °C intervals. At each temperature, the ELP solutions were equilibrated for 2 minutes prior to taking a

---

[2] The experimental work was designed by KS, MAJ and AB, in conjunction with Prof. Henry Margolis at the Forsyth Institute, Boston. Part of the laboratory measurements were carried out at the Forsyth Institute, Boston, with the help of Dr Seo-Young Kwak.

measurement. 10 readings were taken for each temperature. The result given by the DLS software is given as a histogram of hydrodynamic radii (R_H) (Figure 8.1) and average R_H present with the sample. The average result does not have an associated error.

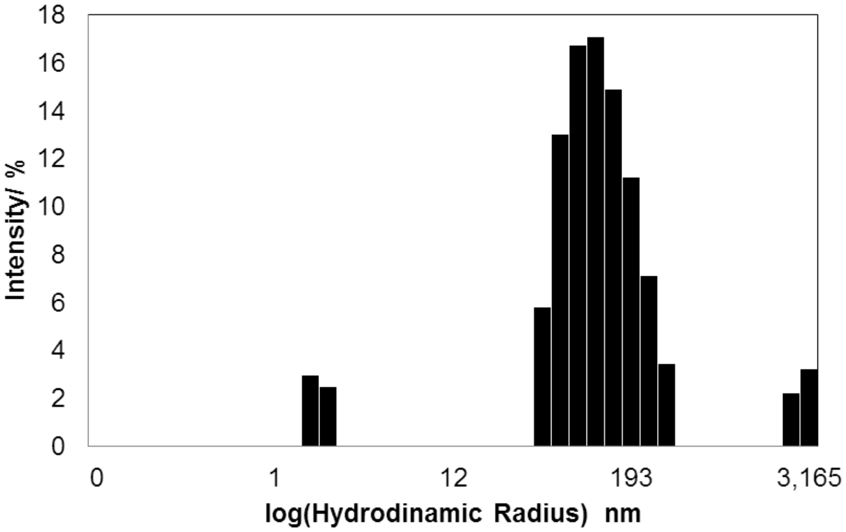

Figure 8.1: Example of an output of results in DLS. A graph like this is produced from 10 averaged acquisitions for each sample at each temperature accompanied with the numerical averages of each of the sizes. Sizes above 1000 nm are generally considered as bubbles/ dust particles/ scratches on the cuvette due to the extremely large size.

Following DLS analysis, the ELPs were analysed in TEM. TEM copper grids were prepared for ELPs below and above ITT. Firstly, the ELP solutions were diluted by a fifth to prevent too much protein accumulating on the TEM grids. To prepare the copper TEM grids below the inverse transition temperature (ITT), 5 µl of each of the ELP solutions was pipetted onto a separate grid and left for 2 minutes at room temperature (19 °C). The remaining solution was removed by blotting. 5 µl of phosphotungstic acid (PTA) stain was pipetted onto the ELP coated copper grids and again left at room temperature for 2 minutes. The remainder of the stain, left on the grid, was removed by blotting. The same procedure was carried out to prepare the above the ITT samples but in a 50 °C oven. Once the samples were completely dry, they were imaged with TEM.

8.2.2 Aggregate Crosslinking

Solutions of 1mg/ml ELPs were heated to 50 °C, well above the ITT, to trigger complete aggregation in either UPW, 10 mM $CaCl_2$ or 20 mM NaCl. After keeping the solutions at 50 °C for 15 minutes, to ensure all protein was aggregated, glutaraldehyde (GTA) crosslinker was added at a range of concentrations (2.5, 1.25, 0.5 and 0.25% v/v). The solutions were left to crosslink at 50 °C for 1 hour (see section 6.1.2 above). After the crosslinking was complete, the solutions were centrifuged to precipitate the aggregates. The supernatant, containing remaining GTA, was removed. The crosslinked ELPs were washed with ethanol and centrifuged again twice before being stored at 5°C in ethanol. The crosslinked ELPs were examined using SEM. The samples were pipetted onto carbon tape, on aluminium stubs, and coated with gold.

8.3 Results and Discussion

8.3.1 Effect of Ionic Solutions on Aggregation of ELP

LR-ELP and STNA15-ELP were added to different ionic solutions, heated and the hydrodynamic radii of the particles in solution were measured. Table 8.1 details the hydrodynamic radii (R_H) of STNA15-ELP and LR-ELP, obtained from DLS, in the different solutions below the ITT.

Conclusions regarding the ELP structure cannot be drawn from DLS alone. The DLS measurements are based on the Brownian motion of spherical particles within a fluid (Hassan *et al*., 2015). Therefore, the reported sizes in Table 8.1 may not be precise since the protein may not have a spherical shape below the ITT. However, a comment can be made about the trend based on the R_H values. The smallest radius observed for STNA15-ELP, 1.4 nm, was in UPW. The addition of any ionic species increases the R_H, where with NaCl the radius increases to 3.6 nm and with $CaCl_2$ to 4.6 nm.

In contrast to STNA15-ELP, the size of the LR-ELP below the ITT does not seem to have an obvious trend in particle size in different solutions. However, the size of the LR-ELP may correlate with the previous FTIR findings where the NaCl seemed to lower the LR-ELP's transition temperature (Table 7.3). These results may show that in NaCl, LR-ELP has the most collapsed form and smallest R_H, in comparison to either in UPW or in $CaCl_2$, prior to aggregation.

Solution	**Hydrodynamic Radius Below ITT/ nm**	
	LR-ELP	STNA15-ELP
UPW	6.0	1.4
20 mM NaCl	5.1	-
10 mM $CaCl_2$	6.0	4.6

Table 8.1: The hydrodynamic radii of STNA15-ELP dissolved in 4 different ionic solutions. Measurements recorded below the ITT (19 °C). The particle size of STNA15-ELP at 19 ℃ could not be read as they were too large and scattered too much light, saturating the detector.

According to Rodríguez-Cabello *et al.*, (2007) an individual ELP molecule, which is folded but not aggregated or associated, will have a size of around 1.8 nm. Upon further heating, ELP molecules associate into a twisted filament of *β*-spirals and form 5 nm particles (Urry, 1992). Heating even further creates large aggregates that can grow up to 2 μm in size. However, the size of an unfolded ELP molecule may not be as easy to predict since polymeric molecules such as ELPs are dynamic in nature. Furthermore, ELPs are highly hydrated below the ITT with water molecules forming ordered structures around the hydrophobic backbone. This water contributes to the size of the molecule given by DLS, since DLS measures the hydrodynamic radius and not the absolute molecular radius. Therefore, if an ELP molecule becomes more unfolded and hydrated it may appear as a larger particle in DLS. In the case of ionic solutions, ions may bind to the ELP and with them more water molecules, again causing an increase in the measured R_H.

If considering the DLS measurements alongside CD and FTIR presented in the previous chapter, the R_H of STNA15-ELP is consistent with protein unfolding in ionic solutions. The R_H of STNA15-ELP more than doubled when $CaCl_2$ was added (Table 8.1). Perhaps binding of ions to the ELP has some contribution to the size and therefore a change is observed.

Figure 8.2 shows the intensity of the light scattered by STNA15-ELP particles, in different solutions and at a range of temperatures, generated by large particles. The sizes of the ELP aggregates were split into two sizes. The first set of sizes represents the individual ELP molecule and was generally measured to be between 1 and ~5 nm, depending on the solution conditions. The second set of sizes is particles that were measured to have R_H above 100 nm. This split in particle sizes was decided based on previous reports of ELP sizes as either individual β-spiral (1-2 nm), associated particles (~5nm) or aggregated particles (>5nm) (Kowalczyk *et al.*, 2014). In this study, we assume that unfolded ELP molecules are larger, in terms of R_H, than the folded β-spiral since it is more hydrated and not as compact.

In UPW (Figure 8.2) majority of STNA15-ELP was already aggregated at 19 °C, with some signal still generated by the scattering of particles below 5 nm. The ITT of STNA15-ELP is 23 °C in UPW, 4 degrees above the lowest temperature probed with DLS. Although this behaviour should not be expected, CD (Figure 7.1) and FTIR (Figure 7.3) data are consistent with this.

In 20 mM NaCl the STNA15-ELP was completely aggregated at 19 °C (Figure 8.2). There was no signal contribution from small particles of STNA15-ELP. In-fact, it was not possible to measure the STNA15-ELP aggregate size above 25 °C as they became too large for DLS to measure. On the contrary, both the CD (Figure 7.6) and FTIR (Figure 7.7) suggest that STNA15-ELP contains the largest amount of random coil structure when in NaCl, compared to both UPW and $CaCl_2$. The contradiction between the experiments is most likely to be due to the fact that in NaCl the ELP aggregates not due to hydrophobic collapse but due to another physiochemical process. However, without further analysis and experimental work it is difficult to establish this second aggregation mechanism.

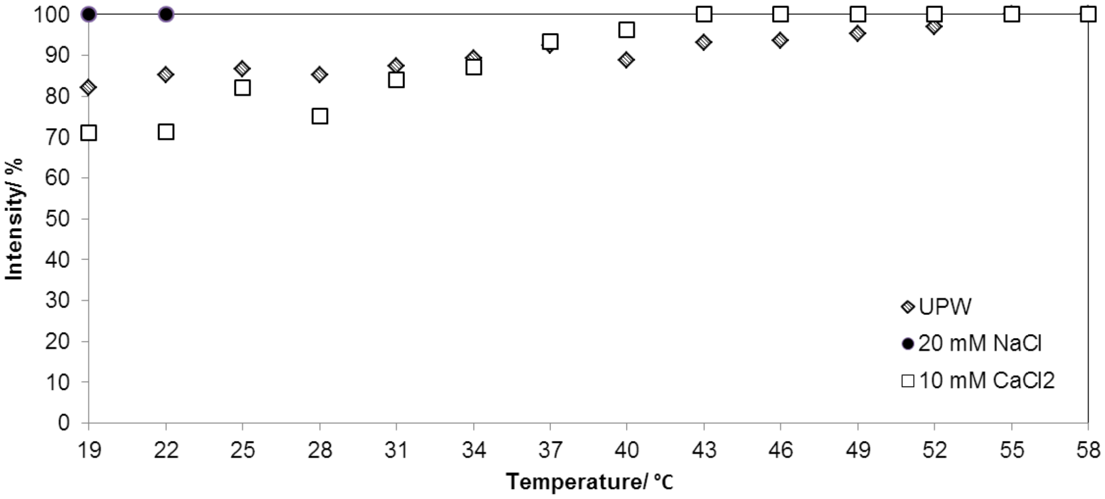

Figure 8.2: DLS data showing the light intensity scattered by large aggregated particles formed by STNA15-ELP in UPW, 20 mM NaCl 10 mM $CaCl_2$. The light intensity scattered by the particles in NaCl was too large to read above 28 °C

STNA15-ELP in a $CaCl_2$ (Figure 8.2) formed less large particles, in comparison to STNA15-ELP in either UPW or NaCl.

This result is as expected since in the previously described experiments ELP exhibited a larger fraction of random coil when in $CaCl_2$ compared to both UPW and NaCl. However, it was expected that many more STNA15-ELP individual particles would be present within the solution below ITT since it should be in its unfolded state. The exact contribution to the intensity profile of DLS from particles that are less than 50 nm in a polydisperse sample is difficult to measure. Particles that are less than 50 nm are known to be weak scatterers of light (Hassan *et al*., 2015). The contribution of the signal from the small particles, therefore, is much less than that generated by the larger particles. Due to this, the intensity cannot give the amount of a particle size present in a polydisperse solution. It is entirely possible that individual ELP molecules were present in a much larger amount than the aggregated particles.

DLS particle measurements of large particles in UPW (Figure 8.3) show that at all temperatures large particles are present. In UPW the amount of aggregated, large particles did not greatly change. The intensity produced by the large particles in UPW ranged from 82% at 19 °C to 100% at 52 °C. In contrast, in NaCl at 19 °C LR-ELP contained a relatively small amount of aggregated particles (25% of intensity).

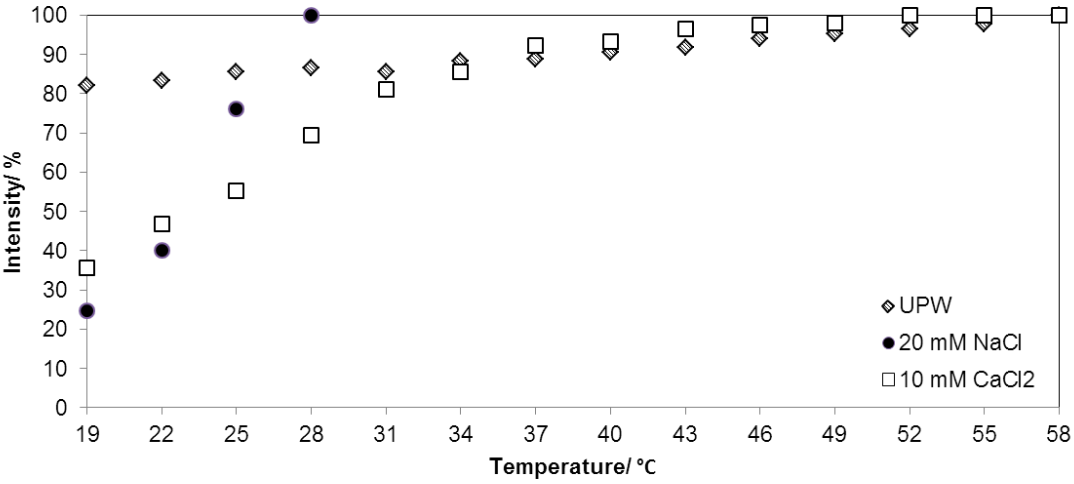

Figure 8.3: DLS data showing the light intensity scattered by large particles formed by LR-ELP in UPW, 20 mM NaCl and 10 mM $CaCl_2$. The light intensity scattered by the particles in NaCl was too large to read above 28 °C.

The light intensity scattered by aggregated particles rose rapidly during heating of the solution. The DLS could not read the sizes beyond 28 °C indicating that the aggregated particles were too large (>1µm) and scattered too much light. In the LR-ELP/ $CaCl_2$ solution, the intensity of large particles was least at 19 °C (36%). The scattered intensity of large particles began to rise thereafter and reached 100% at 52 °C.

The trend seen here is somewhat unexpected, when considering the data in Figure 8.3 alongside CD (Figure 7.2) and FTIR (Figure 7.3). FTIR of LR-ELP, at the same protein concentration as in the DLS studies, shows that in D_2O at 19 °C the ELP exhibited an un-folded state. Hence, one would not expect to see many aggregated particles within the LR-ELP/ UPW solution. However, large particles were observed in DLS at all temperatures. There were no sharp changes in the amount of these particles present. Perhaps, the ELP does not dissolve well in UPW. In this case, even if it is below the ITT, the ELP may aggregate due to hydrophobic interaction. Likewise, when looking at the FTIR data of LR-ELP in ionic solutions (Figure 7.8) it would be expected that 1 mg/ml LR-ELP would either reach the folded state faster in 20 mM NaCl or already have aggregated particles within the solution at 19°C. Both of these are true as seen in Figure 8.3. It appears that the aggregation of LR-ELP is much easier to predict in comparison to STNA15-ELP. Perhaps this is due to the presence of the STNA15 sequence within the ELP that changes this behaviour. The insertion of STNA15 introduces negative charges into a mostly positive molecule. The interaction of the positive and negative residues within a molecule or intermolecular interaction is completely plausible and may be the main factor affecting aggregation behaviour within STNA15-ELP.

The size of the particles formed by ELPs was monitored alongside the scattering intensity. Figure 8.4 shows the STNA15-ELP particle sizes formed in UPW, NaCl and $CaCl_2$. In UPW (Figure 8.4A) the average size of the large particles (R_H > 5nm) remained almost the same during heating. However, in $CaCl_2$ (Figure 8.4C) the large aggregated particles increased in size after the solution was heated beyond 49 °C. In both UPW and NaCl the small particles ($R_H < 5$nm) slightly decreased in size before disappearing. This may show the initial collapse of the ELP into a β-spiral before it begins to aggregate.

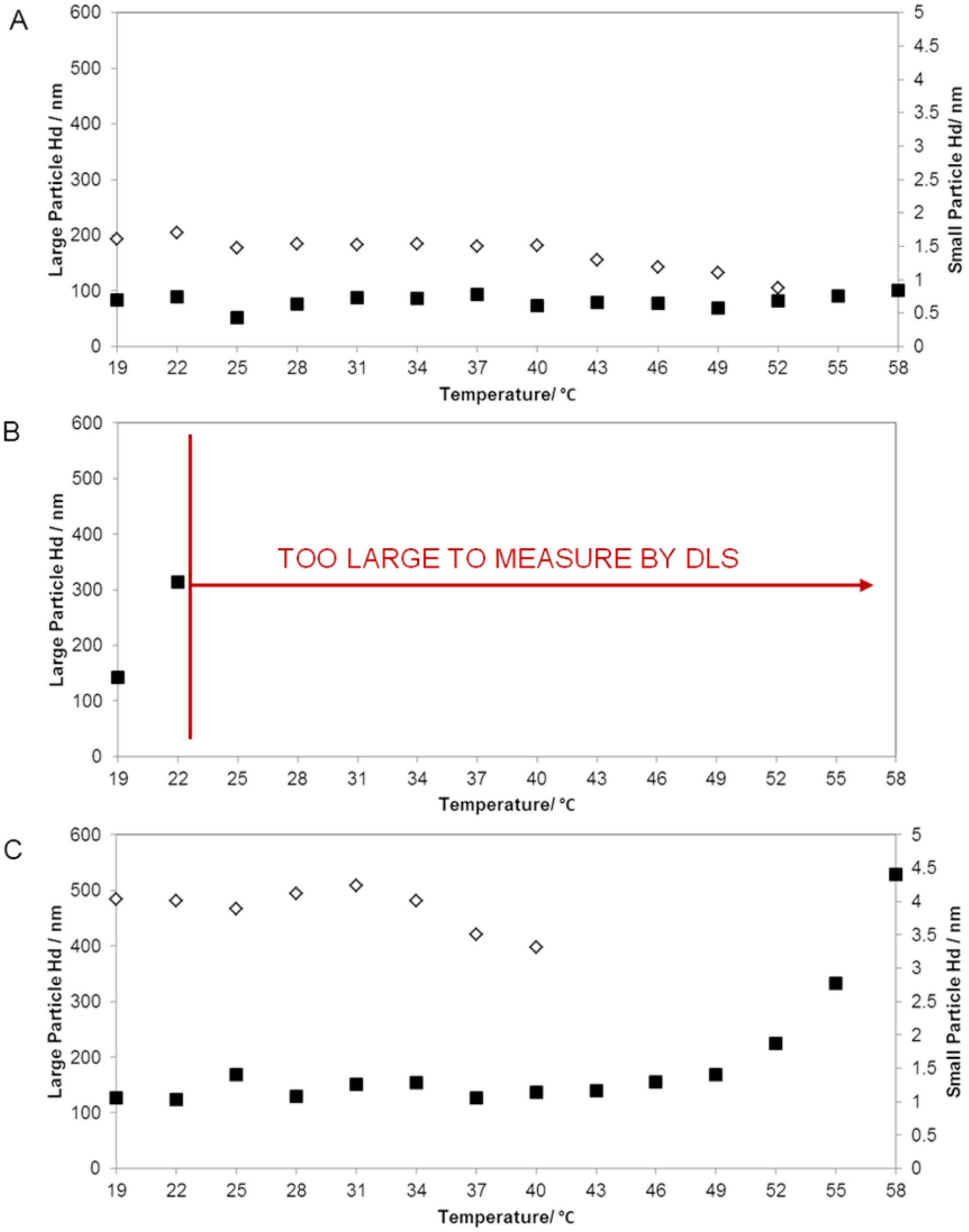

Figure 8.4: Variation in the average hydrodynamic radii (R_H) of large STNA15-ELP particles formed in A) UPW, B) 20 mM NaCl and C) 10 mM $CaCl_2$. The black markers represent the large particles and the white markers represent the small particles. The particle sizes in NaCl were too large to read above 28 °C.

The STNA15-ELP particle formation at 19°C and at 50 °C (i.e. below and above the ITT, respectively) was visualised for all conditions using TEM (Figure 8.6). In UPW, below the ITT, large poorly defined particles can be seen (arrows 1 and 2 in Figure 8.6A). Likewise in NaCl and $CaCl_2$ large aggregates are observed in the TEM (arrows 3 and 4 in Figure 8.6C and E respectively). Arrow 5 in Figure 8.6E points to smaller aggregates found in the $CaCl_2$ solutions. One hundred STNA15-ELP particle sizes, formed at 50 °C, were measured from the SEM images (Figure 8.5) and plotted as a histogram (Figure 8.5). The histogram, and the average particle size, confirm that aggregates formed in $CaCl_2$ are more homogenous in size and are generally smaller in comparison to those formed in UPW and NaCl.

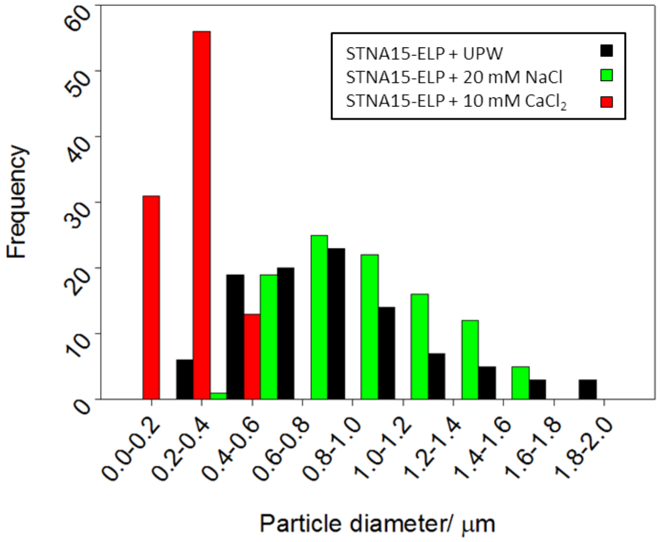

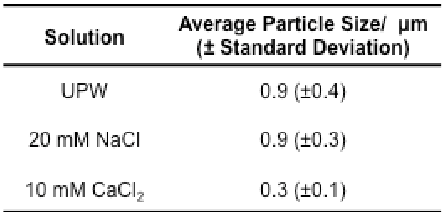

Solution	Average Particle Size/ µm (± Standard Deviation)
UPW	0.9 (±0.4)
20 mM NaCl	0.9 (±0.3)
10 mM $CaCl_2$	0.3 (±0.1)

Figure 8.5: Particle size distribution for particles formed in UPW (black), 10 mM $CaCl_2$ (red) and 20 mM NaCl (green) at 50 °C. The sizes were measured from SEM images, using image J, where n=100. The table lists the average STNA15-ELP in the three solutions, accompanied with the standard deviation.

The STNA15-ELP sample prepared in UPW at 50 °C shows distinct large particles (Figure 8.6B). Above the ITT STNA15-ELP form spherical particles with a smooth appearance. From the TEM image of the STNA15-ELP above the ITT it is clear that there is quite a large distribution of particle sizes, some reaching 500 nm sizes. However, the observed particle sizes do not coincide with the DLS measurements.

DLS measurements suggest that the STNA15-ELP aggregated particles remain the same size during heating in UPW and are a 5th of the size seen in TEM. Although this seems unusual, there may be a simple explanation for the discrepancy. The preparation of samples for DLS requires centrifugation, at 8000 rpm, to remove large dust particles. Centrifugation is a common method for unwanted particle removal. However the resultant supernatant can vary depending on the speed of the process. For example, in one publication, authors have investigated the effect of centrifugation on the observed particle size of didodecyldimethylammonium bromide (DMAB) stabilised nanoparticles (Dandurand *et al*., 2015). The DMAB stabilised particles varied in size from 216 ± 3.4 to 158.6 ± 4.8 nm when the speed was changed from 8800 rpm to 12000 rpm, respectively. The observed size discrepancy between TEM and DLS may be due to the centrifugation of the ELP before the DLS experiments.

Another factor that is quite different between the two experiments is the heating rate of the solutions. For the DLS experiments, the solutions were heated at 3 °C intervals, with measurement time of 100 s and prior stabilisation in between, up to 58 °C. However, for TEM specimen preparation the ELP solutions were placed straight into a 50 °C oven. Perhaps the ELPs undergo mass aggregation when heated at a fast rate. In this case the aggregation behaviour of ELPs may depend on kinetics or thermodynamics. In terms of chemical reactions, thermodynamic products are normally formed in vigorous conditions. On the other hand, kinetic products of a reaction occur in mild conditions (Girotti and Reguera, 2004). Models have been established for some protein aggregation kinetics and how those compete with protein folding (Girotti and Reguera, 2004). The aggregation of proteins has been reported to occur when the limiting factor is time of folding. With sufficient time, proteins will have more time to fold into ordered structures.

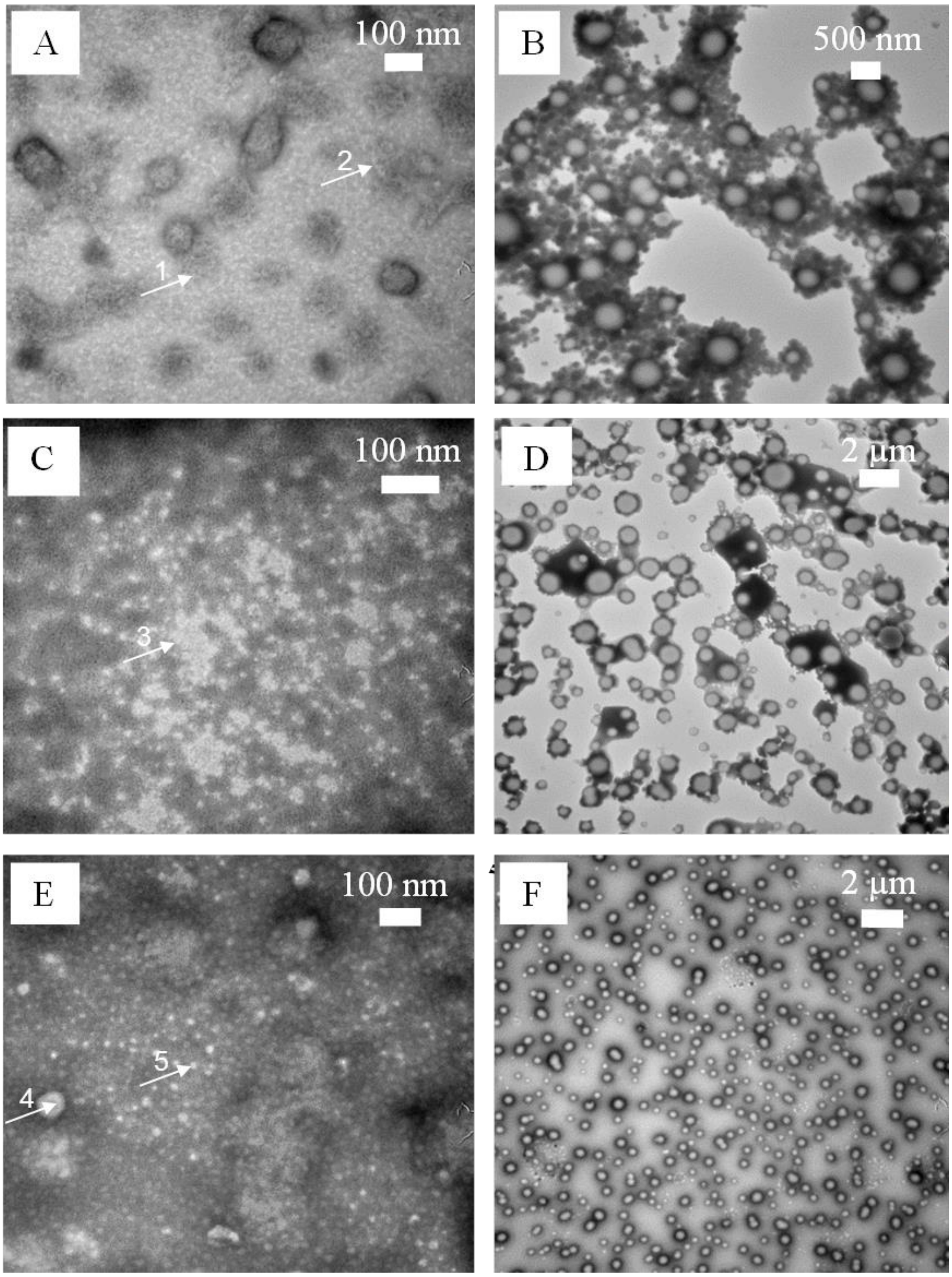

Figure 8.6: TEM images of STNA15-ELP in UPW (A: below and B: above ITT), 20 mM NaCl (C: below, D: above ITT), 10 mM $CaCl_2$ (E: below, F: above ITT).

The appearance of the particles seen in the TEM images of STNA15-ELP in UPW and 20 mM NaCl can be explained in terms of kinetic and thermodynamic behaviour or the down side of centrifugation. However, a clear difference was observed when

STNA15-ELP was added to 10 mM $CaCl_2$. Particles formed within water and NaCl solution at 50 °C appeared to have a heterogeneous distribution of sizes. In contrast, the particles formed in a $CaCl_2$ solution at 50 °C were smaller and seemed to have a narrow size distribution (Figure 8.6F, Figure 8.5).

To further confirm the size distribution of STNA15-ELP, as seen in the TEM images, the particle diameters were measured and plotted as a histogram (Figure 8.5). The distribution of the measured particles coincides with the qualitative observations from the TEM images (Figure 8.6). The STNA15-ELP aggregate particles have the narrowest distribution and contain the smallest particles when in 10 mM $CaCl_2$. The distribution of particle sizes in NaCl and UPW was much wider. Furthermore, the aggregate size in NaCl (from 0.4-1.8 μm) was much larger than the size of the aggregates formed in the $CaCl_2$ solution (from 0.1-0.6 μm) (see Figure 8.5 and Figure 8.6). $CaCl_2$ seems to be effective in controlling the aggregation behaviour of the ELP when the mixture was heated well above the ITT.

The LR-ELP TEM images are shown in Figure 8.8. Qualitatively, the particle sizes observed below and above the ITT do, for the most part, coincide with the DLS results. In particular, when LR-ELP was imaged below the ITT, many large spherical particles are observed in UPW (Figure 8.8A) and in NaCl (Figure 8.8C), which coincide with the presence of large aggregates in the DLS data (Figure 8.3).

Figure 8.7 shows the variation of LR-ELP particles measured by DLS, at a range of temperatures, in UPW (A), NaCl (B) and $CaCl_2$ (C). Large LR-ELP aggregates (R_H> 5nm) in UPW (Figure 8.7A) and 10 mM $CaCl_2$ (Figure 8.7B) seemed to stay the same average size. Large particles were observed in all conditions, regardless of the temperature or ionic solution. The behaviour of LR-ELP and STNA15-ELP aggregation is almost identical.

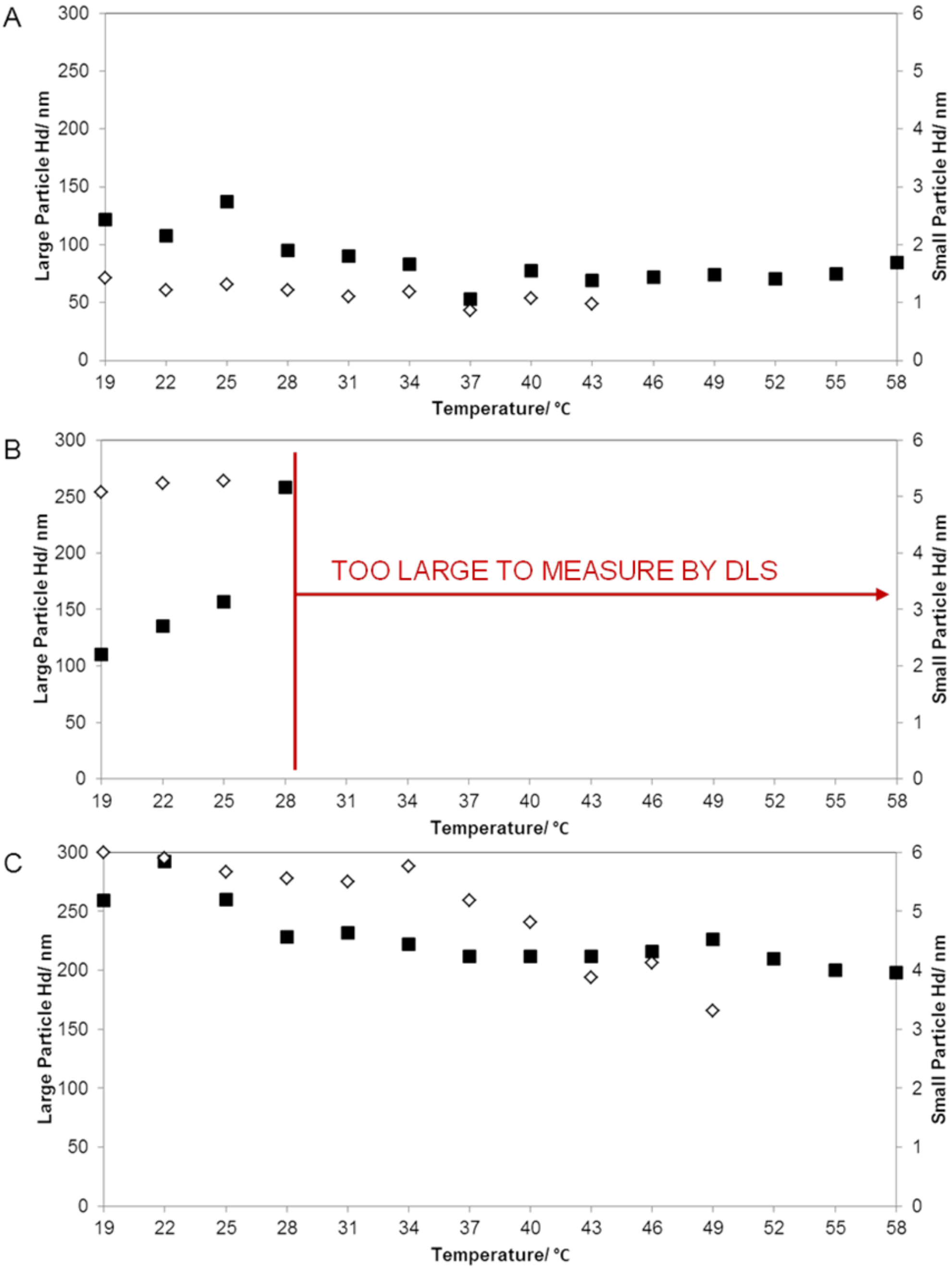

Figure 8.7: Variation in the average hydrodynamic radii (R_H) of LR-ELP particles formed in UPW (A), 20 mM NaCl (B) and 10 mM $CaCl_2$ (D). The black markers represent the large particles and the white markers represent the small particles.

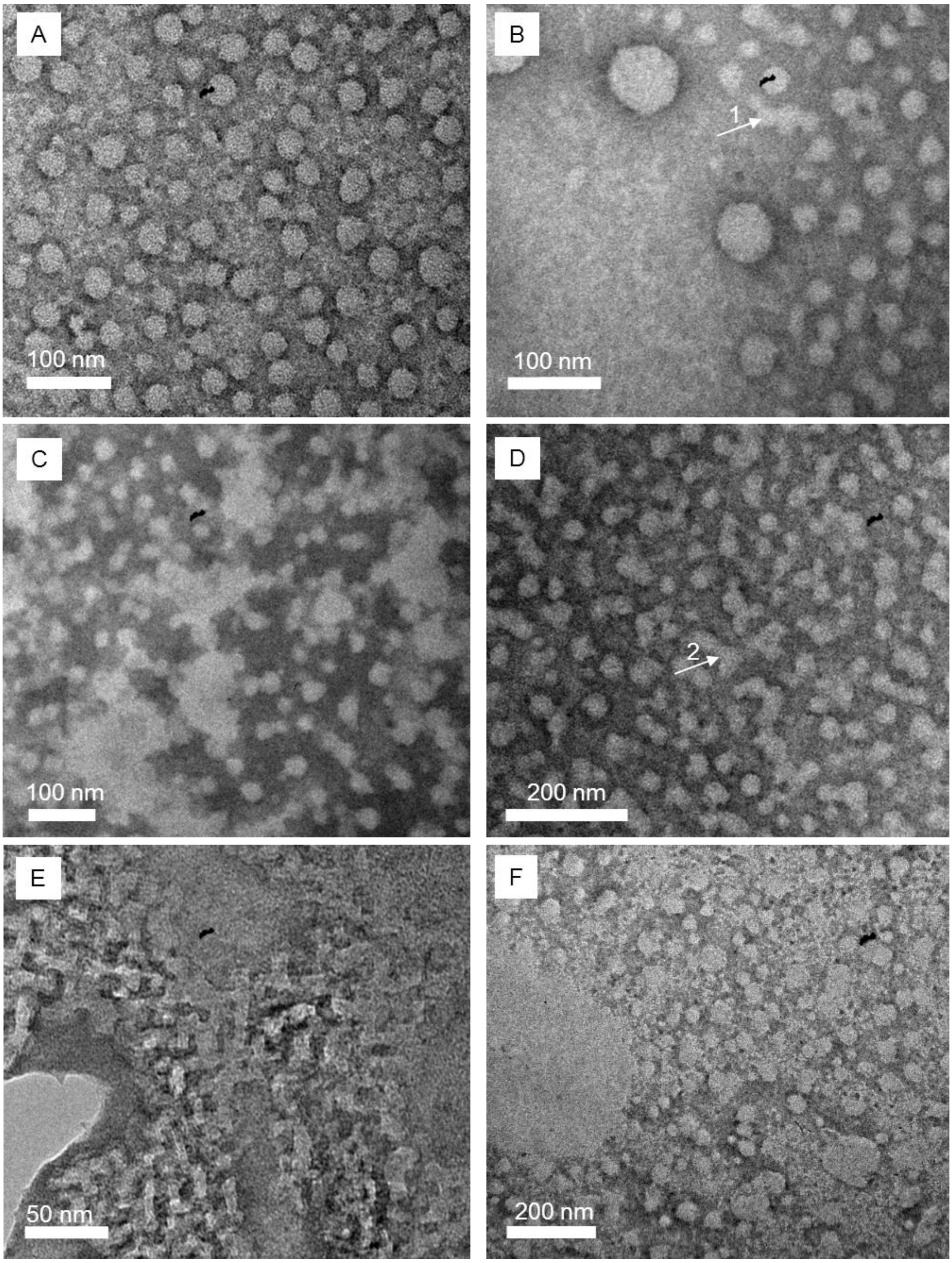

Figure 8.8: TEM images of LR-ELP in UPW (A: below and B: above ITT), 20 mM NaCl (C: below, D: above ITT), 10 mM CaCl$_2$ (E: below, F: above ITT).

However, rather than forming distinct spherical particles, in some cases LR-ELP aggregates assembled into strands of aggregates (arrows 1 and 2 in Figure 8.8B and C respectively). The most noticeable difference between STNA15-ELP aggregation and

LR-ELP occurs in $CaCl_2$. The average size of the LR-ELP large aggregates (Figure 8.7C) is about two times larger than the large aggregates of STNA15-ELP (Figure 8.4C). However, this difference is not apparent in UPW or NaCl. This one discrepancy between the aggregation results of the two proteins shows that STNA15-ELP has a distinct relationship with Ca^{2+} ions. This behaviour is beneficial for biomimetics mineralisation but is not too unexpected. STNA15-ELP has been known to successfully mineralise when implanted into bone and the STNA15 sequence itself has a high affinity to apatite.

8.3.2 Role of Crosslinker Concentration

Elastin-like proteins are often cross-linked for various applications. Some examples of cross-linked ELPs include membranes for mineralised tissue repair (Elsharkawy *et al*., 2016b; Tejeda-Montes *et al*., 2012, 2014a, 2014b), fibres for elastin mimetics (Nagapudi *et al*., 2002) and drug or gene delivery (Dash *et al*., 2011; Fujita *et al*., 2009). ELPs can be cross-linked in a number of ways; however, glutaraldehyde (GTA) is quite common for fixation as the mechanism is fairly well known. The main disadvantage of using GTA is that it is highly toxic and cannot be used for bio-applications. Normally GTA is used in order to either test a hypothesis or to fixate biological specimens for SEM imaging. Other crosslinkers are available that are non-toxic and which have been used for tissue repair (Tejeda-Montes *et al*., 2014a). However, for the purpose of this study a well characterised crosslinker was desired and therefore GTA has been used to crosslink the ELP and for future work other crosslinkers may be considered.

Here, a range of GTA concentrations was examined in order to establish which produces the best stability of ELP particles. Both LR-ELP and STNA15-ELP were successfully crosslinked above their ITT, at 50 °C, in UPW, 20 mM NaCl and 10 mM

$CaCl_2$. The effect of the crosslinking was studied using SEM and it is seen in general that the results of crosslinking are extremely variable (Figure 8.9, Figure 8.10, Figure 8.11, Figure 8.12, Figure 8.13, Figure 8.14). The crosslinking appears to depend on the concentration of GTA, as expected, and also the solution in which the ELPs are dissolved in prior to the crosslinking. Figure 8.9 shows the SE images of STNA15-ELP in UPW, crosslinked in a range of GTA concentrations. GTA concentrations of 2.5 and 1.25% v/v resulted in spherical particles only (Figure 8.9A-C and D-F respectively). Lower GTA concentrations, of 0.5 and 0.25% v/v (Figure 8.9G-I and J-L respectively) yielded a negligible amount of particles.

In contrast to crosslinking in UPW, crosslinking in 20 mM NaCl yielded particles at all GTA concentrations (Figure 8.10). In this case, the morphology of the crosslinked product changed in relation to the GTA concentration. STNA15-ELP crosslinked with 2.5 and 1.25% v/v GTA (Figure 8.10A-C and D-F respectively) mainly yielded spherical particles. The particle size distribution was heterogeneous and in agreement with TEM study (Figure 8.6B). At lower GTA concentrations of 0.5 and 0.25% v/v fibre formation (Figure 8.10H and I) and membrane formation (Figure 8.10J and L) occurs alongside spherical particles.

Crosslinking of STNA15-ELP in 10 mM $CaCl_2$ gave spherical particles at all concentrations of GTA (Figure 8.11). The spherical particles appear to have a homogeneous distribution of size, just as seen in TEM (Figure 8.6F). No fibre formation occurs in this case. However, in some instances STNA15-ELP particles fused together to form chain-like structures (Figure 8.11F).

SEM images of LR-ELP crosslinked in UPW are shown in Figure 8.12. Again, spherical particles are formed in most cases. However, fibrous material was observed in abundance when LR-ELP was cross-linked with 1.25 and 0.5% v/v GTA (Figure 8.12D-E and H respectively). 0.25% v/v GTA crosslinking resulted in poor results, with little crosslinked material observed (Figure 8.12J-L). Shapes, resembling the elongated particles observed in TEM (Figure 8.8D, arrow 2), were seen when LR-ELP was cross-linked with 0.5% v/v GTA (Figure 8.12I).

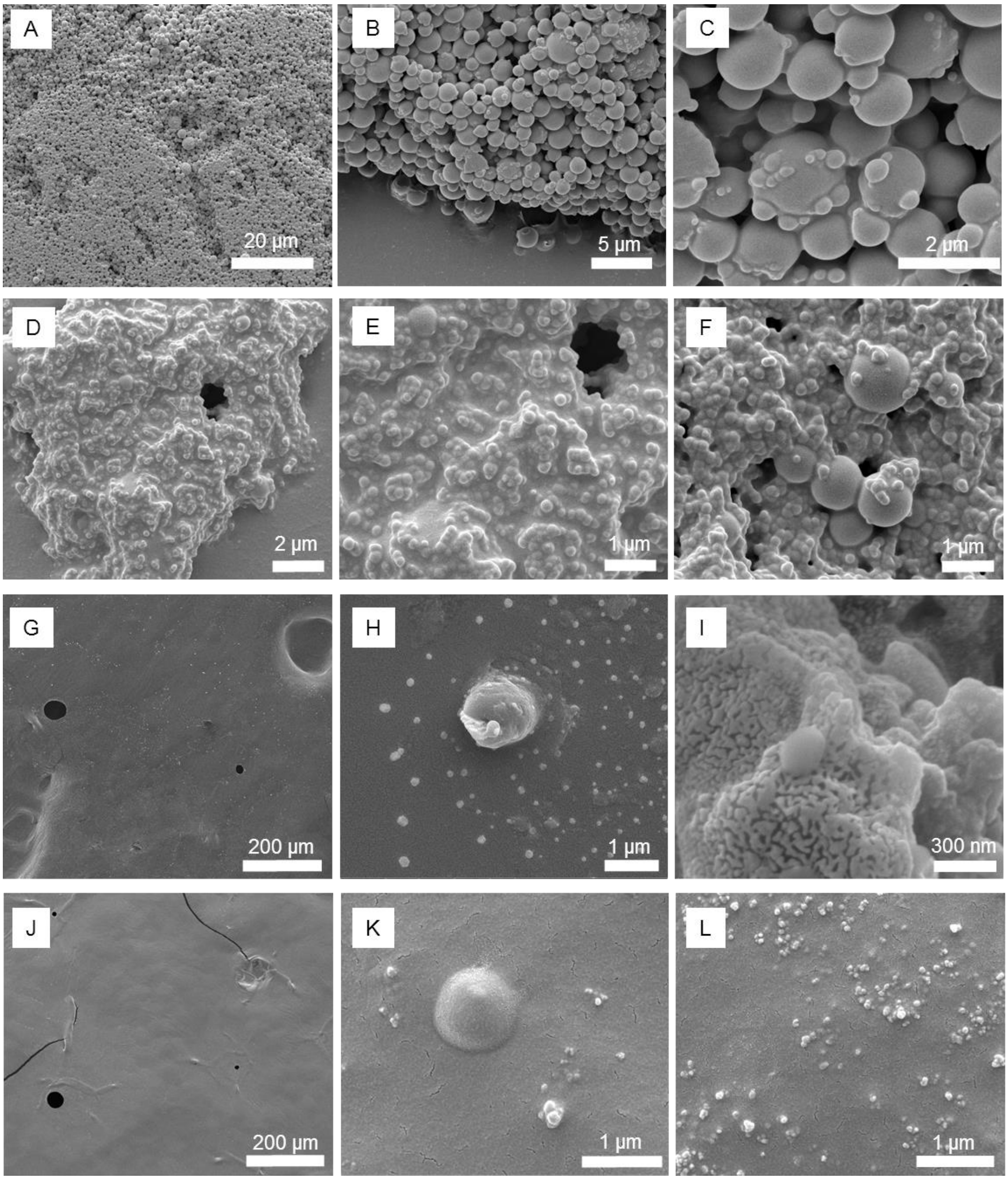

Figure 8.9: SE images of STNA15-ELP in UPW crosslinked in 2.5% GTA (A-C), 1.25% GTA (D-F), 0.50% GTA (G-I) and 0.25% GTA (J-L).

LR-ELP crosslinked in NaCl formed fibrous material in most conditions, alongside spherical aggregates (Figure 8.13). The fibres seem to be aligned aggregates.

Similarly to STNA15-ELP, at the lowest concentration of GTA membranes were also observed (Figure 8.13K).

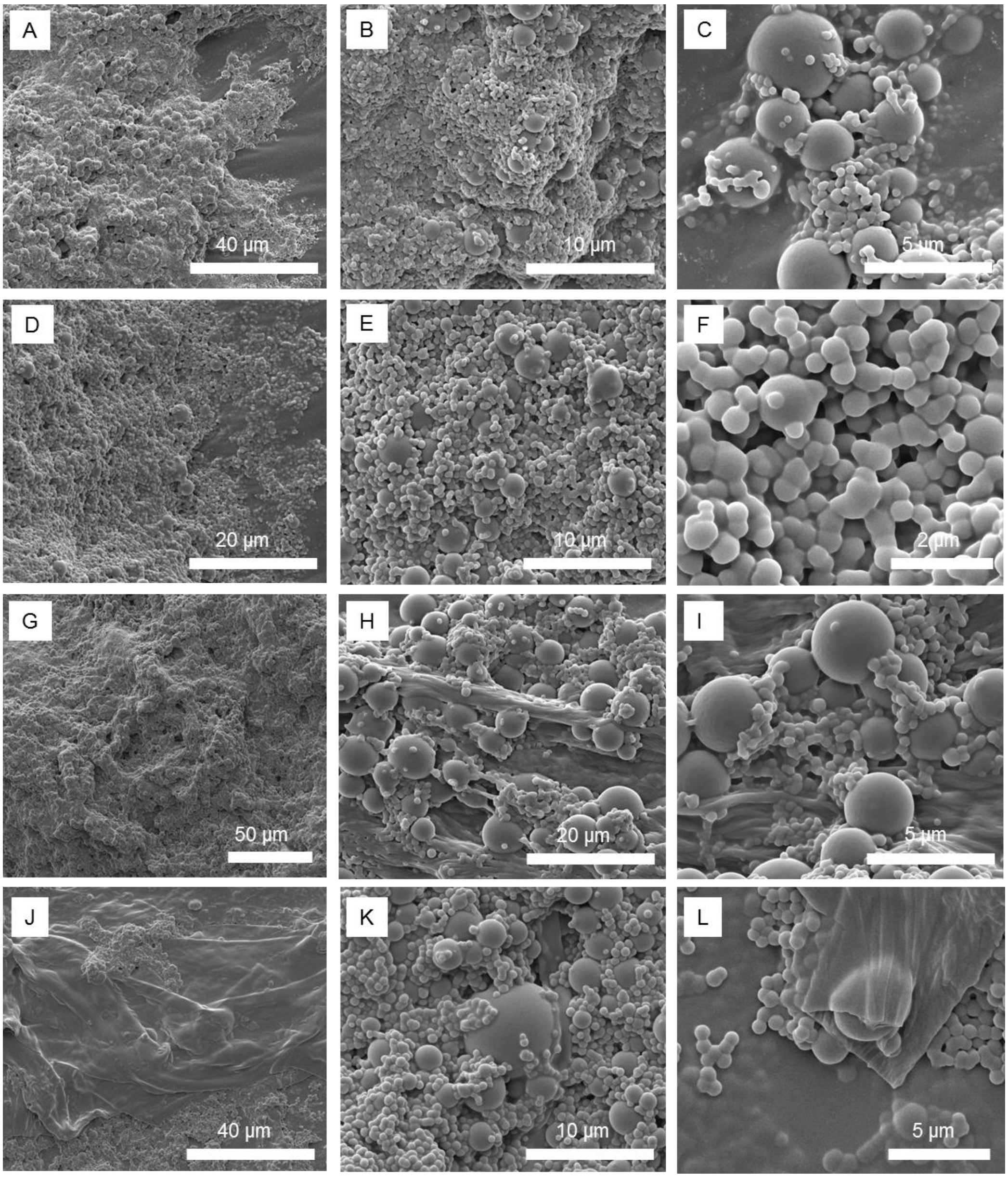

Figure 8.10: SE images of STNA15-ELP in 20 mM NaCl crosslinked in 2.5% GTA (A-C), 1.25% GTA (D-F), 0.50% GTA (G-I) and 0.25% GTA (J-L).

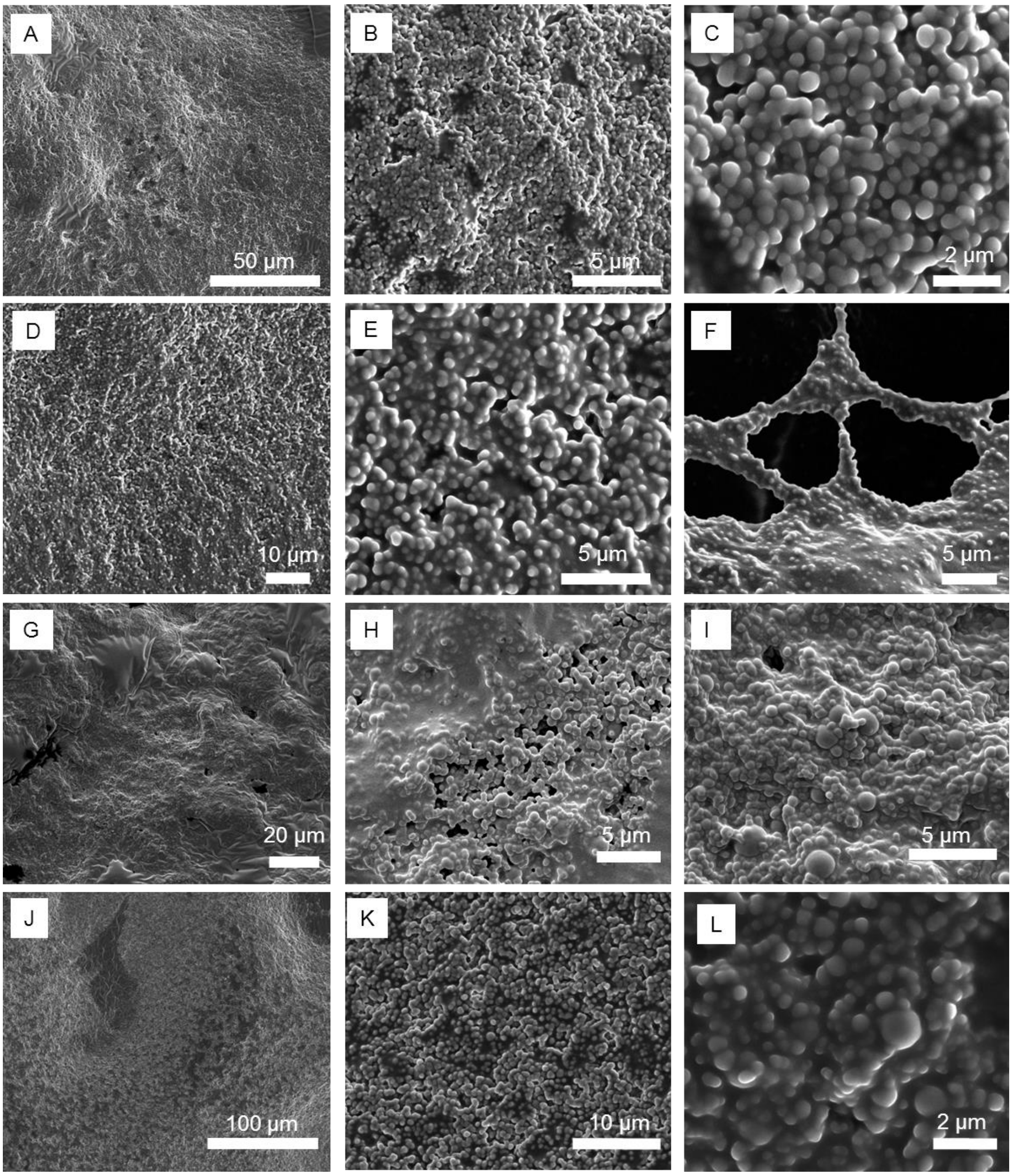

Figure 8.11: SE images of STNA15-ELP in 10 mM $CaCl_2$ crosslinked in 2.5% GTA (A-C), 1.25% GTA (D-F), 0.50% GTA (G-I) and 0.25% GTA (J-L).

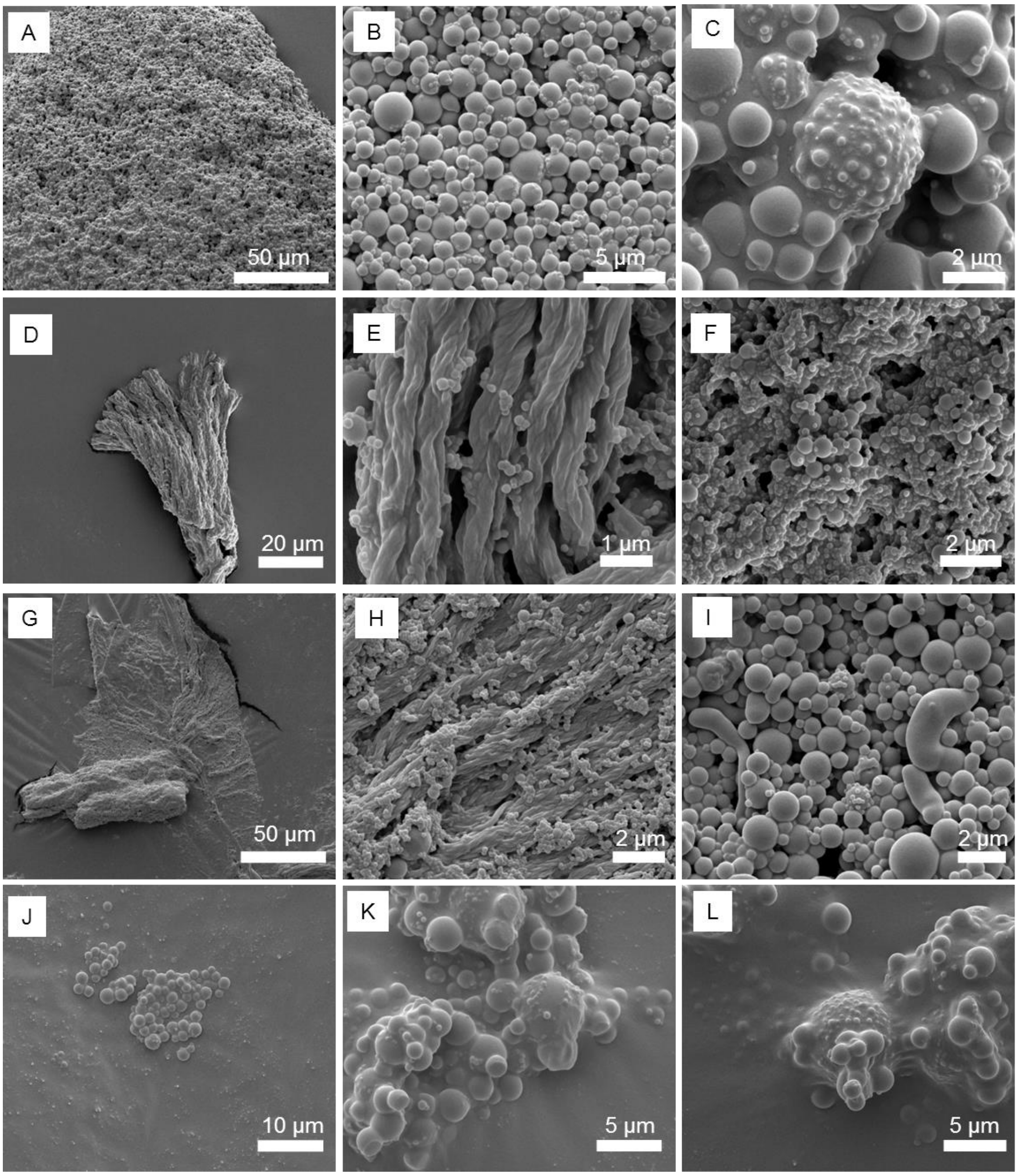

Figure 8.12: SE images of LR-ELP in UPW crosslinked in 2.5% GTA (A-C), 1.25% GTA (D-F), 0.50% GTA (G-I) and 0.25% GTA (J-L).

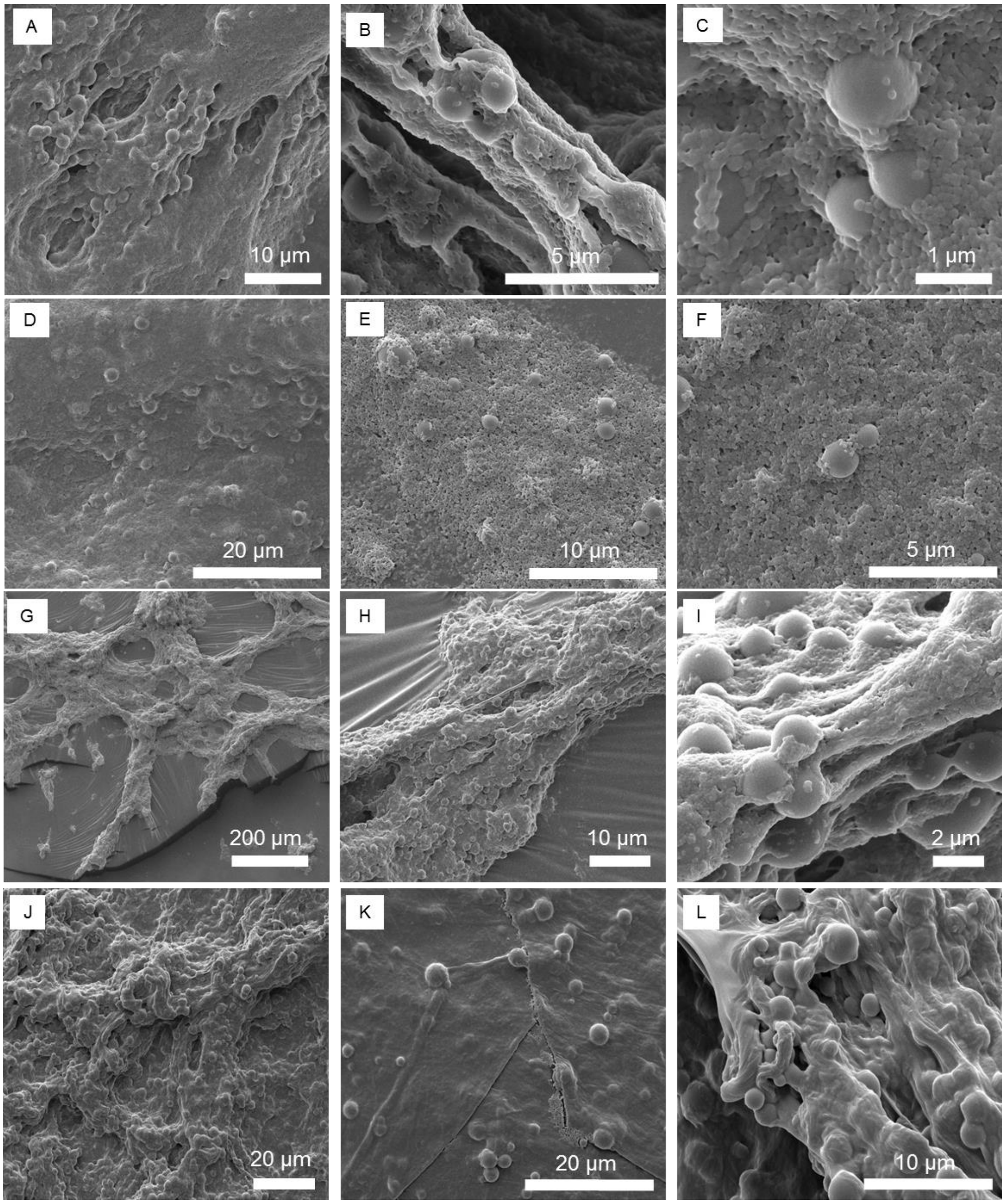

Figure 8.13: SE images of LR-ELP in 20 mM NaCl crosslinked in 2.5% GTA (A-C), 1.25% GTA (D-F), 0.50% GTA (G-I) and 0.25% GTA (J-L).

Poor crosslinking results were obtained when LR-ELP was crosslinked in 10 mM $CaCl_2$ (Figure 8.14). The crosslinked product varied from spherical particles to fibrous material to almost no crosslinked product. Perhaps the best result was achieved with 2.5% v/v GTA (Figure 8.14A-C). In this condition some spherical particles can be distinguished.

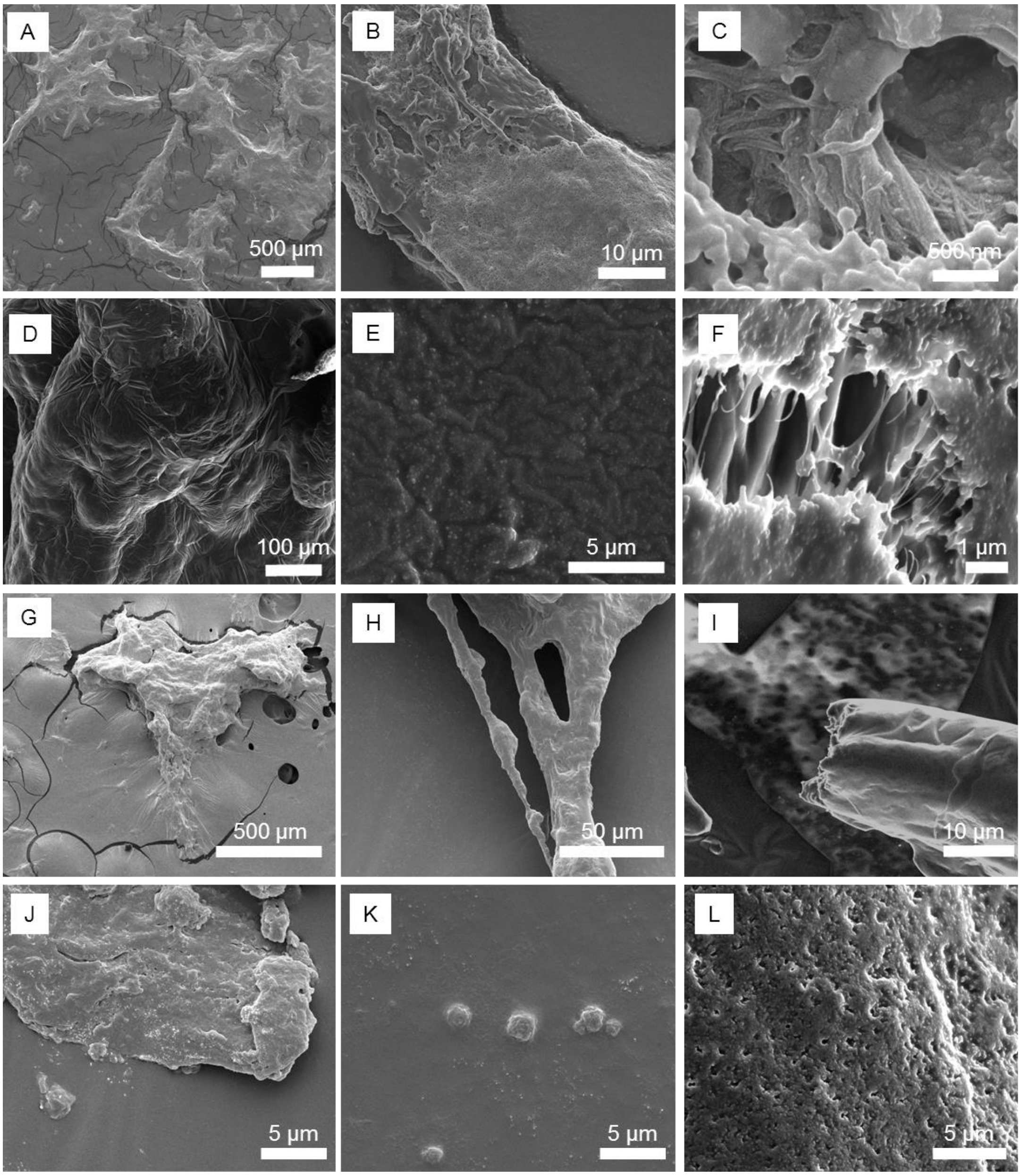

Figure 8.14: SE images of LR-ELP in 10 mM $CaCl_2$ crosslinked in 2.5% GTA (A-C), 1.25% GTA (D-F), 0.50% GTA (G-I) and 0.25% GTA (J-L).

The ELP spherical particle stabilisation with GTA crosslinker was not achieved at all concentrations in all solutions. The amount of crosslinker required to stabilise ELP spherical particles depended on the solution the ELPs were dissolved in. Effective crosslinking for STNA15-ELP in UPW was achieved at 2.5% v/v GTA, in NaCl at 2.5 and 1.25% v/v and in $CaCl_2$ at all concentrations of GTA (2.5, 1.25, 0.5 and 0.25% v/v). LR-ELP spherical particles were crosslinked successfully in UPW with

2.5% v/v, in NaCl with 1.25% v/v and in $CaCl_2$ none of the GTA concentrations produced any substantial amount of crosslinked particles.

ELPs are synthetic proteins and, in most reported cases, form spherical aggregates (such as seen in many cases here) or micelles (for example Dash *et al.*, 2011; Fujita *et al.*, 2009; Park and Champion, 2014). The crosslinking of the ELPs gave a large variation in the resulting aggregate morphology. The formation of the fibrous material is particularly of interest. ELP fibre formation is not often reported in the literature. However, several mechanisms have been proposed for the formation of natural elastin fibres (see Vrhovski and Weiss, 1998). One of these models suggests that globular tropoelastin aggregates come together (Weis-Fogh and Anderson, 1970) and are crosslinked by lysil oxidase (Sato et al., 2007). Although this view is dated, it is quite fitting in this scenario. The globular components of elastin were described as having a hydrophobic core and a hydrophilic outer layer. In a more recent publication the formation of natural elastin fibres *in vivo* was also described to occur via the fusion of tropoelastin globules (Kozel *et al.*, 2006).

GTA crosslinker reacts with nucleophilic side groups, for example lysine's side group $–NH_2$. In LR-ELP and STNA15-ELP lysines contribute to the majority of the charges of the protein. Therefore, the crosslinking of lysine will cause the proteins structure to become hydrophobic. Perhaps this is the drive to an increased hierarchy in the protein structure. At the lowest concentration of GTA, the ELPs begin to form films rather than fibres. These films are formed with both STNA15-ELP (Figure 8.10J and L) and with LR-ELP (Figure 8.13K) in NaCl. Again, this may be the result of the ELPs forming the most favourable structure.

The difference between the ELP crosslinked structures formed in NaCl and $CaCl_2$ may be due to a difference in interaction between ions and ELPs. NaCl has been described to interact with the water which surrounds the ELPs and promote organisation between the folded ELPs (Reguera *et al.*, 2007). This may be the reason why with both STNA15-ELP and LR-ELP fibres are observed after crosslinking. On the other hand, the interaction of STNA15-ELP and Ca^{2+} forms intermolecular bridges (Shi *et al.*, 2011). Ca^{2+} ions have been reported to coordinate with carboxylate groups such as aspartic acid and glutamic acid, both of which are present in STNA15-ELP. This coordination is said to be the cause of the bridge formation. In general, divalent ions have the ability to form these bridges, whereas monovalent ions do not.

The biomineralising matrix is said to be a two component system, containing molecules that nucleate and molecules that act a structural component (Mann, 2001). The formation of the synthetic STNA15-ELP fibres resembles the natural biomineralising matrix where the bulk ELP acts as a scaffold and the STNA15 sequence can act as a nucleator. Furthermore, the fusing of spherical particles into ordered structures resembles enamel formation. Some have described the amelogenin protein as a spherical hydrophobic particle (Fang *et al.*, 2013). These hydrophobic amelogenin particles align and act as a structural component of the enamel matrix that guides the crystal growth. In any case, the crosslinking of the synthetic elastin-like proteins has led to the formation of promising biomimetic organic structures.

8.4 Summary

The crosslinking of the ELPs was affected by the solution chemistry and the amount of GTA crosslinker used. In most cases, apart from LR-ELP and $CaCl_2$, at least one concentration of GTA achieved stable spherical particles. Other crosslinked protein morphologies were also observed. The formation of the ELP fibres, at a range of GTA crosslinking concentrations, can lead to formation of ordered mineralised structures. Further development of the crosslinking technique is needed to control this process. Likewise, more understanding of the effect of the ionic solutions on the structures formed is required. In any case, the fibres formed are a promising result and may be useful in future mineralisation studies.

Lastly, STNA15-ELP particles in $CaCl_2$, crosslinked with GTA concentrations ranging from 2.5 to 0.25% v/v, proved that the particle size can be controlled (Figure 8.11). The control of the particle size inherently leads to the control of nucleating sites in one particle. Further mineralisation of these systems may lead to controlled synthetic biomineralisation. Understanding how these mineralisation sites can be controlled can lead to the ability to induce mineralisation at known distances in membranes, such as those used by Tejeda-Montes *et al*., (2014b).

Chapter 9. COMPARING ELP MINERALISATION IN SOLUTION VS. ON A SURFACE

9.1 Introduction

This chapter investigates the mineralisation of STNA15-ELP in two conditions, constrained or free in solution. Examining the two conditions is important, since in nature, proteins do not float in a medium but are confined in some way. The biomineralisation matrix may be considered to be gel-like rather than a complete fluid. So, we examine what effect constraint has on the mineralising capability of the STNA15-ELP. The ELP is mineralised using a fluoridated calcium phosphate solution. Therefore, we expect the final phase to be a fluorapatite (FAp). The main reason for choosing to form a fluoridated apatite is that it has much better stability in acidic environments and would be more suitable for development of enamel therapeutics.

9.2 Experimental Details

9.2.1 Mineralising Medium

A fluoridated calcium phosphate solution, previously described by Chen et al., (2006), was used to mineralise the STNA15-ELP. Prior to mineralisation experiments, the solution was examined with an ion selective electrode (ISE) in order to measure the pH and calcium, and fluoride concentrations. The ISE experiment was carried out at 37 °C, over a 100 hour period. The behaviour of the mineralising medium, measured by ISE, was also recorded whilst containing STNA15-ELP in the solution. The results of the ISE measurements can be related to the calcium phosphate (CaP) isotherms reported in literature. This relation can indicate which CaP phases are likely to form at which time point.

9.2.2 Mineralising STNA15-ELP

The ELP was either dropped into the mineralising solution directly or coated onto a borosilicate glass slide, at a concentration of 100 g/ml. The coated glass slide was added to the mineralising solution once the ELP was completely dry. Both the free in solution and coated STNA15-ELP samples were incubated for a range of times (15 minutes, 1 and 3 hours, 2, 4, 7, and 8 days). The different time points were needed to understand the mineral formation over the 8 day incubation period. All the incubations were carried out at 37 °C. The 3 hour and 8 day time periods were chosen for chemical characterisation using Raman (for the constrained samples), FTIR (for the free in solution samples), SEM and TEM. The two different techniques were used due to the small sample size produced by the mineralised protein constrained on glass.

Another factor, considered in this chapter, is in what way surface hydrophobicity may, indirectly, influence mineralisation. To evaluate effect of hydrophobicity, PDMS was treated with UV/Ozone to create a range of surface hydrophobicities/ hydrophilicities. The PDMS was treated for 10, 30, 60 and 90 minutes. It is well documented in literature that PDMS surfaces become more hydrophilic as the time of UV/ Ozone treatment is increased, more detail is given further on in the chapter. The PDMS surfaces were coated with STNA15-ELP in the same way as the borosilicate glass slips. These were then incubated for 24 hours, dried overnight at room temperature (19 °C) and coated with carbon for SEM analysis.

9.3 Results and Discussion

9.3.1 Mineralising Medium Characterisation

Prior to biomimetic mineralisation experiments, the mineralising solution was characterised using ISE. The measurement was taken over a 100 h period. The aim of this experiment is mainly to establish where the solution lies on the CaP isotherm as a function of time. This information can help in characterisation of minerals formed.

Figure 9.1 shows the concentration of Ca^{2+} and F^- on a log scale as a function of time, over a 100h period. pH of the same solution is plotted against the right hand axis. The pH of the solution is at 6 when initially mixed. This is expected since the pH is adjusted to 6 before incubation. However, the pH drops rapidly and then stays constant at around 3.8 until the end of the experiment (see Figure 9.1). Both the calcium and fluoride concentrations also initially fall. The calcium concentration subsequently rises over time.

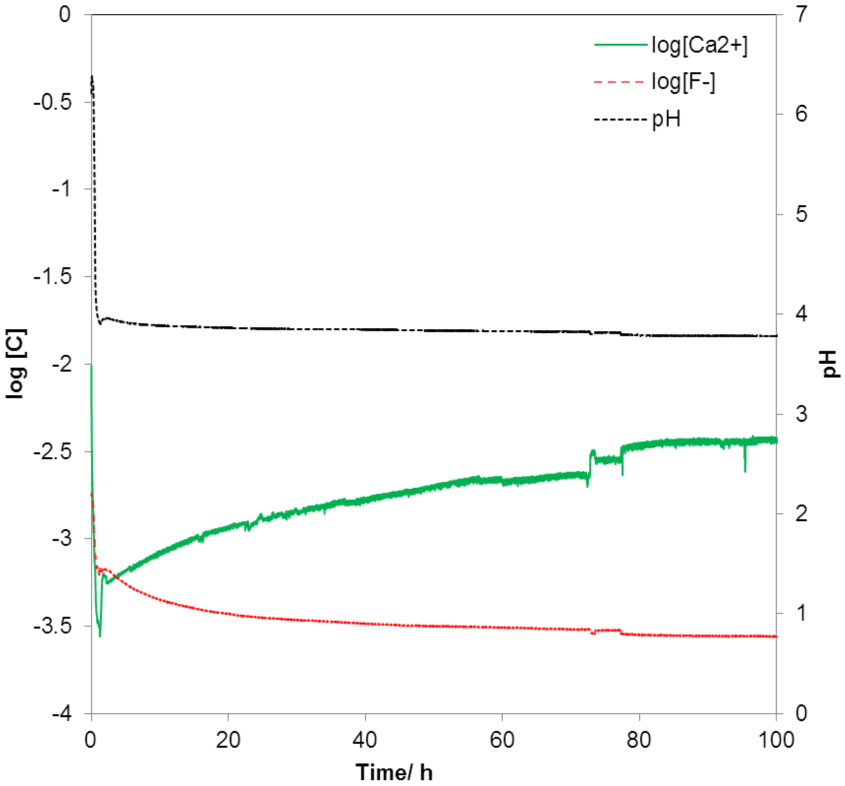

Figure 9.1: ISE data of the fluoridated mineralising solution over a 100 hour period showing the change in pH, the molar calcium ion (log[Ca^{2+}]) and fluoride (log[F^-]) concentrations.

Figure 9.2 shows the detail of the first 2 hours of the 100 hour period shown in Figure 9.1. The calcium ion concentration begins at 10 mM and the fluoride concentration at

1.8 mM. The fluoride concentration is actually 0.2 mM less than the expected 2 mM. However, the discrepancy is most likely due to weighing errors. At closer inspection of the ISE curves it is evident that the fall in pH occurs rapidly over approximately 15 minutes. The pH drop occurs around 15 minutes after the calcium and fluoride concentrations start to fall. Previously, the *in vitro* process of apatite formation has been related to pH changes within the mineralising solution (see for example Kwak et al., (2011)). The fall in pH is therefore associated with biomineral formation.

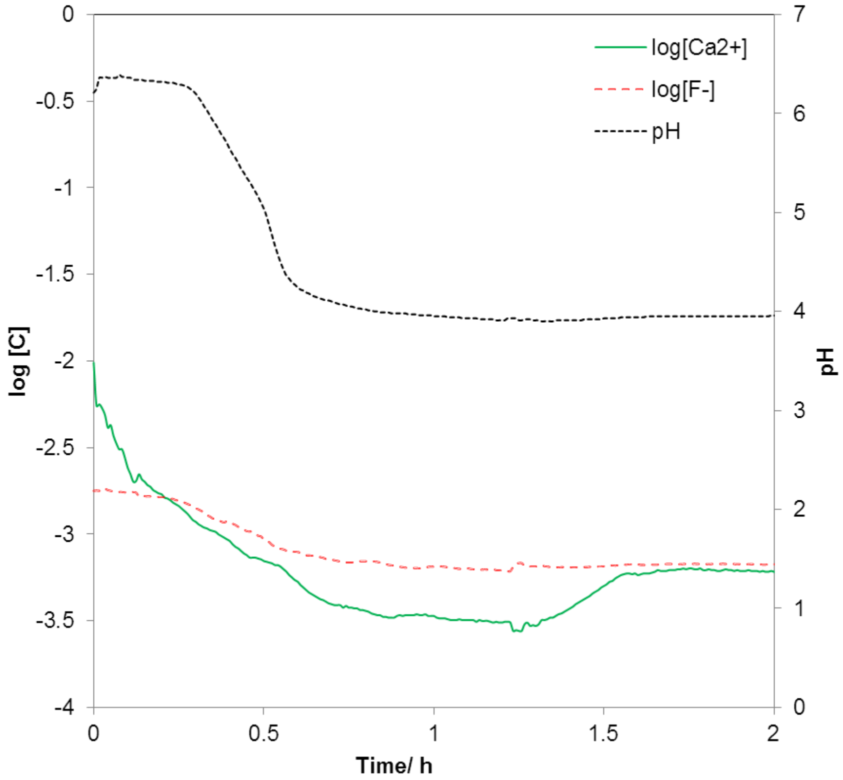

Figure 9.2: ISE data of the fluoridated mineralising solution over a 2 hour period showing the change in pH, the molar calcium ion (log[Ca^{2+}]) and fluoride (log[F^{-}]) concentrations.

An assessment of the ISE graphs, alongside the solubility isotherm described by Elliott (1994) (Figure 9.3) shows that the pH and [Ca^{2+}] move through the brushite (dicalcium phosphate dihydrate – DCPD) and HAp isotherms within the first 2 hours. The change in [Ca^{2+}] and pH suggest that the first crystallographic phase likely to be formed is brushite that may transform to apatite as the pH and [Ca^{2+}] drop. It is important to note that the solution used in this study contains fluoride and therefore is likely to yield fluorapatite (FAp) or fluoride substituted apatite (FHAp) rather than HAp. The FAp isotherm is somewhat different to HAp, but not to a great extent. In fact, some literature indicates that the FAp and HAp isotherms are almost parallel until around pH 4.5 where FAp becomes slightly less soluble (Pan and Darvell, 2007).

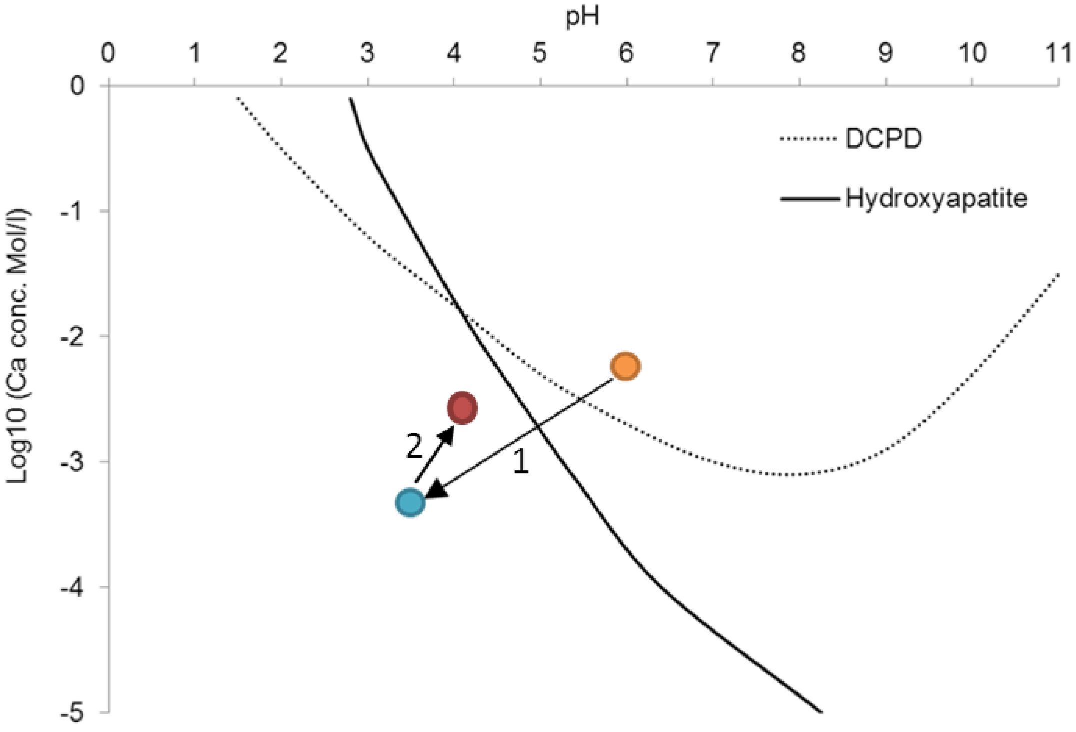

Figure 9.3: Solubility isotherm of DCPD and HAp, redrawn from Elliott, 1994. The change in pH and Ca^{2+} of the mineralisation solution in the first 2 hours is marked with an arrow where the orange circle is the initial pH and [Ca^{2+}] and the blue circle is the pH and [Ca^{2+}] after 3 hours, connected by arrow 1. The red circle depicts the pH and [Ca^{2+}] after 2 days of incubation, connected to the blue circle by arrow 2.

9.3.2 Mineralisation on ELP Coated Substrate

The solution used for the mineralisation of the ELPs has been described in section 6.1 and characterised above. In this study, the STNA15-ELP was coated onto cover slips and mineralised for different amounts of time to investigate the process of the biomimetic mineralisation. Previous studies have suggested that the β-strand proteins take part in biomineralisation (Addadi *et al.*, 1989). STNA15-ELP is chosen since it contains more mineralising sites and, in general, contains a larger amount of β-turn and β-strand structure at any given temperature compared to LR-ELP (for example as in Figure 7.2).

STNA15-ELP coated on borosilicate glass, incubated in the fluoridated mineralising solution at 37°C, produces mineral platelets at both 3 hours and 8 days incubation times, as shown in the SE-SEM images in Figure 9.4 A-B and C-F respectively. The platelets at the 3 hour time point (Figure 9.4A and B) have a morphology similar to reported morphology of brushite (Giocondi *et al.*, 2010; LeGeros and LeGeros, 1972; Ren *et al.*, 2016). The etch pits seen on the crystal surface (Figure 9.4B arrow and Figure 9.7B) also resemble previous reports of etch pits formed on brushite surfaces during dissolution (Giocondi et al., 2010). At the 8 day time period the platelets retain their overall shape but become multi-layered and polycrystalline (Figure 9.4 C-F).

EDX analysis collected at the same time as the images in Figure 8.6 (3hC, Table 9.1) suggests that the platelets at 3 hours are brushite (dicalcium phosphate dihydrate (DCPD)), with a Ca/P ratio of approximately 1. Brushite presence, at the 3 hour time point, was confirmed with SAED (inset Figure 9.4B). Etch pits are visible on the brushite surface due to the dissolution of the crystal (arrow, Figure 9.4B). A previous study reported plate-like brushite to grow with a dominant face in the {010} direction

(Giocondi *et al*., 2010). The etch pits typically form on the {010} faces of the brushite crystals, similar to what is seen in the SEM (Figure 9.4B and Figure 9.7B).

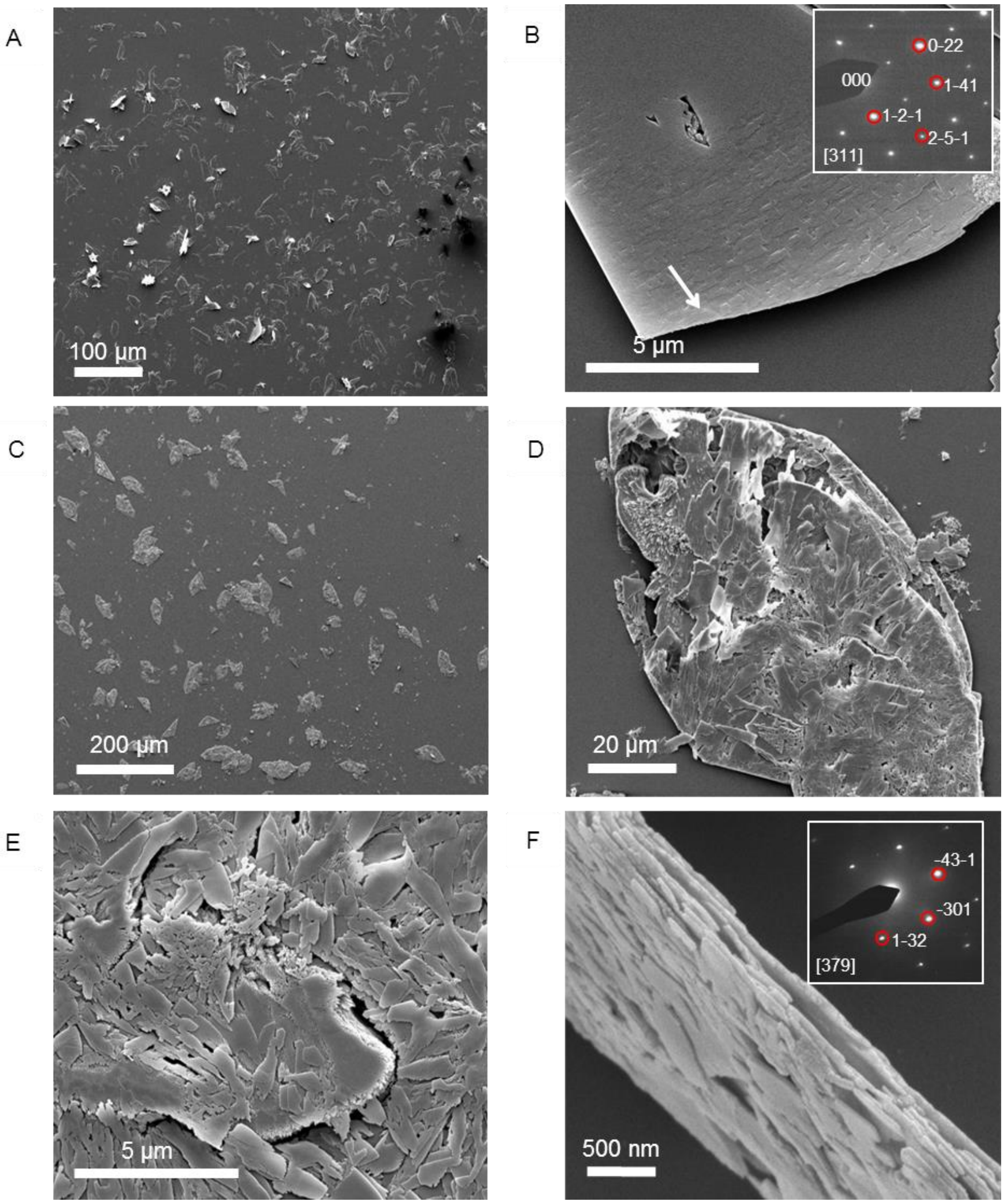

Figure 9.4: SE images of mineral grown on an STNA15-ELP coated substrate at 3 hours (A and B) and 8 days (C, D, E and F). Single crystal platelets dominate the surface at 3 hours with the SAED pattern of brushite, inset of (B). The platelets are polycrystalline FAp at 8 days of incubation. SAED pattern of one of the crystals from the platelet, inset of (F).

The presence of brushite crystals agrees with the behaviour of the solution, described in Section 12.1. However, by 3 hours both the pH and Ca^{2+} concentration are well below what is required for brushite existence. Theoretically, no brushite should be present at this stage. Either HAp should be detected or no mineral at all.

The platelets at day 8 retain their overall original platelet shape (Figure 9.4D) but appear to be a polycrystalline material. The smaller crystals that make up the larger platelets can be seen from the top and side on in Figure 9.4 E and F respectively. EDX analysis of the 8 day sample indicates that the platelets are fluorapatite, with a stoichiometric Ca/P ratio of 1.66 (8dC, Table 9.1). The SAED of one of the crystals making up the platelets present at 8 days is also indicative of apatite (inset of Figure 9.4F), agreeing with the EDX analysis.

	Atomic %	
Element	**3hC**	**8dC**
F	-	29.6
P	48.1	26.5
Ca	51.9	43.9
Ca/P Ratio	0.93	1.66

Table 9.1: EDX data showing the atomic % of elements present in each mineralised sample. 3hC and 8dC samples were incubated with the protein adsorbed on the glass for 3 hours and 8 days respectively. Other detected elements, such as silicon from glass, were subtracted from the data.

The Raman spectra of the mineral formed after 3 hours (Figure 9.5) exhibited a strong, sharp peak at 985 cm^{-1}, typical of the v_2 bending mode of PO_4^{3-} in brushite. The peaks at 381 cm^{-1} (v_8), 878 cm^{-1} (v_3) and 1057 cm^{-1} (v_6) are also indicative of brushite (Casciani and Condrate, 1979; Kim *et al.*, 2002), supporting the SAED and EDX data. The Raman spectrum of the mineral present in the constrained STNA15-ELP sample after 8 days of incubation is that of apatite. Raman spectra of apatite are easily characterized by the strong, sharp peak at 961 cm^{-1}, the v_1 stretching mode of the PO_4^{3-}. Other indicative peaks are visible at 447 and 433 cm^{-1} from the v_2 bending mode of the PO_4^{3-}; 620, 610, 594 and 582 cm^{-1} form the v_4 bending mode of the PO_4^{3-} ; 1076 and 1054 cm^{-1} from the v_3 stretching mode of PO_4^{3-} (Crane et al., 2006).

The control sample, uncoated borosilicate glass, shows that some mineral is present on the surface (Figure 9.6A) at 3 hours. This mineral resembles the shape of the brushite platelets seen in the STNA15-ELP coated samples (Figure 9.4) but is not a whole platelet. In contrast to the coated borosilicate glass slide, no mineral platelets are seen on the uncoated substrate after 8 days of incubation (Figure 9.6B). The early dissolution of the mineral and the lack of mineral at the later time is expected from the pH-[Ca^{2+}] isotherm (Figure 2.8), and suggest that the ELP plays a critical role in stabilising the early mineral phase, seen in Figure 9.4A and B.

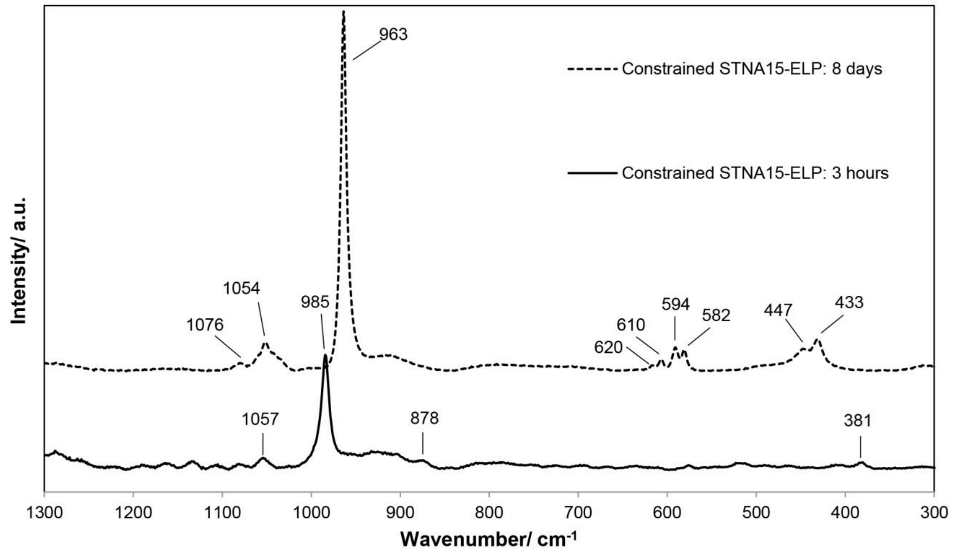

Figure 9.5: Raman spectroscopic data, in the range of 300-1300 cm^{-1}, of the mineral formed on the STNA15-ELP coated substrates at 3 hours and 8 days of incubation.

SEM, EDX and Raman indicate that brushite is the first phase formed in the presence of constrained STNA15-ELP coating and FAp is present after 8 days of incubation.

For instance, brushite typically forms under acidic conditions (Dorozhkin, 2010), such as in this study (pH 6), explaining its presence at early time periods.

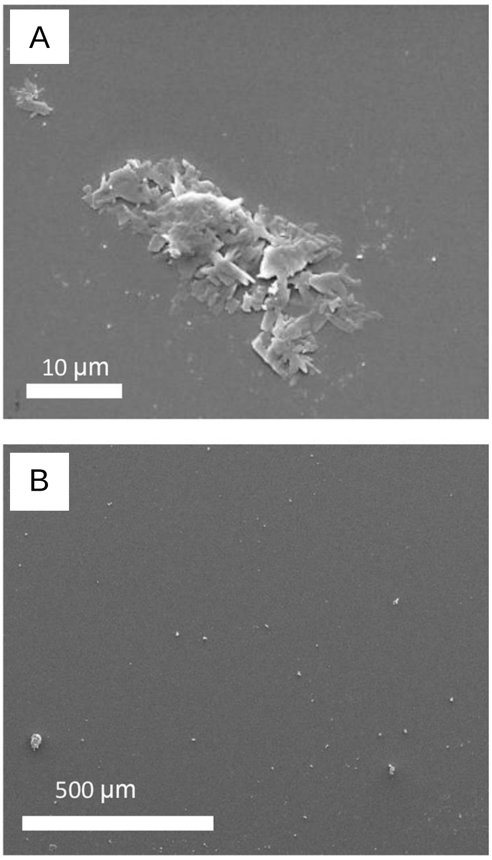

Figure 9.6: SE-SEM images of uncoated borosilicate glass surfaces after A: 3 hour and B: 8 days of incubation in mineralising solution.

Even though brushite seems to be the precursor to apatite in this study, brushite and FAp have different crystal structures and therefore would not easily transform from one to another. Brushite has been reported to have a monoclinic structure (Sainz-Díaz *et al*., 2004) compared to the hexagonal FAp (Elliott, 1994). These different crystal structures lead to the conclusion that the change in mineral chemistry and morphology observed between the 3 hour and 8 day period, coupled with the etch marks on the brushite surface, occurs due to a dissolution and re-precipitation process. The dissolution of brushite and re-precipitation into an apatitic phase has been previously reported and confirms this theory (Johnsson and Nancollas, 1992a).

The previous report also described the brushite crystals as templates for apatite growth. Therefore, we may assume that re-precipitated FAp crystallites are templated by the original brushite crystal, appearing to form a layered ordered structure but retain the original shape.

9.3.3 Time Study of the Mineral Formation and Recrystallisation

The previous section described the initial and final phases formed on the STNA15-ELP coated substrate during the 8 days of incubation in a fluoridated solution. This section attempts to study the change in the phases. Figure 9.7 shows SEM images of the mineral morphologies present at a number of time points. The first mineral seen, at the 1 hour time point, is in a form of a smooth platelet (Figure 9.7A). After 3 hours, these platelets begin to dissolve. The dissolution process is assumed due to the appearance of the etch pits on the crystal surfaces (Figure 9.7B). The appearance of the platelets at 2 days of incubation (Figure 9.7C) suggests that little morphological change occurs after this time point. The platelets at the 2 day point are polycrystalline and these small crystals appear to be flat.

The morphology of the mineral observed at the 8 day incubation point, shown in Figure 9.4D, is similar to the mineral observed at the 2 day incubation point seen in Figure 9.7D. This change of crystalline structure, from platelet, to a polycrystalline material, can also be evidenced when examined with an optical microscope equipped with polarising lenses (Figure 9.8). When viewed with normal light, the 15 minute and 1 hour platelets (Figure 9.8A and B respectively) appear as large single crystals. No birefringence is observed with either of two earliest time points. The 3 hour platelets appear to be undergoing a transformation as they do not look clear any longer (Figure 9.8C) and are birefringent (Figure 8.9D). The 1 day and 3 day platelets clearly appear polycrystalline (Figure 9.8E and G, respectively) and birefringent

(Figure 9.8F and H). The polarised light microscopy reveals that the early platelets are isotropic and not birefringent.

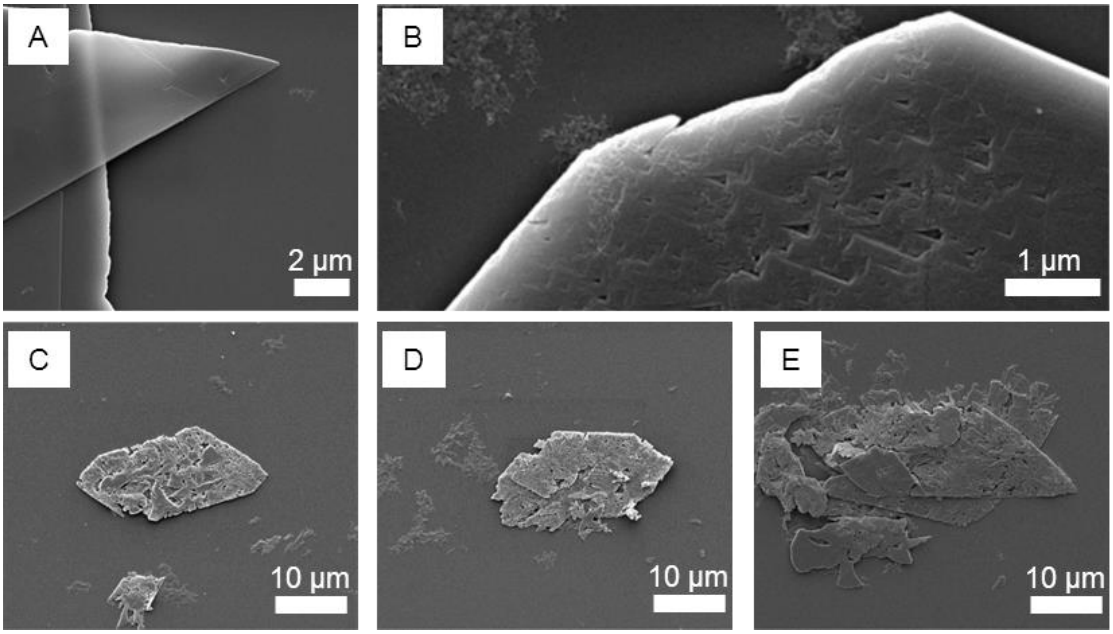

Figure 9.7: SE-SEM images of mineral formed on protein coated borosilicate glass after A: 1 hour, B: 3 hours, C: 2 days, D: 4 days and E: 7 days of incubation in a fluoridated mineralising solution (see the 8 day morphology in Figure 9.4).

The change of phase from brushite to FAp is supported by the EDX measurements (Figure 9.9). The 1 hour and 3 hour mineral has the Ca/P ratio of 1 and no fluorine, marked with a red star on Figure 9.9. The fluorine peak appears in the day 1 measurements. The presence of Si in the spectrum is due to the underlying borosilicate glass substrate.

On the second day of incubation, according to the ISE study, the solution contains ~2 mM of Ca^{2+} and a pH of 3.84 (red dot, Figure 9.3). These values place the solution in the area where neither apatite nor brushite is stable. However, FAp formation is occurring in these conditions. During crystal formation the local environment is depleted of ions and becomes under-saturated with respect to the crystal (Bunn, 1949). The fall in ionic concentration surrounding the crystal causes a gradient to be set up. Further growth of the crystals occurs due to diffusion of ions through the solution to the crystal. Therefore, following the Bunn explanation (1949), an assumption can be made that at some point the local microenvironment of the crystal is under-saturated to such an extent that the crystal is destabilised and begins to dissolve. This assumption can explain the appearance of the etch pits on the brushite surface. As the dissolution of the crystal continues, the local microenvironment will become supersaturated. Perhaps, again, a gradient will be set up but in the opposite direction, promoting the dissolution. This may explain why the calcium ion concentration continually rises during the 100 h incubation period (Figure 9.1).

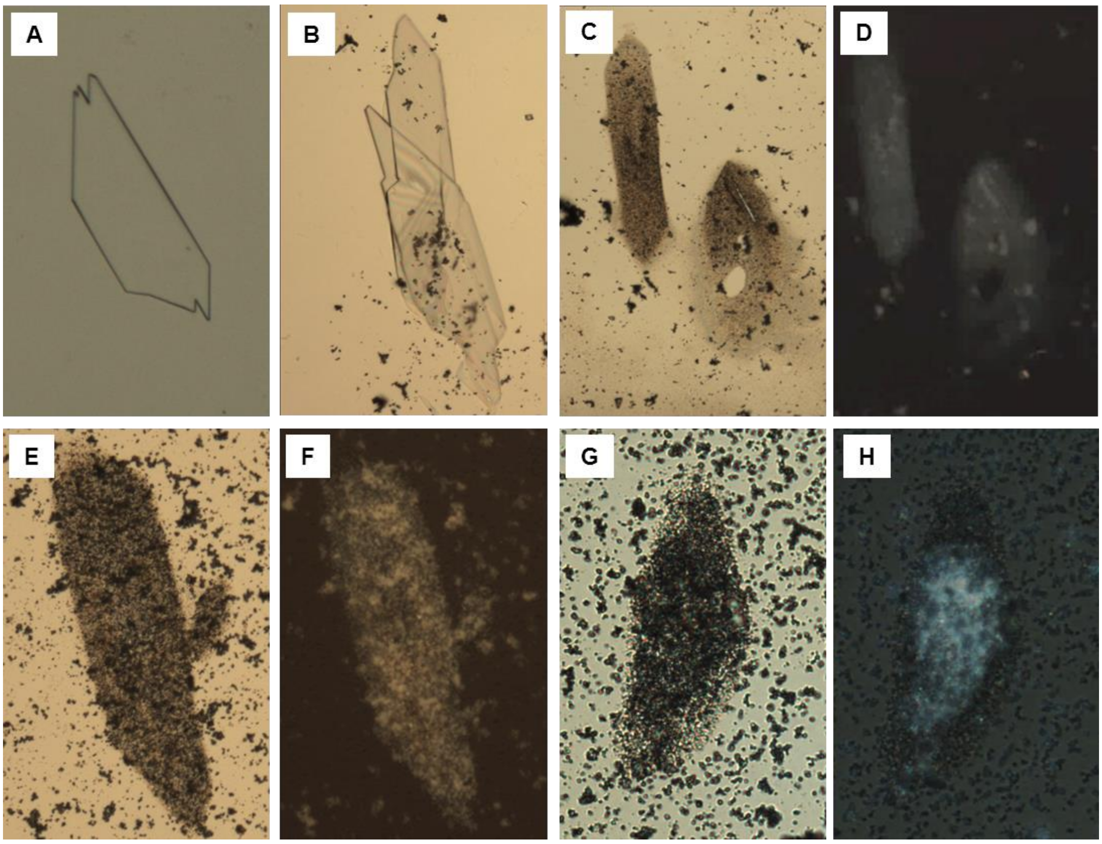

Figure 9.8: Optical micrographs of minerals grown on STNA15-ELP coated substrates after A: 15 minutes, B: 1 hour, C: 3 hours, D: 3 hours (polarised light), E: 1 day, F: 1 day (polarised light), G: 3 days and H: 3 days (polarised light) of incubation in a fluoridated mineralising solution.

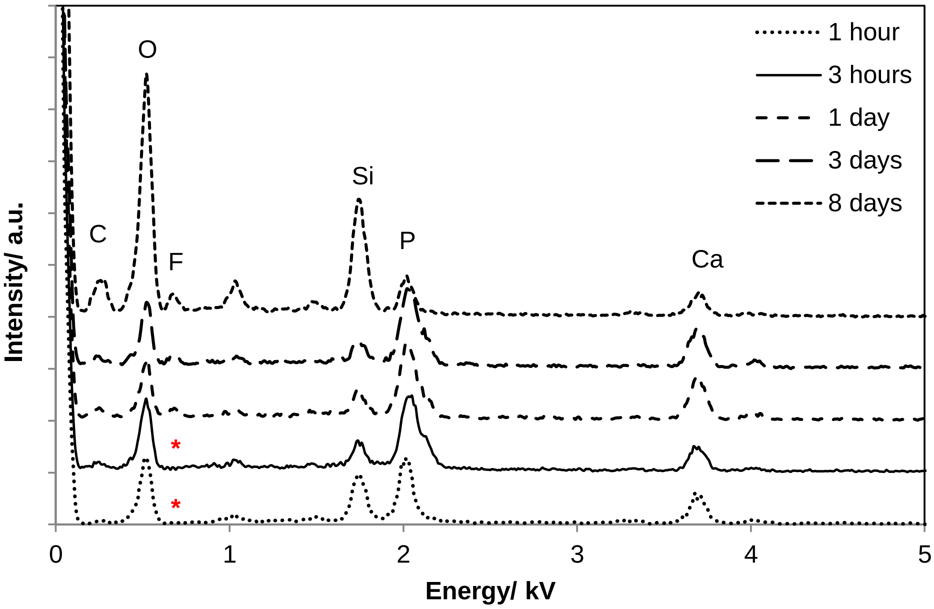

Figure 9.9: EDX data of mineral grown on STNA15-ELP coated borosilicate glass at different time points. The red stars indicate where there was no fluorine detected in the sample.

The re-precipitation of one CaP phase onto another has been discussed previously (Daculsi, 1998; Johnsson and Nancollas, 1992a). In one publication in particular, two hypotheses have been proposed (Daculsi, 1998). The first describes the micro-local supersaturation of the crystal. The micro-local supersaturation is said to occur due to dissolution of the initial crystal and causes the re-precipitation of a new more stable phase on the initial crystal surface. The second hypothesis states that the initial crystal acts as a nucleator of the new phase. The first hypothesis is more likely to occur here since the initial crystal platelets first appear to dissolve (for example Figure 9.7B) and then become a polycrystalline material (Figure 9.4D-F) (also supported by Johnsson and Nancollas, (1992)). Due to the similarity in the overall mineral morphology between the 3 hour and 8 day time points (Figure 9.4), it may be assumed that as the crystals reform in the same platelet template. Perhaps, this mineralisation is a combination of both the hypotheses in one.

9.3.4 Effect of Surface Hydrophobicity on Mineralisation[3]

Results in 9.3.2 clearly show that the STNA15-ELP, when coated on glass, has some kind of effect on the formation pathway of FAp, *via* a brushite phase. Literature often relates the structure of biomineralising proteins to the process itself (for example Addadi *et al*., 1989). Studies around protein adsorption suggest that proteins can change conformation when adsorbed to a surface, including chapter 9 of this thesis. Some reports have shown that protein adsorption is particularly favoured when contact angle (θ) > 65 ºC (Vogler, 2012). In this light, the mineralisation on ELP coated surfaces of varying hydrophobicity was investigated.

PDMS surfaces were treated with UV/Ozone for varying times. Treatment of PDMS with such conditions causes it to become more hydrophilic. The surface of PDMS is said to become hydrophilic due to the lysis of several groups and the addition of –OH groups (Efimenko *et al*., 2002). In this study, PDMS surfaces are treated with UV/Ozone for up to 90 minutes. The contact angles of water on the treated PDMS surfaces are shown in Figure 9.10. The untreated PDMS surface is quite hydrophobic, with a contact angle of 106.5°±3. Treatment of the PDMS surface with the maximum time of 90 minute causes the surface to become extremely hydrophilic, with a contact angle of 19.5°±5. The contact angles of borosilicate glass, used in the above study, and an enamel cross-sectional surface are also plotted in Figure 9.10 for comparison. The contact angle of borosilicate glass is 70.9°±3 and of enamel is 67.3°±2. The treatment of PDMS with UV-Ozone for 30 minutes results in a contact angle comparable to both enamel and the borosilicate glass (67.5°±13).

---

[3] The experimental work was designed by KS and the laboratory measurements were carried out by Mowlni Uthayakumaran, a 3rd year SEMS project student, under the supervision of KS. As such, the description, analysis and interpretation of the measurements presented here are entirely the work of KS.

Following UV/Ozone treatment, PDMS surfaces were coated with STNA15-ELP and mineralised in the fluoridated solution used in the other mineralisation experiments. The results of the mineralisation experiment are shown in Figure 9.11.

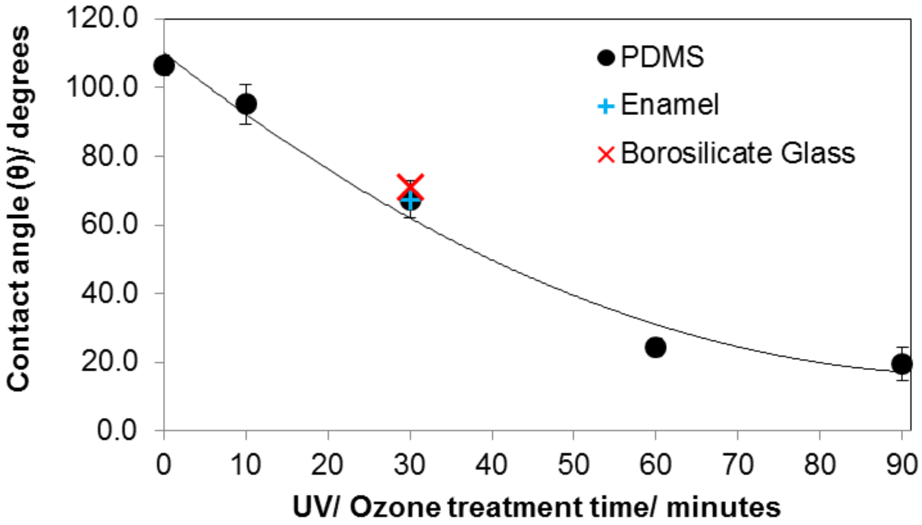

Figure 9.10: Contact angles of water on PDMS surface after different time treatment of PDMS with UV/Ozone. The values for borosilicate glass (substrate used for the other mineralising experiments in this work) and enamel are given for comparison. For PDMS contact angles n=6, for enamel and glass n=3. The PDMS contact angles' standard errors are displayed as error bars on the graph.

The PDMS surfaces treated with UV/Ozone for 0-10 minutes remain un-cracked. After 24 hours of incubation in the fluoridated mineralisation solution, a white precipitate is seen on the PDMS surfaces (Figure 9.11A and B). In contrast, the mineral formed on the 30 minute UV/Ozone treated PDMS (Figure 9.11C) resembles the mineral formed on the borosilicate glass surface. Longer UV/Ozone treatment times of PDMS surfaces appear to cause crack formation (Figure 9.11D and E). Such cracks are known to form due to the shrinkage of PDMS during the UV/Ozone treatment. The UV/Ozone treatment is said to only affect the top layer of the PDMS, perhaps forming a 20-30 nm silicon oxide layer (Efimenko *et al*., 2002). Hence, the treated surface can crack due to surface shrinkage.

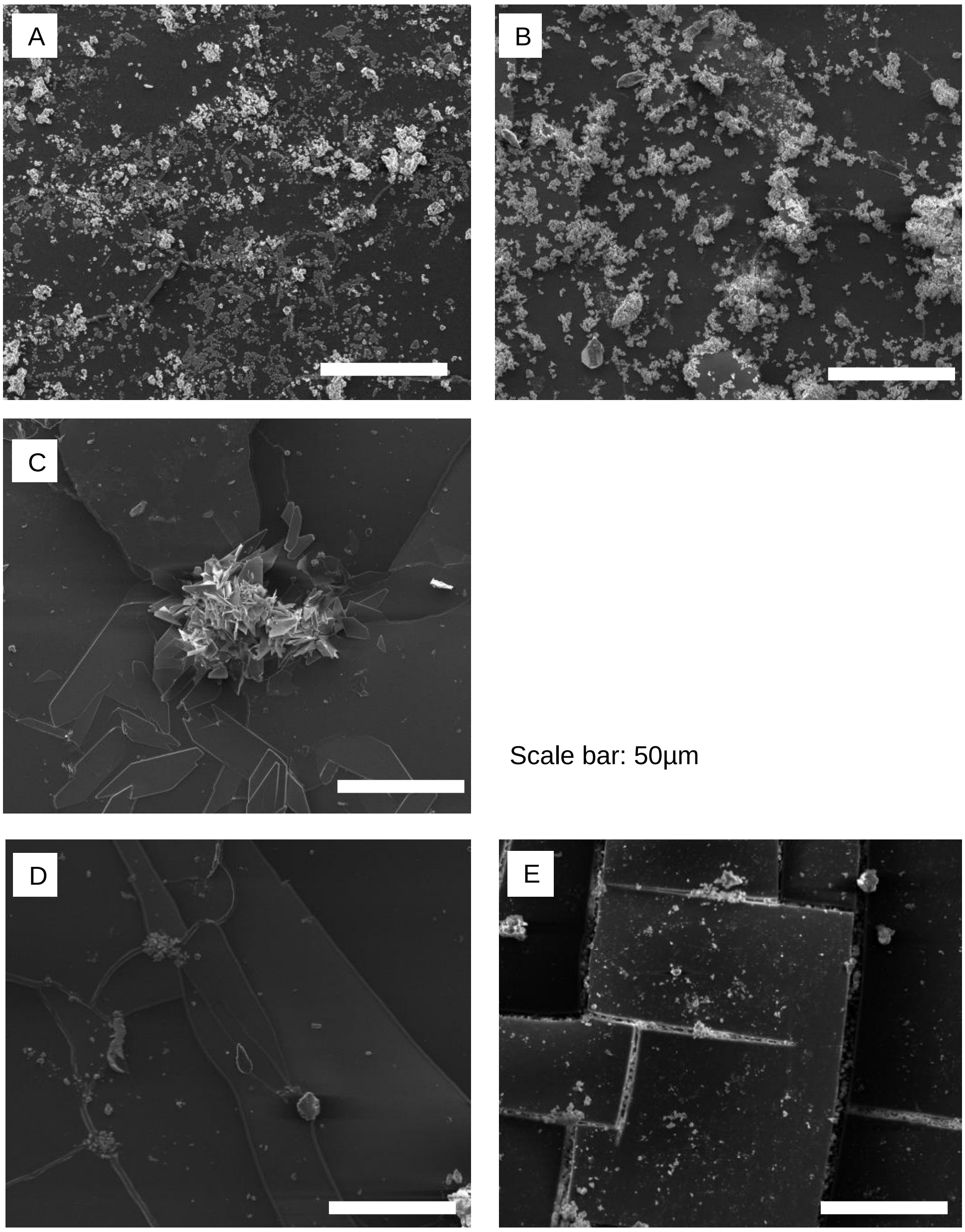

Figure 9.11: SE images of minerals present at 24 hours on STNA15-ELP coated PDMS surfaces treated with UV/ Ozone for A: 0 minutes, B: 10 minutes, C: 30 minutes, D: 60 minutes and E: 90 minutes.

The similar appearance of the mineral on the 30 minute treated PDMS may not be a coincidence. Protein adsorption is said to be particularly favoured when the contact angle (θ) > 65° (Vogler, 2012). Therefore, protein adsorption may not be as efficient when PDMS is treated for any longer. The adsorption of proteins to surfaces is a complicated mechanism and may consist of many interactions between the solvent, surface and protein. The adsorption of the protein may be different on the more hydrophobic PDMS surfaces. The structure of the protein may also change. These factors will control the subsequent exposure of mineralising sites of the protein to the mineralising medium. It is possible that the contact angle of ~67° causes the ELP to have the most favourable conformation for controlled mineralisation, post adsorption.

9.3.5 Mineralisation of ELP in Solution

SE-SEM images of the lyophilised precipitate, formed with STNA15-ELP free in the mineralising solution, are shown in Figure 9.12. After incubation for both 3 hours (Figure 9.12 A-B) and 8 days (Figure 9.12 C-F), needle-like precipitates were visible. However, after 3 hours of incubation the needles were only visible when imaged with BSE since they appeared to be buried within the protein (Figure 9.12B).

EDX of the 3 hour STNA15-ELP precipitate has a Ca/P ratio of 1.48 (3hS, Table 9.2). After incubation for 8 days (Figure 9.12 D-F) an abundance of spherical and dumbbell structures are observed and the EDX of the mineral suggests that a mixture of calcium fluoride (CaF_2) (CaF_2 in Table 9.2, Figure 9.12D arrow) and fluorapatite (8dS in Table 9.2) exists. CaF_2-like material has been previously reported to occur in solutions with high fluoride content, such as the one used in this study (Christoffersen *et al*., 1988; Mohammed *et al*., 2014). The EDX of the needles present in the 8 day sample gave a Ca/P ratio of 1.55. Since the mineral has a typical FAp needle-like morphology (for example Chen *et al*., 2006), the non-stoichiometric Ca/P ratio indicates a calcium deficiency in the apatite, analogous to previous literature (Dorozhkin, 2010). Also, the random orientation of the crystals, in both the 3 hour and 8 day samples, indicates that the nucleation process in solution is spontaneous and the apatite has no preferred growth direction.

	Atomic %		
Element	**3hS**	**8dS**	**CaF_2**
F	38.6	27.9	51.1
P	24.7	28.3	2.8
Ca	36.7	43.8	46.1
Ca/P Ratio	1.48	1.55	16.56

Table 9.2: EDX data showing the atomic % of elements present in each mineralised sample. 3hS and 8dS samples were incubated with the protein in solution for 3 hours and 8 days respectively. EDX data for calcium fluoride (CaF_2) present in the samples is also given.

TEM of the 3 hour precipitate, formed in the presence of STNA15-ELP, showed nano-crystalline mineral. The high resolution TEM (Figure 9.13A) and SAED (inset of Figure 9.13A) of the early precipitate both indicate FAp was already present at 3 hours. The 8 day precipitate was also confirmed to be FAp, both with SAED (inset 1 of Figure 9.13B) and high resolution TEM (inset 2 of Figure 9.13B). The SAED of the spherical particles confirmed the presence of calcium fluoride (inset 3 of Figure 9.13B).

FTIR analysis of precipitate formed in solution with free STNA15-ELP (Figure 9.15), after 3 hours of incubation, shows broad and poorly defined peaks generated by the v_3 asymmetric stretching mode of the apatitic PO_4^{3-} group (1000-1100 cm^{-1}). Further apatitic peaks, generated by the v_4 bending mode of the PO_4^{3-} group, are visible at 603 and 561 cm^{-1} (Kim *et al*., 2002).

FAp and HAp are crystallographically identical and not distinguishable in many analytical techniques. However FAp can be characterized in FTIR by the lack of the OH^- liberation peak at 631 cm^{-1}, normally present in the HAp spectra. The traces in Figure 9.15 lack this liberation peak, indicating that the apatite precipitate is a fluorapatite. A peak indicative of the HPO_4^{2-} group (527 cm^{-1}) is present in the spectra of both the 3 hour and 8 day precipitate formed in the presence of free STNA15-ELP, normally present in octacalcium phosphate (OCP).

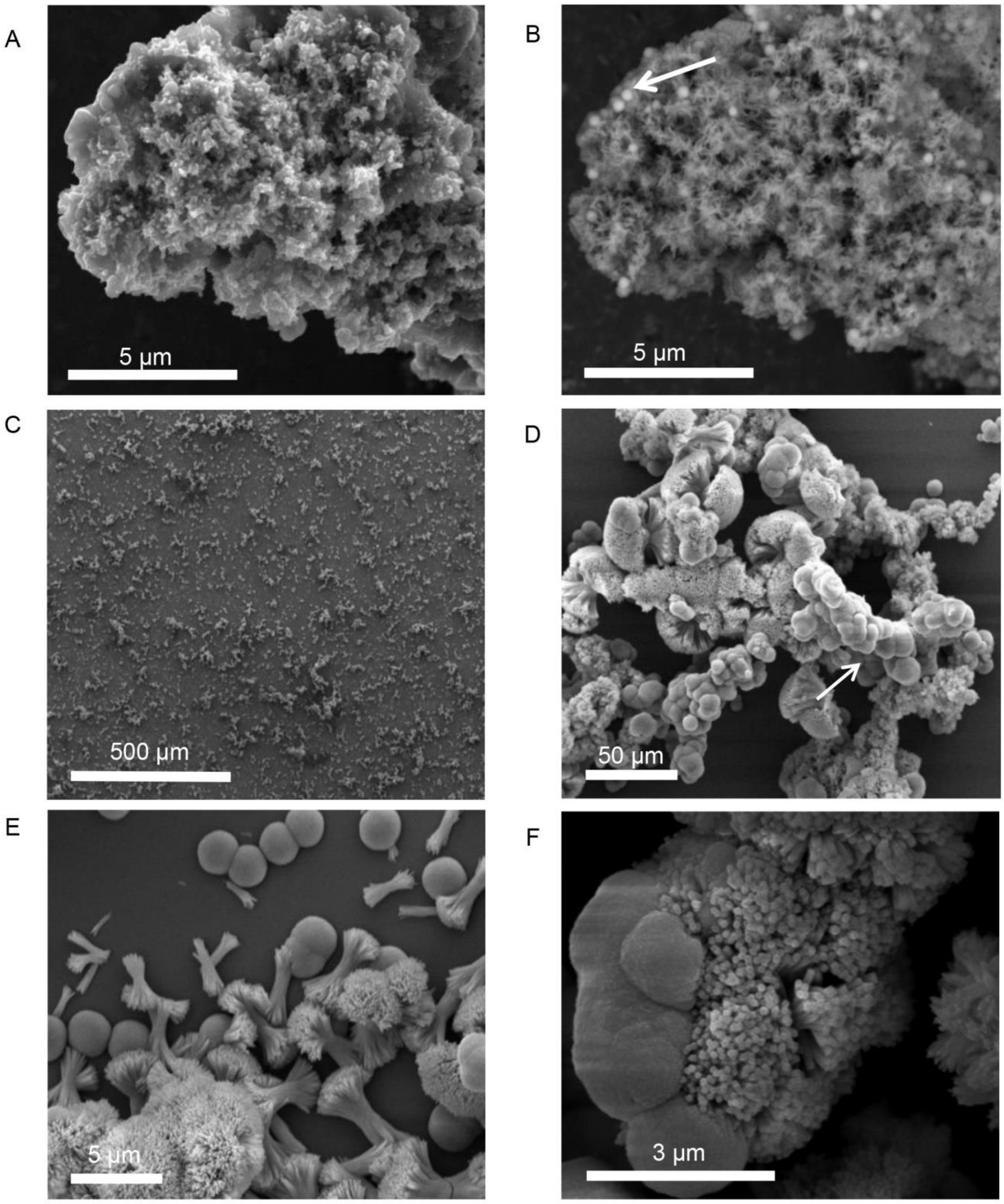

Figure 9.12: SE-SEM images of precipitate formed in solution containing STNA15-ELP at 3 hours (A: SE and B: BSE) and 8 days (SE: C, D, E and F) of incubation. Arrows in B and D point to CaF_2 spheres.

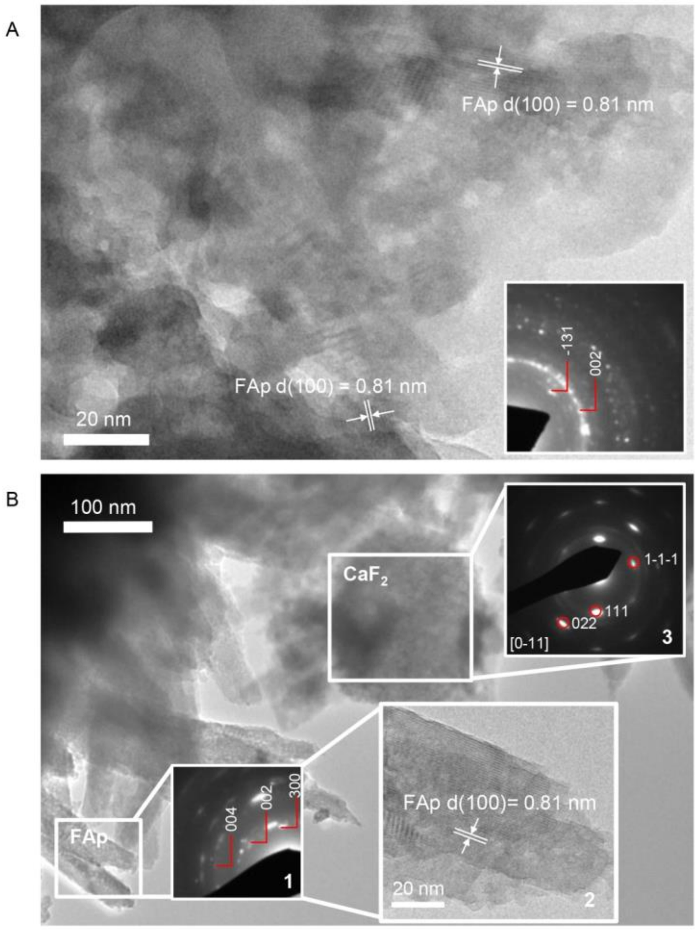

Figure 9.13: TEM images of precipitate present in solution containing STNA15-ELP at (A) 3 hours and (B) 8 days of incubation (inset 2 showing the high resolution TEM image with FAp planes visible). The 3 hour precipitate is a nano-crystalline apatite. At 8 days the apatite has a needle-like form. The needles that were directly in contact had some co-alignment as seen in the SAED pattern (inset 1). The spherical particles, present at 8 days, were confirmed to be CaF_2, from the SAED pattern (inset 3).

SEM of the control precipitate, without any protein, at 3 hours shows typical OCP platelets (Figure 9.14A). The presence of OCP is further confirmed with high resolution TEM and SAED (Figure 9.14B and inset of 11.14B). The 8 day control samples show apatite crystallites with a typical hexagonal needle shape seen in both SEM (Figure 9.14C) and TEM (Figure 9.14D). The TEM of the control needles have regular ends (Figure 9.14D) unlike the needle-like precipitate formed in the presence of STNA15-ELP (Figure 9.13B).

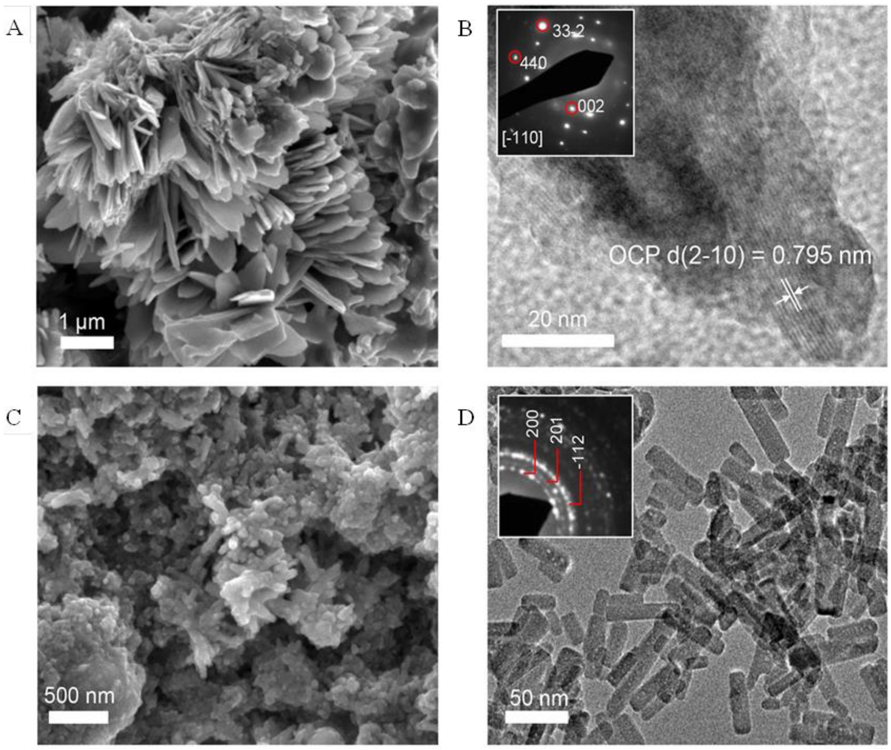

Figure 9.14: Precipitates formed in control conditions. A: SE image of precipitate formed in solution without STNA15-ELP. B: High-resolution TEM image of precipitate formed in solution with no protein and inset of B showing a typical SAED pattern of the precipitate. C: SE image of the precipitate in the control solution with no STNA15-ELP at 8 days. D: TEM image of the precipitate formed in the control solution at 8 days with the inset showing a typical SAED pattern.

FTIR of the control precipitate, formed after 3 hours of incubation, has a typical OCP trace with peaks generated by the v_3 HPO_4^{2-} stretch visible at 1114, 1103 and 1093 cm^{-1}, in addition to the 527 cm^{-1} peak that is visible in the protein containing samples (Berry and Baddiel, 1967; Fowler *et al*., 1993). The control precipitate found in the 8 day samples has a typical FAp FTIR spectrum with well-defined apatitic peaks and an absent OH^- liberation peak.

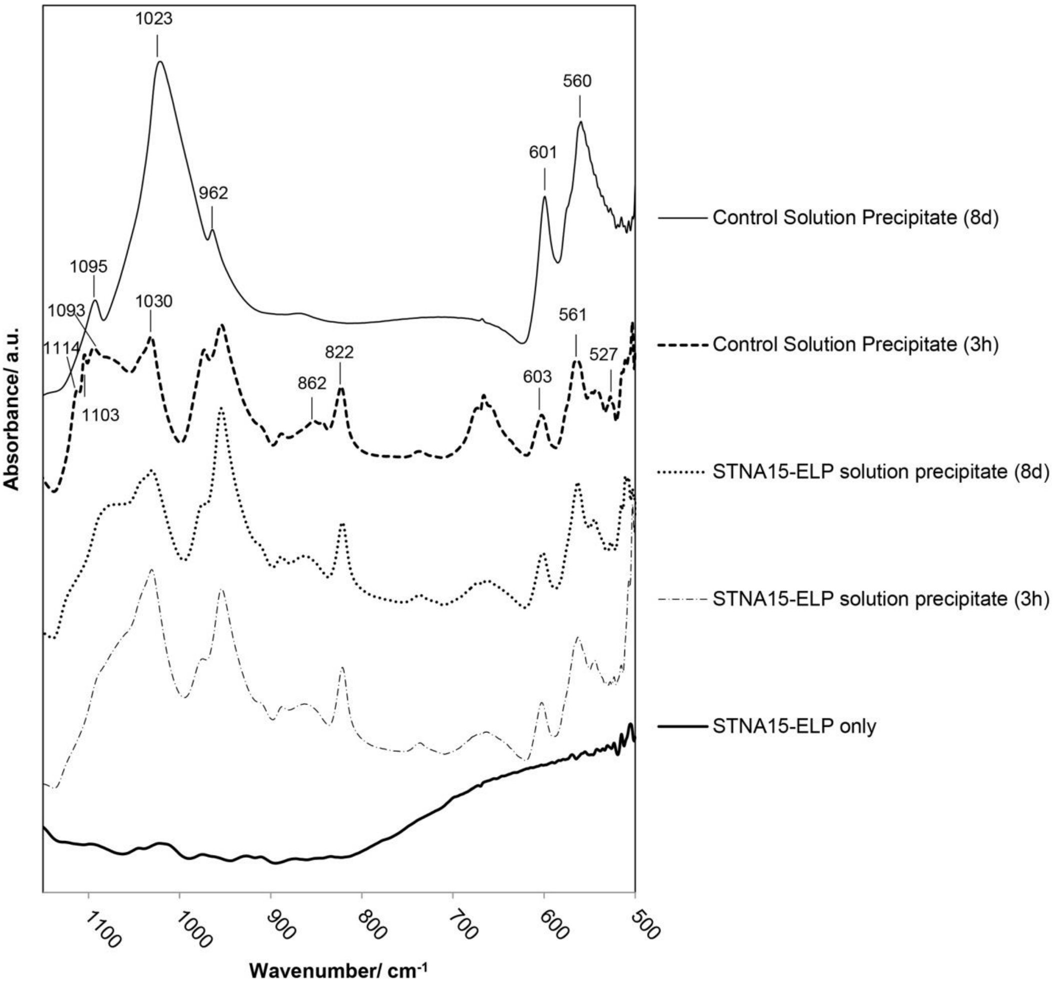

Figure 9.15: FTIR analysis of precipitate formed in solution with and without STNA15-ELP. Without STNA15-ELP OCP forms at 3 hours, transforming to highly crystalline FAp at 8 days. The ELP promotes FAp formation, with the FTIR indicating the presence of nano-crystalline FAp at 3 hours and 8 days. (820 cm^{-1}: residual NO_3).

The FAp crystals initially form within an aggregate of STNA15-ELP where favourable heterogeneous nucleation can occur. The broad peaks of the PO_4^{3-} group, seen in the 3 hour FTIR traces (Figure 9.15) of the precipitate formed in the presence of ELP, indicate that nano-crystalline apatite has formed, as observed in the TEM image (Figure 9.13A). The low Ca/P ratio of the 3 hour precipitate is lower than calcium deficient apatite and is tending towards OCP. Furthermore, the presence of the HPO_4^{2-} peak in the FTIR spectrum is contradicting the presence of apatite.

Figure 9.16 shows the pH profiles of 500 µl of mineralising solution with and without unconstrained STNA15-ELP. The pH drop of the mineralising medium alone does not occur until around 15-30 minutes after the beginning of the incubation. The same is observed in the large volume of 250 ml shown in Figure 9.2. However, when the STNA15-ELP is present, the pH drop occurs within the first 5-10 minutes and at a faster rate. Falling pH within a mineralising medium has previously been associated with apatite formation, both without the influence of proteins or peptides (Habraken *et al*., 2013) and with (Kwak *et al*., 2011; Tsuji *et al*., 2008). Therefore, due to the faster pH drop, it may be assumed that free STNA15-ELP in solution promotes fast apatite formation. The increased rate of apatite formation may be the cause of either the ELP forming a more favourable microenvironment or STNA15-ELP assisting heterogeneous nucleation of apatite, or potentially both.

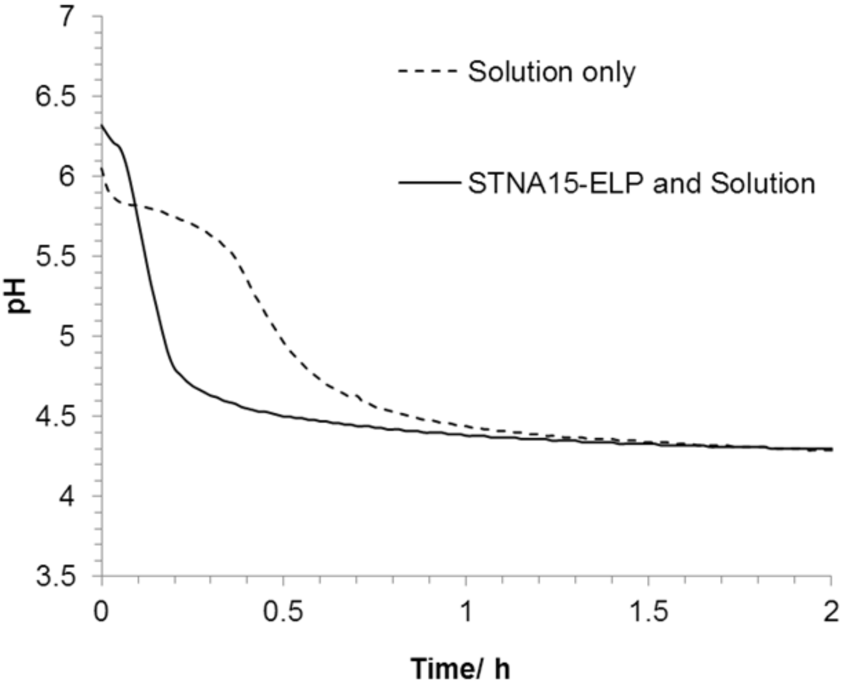

Figure 9.16: ISE data of pH of the mineralising medium with and without STNA15-ELP. The readings were taken using a microelectrode in a solution of 500 µl volume.

Rey *et al*. have extensively analysed nano-crystalline apatite with techniques such as FTIR, NMR and XRD (Drouet *et al*., 2009; Eichert *et al*., 2004; Rey *et al*., 2007a, 2007b). Rey *et al*. have hypothesized that nano-crystalline apatite is imperfect and is surrounded by a hydration layer. Due to this hydration layer, nano-apatite has a striking likeness to OCP. Firstly, the nano-apatite Ca/P ratio is somewhere in between OCP and apatite, and increases with the maturation of the crystals (Drouet *et al*., 2009). Similarly, FTIR of nano-apatite can have non-apatitic characteristics, resembling OCP traces, explaining the presence of the HPO_4^{2-} peak in the FTIR. The initial presence of nano-crystalline apatite can further explain the ragged shape of the crystals seen under TEM (Figure 9.13B). Rey *et al*. (2007b) have postulated that during maturation, the nano-crystals fuse together at the expense of the hydrated OCP-like layer.

Figure 9.7 compares the observed minerals formed in an STNA15-ELP containing mineralising medium (a), on an STNA15-ELP coated borosilicate glass (B) and in an acidic di-block ELP containing mineralising solution (C+D). The acidic di-block ELP was added to the experimental design in order to understand the influence of lysine on biomineralisation. The Ca/P ratios, corresponding to the highlighted areas in Figure 9.17, are listed in Table 9.3 along with the phases that may be present within the samples. The mineralisation on STNA15-ELP coated substrate (section 11.2) and in an STNA15-ELP containing mineralising solution (section 11.5) have been extensively analysed. There is considerable evidence that at 3 hours FAp forms in STNA15-ELP containing solution (for example Figure 9.13 and Figure 9.15) and brushite on a STNA15-ELP coated borosilicate glass (for example Figure 9.5 and Figure 9.4). The minerals formed with the acidic di-block ELP have not been analysed to the same extent as the minerals formed in the presence of STNA15-ELP so the existence of brushite cannot be outright confirmed. However, the Ca/P ratio of

1 does narrow down the CaP phase present to monetite or brushite. This low Ca/P ratio is the same as what was observed with the brushite platelets grown on the STNA15-ELP coated substrate, perhaps indicating that lysines within the ELP sequence play a crucial role in the pathway of FAp formation.

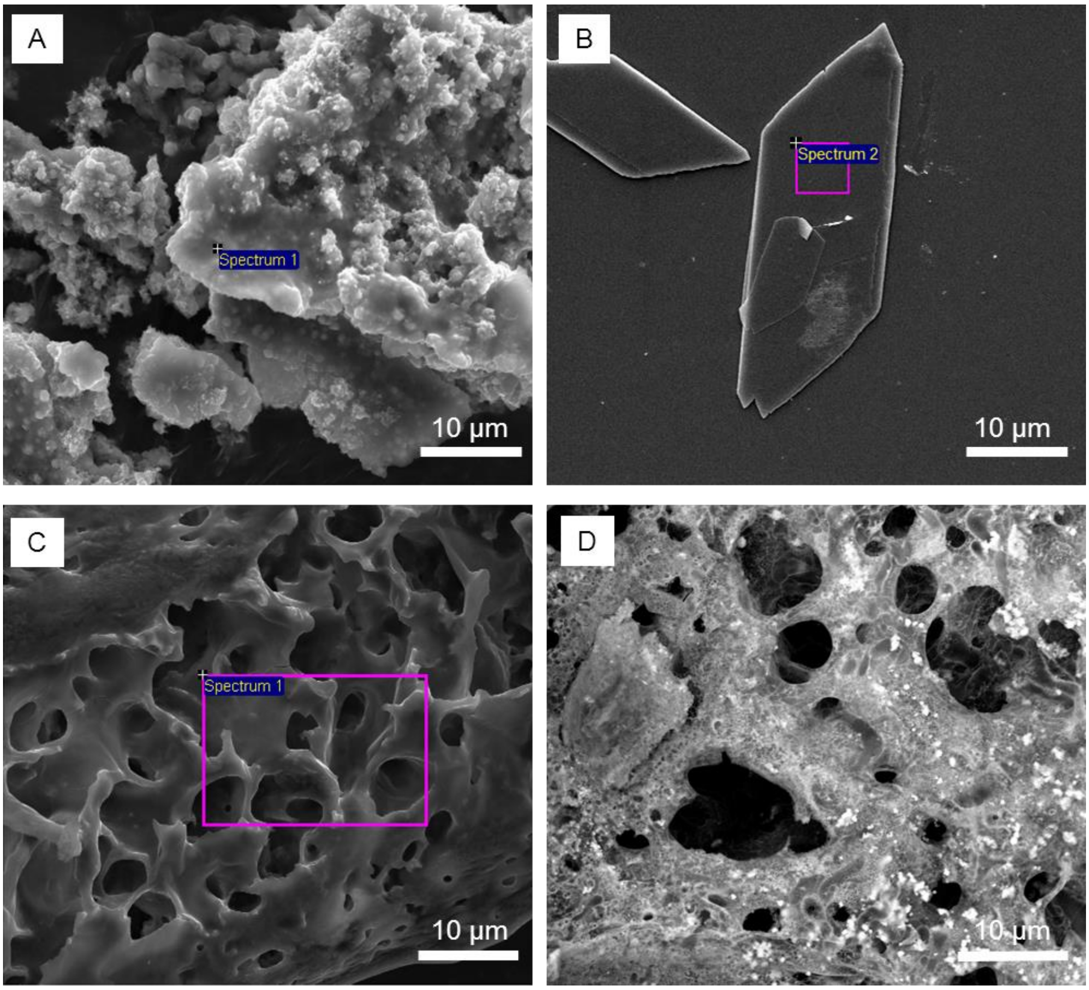

Figure 9.17: SE-SEM images of A) Mineral formed within STNA15-ELP aggregates, B) brushite platelet formed on an STNA15-ELP coated substrate, C) mineral formed when the acidic di-block ELP was added to the mineralising solution. D shows the BSE-SEM image of the precipitate formed with the acidic di-block ELP, showing a highly mineralised matrix. All samples were incubated for 3 hours. The pink squares indicate the position where EDX measurements were taken from.

Un-constrained STNA15-ELP	**Un-constrained Acidic Di-Block ELP**	**Constrained STNA15-ELP**
Ca/P ratio: 1.5	Ca:P ratio: 1	Ca:P ratio: 1
Nano-crystalline FAp	Brushite/ Monetite	Brushite

Table 9.3: Ca/P ratios taken from EDX data of the highlighted areas in Figure 9.7. The corresponding phases that are present or may be present at 3 hours are also listed in the table.

9.4 Summary

STNA15-ELP has shown the ability to form apatite biomimetically, either via a precursor phase or by forming larger crystals through the fusion of smaller mineral subunits. In either case, the apatite that was present after 8 days of incubation was a FAp.

The FAp formation on an STNA15-ELP coated substrate occurred via a brushite precursor. The brushite formed in a plate-like morphology and appeared to dissolve prior to the FAp formation. We believe, that the dissolution of brushite creates a microlocal supersaturation, as described by Bunn, (1949), and drives FAp precipitation. The brushite platelets template the FAp formation, as evidenced by the same platelet shape present at the early 3 hour time point and later 8 day time point. However, the single brushite platelet becomes a polycrystalline FAp platelet after 8 days of incubation.

Constrained STNA15-ELP mineralisation is affected by the hydrophobicity of the surface it is coated on. This was demonstrated by the presence of the brushite platelets on PDMS surfaces with the same contact angle as the borosilicate glass. This result suggests that the way STNA15-ELP adsorbs to a surface has an effect on the mineralisation of FAp.

With STNA15-ELP free in solution, no brushite was detected after 3 hours of incubation. At 3 hours, FAp was already present. However, the FAp had nano dimensions, was a poorly crystalline and had an OCP-like character. The nano-crystals of FAp fused over the incubation period and, at 8 days, appeared as FAp needles with a rugged edge. Without STNA15-ELP in solution, the mineralising medium first produced OCP, which then transformed to FAp by 8 days.

Clear differences are observed in constrained and free in solution STNA15-ELP mineralisation. The way in which STNA15-ELP is added to the mineralising medium affects the mineral morphology and the route of mineral formation.

Chapter 10. GENERAL DISCUSSION

ELP properties have been researched for decades, starting with early publications by Urry *et al.* (for example Urry, 1978, 1992; Urry *et al.*, 1991). Their popularity caught on and their use has been extended to a range of applications, from drug delivery to bone defect repair. The ease of ELP engineering has proved that these proteins can be applied for a large range of bioengineering applications, some which may not have been explored yet. Their similarity to elastin deems them biocompatible with a low cytotoxicity. However, in some ways, the properties of these proteins are still an enigma and the new ELP sequences designed around the world further complicate matters. Furthermore, contradicting research exists regarding the ELP structure below and above the ITT, where one states that the proteins have a neat β-spiral structure (Urry *et al.*, 1976) and other that it is not energetically favourable for a perfect β-spiral to form (Li *et al.*, 2001).

The novelty of ELPs, over other proteins, is their tuneable ITT. The ITT is the cause of hydrophobic collapse, aggregation and solubility of these proteins. In order to utilise these widely available, biocompatible and engineerable proteins more understanding is needed in terms of their thermoresponsive behaviour. This research primarily focused on furthering our understanding of one particular ELP, the STNA15-ELP. As a control, the LR-ELP was utilised and compared to STNA15-ELP. The STNA15-ELP is advantageous in biomineralising applications due to the presence of carboxylic side groups which are said to act as nucleators in biomineralisation. Furthermore, STN15, the peptide sequence on which STNA15 is modelled, is a peptide sequence of the naturally occurring statherin that is thought to aid in the remineralisation of dental enamel. So, here the STNA15-ELP was used to form ordered FAp structures as a step towards the design of enamel-like mineral structures with potential for dental applications.

To gain some insight into the thermoresponsive properties of STNA15-ELP, the protein was examined in three solutions: UPW, 20 mM NaCl and 10 mM $CaCl_2$. A number of studies exist regarding the behaviour of ELPs in ionic solutions (for example Hassouneh *et al.*, 2013; Kherb *et al.*, 2012; Reguera *et al.*, 2007). However, as far as we are aware, none have been published so far with regards to STNA15-ELP. The behaviour of STNA15-ELP in ionic solutions was somewhat unexpected, in particular the $CaCl_2$ solution. In the Hofmeister ion series, Ca^{2+} is considered to be on the side of the salting-in ions, i.e. they assist with solubility (Kherb *et al.*, 2012). On the same ion scale, Na^+ is somewhere in the middle and has a lesser effect on the protein solubility. However, FTIR results suggest that in NaCl STNA15-ELP had the largest proportion of random coil, in comparison to $CaCl_2$ or UPW (Table 7.2). Although all of the techniques here cannot give us specific detail regarding how the ions interact with the protein, literature may hold some clues. Ca^{2+} can coordinate with carboxyl side groups of aspartic and glutamic acid (for example Shen *et al.*, 2016), both of which are present in large numbers within the STNA15-ELP sequence. This interaction of carboxyl groups with Ca^{2+} may lead to ion bridge formation between neighbouring molecules, or even intramolecularly. Carboxyl group interaction with Ca^{2+} may cause a decrease in the overall protein solubility and, therefore, a concurrent decrease in the proportion of random coil conformation (as seen, for example, in Figure 7.6 and Table 7.2).

On the other hand, Na^+ has been said to contribute to the order of the clathrate water structures which surround the hydrophobic domains within the ELP (Reguera *et al.*, 2007). Since ELPs collapse when the order of the water disrupts, it may be that the increased order in water is helping in ELP solubility, rather than diminishing it. Na^+

has also been described as an aid in forming organised structures when the ELPs collapse (Reguera *et al.*, 2007). Perhaps this is the reason why both STNA15-ELP (Figure 8.2) and LR-ELP (Figure 8.3) form large aggregates at lower temperatures compared to when they are in either UPW or $CaCl_2$. Likewise, both STNA15-ELP and LR-ELP both formed fibres when cross-linked in NaCl (for examples see Figure 8.10H and I and Figure 8.13B, H, I, respectively). Although it is difficult to speculate the mechanism by looking at SEM images or DLS graphs, it is certain that changing the ionic solution can control the morphology of the assembled ELP structures. This is beneficial not only for biomineralisation applications but can be extended to other tissue biomimetics, for example tendons or skin etc. Moreover, control of aggregate size of STNA15-ELP (for example with Ca^{2+} ions in Figure 9.5F) has opened potential avenues for controlling the density of nucleating sites.

We believe that the conformation of STNA15-ELP is advantageous for biomimetic mineralisation. In all unconstrained cases, STNA15-ELP appeared to have a larger proportion of ordered conformation when compared to LR-ELP (for example see Figure 7.2, Figure 7.5 and Figure 7.6). Some speculate the β-sheet forming proteins play a key role in biomineralisation (Addadi *et al.*, 1989). Therefore, the more order STNA15-ELP has, the more effective it would be at modulating crystal growth. When STNA15-ELP was constrained on a glass surface, its conformation had the highest proportion of β-turn/ β-sheet (Table 7.5). Hence, it is reasonable to believe that the most effective biomimetic route to forming FAp was in the constrained environment.

The mineralising capability of STNA15-ELP has been described in some detail in this work. The mineralisation of STNA15-ELP is clearly dependent on several factors, including constraint, wettability of adsorbent and ELP conformation. Differences are observed in the mineralisation process and the FAp morphology obtained at the 8 day incubation period between the constrained and unconstrained STNA15-ELP mineralised samples. In the two conditions, STNA15-ELP conforms in different ways, with the constrained ELP gaining order in comparison to when it is free in solution (Table 7.5). In the case of the constrained protein, the ordered STNA15-ELP on the glass surface appeared to restrict the formation of the FAp to polycrystalline platelet morphology, *via* a brushite single crystal precursor. The results strongly suggest that there are two reasons for this. Firstly, the brushite platelets exist for longer periods of time in the presence of STNA15-ELP coating. Reports have shown that other proteins, such as bovine serum albumin, can retard the transformation of brushite to apatite (Xie *et al*., 2001, 2002). Although there is no clear explanation for this, it is speculated that the adsorbed protein prevents water molecules from making direct contact with the surface of the brushite and therefore prevents dissolution.

The second explanation is based on templated mineralisation. The stabilised brushite crystals, surrounded by the protein, slowly dissolved once formed. The dissolution of the crystals was evidenced by the etch pits visible on the crystal surface (Figure 9.4 and Figure 9.7B). As brushite formed, along with the calcium fluoride precipitate, the calcium-pH isotherm shifted to an area where brushite is no longer stable, causing dissolution. The brushite dissolution probably created a local supersaturation of calcium that could reprecipitate as FAp, in the presence of fluoride. The slow FAp formation process allows an ordered structure to form where the FAp crystallites grow along the {010} face of brushite.

Brushite formation seemed to be favoured on a surface with a good wettability. There are also two possible explanations to this behaviour. The first relates to the adsorption of ELPs onto surfaces. Previous studies have reported that protein adsorption is favoured when the contact angle (θ)> 65° (Vogler, 2012). This may be due to the fact that most proteins are hydrophobic and therefore would be attracted to hydrophobic surfaces. The more hydrophobic the surface becomes the more of the protein could potentially adsorb, leaving no parts exposed to the mineralising solution. The second reason for the favoured mineralisation may be that extremely hydrophobic surfaces do not wet well. Therefore, neither the protein solution for coating nor the mineralising solution may wet the surface sufficiently. The adsorption of the ELP to surfaces of varying hydrophilicity was not easy to establish since both the PDMS and ELP are carbon based materials, and not easily distinguishable. Furthermore, it is difficult to make a PDMS covered quartz crystal for QCM studies.

In contrast to the ELP coated surface mineral formation, a different process occurred when the protein was unconstrained and suspended in solution. As seen in Figure 9.12B, the nucleation was random and the growth of the crystals has no preferred orientation. The protein aggregates created an environment that favoured apatite formation over other phases, even at 3 hours of incubation. This may be due to the local buffering effect caused by the lysine amino acids in the STNA15-ELP sequence. Since the lysine groups are likely to interact with the borosilicate surface, this effect is not seen with the STNA15-ELP coating. Other mineralising organic molecules, such as amelogenin (Kwak *et al*., 2011), have shown capability of buffering pH and stabilizing precursor phases. Amelogenin has the ability to stabilise amorphous calcium phosphate in a solution that normally precipitates apatite.

The specific behaviour observed in Chapter 10 can be further supported by the thermoresponsive properties of ELPs related to their inverse transition temperature. ELPs are known to fold and aggregate above their transition temperature. In its folded state, the STNA15-ELP can display, when in solution, its nucleating sites on the aggregate surface causing FAp nucleation all over the aggregate. The nucleation in STNA15-ELP aggregates is consistent with other work where needle like apatite grew from different ELP aggregates (Misbah *et al*., 2016). However, once adsorbed on glass and with some increase in order, the STNA15 sequence of the ELP is no longer concentrated on a surface of a particle but on a flat substrate. In both cases the mineral formation resembles the process of biomineralisation where either a precursor phase is present before a stable mineral is formed (Johnsson and Nancollas, 1992a) or smaller sub-units fuse to form larger, imperfect crystals (for example Robinson, 2007). However, only the constrained protein produced mineral that has a preferential growth direction.

These findings provide information that can lead to synthesis of ordered FAp structures that could lead to the use in enamel therapeutics. However, more importantly, this synthetic biomineralising system has shown that protein constraint and protein conformation both play an extremely important role in the process of biomineralisation. Protein constraint can be related to natural biomineralising processes, where the mineralising proteins exist within a gel-like matrix. In fact proteins, such as amelogenin, have been shown to assemble into fibres and nanospheres, rather than existing in a suspended free form (Carneiro *et al*., 2016).

Chapter 11. CONCLUSIONS

The STNA15-ELP has shown great promise in biomimetic mineralisation. Whether it is constrained or not, STNA15-ELP mineralisation mimicked two pathways proposed in literature: fusing of sub-units or *via* a precursor phase. When it is constrained, the STNA15-ELP has more control over the formation of FAp by stabilising a metastable brushite phase. The slow, controlled mineral formation produced an ordered FAp structure. On the other hand, when it is free in solution, STNA15-ELP mineralises rapidly, with little control, producing randomly oriented FAp crystals.

The experimental work suggests that the mineralisation behaviour of STNA15-ELP is dependent on its conformation. Furthermore, it is likely that the presence of free lysines in the STNA15-ELP, when it is free in solution, allows for the rapid growth of apatite by created a positive environment. However, when it is coated on glass, we postulate that the lysines play a role in the adsorption of STNA15-ELP to the surface. Therefore, with the lysines electrostatically bound to the surface, only the STNA15 sequence plays a part in the mineral formation.

Further conclusions, drawn from the studies reported in this work, are:

1. STNA15-ELP is a good candidate for biomimetic mineralisation.

- Due to the high amount of β- turn/ β-sheet component in the STNA15-ELP conformation, the protein is a good candidate for biomimetic mineralisation.
- Adsorption of STNA15-ELP onto the borosilicate glass substrate changes the ELP conformation. The adsorbed conformation has an increased β- turn/ β-sheet and therefore provides a suitable platform for biomimetic mineral formation.

2. Constrained STNA15-ELP creates a route to forming ordered FAp *via* a metastable precursor phase.

- Constrained ELP is suitable for further development of biomimetic enamel repair.

3. Change in STNA15-ELP conformation, constrained *versus* unconstrained, plays a role in the route of FAp formation and the final FAp morphology.

- Mineralisation pathways of both constrained and unconstrained STNA15-ELP resemble natural biomineralisation.
- Fast mineralisation of unconstrained STNA15-ELP leads to unordered mineral formation.

Chapter 12. FUTURE WORK

This thesis has attempted to grow our understanding of the STNA15-ELP and how we can utilise this protein for biomimetic mineral growth. However, as with all research, each answer posed a number of new questions. This exploration has left the work open ended, with room to grow in all the chapters. Some of the work that can be done in the future is described in this section.

Chapter 7

For a clearer understanding of the effect of ions on the ELPs, a number of techniques can be employed. First technique would be small angle X-ray scattering (SAXS). SAXS of proteins can measure the change in radius of gyration which, in turn, is used to determine the size, shape and conformation of the protein in solution. An amelogenin cleavage product has been examined in such a way, with and without calcium (Le Norcy *et al.*, 2011a). Using SAXS, the authors concluded that calcium caused conformational changes within this particular amelogenin peptide. Similar changes are assumed to be occurring in Chapter 8 of this thesis. Hence, SAXS would give additional insight into the conformational changes of STNA15-ELP. ATR-FTIR gave some interesting results in this thesis. However, transmission FTIR may give clearer results of the ELPs in ionic solutions and so is another technique to add to the future work.

Chapter 8

The crosslinked ELP structures have not yet been mineralised. The next crucial step in Chapter 9 would be to mineralise all the crosslinked ELPs to evaluate their efficacy in forming even sized minerals. If forming STNA15-ELP in Ca^{2+} enables us to control the density of nucleating site, we may be able to control the nucleation of FAp within other ELP crosslinked systems, such as membranes.

Chapter 9

Chapter 10 is, arguably, the most important chapter of the thesis. However, many questions remain regarding how the mineral forms on coated substrates. Some clarification may be obtained with surface techniques such as XPS. XPS may elucidate how the ELP adsorbed to the borosilicate surface. Some of the results suggest that lysines in STNA15-ELP play a role in accelerating FAp formation. With XPS, we may be able to determine if the lysines are interacting with the glass surface. Since ELPs are easily engineered, there is potential to develop a systematic study of ELPs with and without certain amino acids. For example, using an STNA15-ELP without any lysines within the ELP sequence could form an interesting study and answer the question of whether or not lysine contributes to the mineralisation.

The effect of surface hydrophobicity has also left a number of questions. Perhaps a study employing surfaces with different contact angles but same pI (if possible), could be used for future studies. Another possibility would be to further explore the mineralisation of ELPs on PDMS surfaces. Adsorption of STNA15-ELP onto PDMS surfaces would have to be investigated, to determine if and how they adsorb to PDMS surfaces of different hydrophobicities. PDMS coated quartz crystals would need to be designed and made. PDMS coated quartz crystals have already been explored by a Masters student at DPSU and have potential.

Such work would develop the thought that STNA15-ELP preferentially mineralises on a surface with a specific contact angle. Finally, once more is known regarding the organised FAp formation, the STNA15-ELP has to be applied to enamel to develop novel therapeutics.

BIBLIOGRAPHY

Abbarin, N., San Miguel, S., Holcroft, J., Iwasaki, K., and Ganss, B. (2015). The enamel protein amelotin is a promoter of hydroxyapatite mineralization. *J. Bone Miner. Res.* 30, 775–785. doi:10.1002/jbmr.2411.

Addadi, L., Berman, A., Oldak, J. M., and Weiner, S. (1989). Structural and stereochemical relations between acidic macromolecules of organic matrices and crystals. *Connect. Tissue Res.* 21, 127–34; discussion 135. Available at: http://www.ncbi.nlm.nih.gov/pubmed/2691196.

Addadi, L., and Weiner, S. (1985). Interactions between acidic proteins and crystals: stereochemical requirements in biomineralization. *Proc. Natl. Acad. Sci. U. S. A.* 82, 4110–4114. doi:10.1073/pnas.82.12.4110.

Al-Jawad, M., Fragneto, G., Liu, J., Chang, S. R., and Clarkson, B. (2009). Fibronectin adsorption studied using neutron reflectometry and complementary techniques. *Eur. Phys. J. E* 30, 175–179. doi:10.1140/epje/i2009-10472-0.

Al-Jawad, M., Steuwer, A., Kilcoyne, S. H., Shore, R. C., Cywinski, R., and Wood, D. J. (2007). 2D mapping of texture and lattice parameters of dental enamel. *Biomaterials* 28, 2908–14. doi:10.1016/j.biomaterials.2007.02.019.

Aparicio, C., Manero, J. M., Conde, F., Pegueroles, M., Planell, J. a, Vallet-Regí, M., et al. (2007). Acceleration of apatite nucleation on microrough bioactive titanium for bone-replacing implants. *J. Biomed. Mater. Res. A* 82, 521–9. doi:10.1002/jbm.a.31164.

Arnold, F. A., Dean, H. T., Jay, P., and Knutson, J. W. (1956). Effect of fluoridated public water supplies on dental caries prevalence. *Public Heal. reports (Washington, D.C. 1896)* 71, 652–8. Available at: http://www.pubmedcentral.nih.gov/articlerender.fcgi?artid=2031043&tool=pmc

entrez&rendertype=abstract.

Balz, M. H. M. (1999). Influence of Pellicle on Enamel Erosion. 372–379.

Banta, S., Wheeldon, I. R., and Blenner, M. (2010). Protein Engineering in the Development of Functional Hydrogels. *Annu. Rev. Biomed. Eng.* 12, 167–186. doi:10.1146/annurev-bioeng-070909-105334.

Bax, A., Szeverenyi, N. M., and Maciel, G. E. (1983). Correlation of isotropic shifts and chemical shift anisotropies by two-dimensional fourier-transform magic-angle hopping nmr spectroscopy. *J. Magn. Reson.* 52, 147–152. doi:10.1016/0022-2364(83)90267-6.

Beniash, E., Metzler, R. a., Lam, R. S. K., and Gilbert, P. U. P. a (2009). Transient amorphous calcium phosphate in forming enamel. *J. Struct. Biol.* 166, 133–143. doi:10.1016/j.jsb.2009.02.001.

Benning, K. (2014). CD Apps documentation. Available at: http://confluence.diamond.ac.uk/display/B23Tech/CD+Apps+documentation [Accessed September 14, 2017].

Berry, E. E., and Baddiel, C. B. C. (1967). Some assignments in the infra-red spectrum of octacalcium phosphate. *Spectrochim. Acta* 23, 1781–1792. doi:10.1016/0584-8539(67)80061-8.

Bessa, P. C., Machado, R., Nürnberger, S., Dopler, D., Banerjee, A., Cunha, A. M., et al. (2010). Thermoresponsive self-assembled elastin-based nanoparticles for delivery of BMPs. *J. Control. Release* 142, 312–318. doi:10.1016/j.jconrel.2009.11.003.

Blass, J., Köhler, O., Fingerle, M., Müller, C., and Ziegler, C. (2013). Properties and characteristics of wet (HF) and dry (RIE) etched borosilicate glass. *Phys. status solidi* 210, 988–993. doi:10.1002/pssa.201200769.

Boskey, A. L. (1997). Amorphous Calcium Phosphate: The Contention of Bone. *J.*

Dent. Res. 76, 1433–1436. doi:10.1177/00220345970760080501.

Brown, w. E., and Chow, L. C. (1973). Chemical properties of bone mineral. *Charact. Met. Alloy.*, 24–50.

Brown, W. E., Eidelman, N., and Tomazic, B. (1987). Octacalcium phosphate as a precursor in biomineral formation. *Adv. Dent. Res.* 1, 306–313. doi:10.1177/08959374870010022201.

Brown, W. E., Lehr, J. R., Smith, J. P., and Frazier, A. W. (1957). Crystallography of Octacalcium Phosphate. *J. Am. Chem. Soc.* 79, 5318–5319. doi:10.1021/ja01576a068.

Brown, W. E., Schroeder, L. W., and Ferris, J. S. (1979). Interlayering of crystalline octacalcium phosphate and hydroxylapatite. *J. Phys. Chem.* 83, 1385–1388. doi:10.1021/j100474a006.

Brundavanam, S., Eddy, G., Poinern, J., and Fawcett, D. (2014). Growth of Flower-Like Brushite Structures on Magnesium Substrates and Their Subsequent Low Temperature Transformation to Hydroxyapatite. *Am. J. Biomed. Eng.* 4, 79–87. doi:10.5923/j.ajbe.20140404.02.

Brunton, P. A., Davies, R. P. W., Burke, J. L., Smith, A., Aggeli, A., Brookes, S. J., et al. (2013). Treatment of early caries lesions using biomimetic self-assembling peptides--a clinical safety trial. *Br. Dent. J.* 215, E6. doi:10.1038/sj.bdj.2013.741.

Bumbrah, G. S., and Sharma, R. M. (2016). Raman spectroscopy – Basic principle, instrumentation and selected applications for the characterization of drugs of abuse. *Egypt. J. Forensic Sci.* 6, 209–215. doi:10.1016/j.ejfs.2015.06.001.

Bunn, C. W. (1949). Crystal growth from solution. II. Concentration gradients and the rates of growth of crystals. *Discuss. Faraday Soc.* 5, 132. doi:10.1039/df9490500132.

Calero, M., and Gasset, M. (2005). “Fourier Transform Infrared and Circular Dichroism Spectroscopies for Amyloid Studies,” in *Amyloid Proteins* (New Jersey: Humana Press), 129–152. doi:10.1385/1-59259-874-9:129.

Cambridge, U. of (2015). DoITPoMS - TLP Library Ferroelectric Materials - Order of phase transitions. Available at: https://www.doitpoms.ac.uk/tlplib/ferroelectrics/transitions.php [Accessed December 29, 2017].

Carneiro, K. M. M., Zhai, H., Zhu, L., Horst, J. A., Sitlin, M., Nguyen, M., et al. (2016). Amyloid-like ribbons of amelogenins in enamel mineralization. *Sci. Rep.* 6, 23105. doi:10.1038/srep23105.

Casciani, F., and Condrate, R. A. (1979). The Vibrational Spectra of Brushite, CaHPO4·2H2O. *Spectrosc. Lett.* 12, 699–713. doi:10.1080/00387017908069196.

Chen, H., Clarkson, B. H., Sun, K., and Mansfield, J. F. (2005). Self-assembly of synthetic hydroxyapatite nanorods into an enamel prism-like structure. *J. Colloid Interface Sci.* 288, 97–103. doi:10.1016/j.jcis.2005.02.064.

Chen, H., Sun, K., Tang, Z., Law, R. V, Mansfield, J. F., and Clarkson, B. H. (2006). Synthesis of Fluorapatite Nanorods and Nanowires by Direct Precipitation from Solution. *Cryst. Growth Des.* 6, 1504–1508. doi:10.1021/cg0600086.

Chen, P. H., Tseng, Y. H., Mou, Y., Tsai, Y. L., Guo, S. M., Huang, S. J., et al. (2008). Adsorption of a statherin peptide fragment on the surface of nanocrystallites of hydroxyapatite. *J. Am. Chem. Soc.* 130, 2862–2868. doi:10.1021/ja076607y.

Cho, Y., Zhang, Y., Christensen, T., Sagle, L. B., Chilkoti, A., and Cremer, P. S. (2008). Effects of hofmeister anions on the phase transition temperature of elastin-like polypeptides. *J. Phys. Chem. B* 112, 13765–13771.

doi:10.1021/jp8062977.

Chow, L. C., and Brown, W. E. (1973). Reaction of Dicalcium Phosphate Dihydrate with Fluoride. *J. Dent. Res.* 52, 1220–1227. doi:10.1177/00220345730520061001.

Chow, L. C., and Brown, W. E. (1975). Formation of CaHPO4-2H2O in tooth enamel as an intermediate product in topical fluoride treatments. *J. Dent. Res.* 54, 65–76. doi:10.1177/00220345750540013901.

Christoffersen, J., Christoffersen, M. R., Kibalczyc, W., and Perdok, W. G. (1988). Kinetics of dissolution and growth of calcium fluoride and effects of phosphate. *Acta Odontol. Scand.* 46, 325–36. doi:10.3109/00016358809004784.

Ciobanu, G., Carja, G., and Ciobanu, O. (2008). Structural characterization of hydroxyapatite layer coatings on titanium supports. *Surf. Coatings Technol.* 202, 2467–2470. doi:10.1016/j.surfcoat.2007.11.038.

Ciobanu, G., Carja, G., Ciobanu, O., Sandu, I., and Sandu, A. (2009). SEM and EDX studies of bioactive hydroxyapatite coatings on titanium implants. *Micron* 40, 143–146. doi:10.1016/j.micron.2007.11.011.

Cirulis, J. T., and Keeley, F. W. (2010). Kinetics and morphology of self-assembly of an elastin-like polypeptide based on the alternating domain arrangement of human tropoelastin. *Biochemistry* 49, 5726–5733. doi:10.1021/bi100468v.

Cojocari, D. (2016). Amino Acids. Available at: https://en.wikiversity.org/wiki/Amino_acids [Accessed August 31, 2017].

Combes, C., and Rey, C. (2010). Amorphous calcium phosphates: Synthesis, properties and uses in biomaterials. *Acta Biomater.* 6, 3362–3378. doi:10.1016/j.actbio.2010.02.017.

Crane, N. J., Popescu, V., Morris, M. D., Steenhuis, P., and Ignelzi, M. A. (2006). Raman spectroscopic evidence for octacalcium phosphate and other transient mineral species deposited during intramembranous mineralization. *Bone* 39, 434–442. doi:10.1016/j.bone.2006.02.059.

Cuisinier, F. J. G., Steuer, P., Senger, B., Voegel, J. C., and Frank, R. M. (1992). Human amelogenesis I: High resolution electron microscopy study of ribbon-like crystals. *Calcif. Tissue Int.* 51, 259–268. doi:10.1007/BF00334485.

Cuy, J. L., Mann, A. B., Livi, K. J., Teaford, M. F., and Weihs, T. P. (2002). Nanoindentation mapping of the mechanical properties of human molar tooth enamel. *Arch. Oral Biol.* 47, 281–291. doi:10.1016/S0003-9969(02)00006-7.

Czajka-Jakubowska, A. E., Liu, J., Chang, S.-R., and Clarkson, B. H. (2009). The effect of the surface characteristics of various substrates on fluorapatite crystal growth, alignment, and spatial orientation. *Med. Sci. Monit.* 15, MT84-8. Available at: http://www.ncbi.nlm.nih.gov/pubmed/19478709.

Daculsi, G. (1998). Biphasic calcium phosphate concept applied to artificial bone, implant coating and injectable bone substitute. *Biomaterials* 19, 1473–1478. doi:10.1016/S0142-9612(98)00061-1.

Dandurand, J., Samouillan, V., Lacabanne, C., Pepe, A., and Bochicchio, B. (2015). Water structure and elastin-like peptide aggregation: A differential calorimetric approach. *J. Therm. Anal. Calorim.* 120, 419–426. doi:10.1007/s10973-014-4254-9.

Dash, B. C., Mahor, S., Carroll, O., Mathew, A., Wang, W., Woodhouse, K. A., et al. (2011). Tunable elastin-like polypeptide hollow sphere as a high payload and controlled delivery gene depot. *J. Control. Release* 152, 382–392. doi:10.1016/j.jconrel.2011.03.006.

Deakins, M., and Volker, J. F. (1941). Amount of Organic Matter in Enamel From Several Types of Human Teeth. *J. Dent. Res.* 20, 117–121. doi:10.1177/00220345410200020201.

Demichelis, R., Raiteri, P., Gale, J. D., Quigley, D., and Gebauer, D. (2011). Stable prenucleation mineral clusters are liquid-like ionic polymers. *Nat. Commun.* 2, 590. doi:10.1038/ncomms1604.

Dey, A., Bomans, P. H., Muller, F. A., Will, J., Frederik, P. M., de With, G., et al. (2010). The role of prenucleation clusters in surface-induced calcium phosphate crystallization. *Nat. Mater.* 9, 1010–1014. doi:10.1038/nmat2900.

Donnelly, E., and Boskey, A. L. (2011). “Mineralization,” in *Vitamin D* (Elsevier), 381–401. doi:10.1016/B978-0-12-381978-9.10021-6.

Dorozhkin, S. V. (2010). Amorphous calcium (ortho)phosphates. *Acta Biomater.* 6, 4457–4475. doi:10.1016/j.actbio.2010.06.031.

Dorozhkin, S. V. (2011). Calcium orthophosphates. *Biomatter* 1, 121–164. doi:10.4161/biom.18790.

Dorozhkin, S. V. (2013). Calcium orthophosphates in dentistry. *J. Mater. Sci. Mater. Med.* 24, 1335–1363. doi:10.1007/s10856-013-4898-1.

Dorozhkin, S. V., and Epple, M. (2002). Biological and medical significance of calcium phosphates. *Angew. Chemie - Int. Ed.* 41, 3130–3146. doi:10.1002/1521-3773(20020902)41:17<3130::AID-ANIE3130>3.0.CO;2-1.

Dosen, A., and Giese, R. F. (2011). Thermal decomposition of brushite, CaHPO4.2H2O to monetite CaHPO4 and the formation of an amorphous phase. *Am. Mineral.* 96, 368–373. doi:10.2138/am.2011.3544.

Drouet, C. (2013). Apatite formation: Why it may not work as planned, and how to conclusively identify apatite compounds. *Biomed Res. Int.* 2013. doi:10.1155/2013/490946.

Drouet, C., Bosc, F., Banu, M., Largeot, C., Combes, C., Dechambre, G., et al. (2009). Nanocrystalline apatites: From powders to biomaterials. *Powder Technol.* 190, 118–122. doi:10.1016/j.powtec.2008.04.041.

Dunne, C. F., Twomey, B., Kelly, C., Simpson, J. C., and Stanton, K. T. (2015). Hydroxyapatite and fluorapatite coatings on dental screws: effects of blast coating process and biological response. *J. Mater. Sci. Mater. Med.* 26, 5347. doi:10.1007/s10856-014-5347-5.

Eanes, E. D., Gillessen, I. H., and Posner, A. S. (1965). Intermediate States in the Precipitation of Hydroxyapatite. *Nature* 208, 365–367. doi:10.1038/208365a0.

Efimenko, K., Wallace, W. E., and Genzer, J. (2002). Surface Modification of Sylgard-184 Poly(dimethyl siloxane) Networks by Ultraviolet and Ultraviolet/Ozone Treatment. *J. Colloid Interface Sci.* 254, 306–315. doi:10.1006/jcis.2002.8594.

Eichert, D., Sfihi, H., Combes, C., and Rey, C. (2004). Specific characteristics of wet nanocrystalline apatites. Consequences on biomaterials and bone tissue. *Bioceram. Vol 16* 254–2, 927–930. doi:10.4028/www.scientific.net/KEM.254-256.927.

Elliott, J. C. (1994). *Structure and Chemistry of the Apatites and Other Calcium Orthophosphates*. Amsterdam: Elsevier.

Elsharkawy, S., Al-Jawad, M., Agarwal, S., Tejeda-Montes, E., Shuturminska, K., Sanchez, R., et al. (2016a). 1006 - Fabrication of Hierarchically-ordered Enamel-like Crystals for Novel Dental Restorative Materials. in *35th Annual Meeting of the IADR Korean Division* (Seol, Republic of Korea).

Elsharkawy, S., Tejeda-Montes, E., Al-Jawad, M., and Mata, A. (2016b). Preferential nucleation and crystal growth on microfabricated topography. *Mater. Today* 19, 478–480. doi:10.1016/j.mattod.2016.08.002.

Enax, J., Prymak, O., Raabe, D., and Epple, M. (2012). Structure, composition, and mechanical properties of shark teeth. *J. Struct. Biol.* 178, 290–299. doi:10.1016/j.jsb.2012.03.012.

Espanol, M., Portillo, J., Manero, J.-M., and Ginebra, M.-P. (2010). Investigation of the hydroxyapatite obtained as hydrolysis product of α-tricalcium phosphate by transmission electron microscopy. *CrystEngComm* 12, 3318. doi:10.1039/c001754j.

Fang, P.-A., Margolis, H. C., Conway, J. F., Simmer, J. P., and Beniash, E. (2013). CryoTEM study of effects of phosphorylation on the hierarchical assembly of porcine amelogenin and its regulation of mineralization in vitro. *J. Struct. Biol.* 183, 250–7. doi:10.1016/j.jsb.2013.05.011.

Ferguson, V. L., Boyde, A., and Bushby, A. J. (2004). Elastic modulus of dental enamel: effect of enamel prism orientation and mineral content. *MRS Proc.* 841, R2.7/Y2.7. doi:10.1557/PROC-841-R2.7/Y2.7.

Firth, A., Aggeli, A., Burke, J. L., Yang, X., and Kirkham, J. (2006). Biomimetic self-assembling peptides as injectable scaffolds for hard tissue engineering. *Nanomedicine (Lond).* 1, 189–99. doi:10.2217/17435889.1.2.189.

Fowler, B. O., Markovic, M., and Brown, W. E. (1993). Octacalcium Phosphate .3. Infrared and Raman Vibrational-Spectra. *Chem. Mater.* 5, 1417–1423. doi:10.1021/cm00034a009.

Fujita, Y., Mie, M., and Kobatake, E. (2009). Construction of nanoscale protein particle using temperature-sensitive elastin-like peptide and polyaspartic acid chain. *Biomaterials* 30, 3450–3457. doi:10.1016/j.biomaterials.2009.03.012.

Ganss, C., Klimek, J., and Schaffer, U. (1998). Effect of remineralisation and additional fluoridation measures on dental erosion progression in vitro. *Caries Res.* 32, 312.

Gericke, a, Qin, C., Sun, Y., Redfern, R., Redfern, D., Fujimoto, Y., et al. (2010). Different forms of DMP1 play distinct roles in mineralization. *J. Dent. Res.* 89, 355–9. doi:10.1177/0022034510363250.

Gerould, C. H. (1945). Electron microscope study of the mechanism of fluorine deposition in teeth. *J. Dent. Res.* 24, 223–33. doi:10.1177/00220345450240050201.

Gibbs, J. W. (1876). On the Equilibrium of Heterogeneous Substances. *Trans. Connect. Acad.* 3, 108-248-524. doi:10.2475/ajs.s3-16.96.441.

Giocondi, J. L., El-Dasher, B. S., Nancollas, G. H., and Orme, C. a (2010). Molecular mechanisms of crystallization impacting calcium phosphate cements. *Philos. Trans. A. Math. Phys. Eng. Sci.* 368, 1937–1961. doi:10.1098/rsta.2010.0006.

Girotti, A., and Reguera, J. (2004). Design and bioproduction of a recombinant multi (bio) functional elastin-like protein polymer containing cell adhesion sequences for tissue engineering purposes. *J. Mater. ...* 5, 479–484. Available at: http://link.springer.com/article/10.1023/B:JMSM.0000021124.58688.7a [Accessed November 13, 2014].

Girotti, A., Reguera, J., Arias, F. J., Alonso, M., Testera, A. M., and Rodríguez-Cabello, J. C. (2004a). Influence of the molecular weight on the inverse temperature transition of a model genetically engineered elastin-like pH-responsive polymer. *Macromolecules* 37, 3396–3400. doi:10.1021/ma035603k.

Girotti, A., Reguera, J., Rodríguez-Cabello, J. C., Arias, F. J., Alonso, M., and Testera, A. M. (2004b). Design and bioproduction of a recombinant multi(bio)functional elastin-like protein polymer containing cell adhesion sequences for tissue engineering purposes. *J. Mater. Sci. Mater. Med.* 15, 479–484. doi:10.1023/B:JMSM.0000021124.58688.7a.

Goobes, G., Stayton, P. S., and Drobny, G. P. (2007a). Solid state NMR studies of molecular recognition at protein-mineral interfaces. *Prog. Nucl. Magn. Reson. Spectrosc.* 50, 71–85. doi:10.1016/j.pnmrs.2006.11.002.

Goobes, R., Goobes, G., Campbell, C. T., and Stayton, P. S. (2006). Thermodynamics of statherin adsorption onto hydroxyapatite. *Biochemistry* 45, 5576–5586. doi:10.1021/bi052321z.

Goobes, R., Goobes, G., Shaw, W. J., Drobny, G. P., Campbell, C. T., and Stayton, P. S. (2007b). Thermodynamic roles of basic amino acids in statherin recognition of hydroxyapatite. *Biochemistry* 46, 4725–4733. doi:10.1021/bi602345a.

Gower, L. B. (2008). Biomimetic Model Systems for Investigating the Amorphous Precursor Pathway and Its Role in Biomineralization. *Chem. Rev.* 108, 4551–4627. doi:10.1021/cr800443h.

Gower, L. B., and Odom, D. J. (2000). Deposition of calcium carbonate films by a polymer-induced liquid-precursor (PILP) process. *J. Cryst. Growth* 210, 719–734. doi:10.1016/S0022-0248(99)00749-6.

Greenfield, N. J. (2006). Using circular dichroism spectra to estimate protein secondary structure. *Nat. Protoc.* 1, 2876–2890. doi:10.1038/nprot.2006.202.Using.

Guo, C., Campbell, B. E., Chen, K., Lenhoff, A. M., and Velev, O. D. (2003). Casein precipitation equilibria in the presence of calcium ions and phosphates. *Colloids Surfaces B Biointerfaces* 29, 297–307. doi:10.1016/S0927-7765(03)00018-3.

Habelitz, S., Marshall, S. J., MarshallJr, G. W., and Balooch, M. (2001). Mechanical properties of human dental enamel on the nanometre scale. *Arch. Oral Biol.* 46, 173–183. Available at: http://www.sciencedirect.com/science/article/B6T4J-4233N49-9/2/6340f6089472f11ad8a819587bb083d6.

Habraken, W. J. E. M., Tao, J., Brylka, L. J., Friedrich, H., Bertinetti, L., Schenk, A. S., et al. (2013). Ion-association complexes unite classical and non-classical theories for the biomimetic nucleation of calcium phosphate. *Nat. Commun.* 4, 1507. doi:10.1038/ncomms2490.

Halverson, K. J., Sucholeiki, I., Ashburn, T. T., and Lansbury, P. T. (1991). Location of beta-sheet-forming sequences in amyloid proteins by FTIR. *J. Am. Chem. Soc.* 113, 6701–6703. doi:10.1021/ja00017a068.

Hamm, L. M., Giuffre, A. J., Han, N., Tao, J., Wang, D., De Yoreo, J. J., et al. (2014). Reconciling disparate views of template-directed nucleation through measurement of calcite nucleation kinetics and binding energies. *Proc. Natl. Acad. Sci.* 111, 1304–1309. doi:10.1073/pnas.1312369111.

Hassan, P. a, Rana, S., and Verma, G. (2015). Making sense of brownian motion: colloid characterization by dynamic light scattering. *Langmuir* 31, 3–12. doi:10.1021/la501789z.

Hassouneh, W., Nunalee, M. L., Shelton, M. C., and Chilkoti, A. (2013). Calcium binding peptide motifs from calmodulin confer divalent ion selectivity to elastin-like polypeptides. *Biomacromolecules* 14, 2347–2353. doi:10.1021/bm400464s.

Herrero-Vanrell, R., Rincón, A. C., Alonso, M., Reboto, V., Molina-Martinez, I. T., and Rodríguez-Cabello, J. C. (2005). Self-assembled particles of an elastin-like polymer as vehicles for controlled drug release. *J. Control. Release* 102, 113–122. doi:10.1016/j.jconrel.2004.10.001.

Hillson, S. (2005). *Teeth*. 2nd ed. New York: Cambridge University Press.

Hofmeister, F. (1888). Zur Lehre von der Wirkung der Salze - Zweite Mittheilung. *Arch. f??r Exp. Pathol. und Pharmakologie* 24, 247–260. doi:10.1007/BF01918191.

Hunter, G. K., Kyle, C. L., and Goldberg, H. a (1994). Modulation of crystal formation by bone phosphoproteins: structural specificity of the osteopontin-mediated inhibition of hydroxyapatite formation. *Biochem. J.* 300 (Pt 3, 723–728.

Iijima, M., Fan, D., Bromley, K. M., Sun, Z., and Moradian-Oldak, J. (2010). Tooth enamel proteins enamelin and amelogenin cooperate to regulate the growth morphology of octacalcium phosphate crystals. *Cryst. Growth Des.* 10, 4815–4822. doi:10.1021/cg100696r.

Johnsson, M., Richardson, C. F., Bergey, E. J., Levine, M. J., and Nancollas, G. H. (1991). The effects of human salivary cystatins and statherin on hydroxyapatite crystallization. *Arch. Oral Biol.* 36, 631–6. doi:10.1016/0003-9969(91)90014-L.

Johnsson, M. S.-A., and Nancollas, G. H. (1992a). The Role of Brushite and Octacalcium Phosphate in Apatite Formation. *Crit. Rev. Oral Biol. Med.* 3, 61–82. doi:10.1177/10454411920030010601.

Johnsson, M. S., and Nancollas, G. H. (1992b). The Role of Brushite and Octacalcium Phosphate in Apatite Formation. 3, 61–82.

Jordan, S. W., and Chaikof, E. L. (2007). Novel thromboresistant materials. *J. Vasc. Surg.* 45, 104–115. doi:10.1016/j.jvs.2007.02.048.

Kakei, M., Sakae, T., and Yoshikawa, M. (2009). Electron microscopy of octacalcium phosphate in the dental calculus. *J. Electron Microsc. (Tokyo).* 58, 393–398. doi:10.1093/jmicro/dfp034.

Kashchiev, D. (2000). *Nucleation: Basic Theory with Applications*. Oxford: Butterworth Heinemann.

Kawasaki, K., and Weiss, K. M. (2003). Mineralized tissue and vertebrate evolution: the secretory calcium-binding phosphoprotein gene cluster. *Proc. Natl. Acad. Sci. U. S. A.* 100, 4060–4065. doi:10.1073/pnas.0638023100.

Kawasaki, K., and Weiss, K. M. (2006). Evolutionary genetics of vertebrate tissue mineralization: The origin and evolution of the secretory calcium-binding phosphoprotein family. *J. Exp. Zool. Part B Mol. Dev. Evol.* 306, 295–316. doi:10.1002/jez.b.21088.

Kherb, J., Flores, S. C., and Cremer, P. S. (2012). Role of carboxylate side chains in the cation hofmeister series. *J. Phys. Chem. B* 116, 7389–7397.

doi:10.1021/jp212243c.

Kim, J. H., Kim, S. H., Kim, H. K., Akaike, T., and Kim, S. C. (2002). Synthesis and characterization of hydroxyapatite crystals: A review study on the analytical methods. *J. Biomed. Mater. Res.* 62, 600–612. doi:10.1002/jbm.10280.

Kim, W., and Chaikof, E. L. (2010). Recombinant elastin-mimetic biomaterials: Emerging applications in medicine. *Adv. Drug Deliv. Rev.* 62, 1468–1478. doi:10.1016/j.addr.2010.04.007.

Kirkham, J., Firth, A., Vernals, D., Boden, N., Robinson, C., Shore, R. C., et al. (2007). Self-assembling peptide scaffolds promote enamel remineralization. *J. Dent. Res.* 86, 426–430. doi:10.1177/154405910708600507.

Kiss, E. (1993). Temperature dependence of bovine serum albumin adsorption onto a poly (ethylene oxide)-grafted surface. *Colloids Surf. A. Physicochem. Eng. Asp.* 76, 135–140. Available at: http://www.sciencedirect.com/science/article/pii/092777579380071L.

Kokubo, T., Kawashita, M., and Nakamura, T. (2004). Bioactive metals : preparation and properties. 5, 99–107.

Kowalczyk, T., Hnatuszko-Konka, K., Gerszberg, A., and Kononowicz, A. K. (2014). Elastin-like polypeptides as a promising family of genetically-engineered protein based polymers. *World J. Microbiol. Biotechnol.* 30, 2141–2152. doi:10.1007/s11274-014-1649-5.

Kozel, B. A., Rongish, B. J., Czirok, A., Zach, J., Little, C. D., Davis, E. C., et al. (2006). Elastic fiber formation: A dynamic view of extracellular matrix assembly using timer reporters. *J. Cell. Physiol.* 207, 87–96. doi:10.1002/jcp.20546.

Kumar, M., Dasarathy, H., and Riley, C. (1999). Electrodeposition of brushite coatings and their transformation to hydroxyapatite in aqueous solutions. *J.*

Biomed. Mater. Res. 45, 302–10. doi:10.1002/(SICI)1097-4636(19990615)45:4<302::AID-JBM4>3.0.CO;2-A.

Kwak, S.-Y., Green, S., Wiedemann-Bidlack, F. B., Beniash, E., Yamakoshi, Y., Simmer, J. P., et al. (2011). Regulation of calcium phosphate formation by amelogenins under physiological conditions. *Eur. J. Oral Sci.* 119 Suppl, 103–11. doi:10.1111/j.1600-0722.2011.00911.x.

Lacruz, R. S., Nanci, A., Kurtz, I., Wright, J. T., and Paine, M. L. (2010). Regulation of pH during amelogenesis. *Calcif. Tissue Int.* 86, 91–103. doi:10.1007/s00223-009-9326-7.

Le Norcy, E., Kwak, S.-Y., Allaire, M., Fratzl, P., Yamakoshi, Y., Simmer, J. P., et al. (2011a). Effect of phosphorylation on the interaction of calcium with leucine-rich amelogenin peptide. *Eur. J. Oral Sci.* 119, 97–102. doi:10.1111/j.1600-0722.2011.00900.x.

Le Norcy, E., Kwak, S.-Y., Wiedemann-Bidlack, F. B., Beniash, E., Yamakoshi, Y., Simmer, J. P., et al. (2011b). Potential role of the amelogenin N-terminus in the regulation of calcium phosphate formation in vitro. *Cells. Tissues. Organs* 194, 188–93. doi:10.1159/000324827.

Lee, S. H., and Ruckenstein, E. (1988). Adsorption of proteins onto polymeric surfaces of different hydrophilicities - a case study with bovine serum albumin. *J. Colloid Interface Sci.* 125, 365–379. doi:10.1016/0021-9797(88)90001-X.

LeGeros, R. Z., and LeGeros, J. P. (1972). Brushite crystals grown by diffusion in silica gel and in solution. *J. Cryst. Growth* 13–14, 476–480. doi:10.1016/0022-0248(72)90284-9.

Lenk, T. J., Horbett, T. a, Ratner, B. D., and Chittur, K. K. (1991). Infrared Spectroscopic Studies of Time-Dependent Changes in Fibrinogen Adsorbed To Polyurethanes. *Langmuir* 7, 1755–1764. doi:10.1021/la00056a030.

Levitt, S., and Condrate, R. (1970). The Polarized Infrared Spectra of Hydroxyl Ion in Fluorapatite. *Appl. Spectrosc.* 24, 288*289.

Li, B., Alonso, D. O. ., and Daggett, V. (2001). The molecular basis for the inverse temperature transition of elastin. *J. Mol. Biol.* 305, 581–592. doi:10.1006/jmbi.2000.4306.

Li, H., Huang, W., Zhang, Y., and Zhong, M. (2007). Biomimetic synthesis of enamel-like hydroxyapatite on self-assembled monolayers. *Mater. Sci. Eng. C* 27, 756–761. doi:10.1016/j.msec.2006.08.002.

Li, Y., Chen, X., Fok, A., Rodriguez-Cabello, J. C., and Aparicio, C. (2015). Biomimetic Mineralization of Recombinamer-Based Hydrogels toward Controlled Morphologies and High Mineral Density. *ACS Appl. Mater. Interfaces* 7, 25784–25792. doi:10.1021/acsami.5b07628.

Mann, A. B., and Dickinson, M. E. (2006). Nanomechanics, chemistry and structure at the enamel surface. *Monogr. Oral Sci.* 19, 105–31. doi:10.1159/000090588.

Mann, S. (1983). Mineralization in biological systems. *Inorg. Elem. Biochem.*, 125–174. doi:10.1007/BFb0111316.

Mann, S. (1993). Molecular tectonics in biomineralization and biomimetic materials chemistry. *Nature* 365, 499–505. doi:10.1038/365499a0.

Mann, S. (2001). *Biomineralization: Principles and Concepts in Bioinorganic Materials Chemistry*. Oxford: Oxford University Press.

Margolis, H. C., Kwak, S.-Y., and Yamazaki, H. (2014). Role of mineralization inhibitors in the regulation of hard tissue biomineralization: relevance to initial enamel formation and maturation. *Front. Physiol.* 5, 339. doi:10.3389/fphys.2014.00339.

Marshall, D. B., Noma, T., and Evans, A. G. (1982). A Simple Method for Determining Elastic- Modulus–to- Hardness Ratios using Knoop Indentation

Measurements. *J. Am. Ceram. Soc.* 65, c175–c176. doi:10.1111/j.1151-2916.1982.tb10357.x.

Mathew, M., Brown, W. E., Schroeder, L. W., and Dickens, B. (1988). Crystal structure of octacalcium bis(hydrogenphosphate) tetrakis(phosphate)pentahydrate, Ca8(HP04)2(PO4)4.5H2O. *J. Crystallogr. Spectrosc. Res.* 18, 235–250. doi:10.1007/BF01194315.

McDaniel, J. R., Callahan, D. J., and Chilkoti, A. (2010). Drug delivery to solid tumors by elastin-like polypeptides. *Adv. Drug Deliv. Rev.* 62, 1456–1467. doi:10.1016/j.addr.2010.05.004.

Meyer, D. E., and Chilkoti, A. (2004). Quantification of the effects of chain length and concentration on the thermal behavior of elastin-like polypeptides. *Biomacromolecules* 5, 846–851. doi:10.1021/bm034215n.

Misbah, M. H., Espanol, M., Quintanilla, L., Ginebra, M. P., and Rodríguez-Cabello, J. C. (2016). Formation of calcium phosphate nanostructures under the influence of self-assembling hybrid elastin-like-statherin recombinamers. *RSC Adv.* 6, 31225–31234. doi:10.1039/C6RA01100D.

Miyazawa, T., and Blout, E. R. (1961). The Infrared Spectra of Polypeptides in Various Conformations: Amide I and II Bands. *J. Am. Chem. Soc.* 83, 712–719. doi:10.1021/ja01464a042.

Mohammed, N. R., Kent, N. W., Lynch, R. J. M., Karpukhina, N., Hill, R., and Anderson, P. (2013). Effects of fluoride on in vitro enamel demineralization analyzed by 19F MAS-NMR. *Caries Res.* 47, 421–428. doi:10.1159/000350171.

Mohammed, N. R., Lynch, R. J. M., and Anderson, P. (2014). Effects of fluoride concentration on enamel demineralization kinetics in vitro. *J. Dent.* 42, 613–618. doi:10.1016/j.jdent.2013.12.005.

Moradian-Oldak, J., and Paine, M. L. (2010). *Mammalian Enamel Formation*.

doi:10.1002/9780470986325.ch15.

Moscarelli, P., Boraldi, F., Bochicchio, B., Pepe, A., Salvi, A. M., and Quaglino, D. (2014). Structural characterization and biological properties of the amyloidogenic elastin-like peptide (VGGVG)3. *Matrix Biol.* 36, 15–27. doi:10.1016/j.matbio.2014.03.004.

Mukherjee, K., Ruan, Q., Liberman, D., White, S. N., and Moradian-Oldak, J. (2016). Repairing human tooth enamel with leucine-rich amelogenin peptide–chitosan hydrogel. *J. Mater. Res.*, 1–8. doi:10.1557/jmr.2016.64.

Nagapudi, K., Brinkman, W. T., Leisen, J. E., Huang, L., McMillan, R. A., Apkarian, R. P., et al. (2002). Photomediated solid-state cross-linking of an elastin-mimetic recombinant protein polymer. *Macromolecules* 35, 1730–1737. doi:10.1021/ma011429t.

Ndao, M., Ash, J. T., Breen, N. F., Goobes, G., Stayton, P. S., and Drobny, G. P. (2009). A 13 C{ 31 P} REDOR NMR Investigation of the Role of Glutamic Acid Residues in Statherin- Hydroxyapatite Recognition. *Langmuir* 25, 12136–12143. doi:10.1021/la901647n.

Ndao, M., Ash, J. T., Stayton, P. S., and Drobny, G. P. (2010). The role of basic amino acids in the molecular recognition of hydroxyapatite by statherin using solid state NMR. *Surf. Sci.* 604, L39–L42. doi:10.1016/j.susc.2010.02.026.

Norde, W. (1986). Adsorption of proteins from solution at the solid-liquid interface. *Adv. Colloid Interface Sci.* 25, 267–340. Available at: http://www.ncbi.nlm.nih.gov/pubmed/3333131.

Norde, W., and Favier, J. P. (1992). Structure of adsorbed and desorbed proteins. *Colloids and Surfaces* 64, 87–93. doi:10.1016/0166-6622(92)80164-W.

Norde, W., MacRitchie, F., Nowicka, G., and Lyklema, J. (1986). Protein adsorption at solid-liquid interfaces: Reversibility and conformation aspects. *J. Colloid*

Interface Sci. 112, 447–456. doi:10.1016/0021-9797(86)90113-X.

Olszta, M. J., Odom, D. J., Douglas, E. P., and Gower, L. B. (2003). A New Paradigm for Biomineral Formation: Mineralization via an Amorphous Liquid-Phase Precursor. *Connect. Tissue Res.* 44, 326–334. doi:10.1080/03008200390181852.

Onuma, K., and Ito, A. (1998). Cluster Growth Model for Hydroxyapatite. *Chem. Mater.* 10, 3346–3351. doi:10.1021/cm980062c.

OriginLAB (2017). Chapter 16: Curve Fitting. Available at: http://www.originlab.com/pdfs/16_CurveFitting.pdf [Accessed August 25, 2017].

Pan, H. B., and Darvell, B. W. (2007). Solubility of calcium fluoride and fluorapatite by solid titration. *Arch. Oral Biol.* 52, 861–868. doi:10.1016/j.archoralbio.2007.03.002.

Park, W. M., and Champion, J. A. (2014). Thermally triggered self-assembly of folded proteins into vesicles. *J. Am. Chem. Soc.* 136, 17906–17909. doi:10.1021/ja5090157.

Perczel, A., and Fasman, G. D. (2008). Quantitative analysis of cyclic B-turn models. *Protein Sci.* 1, 378–395. doi:10.1002/pro.5560010310.

Posner, A. S., Betts, F., and Blumenthal, N. C. (1980). Formation and structure of synthetic and bone hydroxyapatites. *Prog. Cryst. Growth Charact.* 3, 49–64. doi:10.1016/0146-3535(80)90011-8.

Posner, A. S., and Perloff, A. (1957). Apatites Deficient in Divalent Cations. *J. Res. Natl. Bur. Stand. (1934).* 58, 279–286.

Prieto, S., Shkilnyy, A., Rumplasch, C., Ribeiro, A., Arias, F. J., Rodríguez-Cabello, J. C., et al. (2011). Biomimetic calcium phosphate mineralization with multifunctional elastin-like recombinamers. *Biomacromolecules* 12, 1480–6.

doi:10.1021/bm200287c.

Raj, P. A., Johnsson, M., Levine, M. J., and Nancollas, G. H. (1992). Salivary statherin. Dependence on sequence, charge, hydrogen bonding potency, and helical conformation for adsorption to hydroxyapatite and inhibition of mineralization. *J. Biol. Chem.* 267, 5968–76. Available at: http://www.jbc.org/content/267/9/5968.short [Accessed November 7, 2014].

Raphel, J., Karlsson, J., Galli, S., Wennerberg, A., Lindsay, C., Haugh, M. G., et al. (2016). Engineered protein coatings to improve the osseointegration of dental and orthopaedic implants. *Biomaterials* 83, 269–282. doi:10.1016/j.biomaterials.2015.12.030.

Reguera, J., Urry, D. W., Parker, T. M., McPherson, D. T., and Rodríguez-Cabello, J. C. (2007). Effect of NaCl on the exothermic and endothermic components of the inverse temperature transition of a model elastin-like polymer. *Biomacromolecules* 8, 354–358. doi:10.1021/bm060936l.

Reiersen, H., Clarke, a R., and Rees, a R. (1998). Short elastin-like peptides exhibit the same temperature-induced structural transitions as elastin polymers: implications for protein engineering. *J. Mol. Biol.* 283, 255–64. doi:10.1006/jmbi.1998.2067.

Ren, D., Ruan, Q., Tao, J., Lo, J., Nutt, S., and Moradian-Oldak, J. (2016). Amelogenin Affects Brushite Crystal Morphology and Promotes Its Phase Transformation to Monetite. *Cryst. Growth Des.*, acs.cgd.6b00569. doi:10.1021/acs.cgd.6b00569.

Rey, C., Combes, C., Drouet, C., and Glimcher, M. J. (2009). Bone mineral: Update on chemical composition and structure. *Osteoporos. Int.* 20, 1013–1021. doi:10.1007/s00198-009-0860-y.

Rey, C., Combes, C., Drouet, C., Lebugle, A., Sfihi, H., and Barroug, A. (2007a).

Nanocrystalline apatites in biological systems: Characterisation, structure and properties. *Materwiss. Werksttech.* 38, 996–1002. doi:10.1002/mawe.200700229.

Rey, C., Combes, C., Drouet, C., Sfihi, H., and Barroug, A. (2007b). Physico-chemical properties of nanocrystalline apatites: Implications for biominerals and biomaterials. *Mater. Sci. Eng. C* 27, 198–205. doi:10.1016/j.msec.2006.05.015.

Robinson, C. (2007). Self-oriented Assembly of Nano-apatite Particles: a Subunit Mechanism for Building Biological Mineral Crystals. *J. Dent. Res.* 86, 677–679. doi:10.1177/154405910708600801.

Robinson, C., Connell, S., Brookes, S. J., Kirkham, J., Shore, R. C., and Smith, D. A. M. (2005). Surface chemistry of enamel apatite during maturation in relation to pH: Implications for protein removal and crystal growth. *Arch. Oral Biol.* 50, 267–270. doi:10.1016/j.archoralbio.2004.11.017.

Robinson, C., Kirkham, J., and Shore, R. (1995). *Chemistry of Mature Enamel in Dental Enamel: Formation to Destruction*. CRC Press.

Robinson, C., Weatherell, J. A., and Hallsworth, A. S. (1981). Distribution of magnesium in mature human enamel. *Caries Res.* 15, 70–77. doi:10.1159/000260502.

Rodriguez-Cabello, J. (2004). *Biomaterials.* , eds. N. Hasirci and V. Hasirci Boston, MA: Springer US doi:10.1007/978-0-306-48584-8.

Rodríguez-Cabello, J. C., Prieto, S., Reguera, J., Arias, F. J., and Ribeiro, A. (2007). Biofunctional design of elastin-like polymers for advanced applications in nanobiotechnology. *J. Biomater. Sci. Polym. Ed.* 18, 269–286. doi:10.1163/156856207779996904.

Sainz-Díaz, C. I., Villacampa, A., and Otálora, F. (2004). Crystallographic properties of the calcium phosphate mineral, brushite, by means of First Principles calculations. *Am. Mineral.* 89, 307–313. doi:10.2138/am-2004-2-308.

Sarem, M., and Lüdeke, S. (2015). Circular dichroism: A powerful tool for studying biomineralization promoter proteins. *MRS Bull.* 40, 490–498. doi:10.1557/mrs.2015.116.

Sasaki, S., and Shimokawa, H. (1995). The amelogenin gene. *Int. J. Dev. Biol.* 39, 127–133.

Sato, F., Wachi, H., Ishida, M., Nonaka, R., Onoue, S., Urban, Z., et al. (2007). Distinct Steps of Cross-linking, Self-association, and Maturation of Tropoelastin Are Necessary for Elastic Fiber Formation. *J. Mol. Biol.* 369, 841–851. doi:10.1016/j.jmb.2007.03.060.

Schmitt, L., Lurtz, C., Behrend, D., and Schmitz, K.-P. (2009). "Registered Microhardness of human teeth parts and dental filling composites," in *4th European Conference of the International Federation for Medical and Biological Engineering: ECIFMBE 2008 23--27 November 2008 Antwerp, Belgium*, eds. J. Vander Sloten, P. Verdonck, M. Nyssen, and J. Haueisen (Berlin, Heidelberg: Springer Berlin Heidelberg), 2252–2254. doi:10.1007/978-3-540-89208-3_539.

Selvig, K. A., and Halse, A. (1972). Mineral content and crystal size in mature rat incisor enamel. A correlated electron microprobe and electron microscope study. *J. Ultrasructure Res.* 40, 527–531. doi:10.1016/S0022-5320(72)80040-6.

Serrano, V., Liu, W., and Franzen, S. (2007). An Infrared Spectroscopic Study of the Conformational Transition of Elastin-Like Polypeptides. *Biophys. J.* 93, 2429–2435. doi:10.1529/biophysj.106.100594.

Shellis, R. P., Heywood, B. R., and Wahab, F. K. (1997). Formation of Brushite, Monetite and Whitlockite during Equilibration of Human Enamel with Acid Solutions at37C. *Caries Res.* 31, 71–77. doi:10.1159/000262377.

Shen, X., Shamshina, J. L., Berton, P., Gurau, G., and Rogers, R. D. (2016). Hydrogels based on cellulose and chitin: fabrication, properties, and applications. *Green Chem.* 18, 53–75. doi:10.1039/C5GC02396C.

Shi, J., Gao, Y., Zhang, Y., Pan, Y., and Xu, B. (2011). Calcium Ions to Cross-Link Supramolecular Nanofibers to Tune the Elasticity of Hydrogels over Orders of Magnitude. *Langmuir* 27, 14425–14431. doi:10.1021/la2033862.

Shirahama, H., and Suzawa, T. (1985). Adsorption of bovine serum albumin onto styrene/2-hydroxyethyl methacrylate copolymer latex. *J. Colloid Interface Sci.* 104, 416–421. doi:10.1016/0021-9797(85)90050-5.

Silva, S. V., and Malcata, F. X. (2005). Caseins as source of bioactive peptides. *Int. Dairy J.* 15, 1–15. doi:10.1016/j.idairyj.2004.04.009.

Simmer, J. P., and Hu, J. C. (2001). Dental enamel formation and its impact on clinical dentistry. *J. Dent. Educ.* 65, 896–905. doi:10.1016/0300-5712(88)90052-8.

Sreerama, N., and Woody, R. W. (2000). Estimation of protein secondary structure from circular dichroism spectra: comparison of CONTIN, SELCON, and CDSSTR methods with an expanded reference set. *Anal. Biochem.* 287, 252–260. doi:10.1006/abio.2000.4880.

Sreerama, N., and Woody, R. W. (2004). On the analysis of membrane protein circular dichroism spectra. *Protein Sci.* 13, 100–112. doi:10.1110/ps.03258404.

Subburaman, K., Pernodet, N., Kwak, S. Y., DiMasi, E., Ge, S., Zaitsev, V., et al. (2006). Templated biomineralization on self-assembled protein fibers. *Proc. Natl. Acad. Sci.* 103, 14672–14677. doi:10.1073/pnas.0602952103.

Takeuchi, A., Ohtsuki, C., Miyazaki, T., Kamitakahara, M., Ogata, S., Yamazaki, M., et al. (2005). Heterogeneous nucleation of hydroxyapatite on protein: structural effect of silk sericin. *J. R. Soc. Interface* 2, 373–378.

doi:10.1098/rsif.2005.0052.

Tejeda-Montes, E., Klymov, A., Nejadnik, M. R., Alonso, M., Rodriguez-Cabello, J. C., Walboomers, X. F., et al. (2014a). Mineralization and bone regeneration using a bioactive elastin-like recombinamer membrane. *Biomaterials* 35, 8339–47. doi:10.1016/j.biomaterials.2014.05.095.

Tejeda-Montes, E., Smith, K. H., Poch, M., López-Bosque, M. J., Martín, L., Alonso, M., et al. (2012). Engineering membrane scaffolds with both physical and biomolecular signaling. *Acta Biomater.* 8, 998–1009. doi:10.1016/j.actbio.2011.09.005.

Tejeda-Montes, E., Smith, K. H., Rebollo, E., Gómez, R., Alonso, M., Rodriguez-Cabello, J. C., et al. (2014b). Bioactive membranes for bone regeneration applications: effect of physical and biomolecular signals on mesenchymal stem cell behavior. *Acta Biomater.* 10, 134–41. doi:10.1016/j.actbio.2013.09.001.

Ten Cate, J. M., and Featherstone, J. D. B. (1991). Mechanistic Aspects of the Interactions Between Fluoride and Dental Enamel. *Crit. Rev. Oral Biol. Med.* 2, 283–296.

Tercinier, L., Ye, A., Anema, S. G., Singh, A., and Singh, H. (2014). Interactions of casein micelles with calcium phosphate particles. *J. Agric. Food Chem.* 62, 5983–5992. doi:10.1021/jf5018143.

Tsuji, T., Onuma, K., Yamamoto, A., Iijima, M., and Shiba, K. (2008). Direct transformation from amorphous to crystalline calcium phosphate facilitated by motif-programmed artificial proteins. *Proc. Natl. Acad. Sci. U. S. A.* 105, 16866–70. doi:10.1073/pnas.0804277105.

Urry, D., Luan, C., and Parker, T. (1991). Temperature of polypeptide inverse temperature transition depends on mean residue hydrophobicity. *J. ...* 113, 4346–4348. doi:10.1021/ja00011a057.

Urry, D. W. (1978). Molecular perspectives of vascular wall structure and disease: the elastic component. *Perspect. Biol. Med.* 21, 265–295. doi:10.1353/pbm.1978.0038.

Urry, D. W. (1992). Free energy transduction in polypeptides and proteins based on inverse temperature transitions. *Prog. Biophys. Mol. Biol.* 57, 23–57. doi:10.1016/0079-6107(92)90003-O.

Urry, D. W., Long, M. M., Cox, B. A., Ohnishi, T., Mitchell, L. W., and Jacobs, M. (1974). The synthetic polypentapeptide of elastin coacervates and forms filamentous aggregates. *BBA - Protein Struct.* 371, 597–602. doi:10.1016/0005-2795(74)90057-9.

Urry, D. W., Long, M. M., and Gross, E. (1976). Conformations of the Repeat Peptides of Elastin in Solution: An Application of Proton and Carbon-13 Magnetic Resonance to the Determination of Polypeptide Secondary Structure. *CRC Crit. Rev. Biochem.* 4, 1–45. doi:10.3109/10409237609102557.

Urry, D. W., Peng, S. Q., Hayes, L. C., McPherson, D., Xu, J., Woods, T. C., et al. (1998). Engineering protein-based machines to emulate key steps of metabolism (biological energy conversion). *Biotechnol. Bioeng.* 58, 175–190. doi:10.1002/(SICI)1097-0290(19980420)58:2/3<175::AID-BIT10>3.0.CO;2-C.

Vashisht, R., Kumar, A., Indira, R., Srinivasan, M. R., and Ramachandran, S. (2010). Remineralization of early enamel lesions using casein phosphopeptide amorphous calcium Phosphate: an ex-vivo study. *Contemp. Clin. Dent.* 1, 210–3. doi:10.4103/0976-237X.76385.

Vekilov, P. G. (2010). Nucleation. *Cryst. Growth Des.* 10, 5007–5019. doi:10.1021/cg1011633.

Vogler, E. A. (2012). Protein adsorption in three dimensions. *Biomaterials* 33, 1201–1237. doi:10.1016/j.biomaterials.2011.10.059.

Volmer, M. (1939). Kinetik der Phasenbildung. *Steinkopff: Dresden*.

Vrhovski, B., and Weiss, A. S. (1998). Biochemistry of tropoelastin. *Eur. J. Biochem.* 258, 1–18. doi:10.1046/j.1432-1327.1998.2580001.x.

Wang, L., and Nancollas, G. H. (2008). Calcium orthophosphates: crystallization and dissolution. *Chem. Rev.* 108, 4628–69. doi:10.1021/cr0782574.

Wang, Y., Lin, K., Wu, C., Liu, X., and Chang, J. (2015). Preparation of hierarchical enamel-like structures from nano- to macro-scale, regulated by inorganic templates derived from enamel. *J. Mater. Chem. B* 3, 65–71. doi:10.1039/C4TB01476F.

Weiner, S., Talmon, Y., and Traub, W. (1983). Electron diffraction of mollusc shell organic matrices and their relationship to the mineral phase. *Int. J. Biol. Macromol.* 5, 325–328. doi:10.1016/0141-8130(83)90055-7.

Weis-Fogh, T., and Anderson, S. O. (1970). New molecular model for the long-range elasticity of elastin. *Nature* 227, 718–721. doi:10.1038/227718a0.

What-when-how.com (2018). BETA-TURNS (MOLECULAR BIOLOGY). Available at: http://what-when-how.com/molecular-biology/beta-turns-molecular-biology/ [Accessed January 27, 2018].

White, S. N., Luo, W., Paine, M. L., Fong, H., Sarikaya, M., and Snead, M. L. (2001). Biological organization of hydroxyapatite crystallites into a fibrous continuum toughens and controls anisotropy in human enamel. *J. Dent. Res.* 80, 321–6. doi:10.1177/00220345010800010501.

Wojciechowski, P., Ten Hove, P., and Brash, J. L. (1986). Phenomenology and mechanism of the transient adsorption of fibrinogen from plasma (Vroman effect). *J. Colloid Interface Sci.* 111, 455–465. doi:10.1016/0021-9797(86)90048-2.

Wopenka, B., and Pasteris, J. D. (2005). A mineralogical perspective on the apatite in bone. *Mater. Sci. Eng. C* 25, 131–143. doi:10.1016/j.msec.2005.01.008.

Xie, J., Riley, C., and Chittur, K. (2001). Effect of albumin on brushite transformation to hydroxyapatite. *J. Biomed. Mater. Res.* 57, 357–365. doi:10.1002/1097-4636(20011205)57:3<357::AID-JBM1178>3.0.CO;2-1.

Xie, J., Riley, C., Kumar, M., and Chittur, K. (2002). FTIR/ATR study of protein adsorption and brushite transformation to hydroxyapatite. *Biomaterials* 23, 3609–3616. doi:10.1016/S0142-9612(02)00090-X.

Xin, R., Leng, Y., and Wang, N. (2006). In situ TEM examinations of octacalcium phosphate to hydroxyapatite transformation. *J. Cryst. Growth* 289, 339–344. doi:10.1016/j.jcrysgro.2005.11.010.

Yamagishi, K., Onuma, K., Suzuki, T., Okada, F., Tagami, J., Otsuki, M., et al. (2005). Materials chemistry: a synthetic enamel for rapid tooth repair. *Nature* 433, 819. doi:10.1038/433819a.

Yang, W. H., Xi, X. F., Li, J. F., and Cai, K. Y. (2013). Comparison of crystal structure between carbonated hydroxyapatite and natural bone apatite with theoretical calculation. *Asian J. Chem.* 25, 3673–3678.

Young, R. A., and Mackie, P. E. (1980). Crystallography of human tooth enamel: Initial structure refinement. *Mater. Res. Bull.* 15, 17–29. doi:10.1016/0025-5408(80)90155-5.

Zeng, L., Jiang, L., Teng, W., Cappello, J., Zohar, Y., and Wu, X. (2014). Engineering aqueous fiber assembly into silk-elastin-like protein polymers. *Macromol. Rapid Commun.* 35, 1273–1279. doi:10.1002/marc.201400058.

Zhao, J., Liu, Y., Sun, W., and Zhang, H. (2011). Amorphous calcium phosphate and its application in dentistry. *Chem. Cent. J.* 5, 40. doi:10.1186/1752-153X-5-40.

Appendix A: STNA15-ELP Product Information

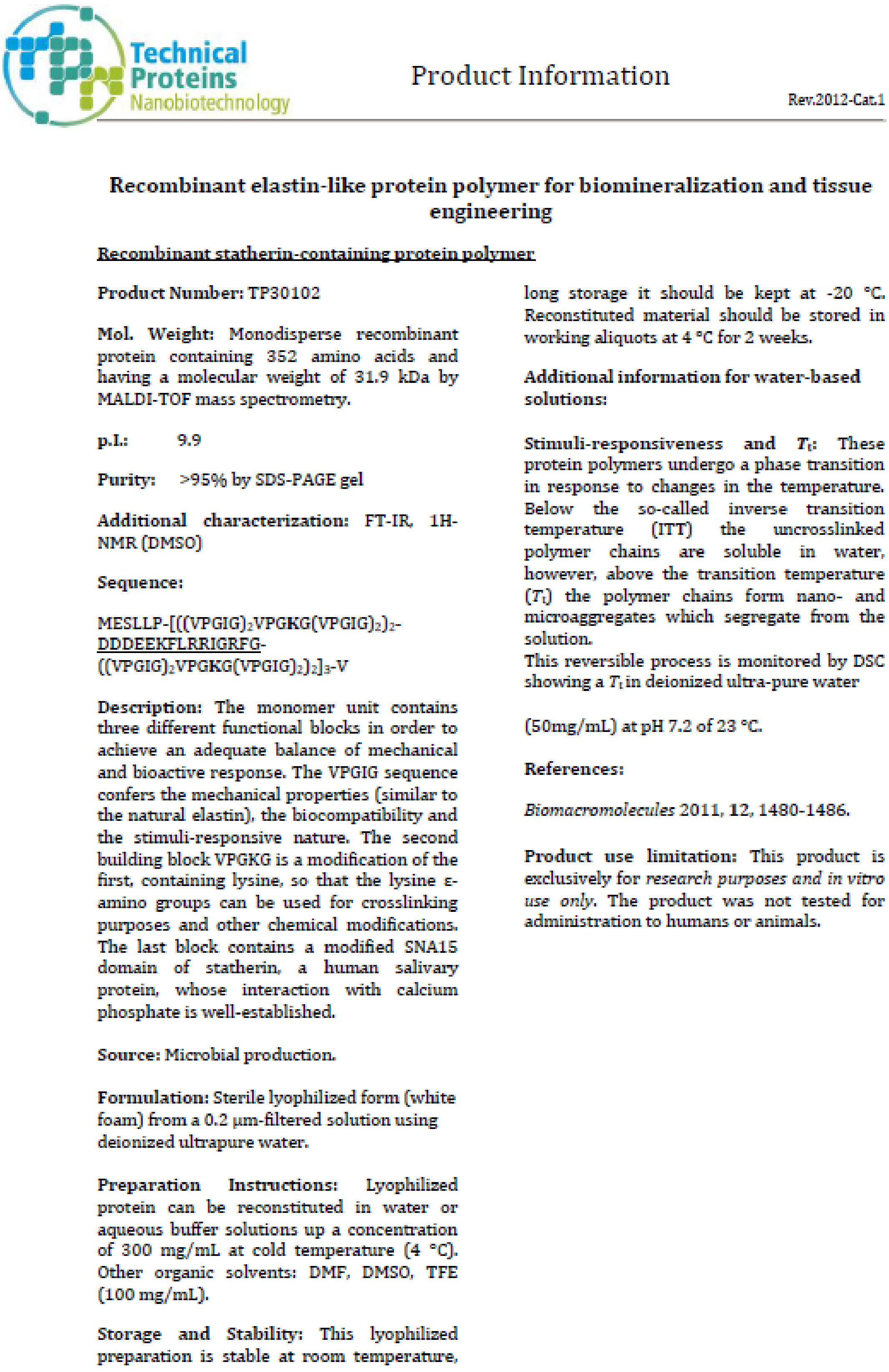

Technical Proteins Nanobiotechnology

Product Information

Rev.2012-Cat.1

Recombinant elastin-like protein polymer for biomineralization and tissue engineering

Recombinant statherin-containing protein polymer

Product Number: TP30102

Mol. Weight: Monodisperse recombinant protein containing 352 amino acids and having a molecular weight of 31.9 kDa by MALDI-TOF mass spectrometry.

p.I.: 9.9

Purity: >95% by SDS-PAGE gel

Additional characterization: FT-IR, 1H-NMR (DMSO)

Sequence:

MESLLP-[((VPGIG)$_2$VPGKG(VPGIG)$_2$)$_2$-
DDDEEKFLRRIGRFG-
((VPGIG)$_2$VPGKG(VPGIG)$_2$)$_2$]$_3$-V

Description: The monomer unit contains three different functional blocks in order to achieve an adequate balance of mechanical and bioactive response. The VPGIG sequence confers the mechanical properties (similar to the natural elastin), the biocompatibility and the stimuli-responsive nature. The second building block VPGKG is a modification of the first, containing lysine, so that the lysine ε-amino groups can be used for crosslinking purposes and other chemical modifications. The last block contains a modified SNA15 domain of statherin, a human salivary protein, whose interaction with calcium phosphate is well-established.

Source: Microbial production.

Formulation: Sterile lyophilized form (white foam) from a 0.2 µm-filtered solution using deionized ultrapure water.

Preparation Instructions: Lyophilized protein can be reconstituted in water or aqueous buffer solutions up a concentration of 300 mg/mL at cold temperature (4 °C). Other organic solvents: DMF, DMSO, TFE (100 mg/mL).

Storage and Stability: This lyophilized preparation is stable at room temperature, long storage it should be kept at -20 °C. Reconstituted material should be stored in working aliquots at 4 °C for 2 weeks.

Additional information for water-based solutions:

Stimuli-responsiveness and T_t: These protein polymers undergo a phase transition in response to changes in the temperature. Below the so-called inverse transition temperature (ITT) the uncrosslinked polymer chains are soluble in water, however, above the transition temperature (T_t) the polymer chains form nano- and microaggregates which segregate from the solution.
This reversible process is monitored by DSC showing a T_t in deionized ultra-pure water

(50mg/mL) at pH 7.2 of 23 °C.

References:

Biomacromolecules 2011, 12, 1480-1486.

Product use limitation: This product is exclusively for *research purposes and in vitro use only*. The product was not tested for administration to humans or animals.

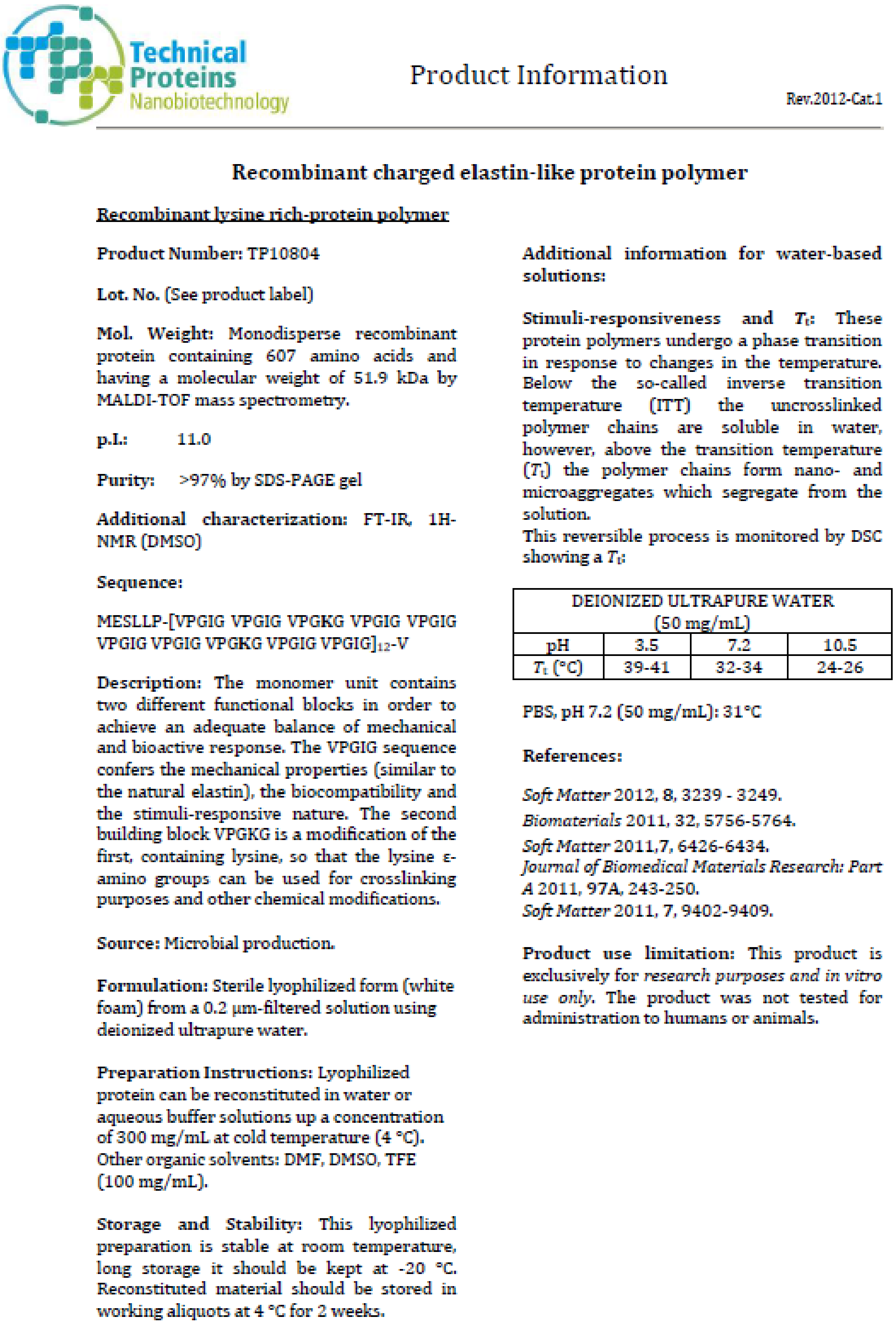

Technical Proteins
Nanobiotechnology

Product Information

Rev.2012-Cat.1

Recombinant charged elastin-like protein polymer

Recombinant lysine rich-protein polymer

Product Number: TP10804

Lot. No. (See product label)

Mol. Weight: Monodisperse recombinant protein containing 607 amino acids and having a molecular weight of 51.9 kDa by MALDI-TOF mass spectrometry.

p.I.: 11.0

Purity: >97% by SDS-PAGE gel

Additional characterization: FT-IR, 1H-NMR (DMSO)

Sequence:

MESLLP-[VPGIG VPGIG VPGKG VPGIG VPGIG VPGIG VPGIG VPGKG VPGIG VPGIG]$_{12}$-V

Description: The monomer unit contains two different functional blocks in order to achieve an adequate balance of mechanical and bioactive response. The VPGIG sequence confers the mechanical properties (similar to the natural elastin), the biocompatibility and the stimuli-responsive nature. The second building block VPGKG is a modification of the first, containing lysine, so that the lysine ε-amino groups can be used for crosslinking purposes and other chemical modifications.

Source: Microbial production.

Formulation: Sterile lyophilized form (white foam) from a 0.2 µm-filtered solution using deionized ultrapure water.

Preparation Instructions: Lyophilized protein can be reconstituted in water or aqueous buffer solutions up a concentration of 300 mg/mL at cold temperature (4 °C). Other organic solvents: DMF, DMSO, TFE (100 mg/mL).

Storage and Stability: This lyophilized preparation is stable at room temperature, long storage it should be kept at -20 °C. Reconstituted material should be stored in working aliquots at 4 °C for 2 weeks.

Additional information for water-based solutions:

Stimuli-responsiveness and T_t: These protein polymers undergo a phase transition in response to changes in the temperature. Below the so-called inverse transition temperature (ITT) the uncrosslinked polymer chains are soluble in water, however, above the transition temperature (T_t) the polymer chains form nano- and microaggregates which segregate from the solution.
This reversible process is monitored by DSC showing a T_t:

DEIONIZED ULTRAPURE WATER (50 mg/mL)			
pH	3.5	7.2	10.5
T_t (°C)	39-41	32-34	24-26

PBS, pH 7.2 (50 mg/mL): 31 °C

References:

Soft Matter 2012, 8, 3239 - 3249.
Biomaterials 2011, 32, 5756-5764.
Soft Matter 2011,7, 6426-6434.
Journal of Biomedical Materials Research: Part A 2011, 97A, 243-250.
Soft Matter 2011, 7, 9402-9409.

Product use limitation: This product is exclusively for *research purposes and in vitro use only*. The product was not tested for administration to humans or animals.

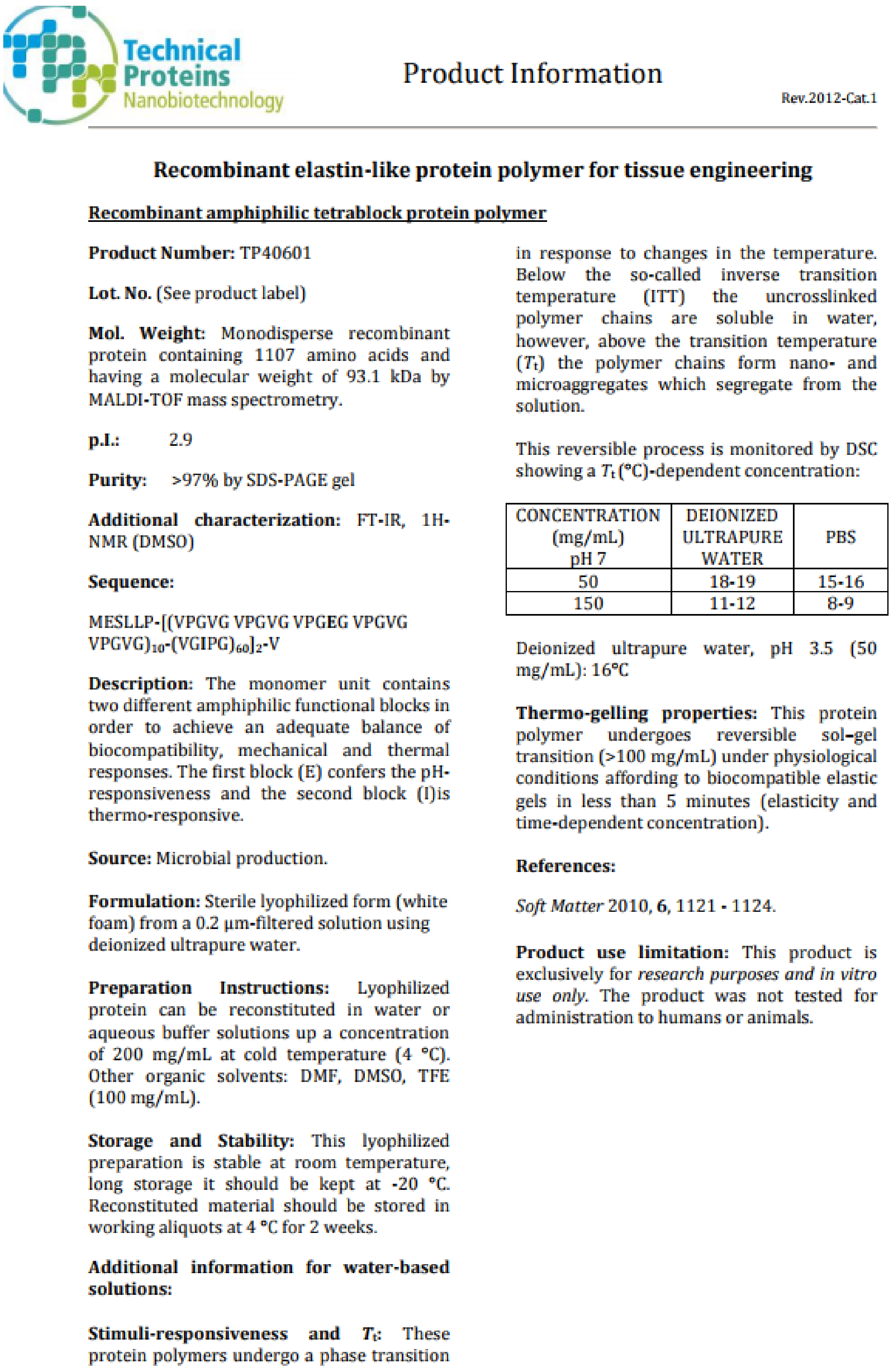

Technical Proteins Nanobiotechnology

Product Information

Rev.2012-Cat.1

Recombinant elastin-like protein polymer for tissue engineering

Recombinant amphiphilic tetrablock protein polymer

Product Number: TP40601

Lot. No. (See product label)

Mol. Weight: Monodisperse recombinant protein containing 1107 amino acids and having a molecular weight of 93.1 kDa by MALDI-TOF mass spectrometry.

p.I.: 2.9

Purity: >97% by SDS-PAGE gel

Additional characterization: FT-IR, 1H-NMR (DMSO)

Sequence:

MESLLP-[(VPGVG VPGVG VPGEG VPGVG VPGVG)$_{10}$-(VGIPG)$_{60}$]$_2$-V

Description: The monomer unit contains two different amphiphilic functional blocks in order to achieve an adequate balance of biocompatibility, mechanical and thermal responses. The first block (E) confers the pH-responsiveness and the second block (I)is thermo-responsive.

Source: Microbial production.

Formulation: Sterile lyophilized form (white foam) from a 0.2 µm-filtered solution using deionized ultrapure water.

Preparation Instructions: Lyophilized protein can be reconstituted in water or aqueous buffer solutions up a concentration of 200 mg/mL at cold temperature (4 °C). Other organic solvents: DMF, DMSO, TFE (100 mg/mL).

Storage and Stability: This lyophilized preparation is stable at room temperature, long storage it should be kept at -20 °C. Reconstituted material should be stored in working aliquots at 4 °C for 2 weeks.

Additional information for water-based solutions:

Stimuli-responsiveness and T_t: These protein polymers undergo a phase transition in response to changes in the temperature. Below the so-called inverse transition temperature (ITT) the uncrosslinked polymer chains are soluble in water, however, above the transition temperature (T_t) the polymer chains form nano- and microaggregates which segregate from the solution.

This reversible process is monitored by DSC showing a T_t (°C)-dependent concentration:

CONCENTRATION (mg/mL) pH 7	DEIONIZED ULTRAPURE WATER	PBS
50	18-19	15-16
150	11-12	8-9

Deionized ultrapure water, pH 3.5 (50 mg/mL): 16°C

Thermo-gelling properties: This protein polymer undergoes reversible sol-gel transition (>100 mg/mL) under physiological conditions affording to biocompatible elastic gels in less than 5 minutes (elasticity and time-dependent concentration).

References:

Soft Matter 2010, **6**, 1121 - 1124.

Product use limitation: This product is exclusively for *research purposes and in vitro use only*. The product was not tested for administration to humans or animals.